

Technische Universität München
Institut für Energietechnik

Lehrstuhl für Thermodynamik

Experimental Investigation and Spectral Modeling of Turbulent Combustion Noise from Premixed and Non-Premixed Flames

Christoph Martin Jörg

Vollständiger Abdruck der von der Fakultät für Maschinenwesen der
Technischen Universität München zur Erlangung des akademischen Grades
eines

DOKTOR – INGENIEURS

genehmigten Dissertation.

Vorsitzender:

Univ.-Prof. Dr. C. L. Bottasso

Prüfer der Dissertation:

1. Univ.-Prof. Dr.-Ing. T. Sattelmayer
2. Assoc. Prof. Dr. ir. J. B. W. Kok,
University of Twente / Niederlande

Die Dissertation wurde am 08.09.2014 bei der Technischen Universität München eingereicht
und durch die Fakultät für Maschinenwesen am 14.04.2015 angenommen.

It is unfortunately true that reference to the general equation (10)

$$P = \frac{\kappa}{4\pi} \frac{(\gamma - 1)^2}{\bar{\rho} \bar{c}^5} f^2 \dot{m}_f H Q_{\max} V_{\text{cor}}$$

[...] leads to some pessimism in the case of noise reduction. This negative view holds because considerations other than noise usually determine most of the factors. That is, one could not seriously suggest altering the chemical kinetic rates or the total firing rate. Moreover, the characteristic impedance is not generally at the designer's command, nor is the fuel-heating value.

- W. C. Strahle
A More Modern Theory of Combustion Noise [130]

Vorwort

Die vorliegende Dissertation entstand während meiner Tätigkeit als wissenschaftlicher Mitarbeiter am Lehrstuhl für Thermodynamik der Technischen Universität München. Sie wurde zu großen Teilen durch die Deutsche Forschungsgemeinschaft gefördert.

Meinem Doktorvater, Herrn Professor Dr.-Ing. Thomas Sattelmayer, möchte ich für die Betreuung dieser Arbeit und die Übernahme des Hauptreferats meinen besonderen Dank aussprechen. Er hat mir durch konstruktive Diskussionen, gezieltes Hinterfragen und gleichzeitig durch den mir gewährten wissenschaftlichen Freiraum wichtige Fähigkeiten vermittelt, die entscheidend zum Gelingen dieser Arbeit beigetragen haben. Assoc. Prof. Dr. ir. J. B. W. Kok danke ich für die Übernahme des Koreferats und Univ.-Prof. Dr. C. L. Bottasso für die freundliche Übernahme des Vorsitzes bei der mündlichen Prüfung.

Dr.-Ing. Christoph Hirsch danke ich für die vielen hilfreichen Hinweise in experimentellen und theoretischen Fragestellungen. Bei Dr. Achim Holzwarth von der Webasto Thermo & Comfort SE bedanke ich mich für die gute Zusammenarbeit im Rahmen des Projekts. Mein Dank geht auch an das Sekretariat und die mechanische Werkstatt für ihre unentbehrliche Unterstützung.

Meinen langjährigen Bürokollegen Patrick Dems und Thomas Fiala danke ich vielmals für die fachlichen Diskussionen und die freundschaftliche Atmosphäre in unserem Büro. In guter Erinnerung wird mir immer die kollegiale Zusammenarbeit und der Zusammenhalt unter den Promovierenden bleiben. Für hilfreiche Gespräche, gemeinsame Unternehmungen und ihre Freundschaft sei an dieser Stelle (in alphabetischer Reihenfolge) Denise Ahrens, Georg Baumgartner, Alejandro Cárdenas, Balbina Hampel, Josef Haßberger, Stephan Parzinger, Michael Wagner und Johannes Weinzierl gedankt. Stellvertretend für alle Studenten und wissenschaftlichen Hilfskräfte, die durch ihre Mitarbeit zum Erfolg dieser Arbeit beigetragen haben, möchte ich meinen späteren Kollegen Peter Katzy und Armin Witte danken.

Abschließend danke ich von ganzem Herzen meinen Eltern und meiner Familie für ihre fortwährende Unterstützung, ihr Vertrauen und den Rückhalt während meiner gesamten Ausbildung.

München, im Juli 2015

Christoph Jörg

Kurzfassung

Die vorliegende Arbeit beschäftigt sich mit der numerischen Vorhersage des von turbulenten Flammen abgestrahlten Lärmspektrums. Dazu wurde ein bestehendes semi-analytisches Modell für Vormischflammen auf nicht vorgemischte Flammen erweitert. Begleitende Experimente lieferten Daten über das Abstrahlverhalten von turbulenten Drallflammen bei verschiedenen Betriebsbedingungen. Die gemessenen Daten dienten zur Validierung des erweiterten Lärmmodells und der darin enthaltenen Modellannahmen.

Eine auf globalen Chemilumineszenzmessungen basierende Korrekturmethode wurde entwickelt, die es ermöglicht, die Menge des tatsächlich reagierenden Frischgases an offenen vorgemischten Flammen zu bestimmen. Das Verfahren erlaubt den direkten Vergleich zwischen gemessenen Lärmspektren von vorgemischten und nicht vorgemischten Flammen und den numerischen Ergebnissen.

Die globale Wärmefreisetzung und die Luftzahl sind die wesentlichen Einflussfaktoren bezüglich des abgestrahlten Lärms turbulenter Flammen. Diese Parameter bestimmen im Wesentlichen die thermische Leistungsdichte der Flamme. Werden nicht vorgemischte und vorgemischte Flammen bei ähnlichen Bedingungen hinsichtlich Strömung und Mischungszusammensetzung betrieben, zeigt sich ein ähnliches Abstrahlverhalten beider Flammentypen.

Die im Experiment beobachteten Trends und Einflüsse werden durch das erweiterte Modell korrekt wiedergegeben. In einem weiteren Schritt wird das Modell auf ein serienmäßiges Wasserheizgerät angewendet. Kombiniert mit einer einfachen numerischen Modellierung der Schallausbreitung innerhalb des Geräts gelingt die korrekte Vorhersage des abgestrahlten Lärms, was die Anwendbarkeit der entwickelten Methode auf industrielle Verbrennungssysteme unter Beweis stellt.

Abstract

The study at hand extends an existing theory of turbulent combustion noise for premixed flames towards the prediction of noise spectra from non-premixed flames. Based on a numerical simulation of the mean reactive flow field, the theoretical combustion noise model predicts the radiated noise spectra. An experimental campaign investigating the influence of flame operating parameters on the spectral noise emission from open natural gas swirl flames delivered reference data to validate the introduced model extensions accounting for the characteristics of noise emission from non-premixed flames.

A novel experimental procedure for the quantification of fuel burnout of open premixed swirl flames under the influence of entrainment ensures comparability between numerical predictions and experimental data recorded from premixed and non-premixed flames.

The results show, that thermal power output and mixture composition are the primary factors of influence governing combustion noise emission. These quantities are closely related to the thermal power density of the flame. Also, premixed and non-premixed flames possess similar noise emission characteristics when operated under similar flow and mixture conditions. Observed trends and amplitude levels can be correctly reproduced by the extended combustion noise model, which enables noise prediction using the developed numerical tool from time averaged simulation data.

In a further step, the model was applied to a commercial marine heating unit. In combination with a simple numerical model of sound propagation inside the heater, the spectrum of the radiated noise was successfully predicted, demonstrating the applicability of the developed approach to typical problems of industrial development.

Contents

	Page
Notation	xv
1 Introduction	1
1.1 Combustion Noise	3
1.2 Prediction of Combustion Noise	8
1.3 Thesis Structure	10
2 Reacting Turbulent Flows	13
2.1 Characteristics of Turbulent Flows	13
2.1.1 Model Spectrum of Turbulence Kinetic Energy	18
2.1.2 Turbulent Swirling Flow	20
2.2 Turbulent Combustion	21
2.2.1 Non-Premixed Combustion	23
2.2.2 Premixed Combustion	25
2.3 Simulation of Turbulent Reacting Flow	28
2.3.1 Averaged Balance Equations	30
2.3.2 Turbulence Modeling	32
2.3.3 Combustion Modeling	34
3 Acoustic Theory	43
3.1 Combustion Noise	43
3.2 Sound Propagation in One-Dimensional Geometries	49
3.3 Acoustic Boundary Conditions	50
3.3.1 Reflection at an Open Pipe End at Ambient Conditions . . .	51
3.3.2 Reflection at an Open Pipe End at Elevated Temperatures .	53
3.4 Measurement of Sound Intensity	55
3.5 Logarithmic Scales	58

4	Spectral Modeling of Turbulent Combustion Noise	59
4.1	The Spectrum of Heat Release	59
4.2	Premixed Turbulent Flames	62
4.2.1	Scaling of the Spectral Amplitude	62
4.2.2	Wave-Number Frequency Transformation	63
4.2.3	Relation Between Lagrangian Frequency and Correlation Spectrum	64
4.2.4	Cutoff Length Scale	64
4.2.5	Statistical Volume of Coherent Heat Release	65
4.2.6	Acoustic Power Spectrum of the Premixed Flame	66
4.3	Non-Premixed Turbulent Flames	67
4.3.1	Coherence Volume	67
4.3.2	Wave-Number Frequency Transformation	68
4.3.3	Generalized Scaling of the Spectral Amplitude	69
4.4	Analysis of Model Characteristics	73
5	Experimental Setup and Measurement Equipment	79
5.1	Open Turbulent Flame Test Rig	79
5.2	Movable Block Swirl Burner	82
5.3	Improvement of Laboratory Acoustics	86
5.4	Measurement Procedure for Acoustic Power Spectra	88
5.5	Determination of Peak Frequency	92
5.6	Measurement Technique for Acoustic Intensity	94
5.7	Repeatability of Intensity Measurements	95
5.8	Chemiluminescence	96
6	Turbulent Combustion Noise from Non-Premixed and Premixed Swirl Flames	99
6.1	Non-Premixed Flame	99
6.1.1	Influence of Thermal Power	100
6.1.2	Influence of Mixture Composition	103
6.1.3	Influence of Swirl Strength	105
6.1.4	Matrix Study on Mixture Composition and Thermal Power	107
6.2	Premixed Flame	109
6.2.1	Fuel Burnout Efficiency of Open Premixed Flames	109

6.2.2 Influence of Thermal Power	115
6.3 Comparison of Conversion Efficiencies Between Premixed and Non-Premixed Flames	116
7 Prediction of Spectral Noise Emission from Turbulent Natural Gas Swirl Flames	121
7.1 Calculation Cycle of Combustion Noise Prediction for Premixed and Non-Premixed Cases	121
7.2 Premixed Flame Simulation	123
7.2.1 CFD-Results	124
7.2.2 Acoustic Results	128
7.3 Non-Premixed Flame Simulation	132
7.3.1 CFD-Results	132
7.3.2 Acoustic Results	137
7.4 Summary of Numerical Results	144
8 Model Application to a Marine Heating Unit	145
8.1 Small Burner Test Rig	145
8.2 Experimental Results	147
8.3 Acoustic Network Model	149
8.4 Noise Source	153
8.5 Numerical Results	153
9 Concluding Remarks	157
Appendix	159
A Mean and Standard Deviation of the Clipped Gaussian Distribution	161
B Iterative Calculation of Adiabatic Flame Temperatures	165
C Acoustic Network Elements	167
C.1 Reflecting End	167
C.2 Duct Element of Uniform Cross Section	168
C.3 Discontinuity in Cross-Sectional Area	168

CONTENTS

List of Figures	171
List of Tables	181
References	183

Notation

Latin Characters

A	clipped Gaussian PDF parameter	-
a	pipe radius	m
a	thermal diffusivity	m ² /s
B	clipped Gaussian PDF parameter	-
C	constant	-
c	reaction progress	-
c	speed of sound	m/s
c'^2	reaction progress variance	-
C_D	constant in the combustion noise model	-
C_d, C_g	constants in the transport equation for the mixture fraction variance	-
C_{EBU}	constant in the eddy break-up combustion model	-
c_ϕ	constant in the peak frequency model	-
c_1	length scale constant in the combustion noise model	-
$c_\mu, c_k, c_{\epsilon_1}, c_{\epsilon_2}$	constants of the k - ϵ model	-
c_p	specific heat capacity at constant pressure	J/(kg K)
C_S	amplitude scaling function of the combustion noise model	-
C_{Schmid}	constant in the Schmid combustion model	-
c_τ	time scale constant in the combustion noise model	-
C_T	virtual concentration in eddy dissipation model	-
c_v	specific heat capacity at constant volume	J/(kg K)
D	diameter	m
d	intensity probe spacer length	m
D	diffusion coefficient	m ² /s
E	specific total energy	J/kg
e	specific internal energy	J/kg
E	velocity spectrum	m ² /s
E_A	activation energy	J/mol
E_q	wave-number spectrum of heat release	W/m ²
f	Riemann invariant propagating downstream	m/s
f	frequency	Hz
f_{peak}	peak frequency	Hz

Notation

f_s	sampling frequency	Hz
g	Riemann invariant propagating upstream	m/s
g	acceleration of gravity	m ² /s
G_{11}	auto-power spectral density	1/Hz
G_{12}	cross-power spectral density	1/Hz
G_ϕ	axial flux of angular momentum	m ² kg/s ²
G_x	flux of axial momentum	m ² kg/s ²
ΔH_r	heat of reaction	J/kg
H_u	lower heating value	J/kg
I	active acoustic intensity	W/m ²
i	imaginary unit	-
i	numerical index	-
J	reactive acoustic intensity	W/m ²
k	numerical index	-
k	turbulence kinetic energy	m ² /s ²
l_c	Corrsin length scale	m
l_{coh}	coherence length scale	m
l_g	Gibson length scale	m
L_I	amplitude level of acoustic intensity	dB
L_P	amplitude level of acoustic pressure	dB
l_t	integral length scale	m
L_W	amplitude level of acoustic power	dB
l_z	mixing zone thickness	m
\dot{m}	mass flow rate	kg/s
N	number of samples	-
n	numerical index	-
p	pressure	Pa
P_{aco}	sound power	kW
P_{th}	thermal power	kW
\dot{q}_v	volumetric rate of heat release	W/m ³
R	gas constant	J/(kg K)
R	outer burner radius	m
R	two point correlation function	-
r	acoustic pressure reflection coefficient	-
r_c	vortex core radius	m
r_E	acoustic energy reflection coefficient	-
S	surface area	m ²
S	swirl number	-
s	entropy	J/K
s_l	laminar flamespeed	m/s
S_m	momentum source	m ² kg/s ²
s_t	turbulent flamespeed	m/s
T	temperature	K
t	time	s
T_{ij}	transfer matrix element	-

T_s	signal duration	s
T'^2	temperature variance	K
u_{kol}	Kolmogorov velocity scale	m/s
u, v, w	cartesian velocity components	m/s
V	volume	m^3
V_{flame}	flame volume	m^3
V_{fv}	volume of finite volumes	m^3
V_{coh}	coherence volume	m^3
W	molecular weight	g/mol
X	molar concentration	mol/ m^3
Y	mass fraction	-
Z	acoustic impedance	N s/ m^3
z	mixture fraction	-
z'^2	mixture fraction variance	-

Greek Characters

α	acoustic absorption coefficient	-
α	angle	deg
α	constant in model spectrum	-
β	constant in model spectrum	-
β_r	exponent in the Arrhenius equation	-
χ_{qq}	correlation spectrum of fluctuating heat release	$(W/m^3)^2$
η_{coh}	coherence efficiency	-
δ	extended length scale	m
δ_{ij}	Kronecker symbol	-
δ_l	laminar flame thickness	m
δ_t	turbulent flame brush thickness	m
ε	turbulent dissipation rate	m^2/s^3
γ	heat capacity ratio	-
Γ	coherence function	-
η_{kol}	Kolmogorov length scale	m
η_{ta}	thermo-acoustic efficiency	-
κ	wave-number	1/m
λ	air excess ratio	-
μ	mean of PDF	-
μ	eddy viscosity	m^2/s
ν	kinematic viscosity	m^2/s
ν	stoichiometric coefficient	mol
ν_F	exponent in the Arrhenius equation	-
ν_{Ox}	exponent in the Arrhenius equation	-
ω	angular frequency	rad/s
$\dot{\omega}_c$	source term of reaction progress	kg/(m^3 s)
ρ	density	kg/ m^3
σ	standard deviation of PDF	-

Notation

σ_ε	constant of the k - ε model	-
ϑ	dimensionless temperature	-
τ	retarded time	s
τ_c	chemical time scale	s
τ_{kol}	Kolmogorov time scale	s
τ_{ij}	stress tensor	N/m ²
τ_t	turbulent time scale	s
ϑ'^2	dimensionless temperature variance	-
ϕ	equivalence ratio	-
ϕ	fuel injection hole angle	deg
ϕ	phase angle	rad
ξ	connecting function	-
$\xi_c'^2$	scalar dissipation rate of reaction progress variance	1/s
ζ_{CFD}	burnout calibration coefficient from CFD	-
ξ	variable block angle of the movable block swirler	deg
ξ_m	maximum block angle of the movable block swirler	deg
ζ_{OH}	burnout calibration coefficient from experiment	-

Abbreviations

AC	Area Change
APE	Acoustic Perturbation Equations
CAA	Computational Aero Acoustics
CMOS	Complementary Metal Oxide Semiconductor
D	Duct
JP4	Jet Propellant 4
CFD	Computational Fluid Dynamics
LES	Large Eddy Simulation
LPG	Liquefied Petroleum Gas
NG	Natural Gas
NP	Non-Premixed
P	Premixed
RANS	Reynolds averaged Navier-Stokes
R	Reflecting End
S	Source Element
TC	Temperature Change

Dimensionless Numbers

Da	Damköhler number
He	Helmholtz number
Ka	Karlovitz number
Le	Lewis number
Ma	Mach number
Re	Reynolds number

Sc Schmidt number

Superscripts

$\hat{\phi}^*$ complex conjugate of ϕ
 $\hat{\phi}$ complex variable ϕ
 $\tilde{\phi}$ Favre average of quantity ϕ
 ϕ' acoustic fluctuation of quantity ϕ
 ϕ'' turbulent fluctuation of quantity ϕ
 $\overline{\phi}$ time average of quantity ϕ
 $\vec{\phi}$ vector quantity ϕ

Subscripts

ad adiabatic
B related to the observer position
calib burnout calibrated
c related to the clipped PDF
 c'^2 related to the reaction progress variance
d downstream
f fuel
+, - wave propagation direction
n normal direction
ref reference condition
s conditions within the source
tot total
u unburnt

1 Introduction

A recent case scenario study completed by the European Commission on the development of energy consumption, origin, and pricing up to the year of 2050 predicts a continuous demand of fossil fuels for industry, transportation, and private homes [17]. Figure 1.1 shows the predicted development in energy consumption for transportation within the European Union for different sources of energy. The data demonstrates the enduring importance of fossil fuels and combustion technologies in future energy supply. Consequently, the continuous use of fossil fuels for future energy supply demands the development of combustion systems with increased efficiency and reduced pollutant emission. Modern combustion systems are frequently designed for operation with turbulent flames to account for these desired properties.

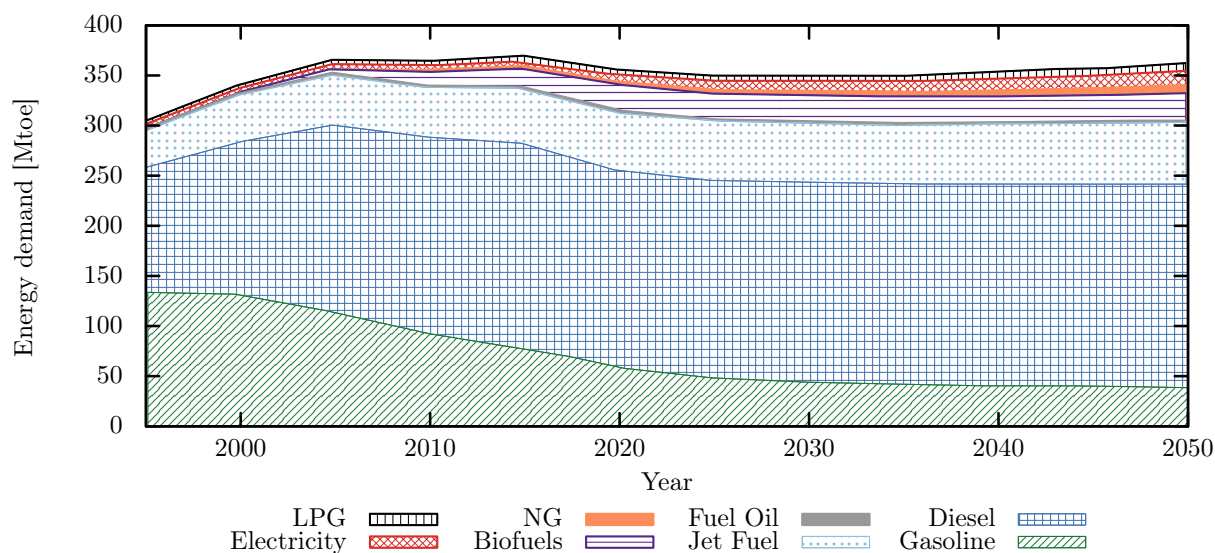


Figure 1.1: Predicted consumption of energy for transportation within the European Union to the year 2050, colored by origin of energy (adapted from [17]).

In turbulent flames, mixing processes between different chemical species or fresh gases and exhaust gases are greatly intensified in comparison to flames operated under laminar flow conditions. The enhanced mixing rates allow greater thermal power densities for technical combustion systems, where installation space or weight is of interest. The time-dependent turbulent fluctuations in mass fractions of chemical species taking part in the combustion reaction, as well as temperature, density, and other quantities influencing the chemical reaction rate are the origin of the acoustic broadband noise which is radiated by turbulent flames. The broadband noise is a characteristic property of turbulent combustion and can be observed in many everyday occasions, such as the hissing noise of a gas cooker or the sound of a flickering candle flame when blown into. Noise emitted by turbulent flames is of great concern in a wide field of technical applications reaching from small scale domestic heating units [103] to rocket motors [41, 113] and gas turbines [26, 131, 133].

In aero-engines, turbulent combustion noise remained a secondary source of noise for a long period of time, when compared to other sources of noise contributing to the overall acoustic emissions of aircraft engines. The overall noise emissions of low-bypass ratio aircraft engines have been dominated by the aerodynamic noise generated in the mixing process between the hot jet of exhaust gases and the ambient atmosphere. The introduction of higher bypass-ratios, and developments concerning nozzle geometry have assisted in reducing the generation and emission of jet noise. Chevron nozzles, visible as sawtooth shaped nozzle geometry on some modern engines, are a characteristic example of such a technology. Consequently, in the effort of further reducing noise radiation by commercial airplanes, previously unimportant sources of sound moved into focus [9, 133]. Internal noise sources of the engine, often termed "core-noise", are predominately related to the unsteady heat release rate within the turbulent flame [26, 85] inside the combustion chamber and thus, to turbulent combustion noise.

The effect of broadband noise emission by a flame can be twofold. First, the sheer emission of broadband noise is of concern in terms of noise regulations in many applications. Second, the broadband acoustic excitation signal provided by the flame may interact with the boundaries of the combustion chamber. Acoustic

pressure waves may be attenuated or reflected at boundaries or leave the combustion system through an intake or outlet opening. Reflected waves may repeatedly interact with the flame and can be amplified if the phase relation between acoustics and heat release is just right. In this case, acoustic energy is continuously fed into the system over time and resonance conditions are established, which may lead to very large pressure amplitudes. These resonance events are characterized by narrow frequency peaks in the spectrum of the acoustic pressure signal inside the combustion chamber, which noticeably exceed the adjacent amplitude levels.

Greater public awareness and more stringent environmental targets have assisted in increasing interest on noise radiation as an important category of a combustion system's overall emissions. This thesis addresses the issue of the broadband noise emission of turbulent flames, the processes linked to its generation and the numerical prediction of combustion noise spectra from turbulent non-premixed and premixed flames. A toolbox is developed, which allows the numerical prediction of combustion noise from premixed and non-premixed turbulent hydrocarbon flames based on an initial simulation of the time-averaged flow field.

1.1 Combustion Noise

Open burning turbulent flames emit a broadband hissing noise which is closely related to the unsteady rate of heat release in the flame [19]. The turbulent fluctuations in mixing rate, species concentrations and other parameters connected to the combustion process are influencing the frequency content of the spectrum of the emitted combustion noise. A macroscopic, descriptive example demonstrating the time dependent processes involved in the generation of combustion noise is given by the experiment performed by Thomas and Williams [136]. In their setup, soap bubbles of up to 5 cm in diameter were filled with different mixtures of combustible gases and ignited electrically. The experiment was set up in an anechoic enclosure and the acoustic pressure signal resulting from the combustion of the bubble was recorded by a microphone. Figure 1.2 shows a sketch of the bubble configuration alongside a typical pressure signal emitted by a reacting soap bubble of natural gas air filling and the Fourier transform of the signal time

series. The short-time pressure pulse in Fig. 1.2b results from the fast expansion of the flame front followed by a contraction which occurs shortly after the available mixture has been consumed and contains a wide range of frequencies. The observed frequency range is concentrated in the lower range below 1000Hz as visible from the signals Fourier transform in Fig. 1.2c. Pulse duration and amplitude levels are closely related to the flame propagation speed which mainly depends on the mixture composition regarding fuel type and air excess ratio. If an accumulation of reacting small scale gas parcels, as they occur in turbulent combustion is considered, the resulting broad band noise spectrum can be imagined to be composed from a large number of such combustion pulses.

The broad-band frequency spectrum emitted by turbulent hydrocarbon flames possesses prominent features, which are universally relevant, few exceptions aside, to a large number of different burner and mixture configurations. These characteristics apply to flames operated in an open environment or an acoustically non-reflective enclosure. Flames operated within a confined space (combustion chamber), acoustically interact with the boundaries of the confinement. The resulting noise spectrum departs from the universal shape of the open flame

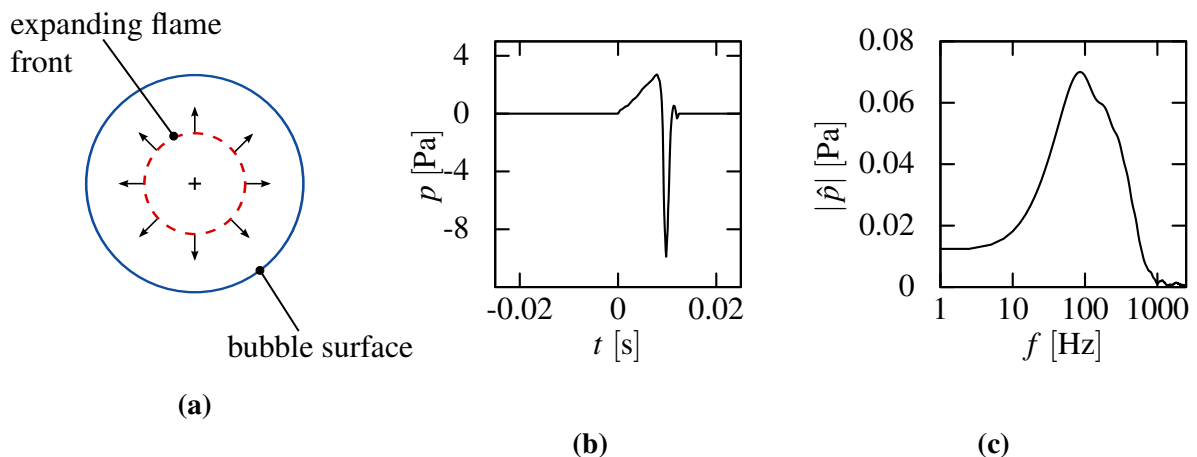


Figure 1.2: The experiment conducted by Thomas and Williams [136]. a): Soap bubble filled with combustible gaseous mixture undergoing combustion. b): Resulting time series of the radiated acoustic pressure. c): Magnitude of the corresponding signal Fourier transform over frequency f .

case. Figure 1.3 shows a typical spectrum of sound pressure emitted by a non-premixed turbulent natural gas (NG) swirl flame at a thermal power output of $P_{\text{th}} = 50\text{kW}$, an air excess ratio of $\lambda = 1.2$ and moderate swirl intensity. A com-

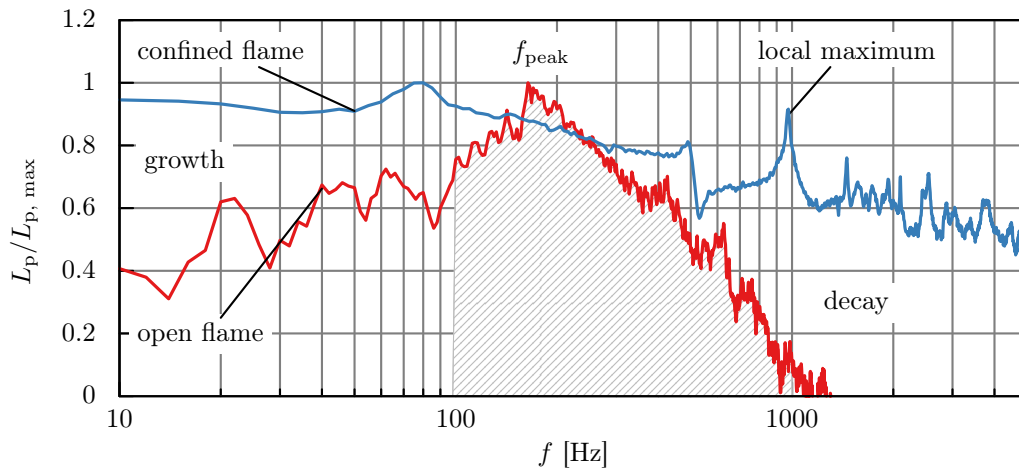


Figure 1.3: General shape of the spectrum of sound pressure emitted by an open burning turbulent swirl flame compared with the spectrum of a confined turbulent swirl flame inside a combustion chamber. The hatched area marks the typical frequency range for peak frequencies of turbulent hydrocarbon flames. Both spectra have been normalized with their corresponding maximum value for better comparability.

parison with a confined turbulent premixed swirl flame¹ of equal thermal power and $\lambda = 1.6$ is given in the red curve. The influence of the enclosure in the confined flame spectrum can be identified as distinct narrow banded peaks in the pressure amplitude. Clearly visible narrow peaks of several dB above the adjacent spectral amplitude levels (local maxima) are generally absent in the spectral noise from open turbulent flames.

There, amplitude levels monotonically increase with frequency until reaching a maximum, usually denoted by the peak-frequency f_{peak} [129]. The hatched area marks the approximate range of peak frequencies typically observed with hydrocarbon fueled flames, located in between $100\text{Hz} \lesssim f_{\text{peak}} \lesssim 1000\text{Hz}$. At frequencies in excess of f_{peak} , the spectrum decays monotonically with frequency. The total sound power emitted by the flame can be calculated by integrating the acoustic power spectrum over all frequencies. This total acoustic power output

¹ The confined flame pressure data was kindly provided by Dipl.-Ing. Michael Wagner.

P_{aco} can be compared to the thermal power setting of the flame P_{th} in the thermo-acoustic efficiency η_{ta}

$$\eta_{\text{ta}} = \frac{P_{\text{aco}}}{P_{\text{th}}}. \quad (1.1)$$

The well known ratio represents the efficiency of conversion between thermal and acoustic energy within the flame. Numbers reported in literature range in between low conversion efficiencies of $\eta_{\text{ta}} = 8 \cdot 10^{-9}$ [115] and $1 \cdot 10^{-5}$ [131] for turbulent hydrocarbon flames. f_{peak} and η_{ta} are used to characterize and distinguish combustion noise spectra from turbulent flames in this thesis.

Table 1.1 gives a summary of experimental studies on turbulent combustion noise conducted from the early 1960s until today which were considered in this thesis. The listed studies contain experiments on hydrocarbon fueled flames, such that the data from Tab. 1.1 may be used to determine ranges for peak frequency and thermo-acoustic efficiency of hydrocarbon flames and as a catalog of studies on turbulent combustion noise, which involves several different fuels. The following fundamental characteristics of influence for turbulent open burning hydrocarbon flames can be extracted from the studies summarized in Tab. 1.1:

- The emitted noise levels increase with the total firing rate and the flow Reynolds number.
- The nozzle shape impacts the noise spectrum by influencing turbulence intensity in the reaction zone.
- Fuel and fuel composition influence peak frequency and peak amplitude.
- Swirling motion of the reacting flow increases emitted noise levels [50].

A recent experimental study on turbulent combustion noise from non-premixed natural gas flames was performed by Singh et al. [118]. In their experiment, a natural gas burner equipped with a double swirler unit is investigated concerning the radiated spectrum of sound pressure. Investigated operating points are placed between global air excess ratios of $\lambda = 0.9 \dots \lambda = 1.41$ at thermal powers up to 24kW. The general conclusion from this study shows that combustion noise spectra from non-premixed flames possess the same general shape properties

Table 1.1: Overview of experimental studies on combustion noise with reported ranges for peak frequency and efficiency of conversion between thermal and acoustic energy for hydrocarbon premixed (P) and non-premixed (NP) flames.

Author	Year	Fuel	Flame	η_{ta}	f_{peak} [Hz]
Smith, Kilham [122]	1963	CH ₄ , C ₂ H ₄ , C ₃ H ₈	P	$5 \cdot 10^{-8}$	-
Kotake, Hatta [69]	1965	NG	P	-	-
Thomas, Williams [136]	1966	N/A	P	$10^{-8} \dots 10^{-6}$	-
Hurle, Price [56]	1968	C ₂ H ₄	P	-	≈ 1000
Giammar, Putnam [46]	1969	NG	NP	$10^{-8} \dots 10^{-6}$	250 – 500
Giammar, Putnam [47]	1972	NG	P	Fit Curve	-
Shivashankara, Strahle [115]	1973	N/A	P	10^{-6}	500
Kumar [71]	1975	CH ₄	P, NP	-	≈ 1000
Strahle, Shivashankara [131]	1976	JP4	NP	$10^{-6} \dots 10^{-5}$	≈ 300
Strahle [129]	1978	C ₂ H ₄	P	-	≈ 500
Putnam, Faulkner [103]	1983	CH ₄	NP	-	≈ 400
Katsuki et al. [65]	1986	C ₃ H ₈	P	-	-
Kotake, Takamoto [70]	1987	C ₃ H ₈	P	-	90 – 200
Ohiwa et al. [94]	1993	C ₃ H ₈	NP	-	200 – 500
Elfeky et al. [33]	1996	CH ₄	P	-	-
Lieuwen, Rajaram [78]	2002	CH ₄	P	-	≈ 300
Singh et al. [120]	2004	CH ₄ /H ₂	NP	-	≈ 1000
Winkler et al. [151]	2005	NG	P, NP	$10^{-8} \dots 10^{-7}$	200 – 500
Wäsle et al. [155]	2005	NG	P	$7 \cdot 10^{-8} \dots 1.1 \cdot 10^{-7}$	70 – 400
Rajaram et al. [107]	2005	NG	P	-	≈ 300
Rajaram, Lieuwen [106]	2009	NG	P	-	100 – 900
Singh et al. [118]	2013	NG	NP	-	250 – 700

as those obtained from premixed flames. Peak frequencies shift towards higher frequencies at higher flow velocities and the spectral amplitude is coupled to the total firing rate. Duchaine et al. [29] investigate partially premixed flames and find that modeling principles and assumptions associated with perfectly premixed flames are still fulfilled for partially premixed flames. This motivates the development of a unified noise model for premixed, partially premixed and non-premixed flames.

A general conclusion from experimental studies published on combustion noise can be drawn as far as that open turbulent hydrocarbon flames radiate broadband noise of similar spectral characteristics, where the detailed properties of the radiated noise concerning peak amplitude, peak frequency and efficiency of conversion are governed by the type of fuel, mixture composition, nozzle geome-

try and swirl intensity. Noise spectra recorded from flames operated in a confined combustion chamber frequently show different spectral characteristics.

1.2 Prediction of Combustion Noise

The generation and propagation of combustion noise involves a broad range of physical time and length scales. Spatial scales involved with the chemical reaction of the combustion process are of the order of millimeters [82], while the wave-length of acoustic pressure waves in the low frequency range is of the order of meters. This diversity of scales and physical processes connected with the generation of turbulent combustion noise motivates the use of hybrid numerical methods for the prediction of noise emissions following a "divide and conquer" strategy.

Frequently, the flow and chemical reaction problem is treated separately from the propagation simulation of the radiated acoustic signal. Multiple sets of equations describing the relevant phenomena with different levels of complexity are available for the modeling of reactive turbulent flow and the propagation of acoustic pressure waves. Table 1.2 summarizes recent numerical studies on combustion noise covering different pairs of numerical methods. Numerical approaches relying on Large Eddy simulation (LES) offer the advantage of direct access to the time-dependent variable fields that are involved in the generation of combustion noise. Direct extraction of the source terms on the right hand side of

Table 1.2: Overview of hybrid numerical methods used in the prediction of turbulent combustion noise.

Author	Year	Fuel	Flame	Flow Simulation	Acoustic Simulation
Klein [67]	2000	CH ₄	NP, P	RANS	Model
Hirsch et al. [52, 53]	2006	CH ₄ /H ₂	P	RANS	Acoustic Analogy/Model
Ihme et al. [57]	2006	CH ₄ /H ₂	NP	LES	Model
Flemming et al. [42]	2007	CH ₄ /H ₂	NP	LES	Wave-Eq.
Bui, Schröder [15]	2007	H ₂	NP	LES	APE
Mühlbauer et al. [88]	2010	CH ₄ /H ₂	NP	RANS	LEE
Ihme, Pitsch [58]	2012	CH ₄ /H ₂	NP	LES	Acoustic Analogy
Silva et al. [116]	2013	C ₃ H ₈	P	LES	Wave-Eq.

the inhomogeneous wave-equation given by [25] is provided following methods originally developed in computational aero-acoustics (CAA). With a certain portion of the low wave-number regime of turbulent motion spatially and temporally resolved, the quantities governing the creation of combustion noise can be evaluated from time series of the solution variables, as performed e.g. in [14]. In a recent study, Singh et al. [119] use LES to predict sound spectra from a swirling turbulent diffusion flame. The regions of effective noise generation are identified to be located within zones of intense shear accompanied by turbulent fluctuations of scalar variables, e.g. the temperature. Their results capture the qualitative features of the combustion noise spectra in two different operating conditions, but peak amplitudes and frequencies are over-predicted by the LES solution indicating the complexity of the underlying physics. From LES solutions, the resulting far field sound power can be computed analytically using a Green's function approach or interpolated/integrated into a suitable set of equations describing acoustic propagation in the domain of interest. Frequently, the LES solution is coupled to a time-domain acoustic solver. This hybrid LES/CAA approach has been applied with both, quantitative and qualitative success to turbulent premixed and non-premixed flames [42]. Alternatively, local fluctuating source terms can be directly evaluated and integrated spatially, to obtain far-field pressure using a Green's function approach for the Lighthill equation [59]. Candel et al. [16] summarize different model approaches and current developments in the field of combustion noise and combustion instabilities. The use of LES for the simulation of reactive flow is computationally expensive when applied to industrial combustion problems and thus, limited in its applicability.

Hybrid approaches based on a time-averaged solution of the reacting flow (Reynolds averaged Navier-Stokes, RANS) offer considerably less computational effort but require suitable modeling of the time-dependent fluctuations of the flow variables, or their spectral distribution if settled in wave-number or frequency space. An example for a time-domain model using time averaged input data from a RANS simulation is the random particle mesh approach proposed by Ewert [34, 88–90]. The key frame of this approach is the modeling of the cross-covariance of a statistical fluctuating sound source Q using a prescribed shape model of the auto-correlation function.

Klein and Kok [67] present a model to calculate the sound pressure emitted from turbulent non-premixed flames based on time averaged field variables from a RANS simulation. This hybrid model relies on an assumed shape for the spectrum of the heat release rate and an empirically determined coherence length scale. The model is successfully used to predict combustion noise spectra for confined turbulent flames.

Hirsch et al. [52, 53] proposed a model for combustion noise from turbulent premixed flames based on a derived connection between the wave-number spectrum of the scalar reaction progress variance and that of the rate of heat release. The fundamental model assumptions have been validated by Winkler [150, 152, 153] and Wäsle [143, 154, 156]. Initially based on spatially resolved experimental data for the input variables, the model has been used previously for the prediction of combustion noise spectra from input data obtained from time-averaged numerical simulations (RANS) of the underlying reactive flow [53]. Weyermann applied the theory to the calculation of noise spectra from turbulent confined flames [146, 147]. Using the model theory to calculate the frequency spectrum of the fluctuating rate of heat release coupled to a one-dimensional acoustic simulation, he was able to calculate the farfield sound-spectrum emitted by an automotive heater.

1.3 Thesis Structure

The noise prediction tool assembled in this thesis is a hybrid, which consists of a CFD simulation of the reacting flow and a combustion noise post-processor. This post-processor calculates acoustic power spectra in an independent subsequent calculation step. Based on the CFD field data, the resulting spectrum of sound power emitted by the flame is calculated using the spectral model for combustion noise developed by Hirsch et al. [52, 53] for premixed flames. For non-premixed flames, the model is modified accordingly, in order to account for flame specific properties, so that noise predictions can be performed for both flame types. Both model configurations are implemented into C routines, which compute the integral acoustic power spectrum based on the supplied input variable fields.

The implementation of the premixed combustion noise model and the newly developed modifications in the non-premixed model are validated by comparison to experimental acoustic spectra recorded from an open turbulent swirl flame. A movable-block swirler allows experiments at different swirl intensities and the test rig can be operated in premixed and non-premixed flame configuration.

The thesis at hand is organized as follows:

The theoretical background of reactive flow modeling is introduced in Chapter 2 followed by the theoretical fundamentals of turbulent combustion noise (Chapter 3). On this basis, the derivation of the combustion noise model proposed by Hirsch et al. [52, 53] is presented in Chapter 4. This model is then extended and modified, to account for specific properties of non-premixed flames concerning noise radiation in Section 4.3.

Validation experiments are conducted using a test rig for unconfined non-premixed and premixed turbulent swirl flames. In order to ensure comparability between premixed and non-premixed thermo-acoustic efficiencies, a burnout correction method is developed, which allows the determination of the fuel burnout efficiency of open premixed flames. The acoustic test rig for the measurement of the noise radiated by the test flame is presented in Chapter 5, followed by experimental results for non-premixed and premixed natural gas swirl flames in Chapter 6. The obtained acoustic data are used to validate the developed model for non-premixed flames as well as the implemented computational routines. The numerical case setups, along with results from CFD simulations and the model predictions obtained with the developed toolkit are presented in Chapter 7. Applicability of the noise prediction toolkit to an industrial application is considered in Chapter 8 where the model formalism is used to predict the radiated sound spectrum from a marine heating unit using the confined flame network element introduced by Weyermann [146] together with the noise toolkit.

2 Reacting Turbulent Flows

The generation of combustion noise is inherently coupled to the processes and dynamics of the combustion reaction under turbulent flow conditions. Complex time-dependent interaction phenomena between processes including mixing dynamics, ignition, and extinction or heat exchange along with fluctuations of the turbulent velocity field govern the local rate of heat release in a flame and thus, the generation and radiation of noise.

2.1 Characteristics of Turbulent Flows

In turbulent flows, vortical structures, frequently termed eddies, are created by unstable velocity gradients in the mean flow. Examples for this situation can be found within the shear layer between two flow streams of different velocity, in boundary layers in the vicinity of solid boundaries or turbulent flow around an obstacle. The transition between laminar and turbulent flow conditions, characterized by the appearance of vortical structures is governed by the ratio of inertial and viscous forces. This ratio is described by the Reynolds number Re

$$Re = \frac{\bar{u} \cdot d}{\nu}, \quad (2.1)$$

where \bar{u} is the average flow velocity, d a characteristic dimension of the flow geometry and ν the kinematic viscosity. At larger Reynolds numbers, small statistical disturbances of the flow velocity are no longer damped sufficiently by viscous forces and may grow in strength over time, as the growth of eddies is a nonlinear phenomenon. In fluid flow through a circular pipe, this transition to turbulence occurs at an approximate Reynolds number of 2000 [31].

The origin, growth, and dissipation of eddies can directly be observed in turbulent jet flow. A Schlieren image of a high Reynolds number jet emerging into

quiescent surroundings is shown in Fig. 2.1. Basic features of turbulent flow can be explained from this example. Along the surface that separates the moving jet fluid from the ambient fluid at rest, a turbulent mixing layer is created. The circular motion of the eddies greatly enhances the exchange of momentum as well as the mixing of scalar quantities.

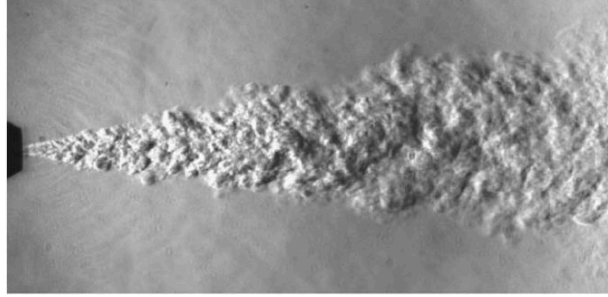


Figure 2.1: Schlieren image of a turbulent jet at large Reynolds number. The distribution of vortices of different sizes along the widening jet is clearly visible (from [140]).

This can be demonstrated by considering the effect of a simple Burgers vortex on the interface line separating two fluid zones from each other. In this theoretical consideration, r_c marks the radius of the vortex core. The zones can represent different fluid materials or differences in scalar concentrations. Vortex motion distorts the initially straight separation line over time. The increasing distortion is shown in Fig. 2.2 for four points in time. The initial reference interface is marked by the dashed line in all images. Two important effects of turbulence on the mixing process can be extracted from this example. The interface line is turned into a spiral shaped contour because the radial velocity is larger in the vortex core region. By increasing the length of the interface line by a factor of four over one full revolution of the vortex, the vortex increases the surface area of the contact interface between the two zones. The mass flow due to molecular diffusion across the interface is given by Fick's law

$$\dot{m}_\phi = -S\rho D_\phi \nabla\phi, \quad (2.2)$$

where D_ϕ denotes the mass diffusion coefficient of the species ϕ , ρ the fluid density and S is the surface area of the interface between the two species. By increasing the contact surface area, the vortex enhances diffusive mass transport. Additionally, fluid is transported by convection from one side of the vortex towards the other. Transport and distortion also cause a considerable reduction of

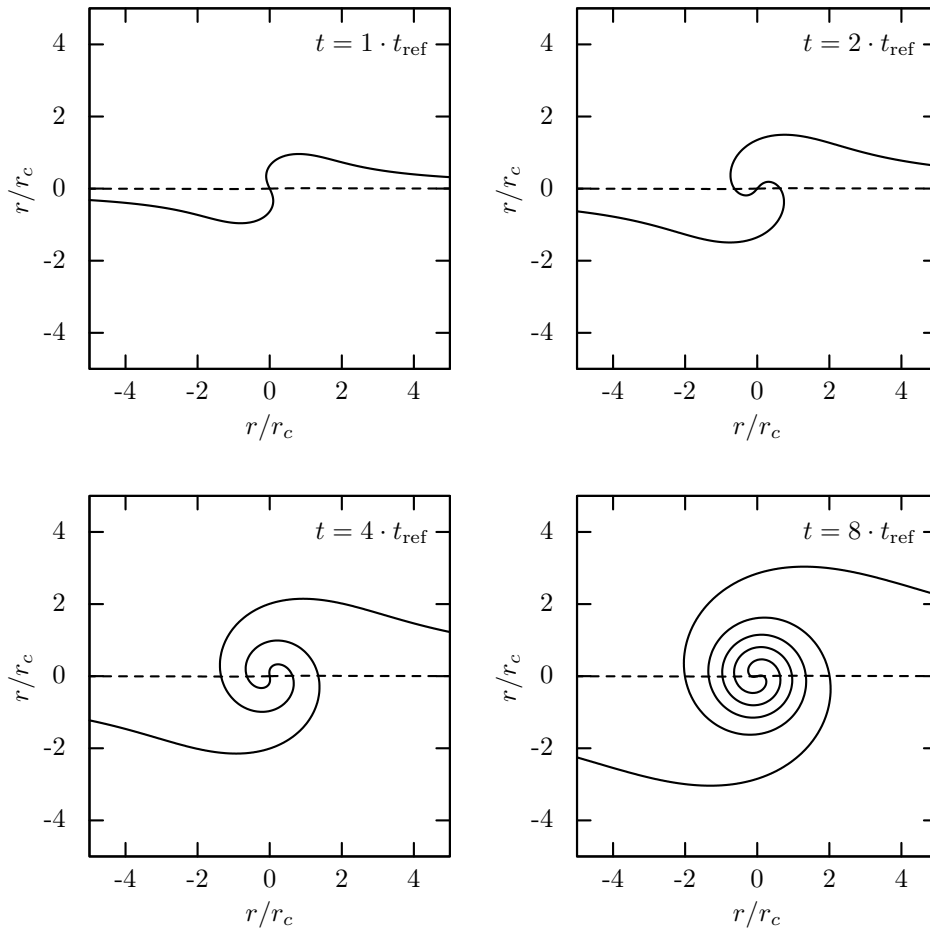


Figure 2.2: The effect of a simple two-dimensional vortex on an initially straight interface line (indicated by the dashed line) separating two fluid zones plotted over the normalized vortex radius. While fluid is transported by convection, the length of the interface line representing the surface area of the fluid fluid interface is increased.

the thickness of individual fluid layers, leading to steepened gradients and enhanced diffusive mass flux according to Eq. (2.2). The influence of turbulent motion on the molecular mixing is of primary interest in turbulent combustion, where the mixing of fuel and oxidizer on the molecular level is often dominating reaction rates.

In turbulence theory, instantaneous velocity components at a fixed point in space x are often split into a statistically stationary mean value and a time dependent

fluctuating part, which is shown in Eq. (2.3) for the velocity component in x -direction u_x :

$$u_x(t) = \bar{u}_x + u_x''(t). \quad (2.3)$$

Herein, the double prime denotes a turbulent fluctuation and the overbar indicates time averaging over the interval $T = t_2 - t_1$:

$$\bar{u}_x = \frac{1}{t_2 - t_1} \int_{t_1}^{t_2} u_x(t) dt. \quad (2.4)$$

The instantaneous velocity $u_x(t)$ depends on the time of observation t and the location of observation x . Turbulence intensity can be characterized by statistical variables describing the fluctuations of the flow velocity and an integral length scale of vortex sizes. The root mean square captures the intensity of the turbulent velocity fluctuations

$$u_{x, \text{rms}}'' = \sqrt{\overline{u_x''^2}} = \sqrt{\frac{1}{t_2 - t_1} \int_{t_1}^{t_2} (u_x(t) - \bar{u}_x)^2 dt}, \quad (2.5)$$

where the indication of the dependance of the velocity on the current location x has been dropped for simplicity. The overall kinetic energy content in the turbulent fluctuations is the sum of the standard deviations of the fluctuating velocity components in each coordinate direction:

$$k = \frac{1}{2} \left(\overline{u_x''^2} + \overline{u_y''^2} + \overline{u_z''^2} \right). \quad (2.6)$$

In isotropic turbulence, Eq. (2.6) simplifies to

$$k \approx \frac{3}{2} \overline{u''^2}. \quad (2.7)$$

Turbulent kinetic energy is transferred between vortices of different sizes. Large eddies absorb kinetic energy from the mean flow strain rate at the large scales. In homogeneous isotropic turbulence the kinetic energy is given by the integral over all wavenumbers κ of the turbulent energy spectrum $E(\kappa)$ [4]:

$$k = \int_0^{\infty} E(\kappa) d\kappa. \quad (2.8)$$

$E(\kappa)$ is the integral over spherical shells of radius κ of the trace of the three-dimensional spectrum, which is itself the three-dimensional Fourier transform of the two-point velocity spectrum tensor [142]. The integral scale l_t of the energy containing large eddies is related to the energy spectrum by

$$l_t = \frac{\pi}{2u''^2} \int_0^{\infty} \frac{E(\kappa)}{\kappa} d\kappa. \quad (2.9)$$

Equation (2.9) demonstrates the strong influence of the large scale turbulence (low wavenumber range) on the integral length scale. Large scale eddies are unstable, which is the origin of the so termed “energy cascade” in turbulent flow. The unstable character of the large eddies leads to their break-up into smaller structures. During the event of eddy break-up, kinetic energy is conserved and transferred to the smaller eddies. The break-up cascade is limited by the minimal possible eddy size which is governed by viscous forces. At the smallest scales, viscous forces dissipate the kinetic energy into internal energy of the fluid.

The smallest scales of turbulent motion have been characterized by Kolmogorov [68]. The conditions at the smallest turbulent scales may be characterized by defining a Reynolds number using the Kolmogorov micro-scales of velocity and length. These scales are uniquely determined by the viscosity ν and the dissipation rate ε in turbulent flow of sufficiently high Reynolds number. The Kolmogorov scales of length, velocity and time are given by [102]

$$\eta_{\text{kol}} = \left(\frac{\nu^3}{\varepsilon} \right)^{\frac{1}{4}}, \quad (2.10)$$

$$u_{\text{kol}} = (\varepsilon \nu)^{\frac{1}{4}}, \quad (2.11)$$

$$\tau_{\text{kol}} = \left(\frac{\nu}{\varepsilon} \right)^{\frac{1}{2}}. \quad (2.12)$$

A Reynolds number calculated from these scales gives value of unity, indicating that at the Kolmogorov micro-scales viscous and inertial forces are of the same

magnitude and the micro-scales characterize the smallest scales of turbulent motion [4]:

$$\text{Re}_{\text{kol}} = \frac{\varepsilon^{\frac{1}{4}} \nu^{\frac{1}{4}} \left(\frac{\nu^{\frac{3}{4}}}{\varepsilon^{\frac{1}{4}}} \right)}{\nu} = 1. \quad (2.13)$$

Between the low wavenumber production range and the dissipative micro-scales, kinetic energy is distributed among eddies of different sizes l_e , where the individual eddy sizes correspond to a wavenumber of

$$\kappa_e = \frac{2\pi}{l_e}. \quad (2.14)$$

Along the wavenumber spectrum, energy distribution follows the well-known $\kappa^{-\frac{5}{3}}$ law formulated by Kolmogorov [68]. In turbulence theory, different model spectra have been proposed to model energy distribution along all wavenumber ranges of turbulence [102, 134].

2.1.1 Model Spectrum of Turbulence Kinetic Energy

The general properties of the wavenumber spectrum of turbulence kinetic energy are shown qualitatively in Fig. 2.3, showing a model spectrum from turbulence theory. A fundamental similarity between the spectrum of turbulent kinetic energy and that of turbulent combustion noise (cf. Fig. 1.3) can be asserted directly, indicating a direct relation between turbulent fluctuations in reacting flow and the resulting spectrum of acoustic noise.

In the scope of the combustion noise model discussed in this thesis, the spectrum function derived by Tennekes & Lumley [134] is used to compute the spectrum of the rate of heat release. The inclusion of the model spectrum into the combustion noise model is described in Sec. 4.1. The model spectrum considered covers the complete wavenumber range, which spans between the vicinity of the turbulent integral length scale l_t and the Kolmogorov length scale η_{kol} . Kinetic energy is fed to the large scales of turbulent eddies in the low wavenumber region of the spectrum. If the Reynolds number is large enough¹, an inertial subrange

¹ Tennekes & Lumley [134] give a minimum turbulence Reynolds number of 4000 as a prerequisite for the existence of an inertial subrange.

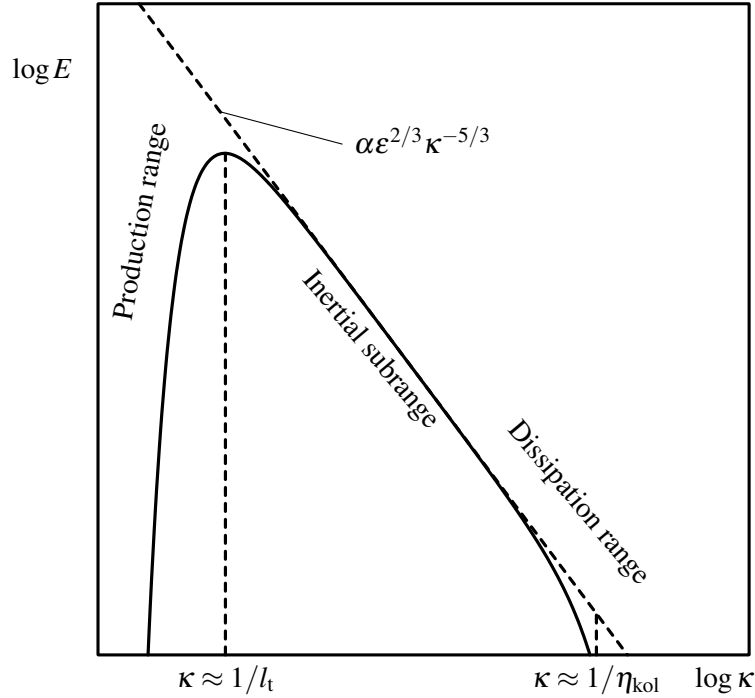


Figure 2.3: Model spectrum of turbulence kinetic energy as given by Tennekes & Lumley [134]. The size of the inertial subrange is governed by the spread between the integral length scale l_t and the Kolmogorov length scale η_{kol} .

exists between the production and dissipation range, where energy is conserved and transferred from larger to smaller eddies at a constant rate. The transfer rate in the inertial subrange is equal to the dissipation rate ϵ at which energy is dissipated on the fine scales. The constant rate of energy transfer equals the rate of dissipation on the fine scales ϵ :

$$\epsilon \approx \frac{u'^3}{l_t}. \quad (2.15)$$

Spectral energy distribution within the inertial subrange was predicted by Kolmogorov to scale as

$$E(\kappa) = C\epsilon^{2/3}\kappa^{-5/3}, \quad (2.16)$$

where C is a constant determined empirically from experimental data and ϵ is the dissipation rate of turbulence kinetic energy. The model spectrum given by

Tennekes & Lumley [134] additionally includes terms governing the spectral shape in the production and dissipation range and is given by

$$E(\kappa) = \alpha \varepsilon^{2/3} \kappa^{-5/3} \exp \left\{ -\frac{3}{2} \left[\pi \beta \sqrt{\alpha} (\kappa l_t)^{-4/3} + \alpha (\kappa \eta_{\text{kol}})^{4/3} \right] \right\}, \quad (2.17)$$

with the model constants $\alpha = 1.5$, $\beta = 0.3$ estimated from theory. The first exponential term in Eq. (2.17) governs the location of the maximum spectrum amplitude through the integral length scale l_t , while the second term models the spectral decay in the high wavenumber range, where eddy sizes approach the Kolmogorov length scale η_{kol} .

2.1.2 Turbulent Swirling Flow

Turbulent swirling flows are widely used in technical applications, with beneficial properties especially applying to turbulent flames. Among the benefits are increased flame stability over a wider range of operating conditions and reduced pollutant emission.

In combustors operated under turbulent conditions, the swirling velocity component is generally imposed by a swirl generator upstream of the burner nozzle before the flow passes a discontinuous increase in cross-sectional area. The centrifugal forces induced by the swirling motion direct the flow outward and create a radial pressure distribution with a minimum on the burner axis. A low pressure region with adverse axial gradient is formed downstream of the nozzle if the swirl intensity is sufficiently high. In the low pressure region hot combustion products are recirculated and ensure continuous ignition of the fresh gas.

The swirl intensity can be characterized by relating the convective fluxes of axial and angular momentum. The swirl number S is the ratio of the convective flux

of angular momentum G_ϕ and the convective flux of axial momentum G_x [132]. These are given by

$$G_\phi = \int_0^R (wr) \rho u 2\pi r dr \quad (2.18)$$

$$G_x = \int_0^R u \rho u 2\pi r dr + \int_0^R p 2\pi r dr. \quad (2.19)$$

The swirl number is then defined as

$$S = \frac{G_\phi}{G_x R}, \quad (2.20)$$

where R denotes the exit radius of the burner nozzle. Addition of a swirling velocity component to the fresh gases has a stabilizing effect on the turbulent flame. The swirling motion and its follow up effects can improve blowout limits by a factor of 5 [39] with respect to the fuel exit velocity. Swirl also increases the entrainment of ambient air into the reaction zone for open flames. The dilution of the unburnt mixture leads to extinction of the outer shear layer of premixed flames and consequently, to incomplete burnout. This effect must be accounted for, when comparing experimental combustion noise from premixed and non-premixed flames by introducing a burnout correction coefficient (see Sec. 6.2.1), so that the actual overall heat release of the flames is known. Swirling flow also involves greater pressure loss and enlarged emission of combustion noise [50], which makes turbulent swirl flames especially suitable for combustion noise research.

2.2 Turbulent Combustion

When compared to laminar combustion, chemical reaction under turbulent flow conditions is characterized by continuous fluctuations of velocity and scalar quantities (among those are temperature, density, species mass fractions and rate of heat release). The time-dependent fluctuations in the rate of heat release act as a source of sound, as one of the main effects of non-stationary rate of heat

release is a volume expansion of the gas [21]. This mechanism is in its essence independent of the flame configuration.

Technical flames can be classified regarding the realization of the mixing process between fuel and oxidizer [98]. In premixed flames, fuel and oxidizer are mixed prior to combustion in a specific mixture ratio. Thus, the maximum flame temperature and other parameters involving the generation of pollutants in the combustion zone may be controlled directly. Premixed flame propagation is mainly controlled by the local flame speed, which is directly influenced by the mixture composition in laminar flames. Turbulent eddies are able to wrinkle the laminar flame, increasing the flame surface and resulting in an increased propagation speed of the turbulent flame.

In many technical applications, fuel and oxidizer enter the combustion chamber in separate streams, primarily for safety reasons. Flames of this structural form are termed non-premixed flames. Turbulent transport brings the reactants together, while the turbulent energy cascade performs their mixing on a fine scale. Reaction rates are highly dependent on this rate of mixing between fuel and oxidizer. The prevailing role of mixing renders non-premixed flames more sensitive to turbulent fluctuations.

A further classification of turbulent flames can be performed based on characteristic time scales of chemical reaction and turbulent mixing. The ratio of the characteristic time scale of turbulent mixing τ_t and that of the chemical reaction τ_c is the turbulent Damköhler number Da_t :

$$Da_t = \frac{\tau_t}{\tau_c}. \quad (2.21)$$

For large values of the turbulent Damköhler number, chemical reaction occurs considerably faster compared to turbulent mixing. Together with other characteristic scales of turbulence chemistry interaction, regime diagrams can be defined, which allow a qualitative distinction of different local flame structures. If the chemical reaction is much faster than the turbulent mixing process of fuel and oxidizer in non-premixed combustion or fresh and burnt gases in premixed combustion, the flame takes the form of a thin wrinkled sheet in both cases. In this fast chemistry limit, reactants and hot products (in premixed flames) or fresh gas streams (in non-premixed flames) are separated by an infinitely thin

flame sheet. The local progress of the reaction can be characterized by a reaction progress variable c , with a parameter value of zero in the fresh gas and unity in the exhaust gas.

2.2.1 Non-Premixed Combustion

The description of non-premixed combustion relies on characteristic time and length scales associated with the mixing between fuel and oxidizer. Other than premixed flames, non-premixed flames do not have a characteristic laminar flame speed and consequently, the definition of a characteristic chemical time scale is not straightforward.

If the diffusivities of all scalars involved in the reactive flow problem are taken to be equal², the remaining conserved scalar quantities are linear functions of the mixture fraction z . The mixture fraction can be seen as a virtual mass fraction with value unity inside the fuel stream and zero in the oxidizer stream. For the definition of the mixture fraction variable, a simplified global one-step reaction is defined, involving fuel (F), oxidizer (O) and reaction products (P):



where v_F , v_O , v_P are the stoichiometric coefficients of fuel, oxidizer and products, respectively. A stoichiometric ratio ν is defined by

$$\nu = \frac{v_O W_O}{v_F W_F}, \quad (2.23)$$

with the molecular weights of fuel and oxidizer, W_F and W_O . The mixture fraction Z is now

$$z = \frac{\nu Y_F - Y_O + Y_{O, \infty}}{\nu Y_{F, 0} + Y_{O, \infty}}, \quad (2.24)$$

where Y_F , Y_O are the local mass fractions of fuel and oxidizer and $Y_{F, 0}$, $Y_{O, \infty}$ denote the initial mass fractions of fuel and oxidizer in the fuel and oxidizer stream. The mixture fraction value at stoichiometric conditions Z_{st} can be computed from

$$z_{st} = \frac{1}{1 + \frac{\nu Y_{F, 0}}{Y_{O, \infty}}} \quad (2.25)$$

²This is the case for most hydrocarbon-air combustion cases.

and is directly related to the air excess ratio λ through

$$\lambda = \frac{z_{st}(1-z)}{z(1-z_{st})}. \quad (2.26)$$

The air excess ratio is connected to the equivalence ratio ϕ through

$$\phi = \frac{1}{\lambda}. \quad (2.27)$$

Describing only the turbulent mixing process of unburnt gases, the mixture fraction is a conserved scalar.

Using the turbulent Reynolds number

$$\text{Re}_t = \frac{u''_{rms} l_t}{\nu}, \quad (2.28)$$

where ν denotes the kinematic viscosity, a regime diagram for non-premixed flames can be created [75]. Here, the turbulent Damköhler number for non-premixed flames is defined as

$$\text{Da}_t = \frac{\tau_t}{\tau_c} = \sqrt{\text{Re}_t} \text{Da}. \quad (2.29)$$

Both parameters span the regime diagram for turbulent non-premixed combustion, as shown in Fig. 2.4. Four fundamental flame regimes can be distinguished:

- $\text{Re}_t < 1$: Molecular diffusive transport is stronger than turbulent transport, thus reaction takes place under laminar conditions.
- $\text{Da}_t < 1$: Large scalar dissipation rates induce flame quenching leading to partial premixing and forming distributed zones of reaction.
- $\text{Da} < 1, \text{Da}_t > 1$: Small eddies close to the high wavenumber end of the turbulent spectrum are able to extinguish some reaction regions forming broken reaction zones.
- $\text{Da} > 1$: For fast chemistry, i.e. $\tau_t \gg \tau_c$, the reaction takes place in a thin flame sheet in the proximity of $z = z_{st}$. Reaction rates are dominated by turbulent mixing.

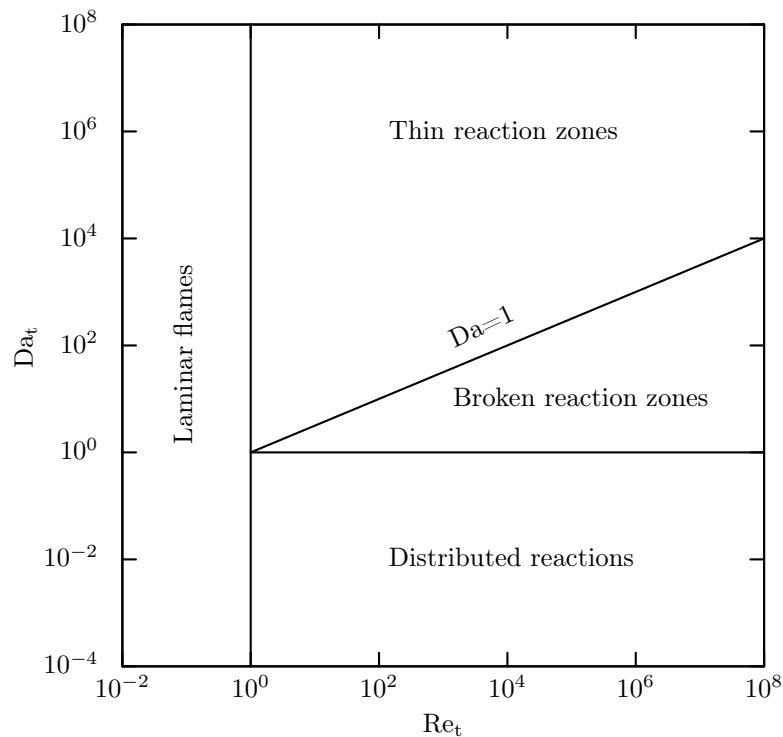


Figure 2.4: Regime diagram of non-premixed turbulent combustion.

For turbulent flames of large Damköhler number, the turbulent mixing process is the essential parameter governing chemical reaction rate. Chemical time scales depending on local mixture composition can be estimated from simplified global reaction schemes. In the scope of this thesis, a constant chemical timescale of $\tau_c = 1 \cdot 10^{-4}$ s, typical for methane combustion is presumed [100] to calculate the global flame Damköhler number for non-premixed flames.

2.2.2 Premixed Combustion

Propagation of laminar premixed flames can be described through the mixture specific laminar flamespeed s_l . This parameter can be determined experimentally and is frequently used in the modeling of premixed combustion. The propagation speed of a wrinkled turbulent flame differs from the laminar flamespeed and is described by an average turbulent flamespeed s_t . The influence of turbulent motion on the flame front itself and vice versa depends on characteristic measures

of turbulence and chemistry. These properties can be distinguished through dimensionless parameters, similar to the those of the non-premixed case.

In regions where $Da_t \gg 1$, chemical processes take place much faster than turbulent mixing, so that the sole modeling of the mixing process delivers a good approximation of the local chemical reaction rate. Interaction between turbulent and chemical processes in the fine scales of turbulence is considered in the turbulent Karlovitz number Ka_t :

$$Ka_t = \frac{\tau_c}{\tau_{kol}} \quad (2.30)$$

The ratio compares a characteristic time scale of the laminar flame with the time scale of the smallest turbulent structures of the flow i.e. the Kolmogorov time scale τ_{kol} . In regions where $Ka_t \ll 1$, diffusive transport processes within the flame take place on a very small time scale, leaving the flame interior unaltered by turbulent motion and creating locally laminar conditions. If $Ka_t \geq 1$, the smallest turbulent structures are able to enter into the flame front and thicken it. If the dimensionless ratio between the turbulent velocity scale and the laminar burning velocity is plotted over the ratio of integral length scale and thickness of the laminar flame, the well-known Borghi diagram of flame regimes is obtained [12]. Specific constant values of Re_t , Da_t and Ka_t define straight lines separating the different flame regimes. The resulting graph is depicted in Fig. 2.5. In the regime $Re_t < 1$ an unwrinkled laminar flame prevails. The turbulent regime beyond $Re_t = 1$ can be separated into four characteristic turbulent flame regimes using Karlovitz- and Damköhler number. Each of the regimes has a characteristic form of flame turbulence interaction:

- $Re_t > 1, \frac{u''_{rms}}{s_l} < 1$: Local laminar flame speed exceeds the turbulent fluctuations of velocity in this flame regime. The flame front travels over the vortical structures at high velocity compared with the turbulent fluctuations of velocity, greatly reducing the wrinkling of the flame. Consequently, this regime is dominated by slightly wrinkled laminar flame fronts. Slight increases in local turbulent propagation speed of the flame are present, originating from the increase in overall flame surface area.
- $Re_t > 1, \frac{u''_{rms}}{s_l} > 1, Ka_t < 1$: This regime is characterized by wrinkling of the flame and the appearance of pockets, separated from the main flame front.

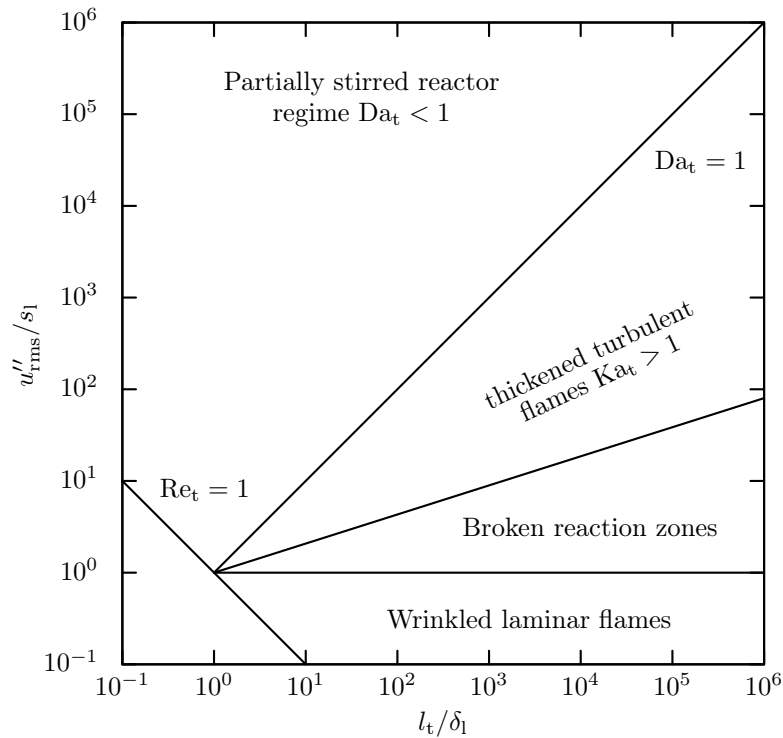


Figure 2.5: Regime diagram of premixed turbulent combustion.

The stronger fluctuations of velocity lead to stronger wrinkling of the flame, while the flame front retains its laminar characteristic. Pockets are formed by local events of extinction and re-ignition.

- $Ka \geq 1$, $Da_t \geq 1$: Within this regime, the characteristic length scale η_{kol} of the small eddies is smaller than the thickness of the laminar flame, allowing small eddies to enter the flame. The enhanced turbulent transport leads to a thickening of the flame in turn allowing larger eddy structures to penetrate the flame.
- $Ka \gg 1$ and $Da_t < 1$: If the chemical time scale τ_c is larger than the turbulent scale $\tau_c > \tau_t$, eddies of all sizes are able to enter the flame. The flame enters the state of perfectly stirred reactor, where the rate of reaction is solely determined by the chemical time scale.

Transitions between the individual regimes are continuous.

2.3 Simulation of Turbulent Reacting Flow

The hybrid simulation of turbulent combustion noise performed in this thesis requires input data of the mean variable fields of the flame to be modeled. The input variable fields are obtained from a numerical simulation of the reactive flow problem using computational fluid dynamics (CFD). The following section introduces the set of balance equations needed for the numerical solution of reactive flows. The variable fields are obtained using a density-averaged formulation of the balance equations in combination with a suitable turbulence model. The combustion process is modeled using a global 1-step chemical reaction scheme, where the rate of reaction is modeled using a modified Schmid model [111, 112] for premixed flames and an Eddy Dissipation model [83] for non-premixed flames. Non-premixed combustion cases were calculated using ANSYS CFX 13 while the axis-symmetric premixed case was calculated using ANSYS Fluent 13. The conservation equations are given in the form as solved by Fluent in the following for the purpose of simplicity.

Conservation of Mass

The equation governing conservation of fluid mass is given by

$$\frac{\partial \rho}{\partial t} + \frac{\partial}{\partial x_j} (\rho u_j) = 0, \quad (2.31)$$

with the fluid density ρ and the velocity component u_j in the direction of x_j .

Conservation of Momentum

Conservation of momentum is given by

$$\frac{\partial (\rho u_i)}{\partial t} + \frac{\partial}{\partial x_j} (\rho u_i u_j) = -\frac{\partial p}{\partial x_i} + \frac{\partial \tau_{ij}}{\partial x_j} + S_m, \quad (2.32)$$

where u_i denotes the cartesian velocity components, p the static pressure and S_m an arbitrary source of momentum. In Eq. (2.32), the stress tensor τ_{ij} is connected with the coefficient of viscosity μ through

$$\tau_{ij} = \mu \left(\frac{\partial u_i}{\partial x_j} + \frac{\partial u_j}{\partial x_i} - \frac{2}{3} \delta_{ij} \frac{\partial u_k}{\partial x_k} \right) \quad (2.33)$$

for constant property Newtonian fluids [102]. In open flames, substantial gradients of density occur between the hot combustion products and the cold ambient atmosphere which generate additional momentum through buoyancy. Buoyancy can have substantial influence on open burning turbulent flames [7]. In the momentum equation, the effects of buoyancy can be taken into account by setting

$$S_m = (\rho - \rho_\infty) g_i, \quad (2.34)$$

where ρ_∞ denotes the ambient fluid density and g_i the vector components of gravity in the local coordinate system.

Species Mass Fractions

The description of reactive flows requires the distinction of chemical species. Single species mass fractions are obtained by solving a transport equation for the corresponding partial density $\rho_k = \rho Y_k$. Species consumption or production through chemical reaction is included in the equations of the component mass fractions Y_k through the source term S_k :

$$\frac{\partial (\rho Y_k)}{\partial t} + \frac{\partial}{\partial x_j} (\rho u_j Y_k) = \frac{\partial}{\partial x_j} \left(\rho D_k \frac{\partial Y_k}{\partial x_j} \right) + W_k \dot{\omega}_k. \quad (2.35)$$

Here, the diffusion of species k into the mixture is modeled using Fick's law. The molecular diffusion coefficient of species k is denoted by D_k and is frequently chosen equal for all species in turbulent combustion [101] when operating with a mixture containing a high concentration diluent such as N_2 . The sum of all local species mass fractions is unity by definition, so that only $n - 1$ transport equations need to be solved to obtain the fields of the n species mass fractions.

Conservation of Energy

Conservation of energy is formulated for the specific total energy

$$E = h - \frac{p}{\rho} + \frac{1}{2}u_i u_i. \quad (2.36)$$

The balance equation for total energy then has the following form:

$$\frac{\partial}{\partial t}(\rho E) + \frac{\partial}{\partial x_j} [u_j(\rho E + p)] = \frac{\partial}{\partial x_j} \left[k \frac{\partial T}{\partial x_j} + \left(\sum_{i=1}^{n_k} \rho D_k h_k \frac{\partial Y_k}{\partial x_j} \right) + u_j \tau_{ij} \right] + \dot{\omega}_E \quad (2.37)$$

Here, the terms on the right hand side represent energy transfer due to conduction, species diffusion, viscous work and heat release from combustion. For combustion problems, the viscous work term can be neglected, as its contribution is small when compared to the heat release by combustion.

To close the system of equations, pressure and density are coupled using the equation of state for an ideal gas. Then fluid pressure p and density ρ are related by

$$\rho = \frac{p}{R^* T}, \quad (2.38)$$

where the specific gas constant of the mixture R^* is related to the universal gas constant R_u through

$$R^* = R_u \sum_{i=1}^{n_k} \frac{Y_k}{W_k}. \quad (2.39)$$

Here, M_k denotes the molar mass corresponding to the mixture component k .

2.3.1 Averaged Balance Equations

An efficient approach to a numerical solution of equations (2.31)-(2.39) for industrial scale flow problems is the solution of averaged balance equations. Details on the averaging process and the splitting of the flow variables into mean and fluctuating part can be retrieved e.g. from Poinson and Veynante [101] or Gerlinger [45].

For reactive flow, density and pressure are split into an averaged and a fluctuating component using the Reynolds decomposition

$$x = \bar{x} + x'', \quad (2.40)$$

where the averaged value is calculated as a time- or ensemble average. The time average of variable x is given by

$$\bar{x} = \frac{1}{\Delta t} \int_t^{t+\Delta t} x dt. \quad (2.41)$$

The remaining variables are decomposed using a density based approach to calculate the average which is generally referred to as Favre averaging [141]:

$$x = \tilde{x} + x'', \quad \text{where } \tilde{x} = \frac{\overline{\rho x}}{\bar{\rho}}. \quad (2.42)$$

Introducing the decomposed variables into the system of equations leads to the following system of equations for the averaged variables, which now includes additional terms of fluctuating quantities:

$$\frac{\partial \bar{\rho}}{\partial t} + \frac{\partial}{\partial x_j} (\bar{\rho} \tilde{u}_j) = 0, \quad (2.43)$$

$$\frac{\partial}{\partial t} (\bar{\rho} \tilde{u}_i) + \frac{\partial}{\partial x_j} (\bar{\rho} \tilde{u}_i \tilde{u}_j) = -\frac{\partial \bar{p}}{\partial x_i} + \frac{\partial}{\partial x_j} (\bar{\tau}_{ij} - \overline{\rho u_i'' u_j''}) + \bar{S}_m, \quad (2.44)$$

$$\frac{\partial}{\partial t} (\bar{\rho} \tilde{Y}_k) + \frac{\partial}{\partial x_j} (\bar{\rho} \tilde{u}_j \tilde{Y}_k) = \frac{\partial}{\partial x_j} \left(\bar{\rho} D_k \frac{\partial \tilde{Y}_k}{\partial x_j} - \overline{\rho u_j'' Y_k''} \right) + M_k \bar{\omega}_k, \quad (2.45)$$

$$\frac{\partial}{\partial t} (\bar{\rho} \tilde{E}) + \frac{\partial}{\partial x_j} \left[\tilde{u}_j (\bar{\rho} \tilde{E} + \bar{p}) \right] = \frac{\partial}{\partial x_j} \left(a \bar{\rho} \frac{\partial \tilde{h}}{\partial x_j} - \overline{\rho u_j'' h''} \right) + \bar{\omega}_E. \quad (2.46)$$

In the energy equation, the viscous work term has been neglected and a Lewis number of unity is assumed

$$\text{Le} = \frac{a}{D} = 1, \quad (2.47)$$

which is a good approximation for the ratio of thermal conductivity a and diffusivity D for natural gas air mixtures. The terms of the form $\overline{\rho u_j'' x''}$ mark additional

turbulent diffusive terms that need to be closed. These turbulent scalar fluxes are modeled using a gradient transport assumption [45]:

$$\overline{\rho u_j'' \widetilde{x''}} = \frac{\mu_t}{Sc_t} \frac{\partial \widetilde{x}}{\partial x_j} \quad (2.48)$$

The additional terms in the momentum equation are the Reynolds stresses which are closed by a suitable turbulence model.

2.3.2 Turbulence Modeling

Turbulence models can roughly be divided into eddy viscosity models and Reynolds stress models. Eddy viscosity models commonly use the Boussinesq hypothesis to model the Reynolds stresses using an isotropic turbulent viscosity μ_t . The Reynolds stresses are then calculated from

$$-\overline{\rho u_i'' u_j''} = \mu_t \left(\frac{\partial \widetilde{u}_i}{\partial x_j} + \frac{\partial \widetilde{u}_j}{\partial x_i} \right) - \frac{2}{3} \delta_{ij} \left(\overline{\rho} k + \mu_t \frac{\partial \widetilde{u}_1}{\partial x_1} \right), \quad (2.49)$$

where μ_t is the turbulent viscosity. The turbulence kinetic energy in terms of the fluctuating velocity components is given by Eq. (2.51). Reynolds stress models solve additional transport equations for the unknown Reynolds stresses and are, thus, more expensive concerning computational resources. Different approaches can be used in the definition and modeling of the turbulent viscosity reflecting in the large number of available turbulence models in literature and commercial CFD codes.

k- ε Model

Launder & Spalding [74] employ a set of two additional transport equations to model the unknown turbulent viscosity in the k - ε model. The turbulent viscosity μ_t is computed from the values of the turbulence kinetic energy k and its dissipation rate ε obtained from the solution of additional balance equations:

$$\mu_t = C_\mu \overline{\rho} \frac{k^2}{\varepsilon}. \quad (2.50)$$

The transport equation for the turbulence kinetic energy is given by

$$\frac{\partial}{\partial t} (\bar{\rho}k) + \frac{\partial}{\partial x_j} (\bar{\rho}\tilde{u}_j k) = \frac{\partial}{\partial x_j} \left[\left(\mu + \frac{\mu_t}{\sigma_k} \right) \frac{\partial k}{\partial x_j} \right] + P_k - \bar{\rho}\varepsilon, \quad (2.51)$$

where the production of turbulence kinetic energy P_k is calculated from

$$P_k = -\bar{\rho}\widetilde{u_i''u_j''} \frac{\partial \tilde{u}_i}{\partial x_j}. \quad (2.52)$$

The balance equation for the dissipation rate ε is given by

$$\frac{\partial}{\partial t} (\bar{\rho}\varepsilon) + \frac{\partial}{\partial x_j} (\bar{\rho}\tilde{u}_j \varepsilon) = \frac{\partial}{\partial x_j} \left[\left(\mu + \frac{\mu_t}{\sigma_\varepsilon} \right) \frac{\partial \varepsilon}{\partial x_j} \right] + \frac{\varepsilon}{k} (C_{\varepsilon 1} P_k - C_{\varepsilon 2} \bar{\rho}\varepsilon). \quad (2.53)$$

For the standard k - ε model the following model constants apply:

$$c_\mu = 0.09, \quad c_k = 1.0, \quad \sigma_\varepsilon = 1.3, \quad c_{\varepsilon 1} = 1.44, \quad c_{\varepsilon 2} = 1.92. \quad (2.54)$$

In the simulations of the non-premixed flame with ANSYS CFX, the standard k - ε model has been used together with a correction term accounting for the effects of swirl on the production of turbulence kinetic energy proposed by Spalart and Shur [123].

Reynolds Stress Model

The Reynolds stress models (RSM) do not use an explicit eddy viscosity to model the unknown Reynolds stresses. Their basic approach is the derivation of transport equations for the unknown anisotropic Reynolds stresses $\bar{\rho}\widetilde{u_i''u_j''}$ in the momentum equation requiring the solution of an additional transport equations for each of the six unknown stress terms [6, 148]. The additional equations include further unclosed correlations of fluctuating quantities which need to be modeled. A variety of different sub-models is available in commercial CFD codes with different modeling approaches for those terms [48, 73].

In the 2D simulations of the premixed swirl flame in the scope of this thesis, the standard formulation implemented in ANSYS Fluent was used [60, 126]. In addition to the Reynolds stresses, the model is closed by a transport equation for the turbulent dissipation rate ε which is given by Eq. (2.53).

2.3.3 Combustion Modeling

Combustion of hydrocarbon fuels comprises numerous sub-reactions and reacts sensitively to changes in the initial conditions controlling the reaction. In laminar combustion, the rate of reaction can be determined by an Arrhenius equation which establishes the connection between reactant concentrations and the temperature. Systems of these equations can be set up to model whole reaction mechanisms. The reaction rates are computed from an Arrhenius expression of the form

$$\dot{\omega}_{\text{Arr}} = A \cdot X_{\text{F}}^{v_{\text{F}}} \cdot X_{\text{Ox}}^{v_{\text{Ox}}} \cdot T^{\beta_{\text{T}}} \cdot \exp\left(\frac{-E_{\text{A}}}{RT}\right), \quad (2.55)$$

where $\dot{\omega}_{\text{Arr}}$ denotes the molar reaction rate and X_{F} , X_{Ox} the molar concentrations of fuel and oxidizer species. The parameters v_{F} , v_{Ox} , β_{T} , A and E_{A} are determined by matching the prediction of Eq. (2.55) to experimental data of the propagation speeds of laminar flames. The exponential term shows the great sensitivity of the reaction rate on the temperature.

To introduce a Reynolds decomposition to account for the influence of turbulent fluctuations, the exponential term needs to be expanded as a Taylor series. This procedure leads to additional correlations of fluctuating quantities which can not be neglected in practical reacting flows, where turbulent fluctuations of local temperature can reach the order of magnitude of the local averaged temperature. If the correlations of fluctuating quantities are accounted for, the unclosed expressions require additional transport equations including the need to model several additional terms. These problems make this approach unfavorable for practical combustion problems [101].

The gap towards a numerically efficient calculation of mean reaction rates in turbulent combustion is closed by different combustion models available in literature and commercial CFD software. These models are used to close the unknown source terms in the transport equations of species mass fractions or reaction progress and are often based on statistical averages of variables describing the progress of the combustion reaction, the assumption of fast chemistry and global one-step reaction schemes. In the scope of this thesis, the CFD modeling is focused on industry standard combustion models as the combustion noise

model is implemented as a pure post-processing tool, which then can be used for combustion noise prediction on the basis of existing simulation data.

The reaction progress c defined by a dimensionless ratio of temperatures in adiabatic conditions [98] is given by:

$$c = \frac{T - T_u}{T_{ad} - T_u}, \quad 0 \leq c \leq 1. \quad (2.56)$$

If the picture of the simple vortex is revisited in the context of chemical reaction occurring in the fast chemistry regime, the interface line separates fresh gas ($c = 0$) from completely burnt exhaust gas ($c = 1$). This situation is shown in Fig. 2.6. When the chemical processes are fast compared to the mixing dynamics, the

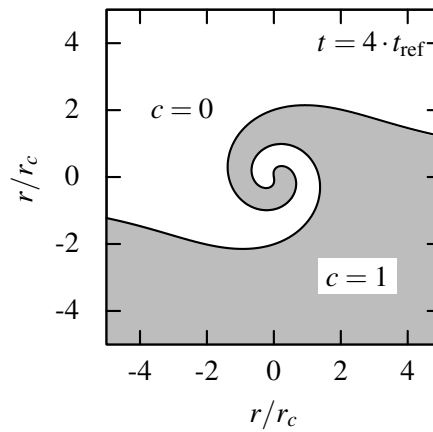


Figure 2.6: Two dimensional mixing of unburnt and burnt gas by a simple vortex in the case of infinitely fast chemistry. The contact surface area between fresh gas and exhaust gas governs the local reaction rate. The increase in contact surface area is determined by the rate of turbulent mixing.

overall reaction rate in Fig. 2.6 is proportional to the flame surface area and the time the two zones spend in direct contact with each other, which is generally modeled by a characteristic turbulent time scale. In this case, the variance of the reaction progress is given by [125]

$$\widetilde{c'^2} = \widetilde{c}(1 - \widetilde{c}), \quad (2.57)$$

as the corresponding distribution function is a double delta distribution with nonzero probability only at $\widetilde{c} = 0$ and $\widetilde{c} = 1$. Within the premixed flame simulation, an additional diffusive transport equation is solved for the reaction progress

and the mixture fraction so that the mixture composition comprising five species can be calculated from just two scalar transport equations [86]. The transport equation for the mean mixture fraction \tilde{z} is given by

$$\frac{\partial}{\partial t} (\bar{\rho}\tilde{z}) + \frac{\partial}{\partial x_j} (\bar{\rho}\tilde{u}_j\tilde{z}) = \frac{\partial}{\partial x_j} \left(\bar{\rho}D_t \frac{\partial \tilde{z}}{\partial x_j} \right), \quad (2.58)$$

while the reaction progress is calculated from

$$\frac{\partial}{\partial t} (\bar{\rho}\tilde{c}) + \frac{\partial}{\partial x_j} (\bar{\rho}\tilde{u}_j\tilde{c}) = \frac{\partial}{\partial x_j} \left(\bar{\rho}D_t \frac{\partial \tilde{c}}{\partial x_j} \right) + \bar{\dot{\omega}}_c, \quad (2.59)$$

where $\bar{\dot{\omega}}_c$ denotes the reaction source term provided by the selected combustion model and D_t is the effective turbulent diffusivity.

Eddy Break-Up Model

A basic model to describe combustion in turbulent flow was introduced by Spalding [124]. The mean reaction rate is expressed as

$$\bar{\dot{\omega}}_c = C_{\text{EBU}} \bar{\rho} \frac{1}{\tau_t} \tilde{c}''^2, \quad (2.60)$$

with a proportionality constant C_{EBU} of order unity and the mean variance of the reaction progress \tilde{c}''^2 . The mixing within the reaction zone is assumed to be performed mainly by the large vortices, so that the turbulent time scale governing this process equals that of the large scales [22], i.e.

$$\tau_t = \frac{k}{\varepsilon}. \quad (2.61)$$

With Eq. (2.57) the turbulent rate of creation of reactedness $\bar{\dot{\omega}}_c$ can be expressed as

$$\bar{\dot{\omega}}_c = C_{\text{EBU}} \bar{\rho} \frac{\varepsilon}{k} \tilde{c}(1 - \tilde{c}). \quad (2.62)$$

A similar approach of connecting the scalar dissipation of the reaction progress variance with the reaction rate is used in the basic model of combustion noise described in Sec. 4.1.

Schmid Model

A general concern with the family of eddy break-up models is the missing influence of reaction kinetics on the calculated rates, because these rates are basically computed as sheer mixing rates. Schmid [111, 112] formulated an improved eddy break-up approach extending the model capabilities towards flame regions where chemical kinetics influence the overall reaction rate, i.e. in regions of low turbulent Damköhler number. The model relies on a proportionality between the mean chemical reaction rate, the integral length scale, the turbulent velocity fluctuation and the turbulent burning velocity of a premixed flame:

$$s_t \propto \sqrt{u''_{\text{rms}} l_t \overline{\dot{\omega}_c}}. \quad (2.63)$$

The mean reaction rate combines the eddy break-up approach with a chemical time scale model, which is implicitly included in the laminar flamespeed and the turbulent Damköhler number. In terms of the scalar transport equation of reaction progress, the mean source term is given by

$$\overline{\dot{\omega}_c} = C_{\text{Schmid}} \cdot \left(\frac{s_l}{\sqrt{\frac{2}{3}k}} + \text{Da}_t^{*-1/4} \right)^2 \frac{\epsilon}{k} \overline{\rho}_u \tilde{c} (1 - \tilde{c}), \quad (2.64)$$

where $C_{\text{Schmid}} = 4.96$. The modified Damköhler number Da_t^* is related to the turbulent Damköhler number through

$$\text{Da}_t^* = 1 + \text{Da}_t^{-2}. \quad (2.65)$$

The model characteristics can be demonstrated when considering the limits of fast and slow chemistry with respect to turbulent mixing time, i.e. large and small values of the turbulent Damköhler number. In flame regions of large Damköhler number $\text{Da}_t \gg 1$, the model reduces to an eddy break-up model and the source term is dominated by the modified scalar dissipation rate of the reaction progress variance. In low Damköhler number regions, the source term is limited by the influence of finite rate chemistry.

Extended Schmid Model

Turbulent premixed flames in an unconfined configuration entrain ambient gas into the outer regions of the fresh gas flow. The entrainment causes statistical fluctuations of the mixture fraction. In the scope of this thesis, Eq. (2.64) is extended in order to account for these fluctuations in the outer shear layer of the flame. The fluctuations are taken into account by introducing a statistically averaged laminar flamespeed into the model. The average flamespeed is computed using a clipped Gaussian probability density function (PDF) [80]. Mean and standard deviation of the PDF are calculated using the approach discussed in the following section. For the determination of the local distribution function of the mixture fraction, an additional transport equation for the mixture fraction variance is solved [45]

$$\frac{\partial}{\partial t} \left(\bar{\rho} \widetilde{z''^2} \right) + \frac{\partial}{\partial x_j} \left(\bar{\rho} \widetilde{u_j z''^2} \right) = \frac{\partial}{\partial x_j} \left(\frac{\mu_t}{Sc_t} \frac{\partial \widetilde{z''^2}}{\partial x_j} \right) - C_d \frac{\varepsilon}{k} \bar{\rho} \widetilde{z''^2} + C_g \frac{\mu_t}{Sc_t} \left(\frac{\partial \widetilde{z}}{\partial x_j} \right)^2, \quad (2.66)$$

with the modeling constants of $C_d = 2.0$ and $C_g = 2.86$ [60]. The mean of the local laminar flamespeed is then computed from

$$\bar{s}_1(z) = \int_0^1 s_1(z) \cdot P(z) dz, \quad (2.67)$$

where $s_1(z)$ is calculated using an experimentally determined flamespeed correlation [127]. Numerical integration then gives $\bar{s}_1(z)$. The effect of the inclusion of mixture fluctuations into the evaluation of local laminar flamespeed is demonstrated in the scatter plot of Fig. 2.7 for an open premixed flame of $P_{th} = 40 \text{ kW}$, $S = 0.8$ and $\lambda = 1.1$. The PDF-averaging broadens the range of laminar flamespeeds calculated for different values of the mean mixture fraction and extends the lean end of zero laminar flamespeed. These lean parameter values of the mean mixture fraction correspond to the mixture diluted by entrainment in the outer zones of the flame.

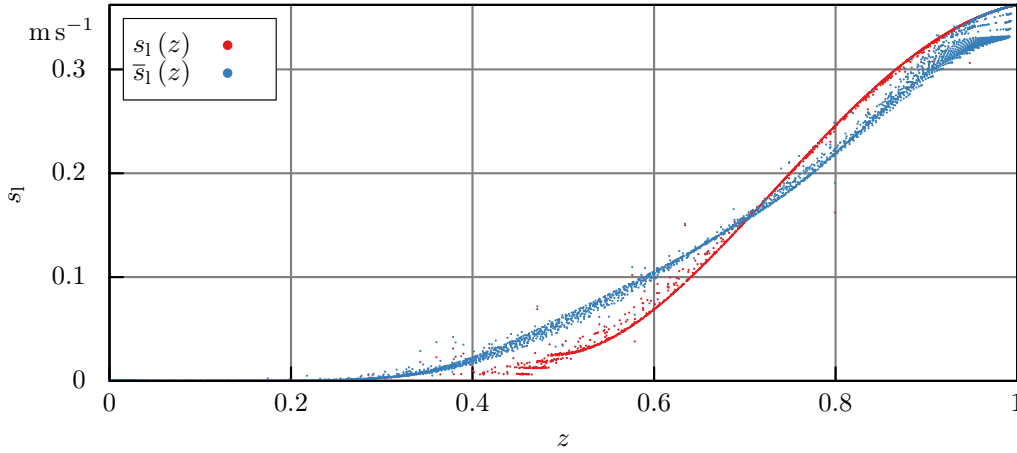


Figure 2.7: Scatter plot comparing the results of direct and PDF-averaged computation of the laminar flamespeed for an unconfined turbulent premixed flame at $P_{\text{th}} = 40\text{kW}$, $S = 0.8$ and $\lambda = 1.1$. Fluctuations of the local mixture fraction caused by the entrainment of ambient air into the flame are accounted for in the PDF-averaged value of the laminar flamespeed.

Clipped Gaussian PDF

The PDF of mixture fraction in hydrocarbon flames is known to be approximated well by a Gaussian distribution function [45, 100]. The Gaussian distribution is generally defined for all real numbers. In order to utilize the Gaussian distribution for the description variables that are limited to a certain domain of definition, the distribution function needs to be modified to ensure the adherence of its general properties. Variables like the mixture fraction or reaction progress are limited to a definition interval between $[0; 1]$. In order to preserve the overall probability, the tails of the distribution exceeding this interval are cut away and the removed area is added to the distribution as Dirac delta peaks on the respective interval limit. This procedure is referred to as clipping [80]. The Gaussian distribution function is given by [104]

$$p(x) = \frac{1}{\sigma\sqrt{2\pi}} \exp\left[-\frac{(x-\mu)^2}{2\sigma^2}\right]. \quad (2.68)$$

Herein, μ denotes the mean or median value of the distribution, while σ denotes the standard deviation. The process of restricting the distribution to the interval of $[0; 1]$ is illustrated in Fig. 2.8. The unwanted tails of the distribution function outside the interval limits are removed and lumped into Dirac delta peaks at 0

or 1, respectively. Clipping changes the distribution of the probability along the x -axis, so that mean and standard deviation of the clipped PDF are different from those of the initial distribution function. The clipped distribution function is then

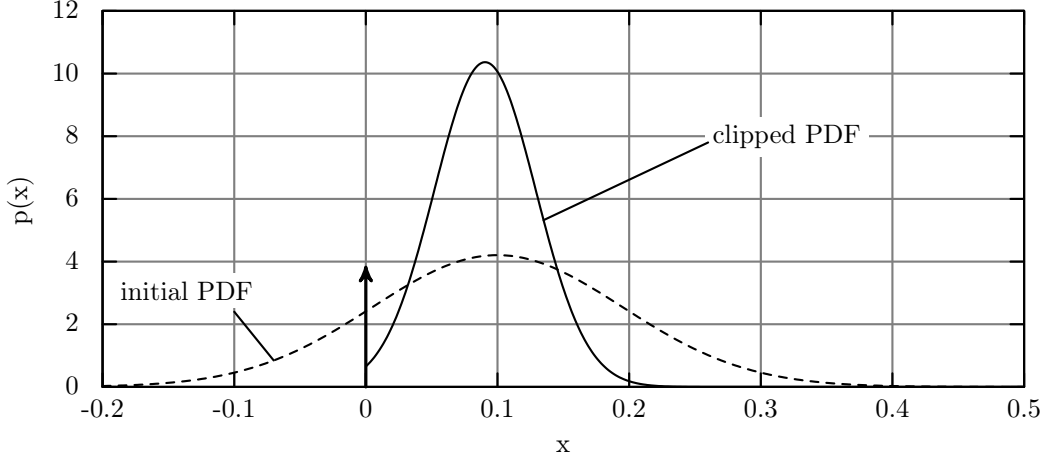


Figure 2.8: Sample plot demonstrating the clipping procedure that is used to fulfill the conservation of probability in the modified distribution. The unwanted tail below $x = 0$ is cut away and added to the clipped distribution as a dirac delta at the lower interval boundary.

given by a Gaussian distribution function inside the valid variable interval and the two delta impulses accounting for the clipped tails

$$p_c(x) = \frac{1}{\sigma_c \sqrt{2\pi}} \exp \left[-\frac{(x - \mu_c)^2}{2\sigma_c^2} \right] \cdot [\text{H}(x) - \text{H}(x - 1)] + A \cdot \delta(0) + B \cdot \delta(1), \quad (2.69)$$

where $\text{H}(x)$ denotes the Heaviside function and $\delta(x)$ is the Dirac delta function. A and B represent the unwanted tails of the initial PDF and are calculated by integrating over the axis range outside the interval:

$$A = \int_{-\infty}^0 p(x) dx = \frac{1}{2} \text{erfc} \left(\frac{\mu_c}{\sqrt{2}\sigma_c} \right)$$

$$B = \int_0^{\infty} p(x) dx = \frac{1}{2} \left[\text{erf} \left(\frac{\mu_c - 1}{\sqrt{2}\sigma_c} \right) + 1 \right]. \quad (2.70)$$

Mean μ_c and standard deviation σ_c of the clipped distribution function are unknown and can be calculated from the first and second moment of the clipped

PDF. The time-averaged mixture fraction is the first moment of the pdf about $z = 0$:

$$\tilde{z} = A + \int_0^1 z \cdot p_c(z) dz + B. \quad (2.71)$$

The mixture fraction variance is the second moment about $z = \tilde{z}$:

$$\tilde{z}''^2 = A + \int_0^1 z^2 \cdot p_c(z) dz + B - \tilde{z}^2. \quad (2.72)$$

Mean and variance of the mixture fraction are known from the solution of their corresponding transport equations, so that the unknown PDF parameters can be retrieved from this system of equations. The fully expanded conditional equations that are solved numerically using an iterative stabilized Newton-Raphson routine are given in Appendix A.

Eddy Dissipation Model

The Eddy Dissipation model proposed by Magnussen and Hjertager [83] is as well based on the fast chemistry assumption. In the simulation model of the non-premixed swirl flame, the model is used to calculate the averaged source terms in the transport equations of the individual species. A characteristic time-scale of the turbulent flow is used to model the characteristic mixing time needed to mix the reactants at the molecular level prior to combustion. The reaction rate of species k is taken to be proportional to the turbulent time scale, i.e.

$$\dot{\omega}_k \propto \frac{\varepsilon}{k}. \quad (2.73)$$

The reaction rate for a one-step chemical reaction is modeled depending on the species mass fraction limiting the reaction. Based on the mass fractions of the reactants (fuel F and oxidizer O), the mean reaction rate is expressed as

$$\bar{\dot{\omega}}_k = v'_k W_k A \bar{\rho} \frac{\varepsilon}{k} \min \left(\frac{Y_F}{v'_F W_F}, \frac{Y_O}{v'_O W_O}, C_T \right), \quad (2.74)$$

where $A = 4$ is a non-dimensional model constant, v'_k is the stoichiometric coefficient of reactant k and W_k is the molecular weight of reactant k . The model

assumes complete combustion and may over-predict the local temperature in regions where e.g. the mixture composition is rich. The temperature dependent term C_T limits the reaction rate in regions where the maximum specified flame temperature T_{\max} has been reached. C_T is introduced as a concentration of a virtual third species into the model, blending the reaction rate smoothly to zero once the local temperature approaches the maximum:

$$C_T = \max \left[(T_{\max} - \bar{T}), 0[\text{K}] \right] \cdot \frac{\bar{\rho} c_p}{\Delta H_R}. \quad (2.75)$$

In the scope of this work, the maximum temperature is set to be the local adiabatic flame temperature, which is calculated iteratively inside the whole domain. The iteration procedure is described in Appendix B.

3 Acoustic Theory

This chapter establishes the basic theoretical fundamentals describing the generation of turbulent combustion noise. Relevant equations needed for the spectral model are presented along with the acoustic theory involved in the experimental recording of combustion noise spectra.

3.1 Combustion Noise

Combustion noise emitted from turbulent flames shows a nearly perfect monopole radiation characteristic which physically corresponds to a volume expansion as the underlying mechanism. The turbulent fluctuations in the quantities determining reaction rates cause time dependent fluctuations of the heat release rate within the flame which is responsible for the volumetric expansion of the gas. When an eddy interacts with the reaction zone, it locally increases the flame surface, which leads to an increase in reaction rate (cf. Sec. 2.3.3). The continuous interaction between the flame and eddies of different sizes (different wave-numbers) causes the broadband acoustic signal typically related to combustion noise. These interaction phenomena can be studied by Direct Numerical Simulation (DNS) of small model flames [87, 144], where the interaction between an initially unperturbed laminar flame front and a single vortex is calculated.

The theoretical fundamentals considering the emission of sound by turbulent and chemical processes in fluid flow were given by Lighthill [79]. A non-homogeneous wave-equation derived from the linearized Euler equations gives the theoretical connection between the time dependent fluctuations of the heat release rate and the resulting acoustic pressure waves. For simplicity, the derivation in the scope of this thesis is shown in one dimension. The linearized Euler

equations for inviscid flow in one dimension are given by the linearized conservation equations for mass

$$\frac{\partial \rho'}{\partial t} + u \frac{\partial \rho'}{\partial x} + \rho \frac{\partial u'}{\partial x} = \frac{D\rho'}{Dt} + \rho \frac{\partial u'}{\partial x} = 0, \quad (3.1)$$

momentum

$$\frac{\partial u'}{\partial t} + u \frac{\partial u'}{\partial x} = \frac{Du'}{Dt} = -\frac{1}{\rho} \frac{\partial p'}{\partial x}, \quad (3.2)$$

and energy

$$\frac{\rho}{c_v} \frac{Ds'}{Dt} = \frac{1}{c^2} \frac{Dp'}{Dt} - \frac{Dp'}{Dt}, \quad (3.3)$$

where the primed quantities denote small perturbations about the mean flow. Taking the divergence of Eq. (3.2) and adding the time derivative of Eq. (3.3) eliminates the acoustic velocity perturbation, and a wave-equation for acoustic pressure waves including an entropy source is obtained:

$$\frac{D^2 p'}{Dt^2} - c^2 \frac{\partial^2 p'}{\partial x^2} = (\gamma - 1) \frac{p}{R} \frac{D^2 s'}{Dt^2}. \quad (3.4)$$

The time derivative of the entropy perturbation is assumed to be connected with the perturbation of the rate of heat release through

$$\frac{Ds'}{Dt} = \frac{q'}{\rho T} = \dot{q}'_v \frac{R}{p}, \quad (3.5)$$

so that Eq. (3.4) becomes [54]

$$\frac{D^2 p'}{Dt^2} - c^2 \frac{\partial^2 p'}{\partial x^2} = (\gamma - 1) \frac{D\dot{q}'_v}{Dt}. \quad (3.6)$$

Here, the right hand side marks the source term of acoustic pressure perturbation originating from fluctuations in the volumetric heat release rate \dot{q}'_v , while the left side describes the propagation of the perturbations with the characteristic sonic velocity c .

For an open burning turbulent flame at low Mach number, the wave-equation in three dimensions including the thermo-acoustic source term can be written as [25, 67, 143]

$$\frac{1}{c_\infty^2} \frac{\partial^2 p'}{\partial t^2} - \frac{\partial^2 p'}{\partial x_i \partial x_i} = \frac{\partial}{\partial t} \left[\frac{\rho_\infty (\gamma - 1)}{\rho_s c_s^2} \cdot \dot{q}'_v \right], \quad (3.7)$$

where the quantities marked with the subscript ∞ refer to ambient conditions while the subscript s refers to conditions within the source volume. If the ratio of specific heats γ is taken to be independent of temperature and the flame is operated at ambient pressure, $\rho_s c_s^2 = \gamma p_\infty = \rho_\infty c_\infty^2$, the fluid properties inside the source zone may be replaced by those of the ambient atmosphere, and Eq. (3.7) can be further simplified to obtain

$$\frac{1}{c_\infty^2} \frac{\partial^2 p'}{\partial t^2} - \frac{\partial^2 p'}{\partial x_i \partial x_i} \approx \frac{\partial}{\partial t} \left(\frac{\gamma-1}{c_\infty^2} \dot{q}'_v \right). \quad (3.8)$$

Here, \dot{q}'_v is a continuously distributed field of fluctuating rate of heat release within the source region (flame). The solution to Eq. (3.8) is obtained employing the corresponding Green's function, assuming that the right hand side represents a distribution of acoustic monopole sources and that the wavelength of the emitted pressure waves is large compared to the size of the flame ($\lambda \gg L_{\text{flame}}$):

$$p'(\vec{x}_B, t) = \frac{\gamma-1}{4\pi c_\infty^2} \cdot \int_{\mathbb{R}^3} \frac{\partial}{\partial t} \frac{\dot{q}'_v \left(\vec{x}_{s,n}, t - \frac{|\vec{x}_{s,n} - \vec{x}_B|}{c_\infty} \right)}{|\vec{x}_{s,n} - \vec{x}_B|} dV_{\text{flame}}. \quad (3.9)$$

The pressure signal at an observer position \vec{x}_B located in the farfield depends on the distance between the observer and the position of the flame (volumetric integral over all heat release rate fluctuations) and the time needed for the pressure perturbation to travel this distance. The solution is restricted in its validity to the acoustic far-field (i.e. the distance between observer and the flame, $r > \lambda$), which needs to be carefully observed for validity, when low frequencies are investigated. Here, time derivative and integration can be interchanged [32] to obtain

$$p'(\vec{x}_B, t) = \frac{\gamma-1}{4\pi c_\infty^2} \cdot \frac{\partial}{\partial t} \int_{\mathbb{R}^3} \frac{\dot{q}'_v \left(\vec{x}_{s,n}, t - \frac{|\vec{x}_{s,n} - \vec{x}_B|}{c_\infty} \right)}{|\vec{x}_{s,n} - \vec{x}_B|} dV_{\text{flame}}. \quad (3.10)$$

The observer at position \vec{x}_B notices the fluctuation generated at the source location after a time lag, that corresponds to his distance to the source $|\vec{x}_{s,n} - \vec{x}_B|$ and the propagation velocity of the fluctuation c_∞ in ambient conditions, i.e.

$$\tau = \frac{|\vec{x}_{s,n} - \vec{x}_B|}{c_\infty}. \quad (3.11)$$

If the spatial distance between the observer position and the flame is large compared to the distance in between sources (i.e. large compared to the size of the flame), it can be assumed equal for all source locations, i.e.

$$r = |\vec{x}_{s, n} - \vec{x}_B|, \quad (3.12)$$

which is shown schematically in Fig. 3.1. Inserting Eq. (3.11) and Eq. (3.12) into

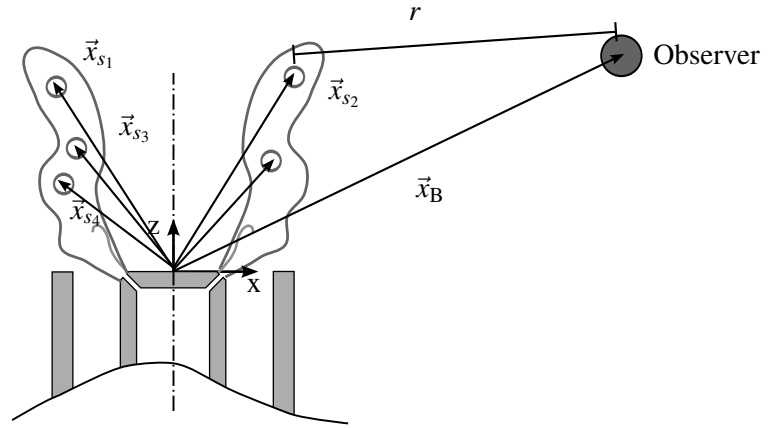


Figure 3.1: Sketch of a turbulent flame assembled from n single sources $\vec{x}_{s, n}$ as in (3.9), showing the observer location \vec{x}_B in the acoustic farfield. As the distance between the flame and the observer position is large compared to the size of the flame, the radius between observer and individual sources is taken equal for all sources.

Eq. (3.10), the solution for the far field pressure fluctuation becomes

$$p'(\vec{x}_B, t) = \frac{\gamma - 1}{4\pi c_\infty^2 r} \cdot \frac{\partial}{\partial t} \int_{\mathbb{R}^3} \dot{q}'_v(\vec{x}_{s, n}, t - \tau) dV_{\text{flame}}. \quad (3.13)$$

As a conserved quantity and for direct evaluation of the thermo-acoustic efficiency, the radiated acoustic power is of primary interest when analyzing the sound spectrum of open burning flames. The acoustic power in free space is the product of fluctuating pressure and velocity integrated over a surface of observation S , that fully encloses the source of interest:

$$P_{\text{aco}} = \int_S \overline{p'(\vec{x}, t) \vec{u}'(\vec{x}, t) \cdot \vec{n}} dS = \int_S \overline{\vec{I} \cdot \vec{n}} dS. \quad (3.14)$$

Here, the acoustic intensity is defined as the time averaged flux of acoustic energy away from the source and S denotes the surface of observation enclosing the source region. The overline denotes a time averaging process. Making use of the symmetric monopole radiation character and the free space impedance $Z = \rho_\infty c_\infty$ if sound is radiated into a non-reflecting environment, the acoustic power is obtained by integrating over the surface area of S :

$$P_{\text{aco}} = \frac{\overline{p'(r,t)^2}}{\rho_\infty c_\infty} \cdot 4\pi r^2. \quad (3.15)$$

Inserting Eq. (3.13) into Eq. (3.15), the farfield acoustic power, generated by the fluctuation in heat release rate is found:

$$P_{\text{aco}} = \frac{4\pi r^2 (\gamma - 1)^2}{16\pi^2 \rho_\infty c_\infty^5 r^2} \overline{\int_V \frac{\partial}{\partial t} \dot{q}'_v(\vec{x}_{s,n}, t - \tau) dV \int_V \frac{\partial}{\partial t} \dot{q}'_v(\vec{x}_{s,n+1}, t - \tau) dV} \quad (3.16)$$

The continuous distribution of sources inside the flame is now taken to be represented by two model sources, $\dot{q}'_{v,1}(\vec{x}_{s,1}, t_1)$ and $\dot{q}'_{v,2}(\vec{x}_{s,2}, t_2)$ which account for the entirety of spatial and temporal coherent sources within the flame. Statistical independence is assumed for the model sources, allowing the simplification of the volume integrals to give

$$P_{\text{aco}} = \frac{(\gamma - 1)^2}{4\pi \rho_\infty c_\infty^5} \overline{\iint_{VV} \frac{\partial}{\partial t} \dot{q}'_v(\vec{x}_{s,1}, t - \tau) \frac{\partial}{\partial t} \dot{q}'_v(\vec{x}_{s,2}, t - \tau) dV dV}. \quad (3.17)$$

Boineau et al. [10, 11] and Wäsle [143] make use of a compound probability function to account for spatial and temporal coherence of the sources within the flame, similar to the modeling approach used by Béchara et al. [5] and Bailly et al. [3] for aero-acoustic source modeling:

$$\overline{\frac{\partial}{\partial t} \dot{q}'_v(\vec{x}_{s,1}, t - \tau) \frac{\partial}{\partial t} \dot{q}'_v(\vec{x}_{s,2}, t - \tau)} = -\frac{\partial^2}{\partial \tau^2} R_{q_1 q_2}(\vec{x}_{s,1}, t_1, r, \tau). \quad (3.18)$$

Here, r and τ are the virtual spatial and temporal separation distances between the two statistical model sources. The modeled correlation is now expressed as a coherence function $\Gamma(r, \tau)$, weighted by the root mean square of the fluctuating heat release rate, so that [143]

$$R_{q_1 q_2}(\vec{x}_{s,1}, t_1, r, \tau) = \dot{q}'_{\text{rms}}{}^2 \cdot \Gamma(r, \tau). \quad (3.19)$$

Ribner [108] proposed the separation of the joint coherence function into its functional components, the spatial and temporal coherence

$$\Gamma(r, \tau) = \Gamma(r) \cdot \Gamma(\tau), \quad (3.20)$$

postulating statistical independence of spatial and temporal coherence. In isotropic turbulence, the spatial part of the coherence function solely depends on the radial distance from the point of measurement, which can be expressed analytically, following experimental reasoning by Boineau et al. [11] and Winkler [150]:

$$\Gamma(r) = \exp\left(-\frac{\pi}{4} \cdot \frac{r^2}{l_t^2}\right). \quad (3.21)$$

Spherical integration of Eq. (3.21) yields a virtual statistical volume within which the heat release rate fluctuations are perfectly in phase, i.e. [146]

$$V_{\text{coh}} = \int_V \Gamma(r) dV = 8l_t^3. \quad (3.22)$$

Combining Eqs. (3.18), (3.19), (3.20), (3.22), and inserting the result into Eq. (3.17), the acoustic power becomes

$$P_{\text{aco}}(\tau) = -\frac{(\gamma-1)^2}{4\pi\rho_\infty c_\infty^5} \int_V -\frac{\partial^2}{\partial \tau^2} \dot{q}_{\text{rms}}'^2 \cdot \Gamma(\tau) \cdot V_{\text{coh}} dV. \quad (3.23)$$

The frequency space counterpart of the coherence function is the Lagrangian correlation spectrum of the fluctuations in heat release.

Applying Fourier transformation to Eq. (3.23), yields the expression for the frequency spectrum of the radiated acoustic power. The second order derivative in time equals a multiplication with $(i\omega)^2$ in frequency space so that the frequency spectrum is obtained as

$$\mathfrak{F} \left\{ -\frac{\partial^2}{\partial \tau^2} \dot{q}_{\text{rms}}'^2 \cdot \Gamma(\tau) \right\} = -(2\pi i f)^2 \chi_{\text{qq}}(f), \quad (3.24)$$

where \mathfrak{F} denotes the Fourier transform. Making use of Eq. (3.24) the Lagrangian frequency spectrum of the acoustic power generated by the flame is ($i^2 = -1$)

$$P_{\text{aco}}(f) = \frac{\pi(\gamma-1)^2}{\rho_\infty c_\infty^5} \int_V f^2 \cdot \chi_{\text{qq}}(f) \cdot V_{\text{coh}} dV. \quad (3.25)$$

A remarkable property of Eq. (3.25) is the strong influence (fifth power) of the ambient sound speed on the radiated sound power. A decrease in ambient temperature of just 10K roughly leads to a 10% increase of the radiated acoustic power at a given source strength χ_{qq} .

The Lagrangian frequency spectrum of the fluctuating heat release rate χ_{qq} and the coherence volume V_{coh} in Eq. (3.25) are primary points of interest in the assembly of the combustion noise model, which is discussed in Chap. 4.

3.2 Sound Propagation in One-Dimensional Geometries

In the course of this study, sound propagation in enclosed combustion systems is investigated in the plain wave regime using acoustic network models. Below the cut-on frequency of higher order modes, the sound field inside a circular duct can be described by a wave equation of the form of Eq. (3.7) in one dimension.

Assuming time harmonic wave propagation, the solution to this equation is given by two wave functions \hat{p}_+ and \hat{p}_- of arbitrary shape propagating in up- and downstream direction

$$\hat{p}(x, \omega) = \hat{p}_+(\omega) \exp(-ik_+x) + \hat{p}_-(\omega) \exp(ik_-x), \quad (3.26)$$

where \hat{p} denotes the complex acoustic pressure. In Eq. (3.26) the two wavenumbers, k_+ for the wave traveling downstream and k_- traveling upstream, account for the influence of the mean flow velocity u on the propagation velocity of the pressure waves, i.e.

$$k_+ = \frac{k_0}{(1 + \text{Ma})}, \quad k_- = \frac{k_0}{(1 - \text{Ma})}, \quad (3.27)$$

where

$$k_0 = \frac{\omega}{c} \quad (3.28)$$

and

$$\omega = 2\pi f. \quad (3.29)$$

The mean flow velocity is included in the mean flow Mach number $\text{Ma} = \frac{u}{c}$.

Based on the solution, one-dimensional acoustic wave propagation in long enclosures can be calculated. If coupled with suitable models describing acoustic interaction with geometrical elements such as changes in cross sectional area, tri-junctions or acoustic boundary conditions, networks of acoustic elements can be set up. These network models offer computationally efficient access to the acoustic behavior of nearly arbitrary complex geometries [40] and may be easily coupled with experimental data for interior coupling or boundary elements.

The quality of results obtainable from one-dimensional acoustic networks largely depends on the modeling of the boundary conditions. Most technical combustion systems involve the modeling of an exhaust duct, where the exhaust gas discharges into an acoustically open environment at ambient conditions. The boundary condition at the exit governs the sound field inside the system as well as the amount of internal acoustic energy that can be emitted into the surroundings. Consequently, the acoustic boundary condition at the exhaust is of great interest in the analysis of combustion noise radiation from combustion systems.

3.3 Acoustic Boundary Conditions

At an acoustic boundary, incident pressure waves (\hat{p}_+) are partially reflected. The transmitted part leaves the system and is radiated into the surroundings, while the reflected wave travels back into the system. The reflection of incident waves at a boundary is governed by the plain wave reflection coefficient. It is defined as the complex valued ratio of the incident and the reflected wave:

$$\hat{r} = \frac{\hat{p}_-}{\hat{p}_+}. \quad (3.30)$$

The amount of acoustic energy leaving the system at the boundary is influenced by the mean flow through the boundary. The influence of the mean exit Mach number on the acoustic energy flux through the boundary

$$\text{Ma}_E = \frac{\bar{u}_E}{c_E} \quad (3.31)$$

is given by the energy reflection coefficient r_E that is related to the pressure reflection coefficient in Eq. (3.30) by [97]

$$r_E = |\hat{r}|^2 \left(\frac{1 - \text{Ma}_E}{1 + \text{Ma}_E} \right)^2. \quad (3.32)$$

In Eq. (3.31), \bar{u}_E denotes the axial flow velocity averaged over the exit plane.

The polar form of the complex reflection coefficient

$$\hat{r} = -|r| \exp(2ik_0\delta) \quad (3.33)$$

is frequently used to analyze reflection coefficient data in amplitude and phase. Here, the parameter δ corresponds to a virtual extended length scale. The imaginary part of the reflection coefficient containing the extended length scale accounts for effects of the inertia of the air flow around the duct exit. If a perfect open end is assumed (i.e. $\hat{p}_+ = -\hat{p}_-$), this additional frequency-dependent length can be thought of as the distance that the incident wave would travel into the opening before being reflected. The virtual extended length can be calculated from measured values of the reflection coefficient phase ϕ at the exit plane from [2]

$$\frac{\delta}{a} \approx \frac{(\pi - \phi)(1 - \text{Ma}_E^2)}{2k_0a}. \quad (3.34)$$

In Eq. (3.34), k_0a denotes the Helmholtz number He with the radius of the circular pipe a .

3.3.1 Reflection at an Open Pipe End at Ambient Conditions

The standard geometric quantities involved with the simplified model problem of an open pipe termination are shown in Fig. 3.2. In the absence of mean flow from inside the pipe, sound reflection at the pipe termination is solely a problem of geometric acoustics. This model problem has been solved by Levine and Schwinger [77]. Silva et al. give empirical equations for the end reflection coefficient and the virtual extended length scale. In the range up to $ka = 4$ the reflection coefficient magnitude can be approximated by [117]

$$|\hat{r}| = \frac{1 + a_1(ka)}{1 + (\beta + a_1)(ka)^2 + a_2(ka)^4 + a_3(ka)^6}. \quad (3.35)$$

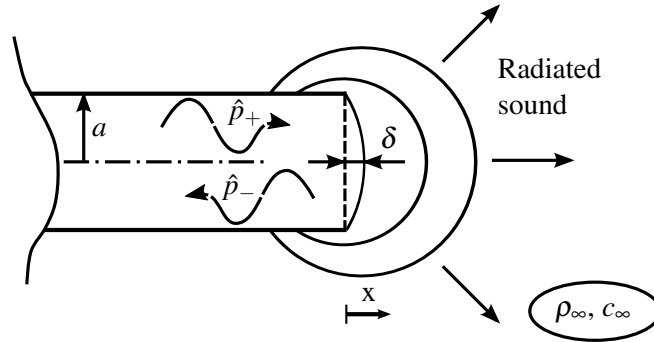


Figure 3.2: Plane wave reflection and sound radiation at an open pipe termination. The virtual extended pipe length δ which represents the phase-shift upon reflection is indicated at the exit plane.

For the virtual extended length they obtain

$$\frac{\delta}{a} = \eta \frac{1 + b_1 (ka)^2}{1 + b_2 (ka)^2 + b_3 (ka)^4 + b_4 (ka)^6}. \quad (3.36)$$

The constants needed to compute the model equations are given in Tab. 3.1 and the resulting model curves for reflection coefficient magnitude and extended length are plotted in Fig. 3.3 over the dimensionless Helmholtz number. At

Table 3.1: Constants needed for the approximate calculation of the pipe termination reflection coefficient [117].

β	η	a_1	a_2	a_3	b_1	b_2	b_3	b_4
0.500	0.6133	0.800	0.266	0.0263	0.0599	0.238	-0.0153	0.0015

low frequencies, total reflection occurs at the termination, i.e. most of the incident acoustic energy is kept inside the pipe for low frequencies. At higher frequencies, the reflection coefficient drops significantly and sound is radiated more efficiently into the surroundings. In practical systems, pipe openings are often discharging fluid into the surroundings as for example an exhaust pipe. The reflection coefficient in the presence of fluid flow from the pipe, especially if the fluid density of the fluid exiting the pipe is different from ambient density, can depart significantly from the no-flow case. This case has been analyzed by Munt [91, 92].

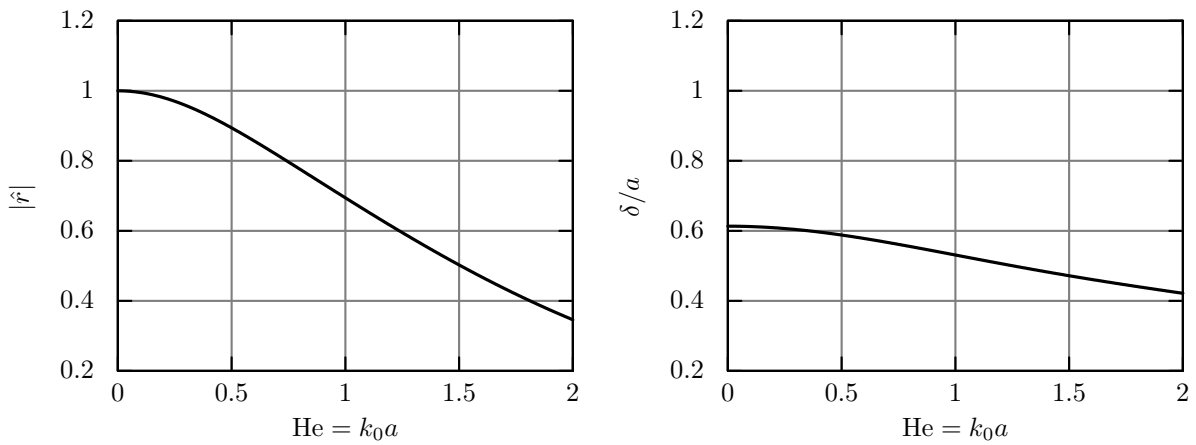


Figure 3.3: Magnitude of the end reflection coefficient (left) and extended length scale (right) of an unflanged duct termination calculated using Eq. (3.35) and Eq. (3.36).

3.3.2 Reflection at an Open Pipe End at Elevated Temperatures

In the presence of mean flow discharging from the pipe end into the surrounding atmosphere, a shear layer is formed from the pipe edge, that is able to interact with acoustic pressure waves radiated from the pipe. The interaction can either result in additional damping of incident pressure waves or amplification. The transfer of vortex energy from the shear layer into acoustic energy prior to reflection leads to reflection coefficients in excess of unity. If the fluid density inside the jet is lower compared to the ambient density (hot exhaust gas), the magnitude of the reflection coefficient drops dramatically, and sound radiation into the opening is enhanced [62]. This effect is considered in the modeling of sound radiation from an industrial marine coolant heater in Chap. 8.

The model problem as originally considered by Munt is sketched in Fig. 3.4. Inside the duct, fluid flows at a constant Mach number Ma_i and density ρ_i . The internal fluid exits the pipe and forms an infinitely thin shear layer which cylindrically extends to infinity.

The acoustic field inside and outside the duct is modeled using a convective wave equation in cylindrical coordinates. The ambient surroundings are assumed to be non-reflective and the vortex layer is assumed to extend infinitely along x in its initial cylindrical shape. The vortex layer also separates the pipe fluid from the

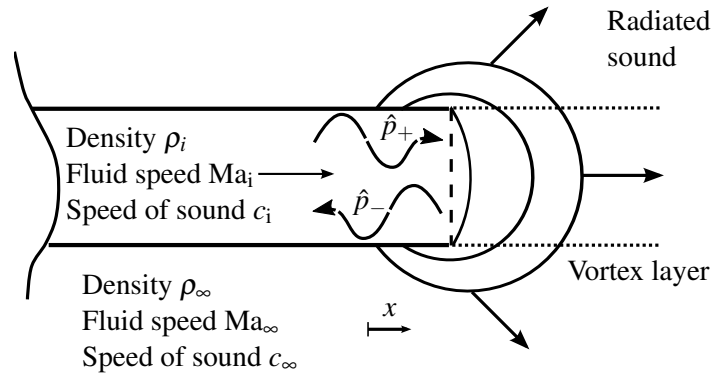


Figure 3.4: Plane-wave reflection and sound radiation at an open pipe termination in the presence of mean flow as considered by Munt [91, 92].

ambient fluid. The pipe walls are assumed to behave acoustically rigid, perfectly reflecting all incident sound. Across the vortex sheet, pressure is continuous and continuity of particle displacement is applied. The model equations are solved numerically using a complex Newton-Raphson iterative root finding algorithm in the course of this study.

Figure 3.5 shows the influence of exhaust flow temperature on the end reflection coefficient of a pipe with low speed mean flow of $u = 8 \text{ m/s}$ and a temperature of 1900 K . When compared to the Levine and Schwinger reference solution for ambient conditions and quiescent medium, the dominant influence of the exhaust gas temperature is obvious. For temperatures commonly observable in exhaust

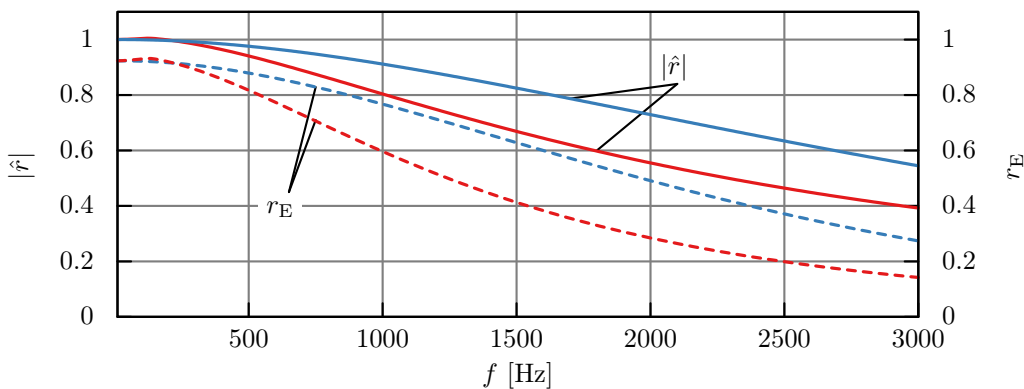


Figure 3.5: Magnitude of the pressure reflection coefficient ($|\hat{r}|$) and the energy reflection coefficient (r_E) at a circular pipe exit plane for an exhaust flow temperature of $T_i = 1900 \text{ K}$ and an ambient temperature of $T_\infty = 293 \text{ K}$ calculated using the Munt model [91, 92] (—) compared to the isothermal solution of Levine & Schwinger [77] (---).

gas flows, a drop in the reflection coefficient of 0.2 in the medium frequency range occurs. Consequently, sound radiation is more efficient at higher temperatures. The energy reflection coefficient computed from Eq. (3.32) depicts a similar trend. With increasing temperature gradient between exhaust gas and ambient atmosphere, an increasing amount of acoustic energy is able to exit the system and is radiated into the environment at the exhaust exit. The corresponding energy reflection coefficient rests below unity at all times, indicating that some acoustic energy is transported outside the pipe for all frequencies.

3.4 Measurement of Sound Intensity

To determine sound intensity experimentally, sound pressure and particle velocity need to be measured. Beneath methods where the particle velocity is recorded directly, the commonly applied method is based on the measurement of the local pressure gradient using two closely-spaced microphones. This configuration is known as a p-p intensity probe. In quiescent atmosphere, products of fluctuating quantities and mean flow quantities can be neglected and the linearized equation for momentum conservation simplifies to

$$\frac{\partial u'}{\partial t} + \frac{1}{\rho} \cdot \frac{\partial p'}{\partial x} = 0. \quad (3.37)$$

Integration gives an equation for the sound particle velocity depending on two pressure readings at a distance of d from each other:

$$u' \approx \frac{-1}{\rho} \int_{-\infty}^t \left(\frac{\partial p'}{\partial x} \right) dt \approx \left(\frac{-1}{\rho d} \right) \int_{-\infty}^t [p'_2(\tau) - p'_1(\tau)] d\tau. \quad (3.38)$$

Here, the pressure gradient in direction x has been approximated by a finite difference of the pressure readings for a very short separation distance, i.e.

$$\frac{\partial p'}{\partial x} = \lim_{\Delta x \rightarrow 0} \left(\frac{\Delta p'}{\Delta x} \right) \approx \frac{p'_2 - p'_1}{\Delta x}, \quad (3.39)$$

and Δx is equivalent to d , if the coordinate system is aligned with the probe axis. The fluctuating sound pressure at the probe center is the geometric average of the two pressure readings:

$$p' = \frac{p'_1 + p'_2}{2}. \quad (3.40)$$

Combining the above expressions for pressure and particle velocity, the expression for the acoustic intensity in time-domain is

$$I_d = \frac{1}{2\rho d} [p'_2(t) + p'_1(t)] \int_{-\infty}^t [p'_2(\tau) - p'_1(\tau)] d\tau. \quad (3.41)$$

This equation can be simplified by making use of the property that the time derivatives approach zero for very long averaging times [25, 96], which reduces the computational effort:

$$I_d = \frac{1}{\rho d} p'_1(t) \int_{-\infty}^t p'_2(\tau) d\tau. \quad (3.42)$$

The experimental determination of sound intensity spectra in the scope of this work is performed using an alternative approach in frequency space. Fahy et al. [35–37] and Chung [20] independently derived a formulation for the sound intensity in frequency domain which is based on the Fourier transform of the cross correlation function of sound pressure and particle velocity.

Sound intensity in frequency space is defined as

$$\hat{I} = \hat{p} \cdot \hat{u}^*. \quad (3.43)$$

For pure-tone sound fields, the concept of an active and a reactive component of sound intensity can be demonstrated by considering the representation [61]

$$\hat{I} = \frac{1}{2} \text{Re} \{ \hat{p} \cdot \hat{u}^* \} + \frac{1}{2} \text{Im} \{ \hat{p} \cdot \hat{u}^* \}, \quad (3.44)$$

where

$$I = \frac{1}{2} \text{Re} \{ \hat{p} \cdot \hat{u}^* \} = \frac{1}{2} |\hat{p}| \cdot |\hat{u}| \cdot \cos \phi \quad (3.45)$$

denotes the active intensity, \hat{p} , \hat{u} denote the complex amplitudes of pressure and particle velocity and ϕ the phase difference between both signals. Equation (3.45) shows, that the active sound intensity component reaches its maximum value, if the phase difference between pressure and particle velocity is zero. This is the case in acoustically non-reflective free-field conditions. The reactive intensity component is defined as

$$J = \frac{1}{2} \text{Im} \{ \hat{p} \cdot \hat{u}^* \} = \frac{1}{2} |\hat{p}| \cdot |\hat{u}| \cdot \sin \phi, \quad (3.46)$$

which vanishes if the phase difference between both signals is zero and reaches its maximum for $\phi = \pi/2$. The phase difference of $\pi/2$ corresponds to perfectly reflective acoustic conditions found for example inside a pipe with two closed ends. The resulting reactive sound field is purely imaginary, which corresponds to standing waves.

The two intensity components can be computed from auto- and cross-spectral densities of the corresponding pressure signals for broadband signals. The reactive sound intensity is then given by [25]

$$J(\omega) = -\frac{1}{2\omega\rho d} [G_{p_1p_1}(\omega) - G_{p_2p_2}(\omega)], \quad (3.47)$$

where $G_{p_1p_1}(\omega)$, $G_{p_2p_2}(\omega)$ denote the auto-power spectral densities of the two pressure signals. The active intensity spectrum can be obtained from [35]

$$I(\omega) = -\frac{1}{\omega\rho d} \text{Im} [G_{p_1p_2}(\omega)], \quad (3.48)$$

where $G_{p_1p_2}(\omega)$ is the cross-power spectral density of the pressure readings. The spectral densities can be evaluated in a computationally efficient way in frequency space. The technique allows a direct distinction between reactive acoustic intensity due to standing waves (room acoustics) and the active intensity component, representing the actual acoustic energy radiated by the source. In the partially reverberant laboratory, this technique is used to determine the acoustic power spectra.

Prior to the intensity calculation, the time average mean value is removed from the time series and a bandpass filter is applied to remove high and low frequency noise from the signal. The cross- and auto-spectral densities are then

calculated using the method proposed by Welch [145]. This method for the estimation of power spectra is based on the sectioning of the initial time series data into segments. Individual segments are permitted to overlap. The segments are windowed before their periodogram is calculated using fast Fourier transform. Then, the estimated spectrum $P(f)$ is given by the average of the k individual periodograms, i.e.

$$P(f) = \frac{1}{k} \sum_{k=1}^k I_k(f). \quad (3.49)$$

The averaging process reduces the noise in the resulting power spectrum, which makes the method useful for processing of long time-series and high sampling rates.

3.5 Logarithmic Scales

Sound pressure, intensity and power are quantities of high dynamic amplitude ranges. A silent conversation takes place at sound pressures around $2 \cdot 10^{-2}$ Pa, while the sound emitted by a gunshot reaches pressure amplitudes of about 200Pa. Because of the large amplitude ranges, acoustic variables are evaluated on a logarithmic scale using the logarithmic unit decibel. The quantities are normalized with reference values, that approximately correspond to the human threshold of hearing. The logarithmic scales for sound pressure, intensity and power are calculated from [137]:

$$L_p = 20 \cdot \log_{10} \left(\frac{p_{\text{rms}}}{p_{\text{ref}}} \right), \quad p_{\text{ref}} = 20 \cdot 10^{-6} \text{Pa} \quad (3.50)$$

$$L_I = 10 \cdot \log_{10} \left(\frac{I}{I_{\text{ref}}} \right), \quad I_{\text{ref}} = 10 \cdot 10^{-12} \text{W} \quad (3.51)$$

$$L_W = 10 \cdot \log_{10} \left(\frac{P_{\text{aco}}}{P_{\text{aco, ref}}} \right), \quad I_{\text{ref}} = 10 \cdot 10^{-12} \text{W} \quad (3.52)$$

4 Spectral Modeling of Turbulent Combustion Noise

This thesis extends the spectral model proposed by Hirsch et al. [52, 53] towards the prediction of acoustic power spectra from turbulent non-premixed flames. The method provides a model of the correlation spectrum of the heat release fluctuations (Eq. (3.25)) which is needed to calculate the acoustic power radiated into the farfield. Before the extended model for non-premixed flames is introduced, the premixed model is re-established in order to provide the theoretical basis for the model extension.

4.1 The Spectrum of Heat Release

From Eq. (3.25) the acoustic power spectrum, resulting from the combustion in the reaction zone of a turbulent flame, can be obtained if the Lagrangian correlation spectrum of the fluctuating heat release rate is known. Hirsch et al. [52] establish a connection between the local rate of heat release and the scalar variance of the reaction progress. The spectrum of heat release is then derived by introducing a model spectrum from turbulence theory to model the fluctuations of reaction progress, which is formally treated as passive scalar quantity. Under the prerequisite of turbulent flow conditions (Re large), the mean rate of turbulent reaction depends on the local mean scalar dissipation rate of the reaction progress variance [52, 53, 98]:

$$\bar{\dot{\omega}} = \rho_u Y_{f,u} C_D \frac{\varepsilon}{k}. \quad (4.1)$$

Here the subscript u refers to conditions in the unburnt gas and the model constant is $C_D = 2$. Equation (4.1) can be directly transformed to wave-number space

if we accept the premise that this expression also holds for the auto-correlation of the scalar quantities, i.e.

$$R_\omega = \rho_u Y_{f,u} C_D \frac{\varepsilon}{k} R_{c'^2}. \quad (4.2)$$

In turbulent flow of sufficiently high Reynolds number, a wave-number range exists, where turbulent scales are locally isotropic. As the large scale motion is influenced by the dimensions of the bounding geometry and can not be modeled on a general basis, the assumption of isotropy at the large scales is taken at this point. The transformation of Eq. (4.2) to wave-number space leads to

$$E_\omega(\kappa) = \rho_u Y_{f,u} C_D \frac{\varepsilon}{k} E_{c'^2}(\kappa), \quad (4.3)$$

implicitly prescribing that the turbulent dissipation rate ε and the kinetic energy k possess no spatial fluctuations in wave-number space. Wave-number spectra of passive scalars have been shown to be in close agreement with corresponding velocity spectra. Cheng et al. [18] perform an experimental study on active scalar spectra in premixed flames and show that the spectrum of the reaction progress is strongly coupled to the velocity spectrum. Consequently, Eq. (4.3) can be evaluated if the wave-number spectrum of the scalar variance of the progress variable is known. Hirsch et al. [53] propose the use of the scalar model spectrum derived by Tennekes and Lumley, (Eq. (2.17)) [134]. The scalar variance spectrum is modeled as

$$E_{c'^2}(\kappa) = C_s \bar{\xi}_{c'^2} \varepsilon^{-\frac{1}{3}} \kappa^{-\frac{5}{3}} \cdot \exp \left[-\frac{3}{2} \left(\pi \beta \alpha^{\frac{1}{2}} (\kappa l_t)^{-\frac{4}{3}} + \alpha (\kappa \eta_{c'^2})^{\frac{4}{3}} \right) \right], \quad (4.4)$$

where C_s is a constant of order unity and $\bar{\xi}_{c'^2}$ is the mean scalar dissipation rate of the quantity in question. The model resembles the well known $k^{-5/3}$ law of spectral decay with two additional length scales, that account for the effects of production and dissipation of spectral energy at the low and high wave-number ends of the spectrum. Inserting the scalar dissipation rate of the reaction progress variance,

$$\bar{\xi}_{c'^2} = \frac{\bar{q}_v}{\rho_u Y_{f,u} H_u} \quad (4.5)$$

into Eq. (4.4), the spectrum becomes

$$E_{c''2}(\kappa) = C_S \frac{\bar{q}_v}{\rho_u Y_{f,u} H_u} \varepsilon^{-\frac{1}{3}} \kappa^{-\frac{5}{3}} \cdot \exp \left[-\frac{3}{2} \left(\pi \beta \alpha^{\frac{1}{2}} (\kappa l_t)^{-\frac{4}{3}} + \alpha (\kappa \eta_{c''2})^{\frac{4}{3}} \right) \right]. \quad (4.6)$$

Equations (4.3) and (4.6) can be combined to obtain the wave-number spectrum of the fluctuations in heat release rate independent of the combustion model used in the calculation of the reactive mean flow field [52, 146]:

$$E_q(\kappa) = C_S C_D \bar{q}_v \frac{\varepsilon^{\frac{2}{3}}}{k} \cdot \kappa^{-\frac{5}{3}} \cdot \exp \left[-\frac{3}{2} \left(\pi \beta \alpha^{\frac{1}{2}} (\kappa l_t)^{-\frac{4}{3}} + \alpha (\kappa \eta_{c''2})^{\frac{4}{3}} \right) \right]. \quad (4.7)$$

In Eq. (4.7), the spectrum of the scalar fluctuations also follows the $\kappa^{-5/3}$ scaling law, and is weighted by the local rate of heat release and the turbulence kinetic energy and dissipation rate. The production range is located at wave-numbers below $\kappa l_t \approx 1$ and the dissipation range begins at wave-numbers in excess of $\kappa \eta_{c''2} \approx 1$. l_t denotes the length scale of the integral scales of turbulence while $\kappa \eta_{c''2}$ corresponds to the Kolmogorov length scale, but is defined differently in the course of scalar spectra [52]. The constant C_S and the cutoff length $\eta_{c''2}$ resemble the influence of the chemical reaction on the scalar spectrum.

The influence of a first order chemical reaction on the scalar spectrum has been studied theoretically by Corrsin [23]. Based on a scalar transport equation with first order source term for the scalar quantity θ

$$\frac{\partial \theta}{\partial t} + u_i \frac{\partial \theta}{\partial x_i} \approx -C\theta, \quad (4.8)$$

where diffusive effects are neglected, Corrsin derives a wave-number spectrum including the effect of the reaction on spectral amplitude

$$G(\kappa) \approx B \kappa^{-5/3} \cdot \exp \left\{ 3C \varepsilon^{-1/3} \kappa^{-2/3} \right\} \quad (4.9)$$

in the inertial subrange. Here, the constant C accounts for the intensity of the chemical reaction. The reacting scalar θ is taken to be so dilute, that the effect of the reaction on the flow-field is negligible. It is found for the scalar spectrum, that the chemical reaction has negligible effect on the scalar amplitude at wave-numbers in excess of $\kappa_c = C^{3/2} \varepsilon^{-1/2}$. At κ_c itself, the consumption of spectral energy is of the same order as the convective spectral transfer.

4.2 Premixed Turbulent Flames

An active scalar quantity is influenced in its spectral amplitude by chemical reaction. The active scalar characteristic of the reaction progress variance is accounted for by considering two effects in the model, the spectral cut-off and the effects of finite rate chemistry on the spectral amplitude. The specific modeling of these effects depends on the flame type and is shown in its original state for premixed flames in the following.

4.2.1 Scaling of the Spectral Amplitude

The scaling function proposed by Hirsch et al. [53] is based on the combustion model developed by Schmid [111, 112], and relates the actual parameter value of the reaction progress variance to its theoretical maximum for the limiting case of infinitely fast chemical reaction at $Da_t \rightarrow \infty$

$$C_s = \frac{\alpha \widetilde{c''^2}(Da_t)}{C_D \widetilde{c''^2}(Da_t \rightarrow \infty)} = \frac{\alpha \widetilde{c''^2}}{C_D \widetilde{c}(1 - \widetilde{c})}, \quad (4.10)$$

with the model constants $\alpha = 1.5$ and $C_D = 2$. The maximum scalar variance is given by $\widetilde{c''^2}_{\max} = \widetilde{c}(1 - \widetilde{c})^1$. Inserting the formulation for the heat release rate given by Schmid into the ratio in Eq. (4.10), the scaling function becomes [53, 112]

$$C_s = \frac{\alpha}{C_D} \left[\frac{\frac{s_1}{\sqrt{\frac{2}{3}k}} + (1 + Da^{-2})^{-0.25}}{\frac{s_1}{\sqrt{\frac{2}{3}k}} + 1} \right]^2. \quad (4.11)$$

The scaling function accounts for the effects of finite rate chemistry on the spectrum of the heat release rate fluctuations. At low Damköhler numbers (homogeneous reactor limit), the function provides the correct asymptotic behavior, by scaling the spectral amplitude to zero. In this regime, no fluctuations of the rate of heat release exist [53]. As such, the amplitude scaling function is an important

¹This relation holds for variables defined in the interval between 0 and 1, if only the maximum and minimum variable values occur [86].

part of the model making it essentially independent of the combustion model that is used in the initial CFD simulation and the range of Damköhler numbers found in the input data.

4.2.2 Wave-Number Frequency Transformation

The model spectrum derived in Eq. (4.7) is formulated in wave-number space. In Eq. (3.25), the Lagrangian correlation spectrum $\chi_{qq}(f)$ is needed to compute the spectrum of the radiated acoustic power. Tennekes & Lumley [134] propose a mapping function between the Eulerian wave-number spectrum and the Lagrangian frequency spectrum based on the argument that both spectra should include equal spectral energy. By projecting the similarity between the frequency spectra of kinetic energy and reaction progress into wave-number space, the mapping can be used universally to transform between spectra of any quantity. Within the inertial convective subrange, Lagrangian frequency and Eulerian wave-number spectra scale as

$$\chi_q(\omega) = \alpha^{3/2} \varepsilon \kappa^{-2/3} \quad (4.12)$$

and

$$E_q(\kappa) = \alpha \varepsilon^{2/3} \kappa^{-5/3}, \quad (4.13)$$

with the modeling constant of $\alpha = 1.5$. By assuming equal energy content in the corresponding Lagrangian and Eulerian spectra, a transfer function between both spectral ranges can be derived. Performing the integration [143],

$$\int_{\kappa_1}^{\kappa_2} E_q(\kappa) d\kappa = \int_{\omega_1}^{\omega_2} \chi_q(\omega) d\omega \quad (4.14)$$

after inserting Eq. (4.12) and Eq. (4.13), a relation between the Lagrangian angular frequency and the Eulerian wave-number is obtained:

$$\kappa(f) = \left(\frac{2}{3}\right)^{3/2} \frac{\omega^{3/2}}{\alpha^{3/4} \varepsilon^{1/2}}. \quad (4.15)$$

Here, $\omega = 2\pi f$ and the turbulent dissipation rate is given by

$$\varepsilon = \frac{l_t^2}{\tau_c^3}. \quad (4.16)$$

In the model for the heat release rate fluctuation spectrum, the characteristic time scale is modeled as the passing time of the large eddies through the turbulent flame brush, i.e.

$$\tau_c = c_\tau \cdot \frac{\delta_t}{s_t}, \quad (4.17)$$

with the constant of proportionality $c_\tau \approx 0.5$ [52]. The turbulent flame brush thickness δ_t and the turbulent burning velocity s_t are calculated from the relations given by Schmid [111, 112].

The angular frequency spectrum is connected to the frequency spectrum by a constant factor of² 2π , so that the full transformation between Eulerian wave-number spectrum and Lagrangian frequency spectrum is

$$\chi_q(f) = \frac{\kappa(f)}{\pi f} E_q(\kappa(f)). \quad (4.18)$$

4.2.3 Relation Between Lagrangian Frequency and Correlation Spectrum

The correlation spectrum $\chi_{qq}(f)$ which is needed in Eq. (3.25) is defined as the product of $\chi_q(f)$ with its complex conjugate [114, 146]

$$\chi_{qq}(f) = \chi_q(f) \cdot \chi_q^*(f) = \chi_q(f)^2 = \left[\frac{\kappa(f)}{\pi f} \right]^2 \cdot [E_q \kappa(f)]^2, \quad (4.19)$$

where * denotes the complex conjugate.

4.2.4 Cutoff Length Scale

In the premixed combustion noise model, the cutoff-length-scale $\eta_{c/2}$ is an effective Corrsin scale [143] that accounts for the smoothing of scalar fluctuations on the fine scales by the chemical reaction which is responsible for the spectral cutoff. The effective cutoff length is given by the maximum of

$$\eta_{c/2} = \max(c_g l_g, l_c), \quad l_g = \frac{s_1^3}{\varepsilon}, \quad l_c = \frac{a^3}{\varepsilon}^{1/4}, \quad (4.20)$$

² After the substitution of $\omega = 2\pi f$ in Eq. (4.14) the integration variables are related through $d\omega = 2\pi df$.

with the constant $c_g = 3.0$, as determined experimentally [143, 150].

4.2.5 Statistical Volume of Coherent Heat Release

The coherence volume introduced in Eq. (3.22) is modeled by setting an appropriate coherence length scale l_{coh} for the statistical size of the coherent volumes [13, 56, 128]. The effect of the model coherence volume is twofold: Physically, sources located a considerable distance apart from each other emit sound at a random phase difference, which can cause destructive interaction and reduce the overall signal amplitude of the emitted noise. Additionally, the efficiency of sound radiation from a spherical source is closely related to its size.

The overall efficiency of noise radiation by the entity of all sources within the flame volume is accounted for by the size of the virtual statistical coherence volume V_{coh} . This concept is illustrated in Fig. 4.1. The theoretical maximum of the

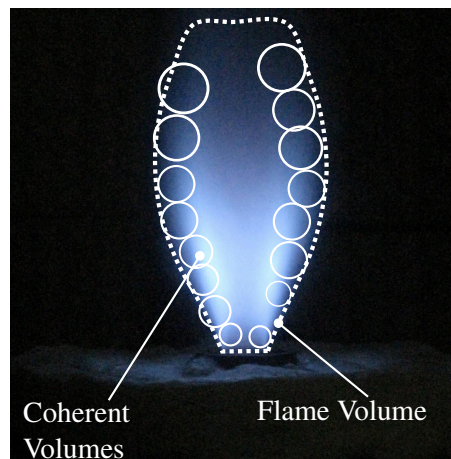


Figure 4.1: Paradigmatic concept of coherent noise sources in a turbulent flame. The spatial coherence of the fluctuating heat release rate is accounted for by statistical coherence volumes, inside which the heat release rate is assumed to be completely coherent.

radiation efficiency is reached, if the ratio between coherence volume and flame volume reaches unity, i.e. sound radiation within the flame volume is entirely coherent. The coherence of the individual sources influences the total transfor-

mation efficiency between thermal and acoustic energy in the flame. Wäsle [143] defines the coherence efficiency as

$$\eta_{\text{coh}} = \frac{V_{\text{coh}}}{V_{\text{flame}}} \quad (4.21)$$

and the turbulent flame thickness as length scale characterizing the coherence of the fluctuating heat release rate ($l_q = \delta_t$). Volume integration of the coherence function Eq. (3.21) yields the statistical coherence volume [146]

$$V_{\text{coh}} = 8 \cdot l_q^3 = 8 \cdot \delta_t^3, \quad (4.22)$$

The turbulent flame thickness δ_t is defined by Schmid [111]

$$\delta_t = \delta_l + (1 + \text{Da}_t)^{1/4} l_t, \quad (4.23)$$

with the laminar flame thickness $\delta_l = a/s_1$. For large turbulent Damköhler numbers (fast chemistry), the turbulent flame thickness approaches l_t , as $\delta_l \ll l_t$, which illustrates the influence of turbulence on the phase and size distribution of the individual sources and, thus, on the efficiency of conversion between thermal and acoustic energy in the flame.

4.2.6 Acoustic Power Spectrum of the Premixed Flame

With the free field solution of the inhomogeneous wave-equation discussed in Sec. 3.1, the model spectrum and frequency wave-number mapping, the model spectrum of the far-field acoustic power is

$$P_{\text{aco}}(f) = \frac{\pi(\gamma-1)^2}{\rho_{\infty}c_{\infty}^5} \int_{V_{\text{flame}}} [f \cdot \chi_q(f)]^2 \cdot V_{\text{coh}} dV_{\text{flame}}, \quad (4.24)$$

which can be evaluated from local mean field variables of a numerical CFD RANS simulation. Volume integration over the total flame volume gives the acoustic power spectrum emitted by the flame.

4.3 Non-Premixed Turbulent Flames

Although originally developed for premixed flames, the spectral model for combustion noise developed by Hirsch et al. [53] is independent of flame type in its coupling between the spectra of the fluctuating heat release rate and reaction progress variance (Eq. (4.1)) [146].

For the extension of the model towards non-premixed flames, the following modifications are introduced:

- Reformulation of the length-scale governing the local coherence of heat release fluctuations. For premixed flames, the turbulent flame thickness is governing the local coherence volume of noise radiation. The corresponding length scale in non-premixed flames is the thickness of the mixing zone. The spherical shape of the volumes is retained.
- Modification of the frequency-wave number transformation function to account for the sensitivity of non-premixed flames to turbulence.
- Formulation of a generalized amplitude scaling function that is able to account for regions of low Damköhler numbers independent of the individual flame type. The generalized scaling function is based on the combustion model developed by Philipp [100], which uses a joint probability density function approach of mixture fraction and reaction progress to calculate mean reaction rates for premixed and non-premixed flames.

4.3.1 Coherence Volume

In turbulent non-premixed flames, the integral length scale l_t is of the order of magnitude of the thickness of the mixing zone between fuel and oxidizer. The thickness of the mixing zone, l_z , can be estimated from the mean mixture fraction gradient [101]

$$l_t \approx l_z \approx \frac{1}{|\nabla \bar{z}|}. \quad (4.25)$$

Similar to the turbulent flame thickness δ_t in the premixed case, l_z accounts for the influence of both, chemistry and turbulence on the spatial distribution of scalar fluctuations of the rate of heat release. Following the reasoning of Wäsle, l_z is used in the non-premixed model to represent the characteristic length scale of heat release. The coherence volume then becomes

$$V_{\text{coh}} = \frac{8}{|\nabla \bar{z}|^3} \approx 8 \cdot l_t^3, \quad (4.26)$$

in the non-premixed model. This formulation resembles the close connection between the spatial distribution of the mixture fraction, that is dictated by the turbulent velocity field and that of the heat release rate.

4.3.2 Wave-Number Frequency Transformation

Turbulent non-premixed flames in the fast chemistry regime can be treated as thin surface concentrated at or close to the surface of stoichiometric mixture fraction [149]. This surface is wrinkled by vortices of different sizes which are convected past the flame. Turbulent transport merges the reactants, while molecular diffusion performs mixing on the fine scales. Turbulent transport is the dominating mechanism governing the chemical reaction. Consequently, the non-premixed flame is influenced largely by the turbulent motion [101].

Hirsch et al. [52] adapt the relation given by Tennekes and Lumley to obtain a transformation function between Eulerian wave-number and Lagrangian frequency (Sec. 4.3.2). In their model formulation for premixed flames, the chemical time scale is used in Eq. (4.17) to express the turbulent dissipation rate. To account for the greater influence of the turbulent motion on the non-premixed flame, the initial formulation for the dissipation rate by Tennekes and Lumley is retained in the non-premixed model, resulting in the following mapping function between Eulerian wave-number and Lagrangian frequency

$$\kappa(f) = \left(\frac{2}{3}\right)^{3/2} \frac{\omega^{3/2}}{\alpha^{3/4} \epsilon^{1/2}}, \quad (4.27)$$

where ε is given by

$$\varepsilon = \frac{l_t^2}{\tau_t^3} \quad (4.28)$$

and ω denotes the angular frequency

$$\omega = 2\pi f. \quad (4.29)$$

The turbulent time and length scale are linked to the turbulence variables from the CFD solution by

$$l_t = c_1 \cdot \frac{k^{\frac{3}{2}}}{\varepsilon} \approx c_1 \cdot \frac{1}{|\nabla \bar{z}|}, \quad \tau_t = c_\tau \cdot \frac{k}{\varepsilon}, \quad (4.30)$$

using a similar approach to that of Mühlbauer et al. [89]. Both constants of proportionality are of order one, but need to be defined in the modeling process, as the combustion noise model reacts sensitively to slight changes in the input fields of the turbulence variables. These variables, along with the computed rate of heat release are highly dependent on the combination of the selected turbulence and combustion model. In the scope of this thesis, a set of constants is derived, that matches the combination of the k - ε -model in combination with the eddy dissipation combustion model for non-premixed flames.

4.3.3 Generalized Scaling of the Spectral Amplitude

The basis of the spectral noise model is given by the connection between the scalar variance of the reaction progress and the local rate of heat release. This modeling approach makes the scaling of the spectral amplitude necessary in regions, where the chemistry is substantially influencing the rate of reaction (low Damköhler numbers). In the premixed model, this is realized by the amplitude scaling function C_s , which is formulated based on the Schmid combustion model [111]. Here, the scaling of the spectral amplitude is performed in regions where the scalar variance of the reaction progress departs from its theoretical maximum value (cf. Eq. (4.10)). The theoretical maximum value for the variance of an arbitrary scalar variable ϕ defined between zero and unity can be shown to follow the parabola [86]

$$\phi_{\max}''^2 = \phi(1 - \phi). \quad (4.31)$$

This corresponds to the limit of infinitely fast chemistry, where fresh gases are separated from the burnt gases by a flame sheet of infinitely small thickness and consequently, no intermediate states exist in terms of reaction progress (cf. Fig. 2.6). In this limiting case of maximum scalar variance, the assumption of fast chemistry is fully given, so that no scaling of the spectral amplitude is necessary.

In regions where the chemical timescale approaches the order of magnitude of the mixing time scale, substantial premixing occurs prior to combustion and the reaction progress variance is reduced by effects of finite rate chemistry [52]. These regions are still contributing to the overall heat release, but the amplitude of the spectral fluctuations is reduced, which is consistent with Eq. (3.7).

Consequently, regions of low Damköhler number contribute less to the overall spectral amplitudes. This limiting case can be identified in a generalized formulation, if the true value of the local reaction progress variance is calculated from a generalized set of variables. The theoretical basis for the generalized scaling function is taken from Eq. (4.10):

$$C_s = \frac{\alpha}{C_D} \frac{\widetilde{c''^2}(\text{Da})}{\widetilde{c''^2}(\text{Da} \rightarrow \infty)} = \frac{\alpha}{C_D} \frac{\widetilde{c''^2}}{\widetilde{c}(1 - \widetilde{c})}. \quad (4.32)$$

Beyond the constants, Eq. (4.32) includes the values of reaction progress mean and variance. The mean reaction progress can be calculated directly by considering the dimensionless temperature ϑ and assuming adiabatic conditions [72, 98, 100]:

$$\widetilde{c} = \widetilde{\vartheta} = \frac{\widetilde{T} - T_u}{T_{\text{ad}} - T_u}. \quad (4.33)$$

Here the subscript T_u refers to the unburnt gas temperature while T_{ad} denotes the adiabatic flame temperature. The reaction progress variance is a parameter, which is influenced by both, chemical reaction and turbulent motion and is commonly not directly available in a reactive RANS simulation model. The solution of a transport equation for the variance of reaction progress is troublesome as it involves multiple additional modeling assumptions for correlations with turbulent fluctuating velocity and the influence of the chemical reaction on production or dissipation of scalar variance.

An alternative access to the scalar variance of reaction progress is the evaluation of moments of the joint-PDF (JPDF) of temperature and mixture fraction as used by Philipp [100] to calculate the mean reaction rate of a one-step kinetic reaction for methane combustion. The time averaged source term in the scalar transport equation of fuel (CH_4) is calculated from³

$$\bar{\dot{\omega}}_{\text{CH}_4} = \int_0^1 \int A \cdot X_{\text{CH}_4}^{\nu_{\text{CH}_4}} \cdot X_{\text{O}_2}^{\nu_{\text{O}_2}} \cdot \rho^{\nu} \exp\left(\frac{-T_{\text{init}}}{T}\right) \cdot P(z, T) \, dz dT, \quad (4.34)$$

where X_{CH_4} , X_{O_2} are the concentrations of fuel and oxidizer, z denotes the mixture fraction and $P(z, T)$ is the joint probability density function of mixture fraction and temperature. If the temperature is included into the model in its non-dimensional form ϑ (cf. Eq. (4.33)) it represents the reaction progress if adiabatic conditions are assumed. According to this variables definition between zero and unity, a Gaussian shape of its PDF can be assumed as well. In the following, the scalar variance of the reaction progress is retrieved from the variances of mixture fraction and temperature by rearranging the basic equations of the joint-PDF combustion model described by Philipp [100].

In adiabatic conditions, ϑ , as defined in Eq. (4.33) represents the reaction progress [98, 143]. By presuming mixture fraction and reaction progress to behave statistically independent from each other, the JPDF can be assembled from two single-variable clipped Gaussian distribution functions (cf. Eq. (2.69)):

$$P(z, \vartheta) = P_z(z) \cdot P_{\vartheta}(\vartheta). \quad (4.35)$$

The connection between mean and variance of the reaction progress and known values of mean and variance of mixture fraction and temperature can now be established by calculating the first and second moment of the JPDF. From the definition of ϑ Eq. (4.33) we write

$$T - T_u = \vartheta \cdot (T_{\text{ad}} - T_u). \quad (4.36)$$

Averaging gives the relation between the JPDF of z and ϑ and the local temperature:

$$\bar{T} - T_u = \iint_{\vartheta z} \vartheta \cdot [T_{\text{ad}}(z) - T_u] \cdot P(z) \cdot P(\vartheta) \, dz d\vartheta \quad (4.37)$$

³The original model by Philipp includes a further term to model the formation of CO.

With T_{ad} being a function of the mixture fraction only, the double integral can be split so that

$$\bar{T} - T_u = \underbrace{\int_{\vartheta} \vartheta P(\vartheta) d\vartheta}_{=\bar{\vartheta}} \underbrace{\int_z [T_{\text{ad}}(z) - T_u] P(z) dz}_{=T_{\text{ad}} - \bar{T}_u}. \quad (4.38)$$

Equation (4.38) can be rearranged to obtain an equation for the PDF averaged dimensionless temperature $\bar{\vartheta}$:

$$\bar{\vartheta} = \frac{\bar{T} - T_u}{T_{\text{ad}} - \bar{T}_u} = \frac{\bar{T} - T_u}{\int_z [T_{\text{ad}}(z) - T_u] P(z) dz}. \quad (4.39)$$

This is a function of known quantities only and can be directly calculated from the assumed PDF of the mixture fraction. The variance is obtained from the second moment by following a similar approach:

$$\overline{T'^2} = \iint_{\vartheta z} [T - \bar{T}]^2 P(z) P(\vartheta) dz d\vartheta. \quad (4.40)$$

Making use of equation (4.39) $\overline{T'^2}$ can be expressed as:

$$\overline{T'^2} = \iint_{\vartheta z} [T_{\text{ad}}(z) - T_u]^2 (\vartheta - \bar{\vartheta})^2 P(z) P(\vartheta) dz d\vartheta. \quad (4.41)$$

As $[T_{\text{ad}}(z) - T_u]^2$ solely depends on $P(z)$ and $(\vartheta - \bar{\vartheta})^2$ solely depends on $P(\vartheta)$, the double integral can be separated to give

$$\overline{T'^2} = \underbrace{\int_{\vartheta} (\vartheta - \bar{\vartheta})^2 P(\vartheta) d\vartheta}_{=\overline{\vartheta'^2}} \cdot \int_z [T_{\text{ad}}(z) - T_u]^2 P(z) dz. \quad (4.42)$$

The first integral is the variance $\overline{\vartheta'^2}$, which gives the dependency between $\overline{T'^2}$ and $\overline{\vartheta'^2}$:

$$\overline{\vartheta'^2} = \frac{\overline{T'^2}}{\int_z [T_{\text{ad}}(z) - T_u]^2 P(z) dz}. \quad (4.43)$$

Using the derived expressions for the reaction progress and its variance, the generalized amplitude scaling function C_S can be formulated analogous to the reasoning of the premixed model (cf. Eq. (4.10)):

$$C_s = \frac{\alpha}{C_D} \cdot \frac{\overline{\vartheta'^2}}{\overline{\vartheta}(1 - \overline{\vartheta})}. \quad (4.44)$$

The generalized amplitude scaling function is based solely on the PDF of the mixture fraction and the averaged values of temperature and temperature variance. Temperature variance can be obtained by solving a transport equation or by using a simple algebraic expression based on the assumption of balance between production and dissipation of scalar variance and the absence of convective effects [45, 157]. In the simulations performed in the scope of this thesis, scalar transport equations for the temperature variance and the mixture fraction variance are solved in parallel to the flow and combustion simulation.

4.4 Analysis of Model Characteristics

A comprehensive understanding of the computational model behavior for non-premixed flames including the generalized amplitude scaling function can be obtained by analyzing model predictions for prescribed parameter values for a range of frequencies and turbulent time scales. The remaining input parameters are taken to be constant and are extracted from a single finite volume within the reaction zone of a CFD RANS simulation of a turbulent non-premixed swirl flame to ensure the selection of realistic relations between the individual parameters. If the model equations are evaluated on one single volume only, the volume integration in Eq. (3.17) simplifies to a multiplication with the cell volume V_{fv} , i.e.

$$P_{aco}(f) = \frac{\pi(\gamma - 1)^2}{\rho_\infty c_\infty^5} [f \cdot \chi_q(f)]^2 \cdot V_{coh} \cdot V_{fv}, \quad (4.45)$$

where the frequency spectrum of heat release rate $\chi_q(f)$ is given by Eq. (4.18). Additionally, it is assumed that the model heat release is taking place at non-premixed conditions so that the heat release can be described analytically by the eddy dissipation model (cf. Eq. (2.74)).

In this simplified set up, the model response to an alternation of the turbulent time scale can be investigated along a range of frequencies including the effect of the turbulent time scale on the mean reaction rate. For this purpose, the model equation of the non-premixed combustion model is coupled with the eddy dissipation model for the mean rate of heat release. The constant parameters needed for the evaluation of the model equations are listed in Tab. 4.1. From the pre-

Table 4.1: Constant parameter values used in the analysis of the simplified non-premixed combustion noise model.

z	$z'^{1/2}$	T_u	k	V_{fv}	c_∞	ρ_∞
0.0549602	0.0002596979	393 K	$9.6 \text{ m}^2/\text{s}^2$	$3.35 \cdot 10^{-8} \text{ m}^3$	343 m/s	$1.21 \text{ kg}/\text{m}^3$

scribed turbulent time scale, the dissipation rate is calculated using Eq. (4.30) as

$$\varepsilon = c_\tau \cdot \frac{k}{\tau_t}. \quad (4.46)$$

The predicted radiation of sound power is evaluated for turbulent time scales of $\tau_t = 0.1 \text{ ms} \dots 2 \text{ ms}$ and frequencies of $f = 10 \text{ Hz} \dots 1500 \text{ Hz}$. A contour plot of the calculated results is shown in Fig. 4.2. The radiation of sound power is predicted to be most effective in the low frequency range at longer turbulent time scales for the given parameters. This correctly captures the trend which is visible in the majority of experiments with turbulent hydrocarbon flames, that the peak output is located in the low frequency range. An analysis of parameters influencing the predicted peak frequency can be performed by considering the maximum of the predicted sound power amplitude, which is given by the first derivative of Eq. (4.45) with respect to frequency:

$$\frac{dP_{\text{aco}}(f)}{df} = 0. \quad (4.47)$$

In order to evaluate Eq. (4.47) combined with the eddy dissipation model for the mean rate of heat release analytically, the exponential term governing spectral cutoff as well as the amplitude scaling function have been removed as they do not influence the location of the peak amplitude. Here, the eddy dissipation model has been simplified such that the limiting species is the oxidizer (lean or

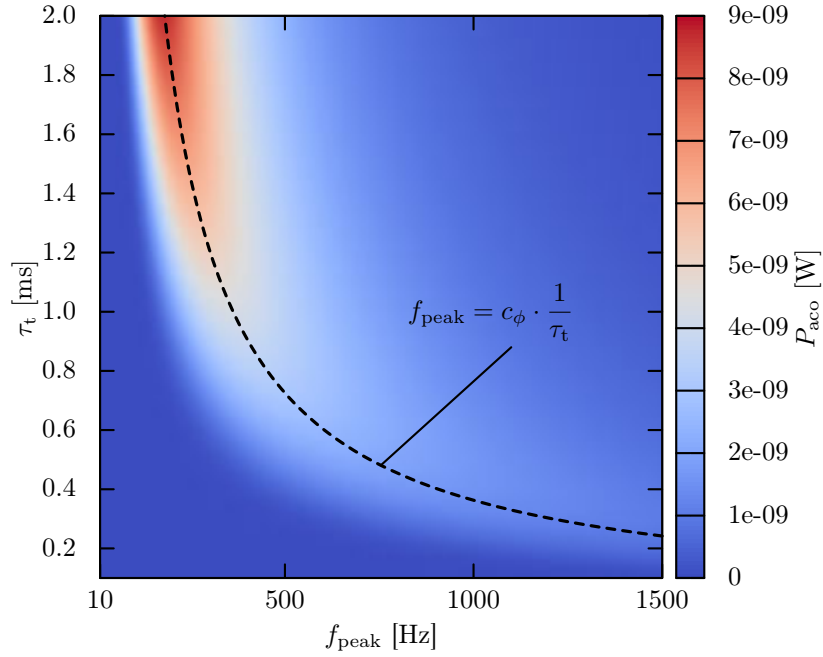


Figure 4.2: Contour plot of radiated acoustic power for different turbulent time scales over peak frequency as predicted by the simplified noise model analysis. The evaluation of the expression for the peak frequency (Eq. (4.49)) is shown by the dashed line.

stoichiometric combustion). The resulting equation for the computation of the local peak frequency is obtained as

$$P_{\text{aco}}(f) = \frac{H_u^2 A^2 \sqrt{k} V_{\text{fv}} Y_{\text{O}}^2 \alpha^{7/2} (\gamma - 1)^2 \left(\frac{1}{\alpha^{3/4} \sqrt{\varepsilon}} \right)^{2/3} \varepsilon^{4/3} \rho}{c_\infty^5 \pi^2 f^2 v_{\text{st}}^2} \cdot \exp \left[-\frac{3\sqrt{\alpha}\beta}{4\pi} \cdot \left(\frac{k^{3/2} f^{3/2}}{\alpha^{3/4} \varepsilon^{3/2}} \right)^{-4/3} \right], \quad (4.48)$$

where H_u denotes the lower heating value of the fuel, which is set to the value of methane. The derivative Eq. (4.47) is zero at the peak location, i.e. from Eq. (4.48) the location of the peak frequency can be calculated through

$$f_{\text{peak}} = \frac{\sqrt{\frac{3}{\pi}} \alpha^{3/4} \sqrt{\beta} \varepsilon}{2k}, \quad (4.49)$$

with physical dimension of a frequency 1/s. The peak frequency depends linearly on the mixing rate, outlining the dominating role of integral turbulence quantities

in the generation of combustion noise in flames of high Damköhler number. If the constants in Eq. (4.49) are cast into a single constant c_ϕ , the local frequency of peak acoustic emission is related to the local quantities of turbulence by

$$f_{\text{peak}} = c_\phi \cdot \frac{\varepsilon}{k} = c_\phi \cdot \frac{1}{\tau_t}, \quad (4.50)$$

with the constant $c_\phi = 0.363$. This is in agreement with the findings of Strahle [130] and in close agreement to the constant of proportionality given by Wäsle of $c_\phi \approx 0.4$ [143]. In the fast chemistry limit, f_{peak} is determined solely by the ratio of turbulence kinetic energy and dissipation rate, or turbulent macroscopic time scale. The trace of peak frequencies calculated from Eq. (4.49) is plotted in Fig. 4.2, showing that the simplified calculation of the peak frequency matches the amplitude data computed numerically using the non-simplified model. Equation (4.50) can thus be used to quickly analyze field data obtained from a reactive RANS simulation regarding the main frequency contribution of different flame regions to the overall acoustic emissions.

Influence of RANS Input Data on the Noise Prediction

The validation of the premixed combustion noise model was performed by Winkler [150]. The predictive capabilities are demonstrated by Wäsle [143] using experimentally determined field data. The greatest concern, as pointed out by Winkler, is the need of spatially resolved data for the time averaged rate of heat release, which can not be easily obtained by experiment. If numerical data is used, similar problems exist. Chemical reaction in turbulent flames is a fine scale process involving a large number of reactions and influenced by all scales of turbulent motion. In CFD, extensive modeling and simplification is often performed in the numerical solution process, ranging from spacial discretization and turbulence modeling to the modeling of the combustion reaction. The ongoing development in combustion modeling together with some unsolved problems is for example outlined by Bilger et al. [8].

Beyond the need to model the combustion process, turbulent quantities are fully modeled in RANS by turbulence models. In the spectral noise model, prediction of the peak frequency scales linearly with the local ratio of turbulence kinetic

energy and dissipation rate (Eq. (4.49)). Most combustion models rely on turbulent properties as they model the mean reaction rate using a turbulent time scale, which is determined from the parameter values of turbulence kinetic energy and dissipation rate. The predicted model amplitude is proportional to $k^{7/2}\epsilon^{-5/3}$. This shows the strong dependency of the noise prediction on the calculated turbulence quantities in the simulation of the input variable fields for the combustion noise model.

As well, the derivation of the semi-analytic spectral model for turbulent combustion noise based on time-averaged RANS data involves assumptions concerning the general spectral shape and the behavior of the reaction progress variance as an active scalar variable [67, 88]. In deriving the spectral model for turbulent combustion noise, the following assumptions were introduced:

- Compactness: the flame is acoustically compact with respect to the wavelength, and no reflection or refraction effects occur within the flame.
- Convective effects on sound radiation are not considered, the sound radiation follows an exact monopole radiation characteristic (unidirectional).
- The underlying turbulence is homogeneous and isotropic.
- The Lagrangian frequency spectrum is a simple rearrangement of the Eulerian wave-number spectrum.
- The fluctuation spectrum of the progress variable is closely related to the spectrum of turbulence kinetic energy.

Some parameters involved in the modeling can not be directly accessed by experiment, rendering the validation of model assumptions difficult in some cases. However, if integral characteristics of the studied flow problem are reproduced successfully, qualitative predictions regarding the effect of modifications in geometry or operating conditions can be made, and the spectral content and amplitude level of the radiated noise can be predicted with good agreement to experimental data.

5 Experimental Setup and Measurement Equipment

The development of the extended spectral model for combustion noise from non-premixed flames is accompanied by measurements of combustion noise spectra from a turbulent natural gas swirl flame enclosed in a low-reflective measuring chamber. The measured spectra are used to validate the model extension. A recent study by Singh et al. [119] investigates combustion noise from a turbulent non-premixed swirl flame in a double swirler configuration. The results indicate that non-premixed swirl flames possess similar universal spectral characteristics as observed with premixed flames. Therefore, a variable swirl burner of movable-block type [50, 76] available at the institute, is operated in non-premixed and premixed flame configuration to allow a comparison between flame types at similar operating conditions. The acoustic optimization of the laboratory was performed employing the methods described by Wäsle [143].

5.1 Open Turbulent Flame Test Rig

The test-rig layout is shown schematically in Fig. 5.1. Inside the laboratory room of $L = 9.5$ m, $W = 5.5$ m and $H = 7.2$ m the burner is placed centered underneath the exhaust hood in a vertical distance of 1.10 m above the ground. The burner is surrounded by a semi-anechoic chamber of sound absorbing foam panels. The chamber forms a cubic enclosure with an edge length of 2.4 m with the burner nozzle located at the geometric center of the chamber. Air and natural gas are taken directly from the lab gas and air supply lines. Natural gas in Munich possesses a methane mole fraction of 96.18%¹. Combustion air is supplied to the burner through a Bronkhorst F-206AI-AGD-66-V (3.5 – 175 m³/h) digital mass

¹ Number extracted from the monthly report on city gas quality of Stadtwerke München, 01/2013

flow controller with an inline acoustic silencer, to attenuate any flow noise from the mass flow control valve. Natural gas fuel is supplied through a Bronkhorst F-203AC-FA-44V mass flow controller (max. 300L/min). The fuel supply line can be connected to either the static mixer or the central body, allowing simple interchange between operation modes. A static mixer [110] is mounted directly in line with the standard air supply, feeding perfect fuel-air mixture or combustion air directly into the swirl generator casing, depending on the operating configuration. In non-premixed configuration, natural gas fuel is directly supplied into the combustion zone through the central body. The burner with its movable block type swirl generator is designed for a nominal thermal power of 50kW at an air excess ratio of $\lambda = 1.1$. Within the measuring chamber, the sound intensity radiated by the flame is recorded using a two microphone (p-p) intensity probe² with a 25 mm spacer. To avoid perturbation from the exhaust vent, the chimney suction blower is switched off during acoustic measurements. Accumulation of

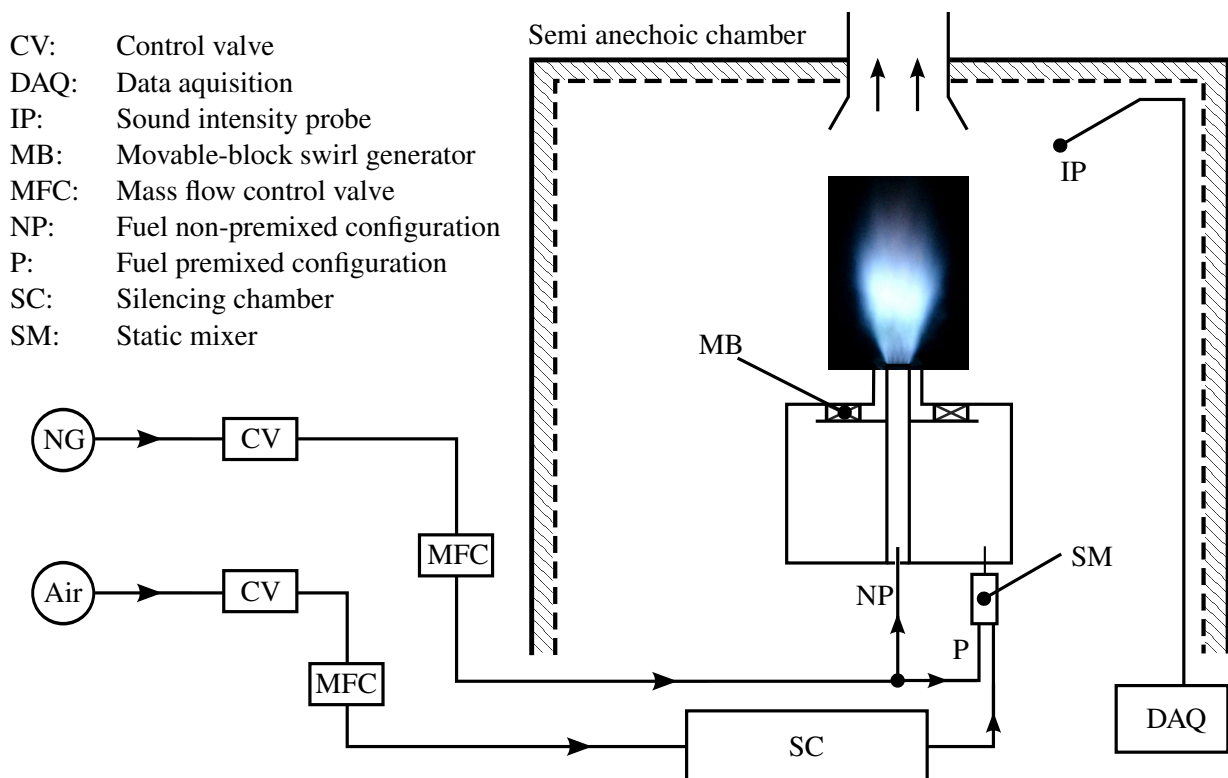


Figure 5.1: Schematic of the open turbulent flame test rig. The flame can be operated in premixed or non-premixed configuration.

² G.R.A.S. 40AK 1/2".

combustion products due to insufficient natural draft is avoided by switching on the blower in between individual measurements.

5.2 Movable Block Swirl Burner

Swirling flow is generated by a tangential swirler, which is adjustable in the output swirl number by altering the ratio of radial and tangential mass flow rates of the fresh gas. The swirler principle allows the calculation of the swirl number S from the geometric parameters of the combination of fixed and movable blocks [6, 76]. A cross sectional schematic diagram of the geometric quantities determining the swirl number of this device is shown in Fig. 5.2. The parameter values of the swirl generator operated in the scope of the experiments are listed in Tab. 5.1. The movable blocks can be rotated around the burner axis between

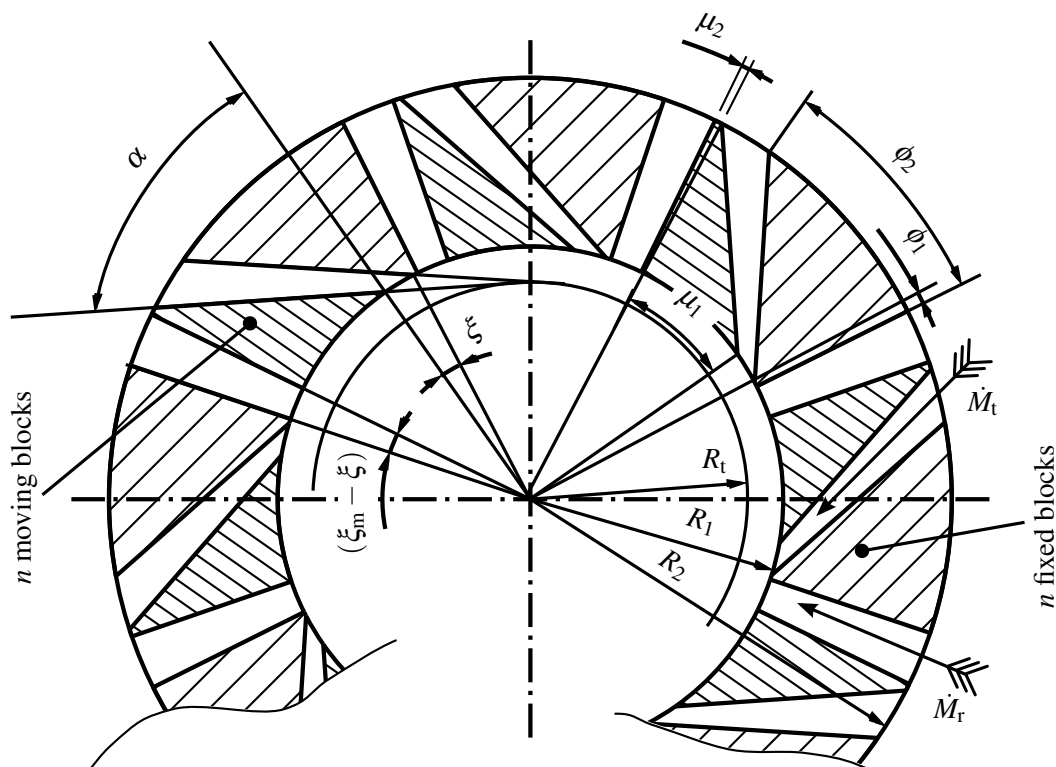


Figure 5.2: Cross sectional view of the geometric quantities of the movable-block swirler unit determining the swirl number (adapted from [76]). The swirl number can be adjusted continuously by altering the ratio between radial and tangential momentum of the flow.

Table 5.1: Dimensions of the movable-block swirl generator.

n	R_1	R_2	R_t	α	ϕ_1	ϕ_2	μ_1	μ_2	ξ_m
8	48 mm	80 mm	41 mm	58.9°	1.0°	29.0°	29.0°	1.0°	15.0°

$\xi = 0^\circ$ and $\xi_m = 15^\circ$. From the main geometric parameters, the swirl number can be calculated from [6, 50]

$$S = \frac{2\pi}{n\xi_m} \cdot \frac{\sin(\alpha) \cos(\alpha) \left[1 + \tan(\alpha) \tan\left(\frac{\xi}{2}\right) \right] \frac{\xi}{\xi_m}}{\left\{ 1 - \left[1 - \cos(\alpha) \left(1 + \tan(\alpha) \cdot \tan\left(\frac{\xi}{2}\right) \right) \right] \frac{\xi}{\xi_m} \right\}^2} \cdot \frac{R_0}{2B} \left(1 - \frac{r_0^2}{R_0^2} \right), \quad (5.1)$$

where B denotes the axial height of the radial and tangential flow channels and r_0, R_0 denote the inner and outer radius of the annular duct connecting the swirler with the nozzle. The theoretical dependency of S on the block angle ξ , resulting from Eq. (5.1) is shown for the swirl generator with the dimensions as given in Tab. 5.1 in Fig. 5.3. It should be noted that the original form of Eq. (5.1) as given in [6] has been corrected later by squaring the denominator [43, 50], and is given here in its corrected form. The variable swirl allows the experimental investigation of a large variety of different operating points and the choice of

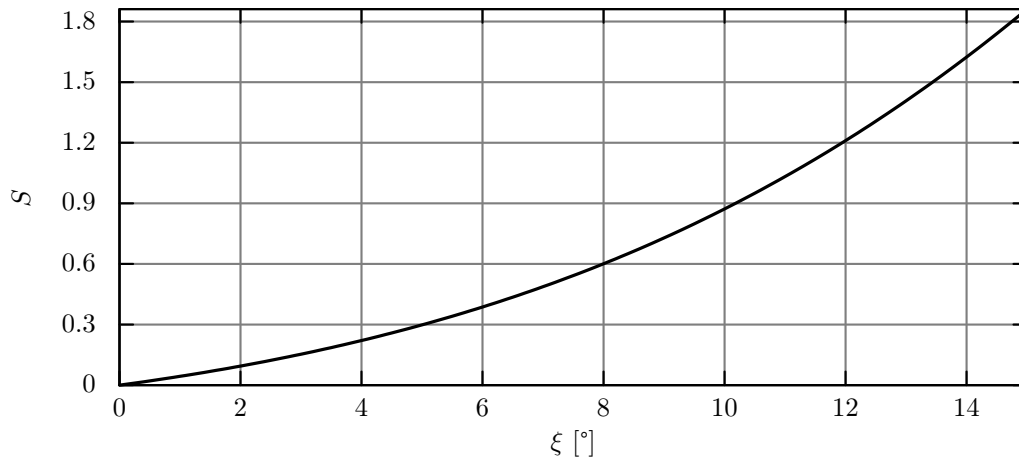


Figure 5.3: Swirl number of the movable-block swirl generator depending on the adjustable block angle ξ . The maximum block angle of $\xi_m = 15^\circ$ leads to a maximum swirl number of $S = 1.86$.

stable operating ranges of both, open non-premixed and premixed flames at similar power and mixture settings.

The general flow properties of the test rig burner are shown in Fig. 5.4 in the configuration for non-premixed operation. Coming from the swirler, the com-

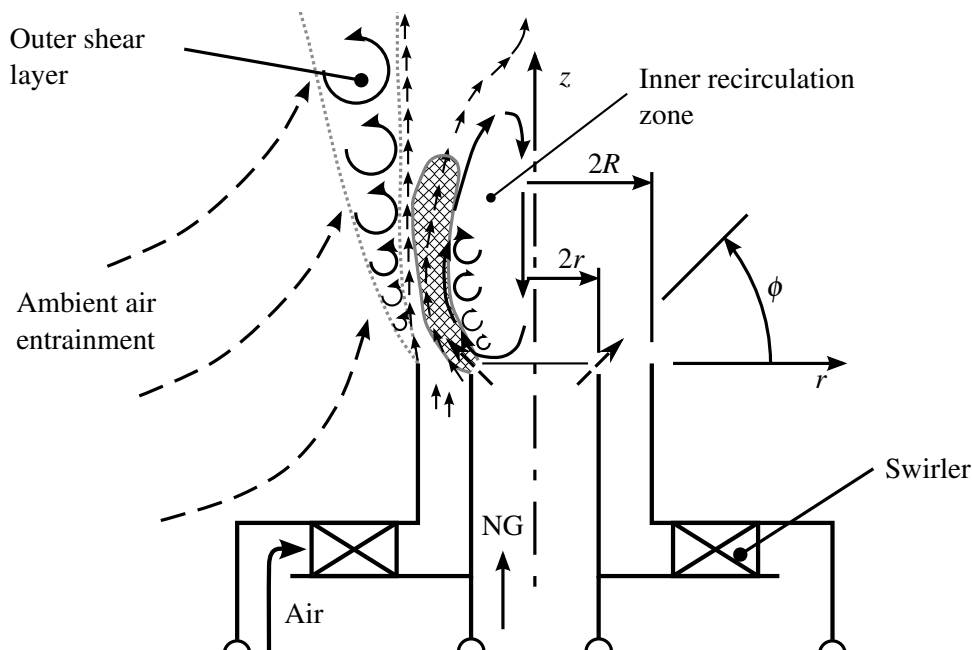


Figure 5.4: Schematic of the basic nozzle dimensions and general properties of the flow field of the flame produced by the movable-block burner in non-premixed configuration. Natural gas fuel enters the inner shear layer through narrowly spaced injection holes in the center body. Combustion products are recirculated along the burner axis downstream of the center body.

bustion air enters an annular gap around the center body. The natural gas fuel is transported inside the center body. At the burner exit plane, the natural gas stream exits the center body through a total of 16 narrowly spaced fuel injection holes at an angle of $\phi = 45^\circ$ with respect to the burner exit plane. As shown in Fig. 5.4, the fuel is directly injected into the inner shear layer that separates the recirculated combustion products from the annular flow, thereby enhancing the mixing process and forming a blue flame. This type of flame is frequently referred to as type-II non-premixed or diffusion flame in literature [50, 55, 100]. The corresponding term of a type-I non-premixed flame refers to a luminous yellow flame which results from injecting the fuel through a single coaxial hole in the center body. Inner and outer diameter of the annular duct are $r_0 = 26$ mm and $R_0 = 50$ mm. The Reynolds number of the nozzle flow is calculated with refer-

ence to the outer diameter of the annulus [50], using the mean axial velocity \bar{u} within the annular duct:

$$\text{Re} = \frac{\bar{u} \cdot 2R}{\nu}. \quad (5.2)$$

Figure 5.5 shows a direct comparison of the three different flame types investigated in the scope of this study. The images show the same operating point con-



(a) Open type-II non-premixed flame.

(b) Open premixed flame.

(c) Confined premixed flame.

Figure 5.5: Flame types at $P_{\text{th}} = 50\text{kW}$, $\lambda = 1.2$ and $S = 0.6$.

cerning thermal power, mixture composition and swirl number for each flame. The comparison between premixed and non-premixed flame in unconfined operation reveals close similarity of the basic flame geometry. The main reaction zone of the non-premixed flame is located within the inner shear layer in the vicinity of the fuel injection holes and remains attached to the center body rim in stable flame operation. This basic shape is almost identical to the premixed flame shape, where slightly shorter flame lengths are observed. The outer zone of the open burning flame is subjected to the effects of entrainment of ambient air (Sec. 2.1.2). For premixed flames, the dilution of the mixture in the outer flame zone leads to the extinction of the outer shear layer, leaving a part of the fresh gas unburnt. This region of diluted mixture is not present in the non-premixed flame, as fuel is only injected into the inner shear layer. In order to quantify the amount of unburnt fuel in the premixed case, the confined flame as shown in Fig. 5.5 right is considered as reference case.

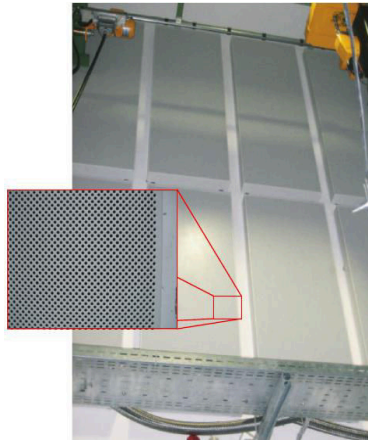
The developed method for the quantification of fuel burnout is described in Sec. 6.2.1. In order to study the effects of entrainment on the fuel burnout and to

be able to compare premixed and non-premixed flame noise, the entrainment of ambient air is obstructed by placing a glass tube of 160 mm in diameter around the flame. Shielding of the flame blocks the dilution of the outer shear layer with ambient air and leads to recirculation of burnt gas along the outer shear layer as well. This leads to complete burnout of the supplied fresh gas mixture within the confinement tube.

5.3 Improvement of Laboratory Acoustics

The experimental acquisition of acoustic quantities in a reflective environment is connected to several concerns. Quantities like sound pressure and intensity from a specific source are commonly recorded in specially designed semi-anechoic or anechoic chambers. Walls, ceiling and often also the floor of these chambers are tiled with specially designed absorptive elements of pyramid or wedge-like shape [30, 139]. The design of the chamber walls aims at minimizing the reflection of acoustic pressure waves, i.e. at absorbing a large fraction of the incident acoustic energy. The construction of such an anechoic chamber requires considerable effort as it includes the need to damp broadband acoustic oscillations that include low frequency content corresponding to wave-lengths of the order of meters. Consequently, the wedge structures have to reach a considerable distance into the room, where they meet non-zero sound particle velocity that results in viscous dissipation of sound energy.

The laboratory holding the experimental setup for combustion noise in the course of this study does not offer anechoic-conditions. So partially reverberant sound field conditions have to be accounted for in the measurements. The improvements of the laboratory acoustics closely follow the procedure used by Winkler [150] and Wäsle [143] for their studies of premixed turbulent combustion noise. A major area fraction of the laboratory walls is covered with sound absorbing panels as shown in Fig. 5.6a. The panels consist of a sheet metal frame filled with rock wool and are covered by a perforated metal sheet cover providing dissipative acoustic damping. The measures to account for the partially reflective measurement environment are twofold: First, the measurements are conducted



(a) Sound absorbing panels on the walls of the laboratory (from [143]).



(b) Sound absorbing chamber holding the burner and the probe support frame.

Figure 5.6: Measures to improve the acoustic properties of the laboratory.

using a p-p sound intensity probe, which allows the separation between reverberant and active components of the sound field in the laboratory. Second, the burner is enclosed by a cubic shaped chamber assembled from sound absorbing panels to minimize aliasing effects (Fig. 5.6b).

The cubic shaped enclosure with edge length of $l = 2.4$ m is positioned symmetrically to the center axis of the burner. Sound absorbing foam panels with pyramid shaped surface structure form the walls of the cubic enclosure. The panels³ manufacturer states the sound absorbing capabilities plotted in Fig. 5.7. The energetic absorption coefficient α_n is connected to the magnitude of the reflection coefficient by [49]

$$\alpha_n = 1 - |r_n|. \quad (5.3)$$

The normal incidence pressure reflection coefficient R_n drops below 0.5 above a frequency of 250 Hz. At lower frequencies, the thickness of the panels of $t = 100$ mm is insufficient to effectively dissipate acoustic energy due to low fluctuating velocity. At low frequencies, however, aliasing effects caused by are of minor significance and the effect of the reverberant portion of the sound field can be effectively accounted for by the applied intensity probe.

³ Sahlberg pinta PYRAMIDE No. 5515077

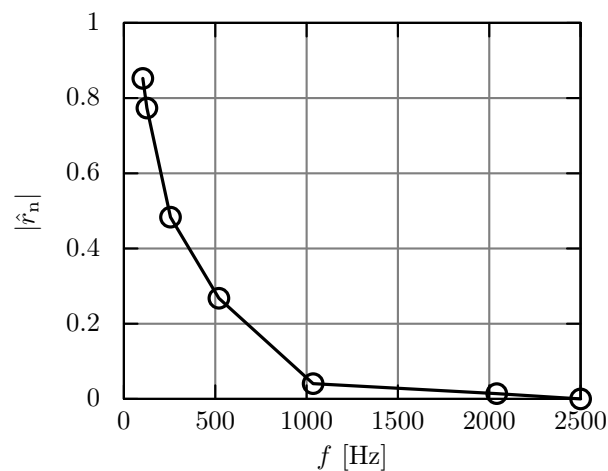


Figure 5.7: Magnitude of the normal incidence reflection coefficient of the sound absorbing panels enclosing the flame [143].

5.4 Measurement Procedure for Acoustic Power Spectra

Acoustic power spectra for all operating conditions are determined according to the norm DIN EN ISO 9614-1 [28, 38]. The norm formalities describe the necessary procedures for the determination of the acoustic power radiated by an arbitrary source in a reflective environment. For the measurement environment the following requirements apply:

- The measurement zone should remain unchanged with respect to its geometry and items between experiments.
- The measurement positions must be placed on a virtual surface enclosing the source, with a minimum of 1 measurement position per square meter of surface area.
- A minimum of 10 measurement positions is required.

To comply with the requirements, the burner is enclosed by a virtual measurement sphere of radius $R = 990$ mm. The center of the sphere is located at the burner nozzle, and the intensity probe axis is always aligned directly with the line of sight towards the nozzle. The spherical surface is subdivided into $n = 18$ sub-surfaces. Figure 5.8 shows the measurement principle with the measurement

positions on the virtual surface (indicated red) and the probe support frame. Each of the sub-surfaces represents a fraction of the overall radiated acoustic power, which depends on the face normal of the acoustic intensity and the surface area of the sub-face:

$$P_{k,i}(\omega) = I_{n,k,i}(\omega) \cdot S_{k,i}. \quad (5.4)$$

Here, $I_{n,k,i}(\omega)$ denote the spatial averages of the active acoustic intensity in the face normal direction and $S_{k,i}$ the surface area of the corresponding sub-surface. The center level surfaces are denoted by $S_{2,i}$, while the triangular bottom and top level faces are denoted by $S_{1,i}$, $S_{3,i}$. The total acoustic power radiated by the flame is given by the sum of the individual powers:

$$P_{\text{aco}}(\omega) = \sum_{k=1}^3 \sum_{i=1}^6 I_{n,k,i}(\omega) \cdot S_{k,i}. \quad (5.5)$$

In the laboratory, the acoustic properties of the boundaries remain unchanged over time, and the positioning of large items around the experimental setup is

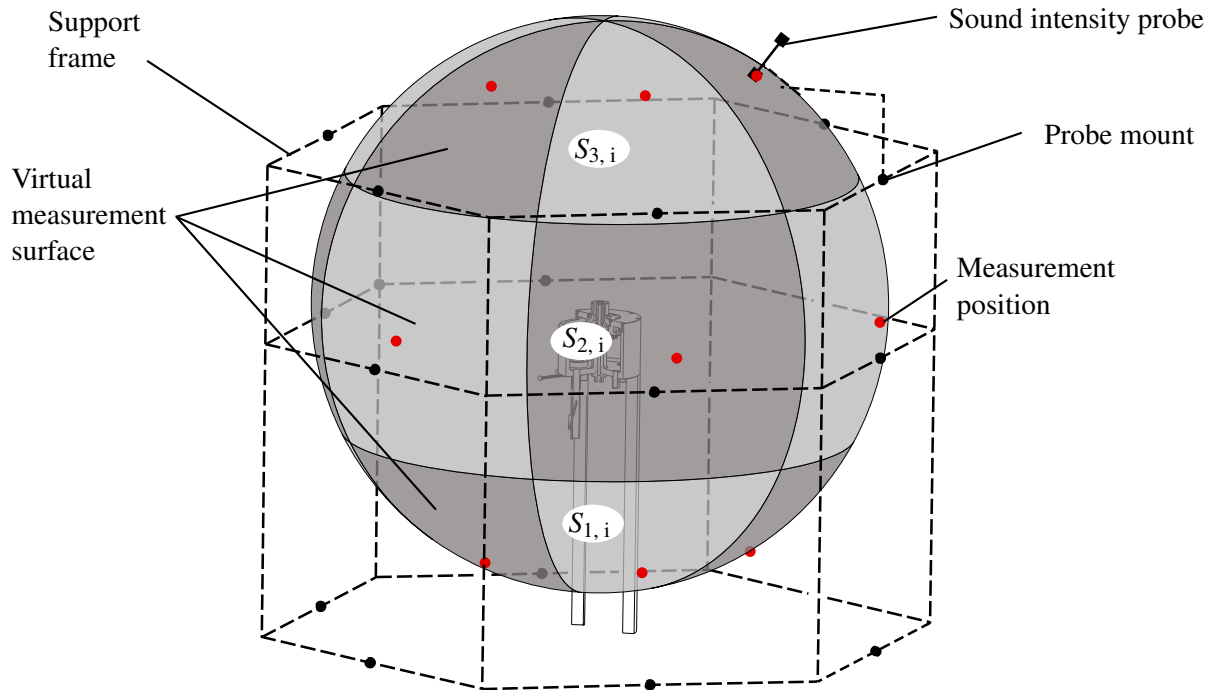


Figure 5.8: Schematic of the measurement setup showing the probe support frame and the individual measurement positions on the measurement surfaces $S_{k,i}$ enclosing the flame.

kept constant. The directional radiation characteristics of the flame are solely determined by the acoustic properties of the surroundings which remain unaffected by the current operating point. Thus, a constant ratio $\zeta(\omega)$ between the total sound power radiated by the flame and that of an arbitrary single sub-surface can be defined, which is unique for the laboratory. This procedure reduces the experimental effort needed for the determination of the total radiated acoustic power. The ratio function $\zeta(\omega)$ is measured using a reference power setting of the non-premixed flame covering the whole frequency range of interest with sufficient amplitude levels. The reference sound source is a non-premixed flame of $P_{\text{th}} = 55 \text{ kW}$ at $\lambda = 1.5$ and $S = 0.8$. Figure 5.9 shows the 18 individual spectra of sound power $P_{k,i}(\omega)$ measured at the reference operating point. The overall amplitude levels are equal for the corresponding six sensor positions i in the same face level k . Between the different levels, the amplitude is equal for levels 3 and 2, that is the top and center level. For the bottom level, the overall amplitudes are lower which can be attributed to the acoustic shadowing by the swirler casing.

The connecting function $\zeta(\omega)$ relating the acoustic power spectrum measured at one of the 18 measurement locations to the total radiated sound power is defined as

$$\zeta(\omega) = \frac{P_{\text{aco, tot, ref}}(\omega)}{P_{k,i}(\omega)}, \quad (5.6)$$

where $P_{\text{aco, tot, ref}}$ and $P_{k,i}$ are the active components of the respective acoustic power spectra. Exemplary, the resulting connecting function between the acoustic power spectrum at measurement surface $S_{3,1}$ and that of the total acoustic power is shown in Fig. 5.9 bottom, where the function level is calculated from

$$L_{\zeta}(f) = 10 \cdot \log \left(\frac{\zeta(f)}{\zeta_{\text{ref}}} \right), \quad (5.7)$$

where the reference $\zeta_{\text{ref}} = 1$ has been chosen arbitrarily. The ratio function computed using the reactive intensity component shows a rough trend with distinct peaks in the lower frequency range when compared to the active ratio function. This can be attributed to the effects of room acoustics, which are included in the reactive part of the function.

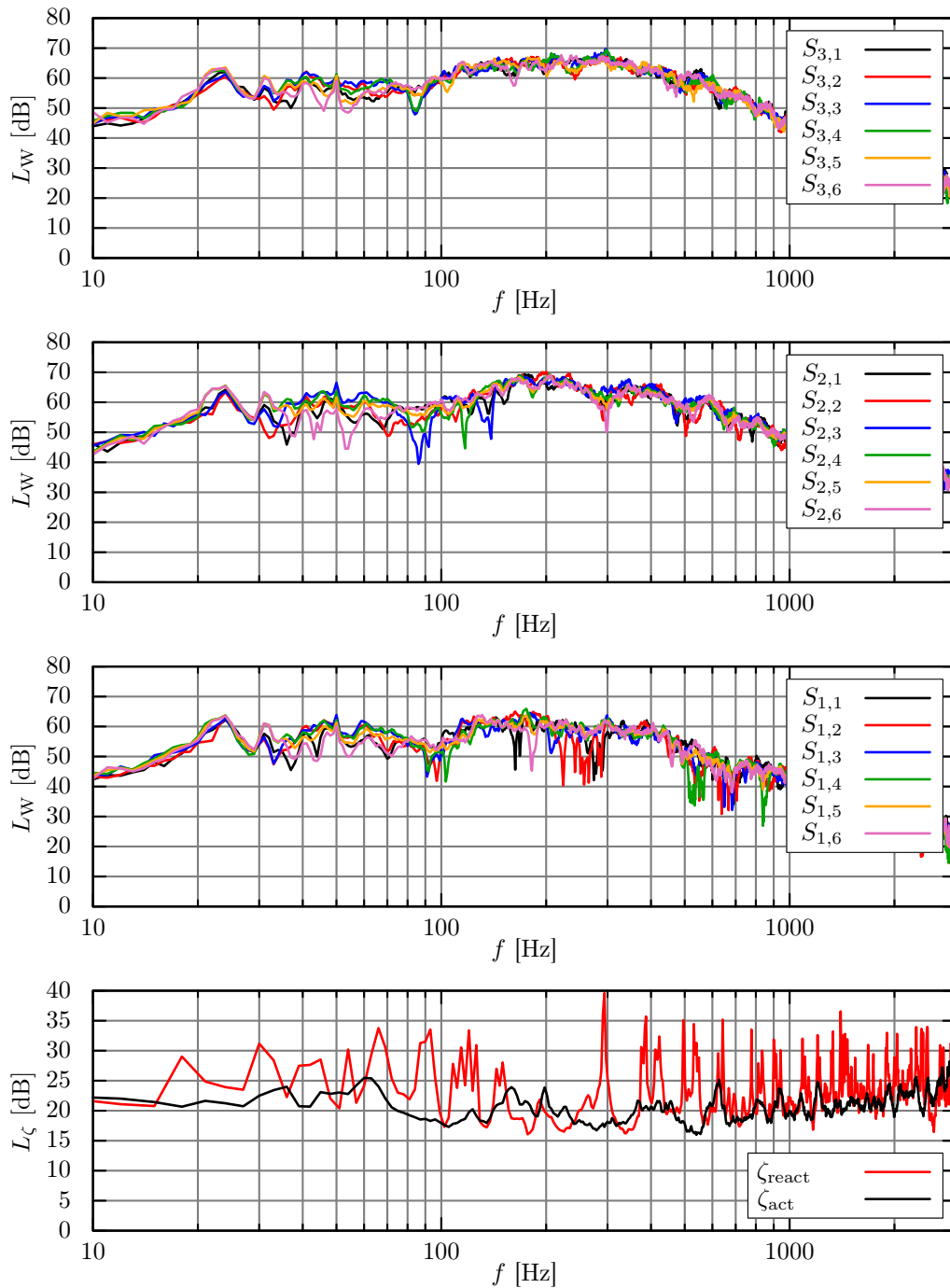


Figure 5.9: Sound power spectra for the 18 individual measurement positions and ratio functions computed from active intensity data. The plots show 6 spectra for each of the 3 face levels described in Fig. 5.8. Sound power level calculated with reference of $P_{ref} = 1 \cdot 10^{-12} \text{W}$. The bottom plot shows the calibration function ζ relating the sound power represented by a single measurement surface to the total sound power radiated by the flame. The calibration function is plotted based on active and reactive sound intensity used in the calculation of sound power.

5.5 Determination of Peak Frequency

The extraction of the peak frequency from spectral experimental data requires a robust computational routine which ensures repeatability and constant accuracy for different grades of noise in the spectrum to be analyzed. A simple extraction of the global maximum is prone to erroneous results as measured combustion noise spectra contain local peaks which may exceed the broadband maximum. Possible approaches to reduce spectral noise include logarithmic filtering/smoothing and the reduction of spectral resolution. These methods directly affect the input spectrum and thus, may alter the peak frequency result in random directions, depending on the specific quality of the input spectrum.

In the course of the study at hand, best results were achieved by fitting a polynomial of the form

$$f(x) = c_1x^n + c_2x^{n-1} + \dots + c_nx + c_{n+1}, \quad (5.8)$$

to the experimentally measured spectra, where $n = 10$. An exemplary result of the fitting process is shown in Fig. 5.10. The fitting routine is limited to the frequency range between 0 Hz and 2000 Hz as suggested by the typical frequency range of combustion noise measured in the experimental campaign. At 2000 Hz, the input data for the polynomial fit is truncated, leading to the cutoff in the fit data and

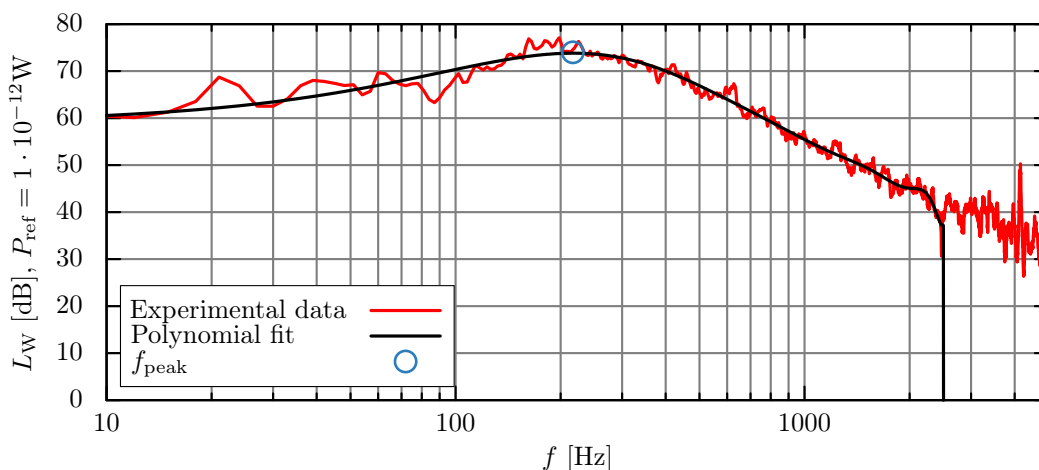


Figure 5.10: Determination of the peak frequency using a polynomial fit function in the lower frequency range.

effectively enhancing the fit quality through the reduction of input data vector length.

5.6 Measurement Technique for Acoustic Intensity

For the measurement of active and reactive sound intensity components, a commercial G.R.A.S. 40AK $\frac{1}{2}$ in intensity probe was used. The two $\frac{1}{2}$ in pressure microphones are separated by a distance piece of $\Delta x = 25$ mm. The probe microphones are capable of recording sound pressure amplitude levels in the range $20\text{ dB} < L_p < 152\text{ dB}$ and cover a frequency range of $2.5\text{ Hz} < f < 10000\text{ Hz}$. The membrane inside the condenser microphones converts the fluctuating pressure signal into a fluctuation of electric capacity which in turn causes a voltage fluctuation. This signal is pre-amplified by G.R.A.S. 26AA pre-amplifiers mounted directly to the microphones. A Bruel & Kjaer Nexus 2690 amplifier performs high and low pass filtering at $f_{\text{high}} = 5\text{ Hz}$ and $f_{\text{low}} = 6000\text{ Hz}$ and applies individual microphone sensitivities. The conditioned signal time series is recorded by data acquisition software and hardware using a PC. The time series of the pressure signals from both microphones are recorded at a sampling rate of $f_s = 50\text{ kHz}$. The recorded signal duration is $T_s = 5\text{ s}$ for each time series. A total of 10 time series are recorded during each measurement giving an overall recording time of $T_{\text{tot}} = 50\text{ s}$ per measurement including a total of $N = 2500000$ samples. The cross spectral density between the individual time series of sound pressure is evaluated using Welch's method of spectrum estimation [145]. The 10 intensity spectra are then averaged for the active and reactive intensity spectra. An exemplary evaluation of active and reactive intensity spectra is shown in Fig. 5.11. Outside the very low frequency range, the reactive intensity shows lower amplitude levels, which indicates the effectiveness of the absorptive material installed around the test rig and along the laboratory walls. The sound field around the flame can thus be characterized as active sound field for frequencies above $f_{\text{low}} = 50\text{ Hz}$, where the indicator for active sound fields [61],

$$I \gg J \tag{5.9}$$

is fulfilled.

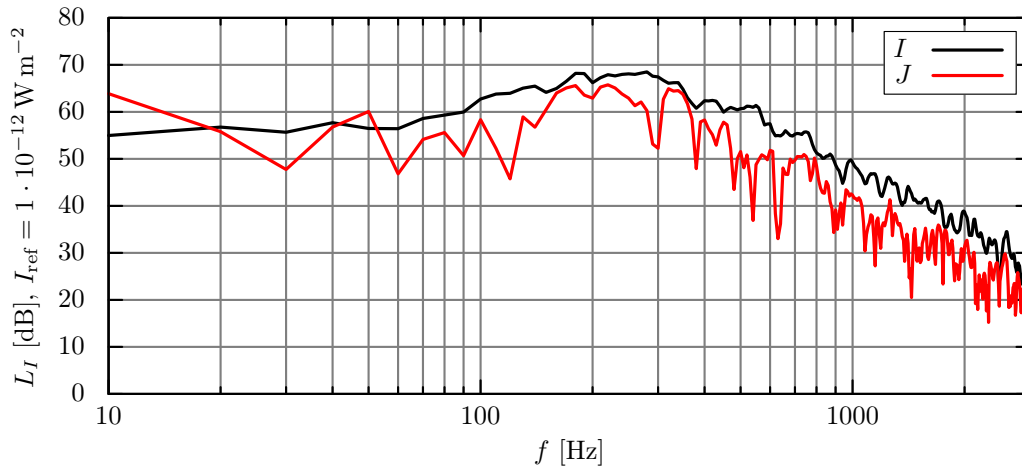


Figure 5.11: Active (I) and reactive (J) part of sound intensity radiated by a turbulent non-premixed flame. The influence of the reverberant sound field is visible below 100 Hz in the reactive part of the spectrum, where the acoustic damping potential of the laboratory is low. The spectra are calculated by averaging over 10 individual spectra.

5.7 Repeatability of Intensity Measurements

The quality of the obtained intensity spectra is analyzed by studying a statistical significant amount of single spectra of one operating point. 100 time series of the turbulent non-premixed flame at a constant operating point of $P_{th} = 50 \text{ kW}$, $\lambda = 1.2$ and $S = 0.6$ were recorded for that purpose. A scatter plot of the resulting 100 spectra of active acoustic intensity is shown in Fig. 5.12. The match between the individual spectra with respect to shape and peak frequency is good. The amplitude levels show a spread of 5 dB in the frequency range between 30 Hz and 3000 Hz. In the range below 30 Hz, the sound field is dominated by its reactive component, which enlarges the data variation. In excess of 3000 Hz, the statistical fluctuations in amplitude and frequency grow due to the increasing influence of wave interferences on the probe. In the frequency range that is of significance for the analysis of turbulent combustion noise, the repeatability of the measurements is good with small fluctuations in the spectral amplitudes. The repeatability and deviations between single realizations of spectral measurements are within the ranges reported by Wäsle [143].

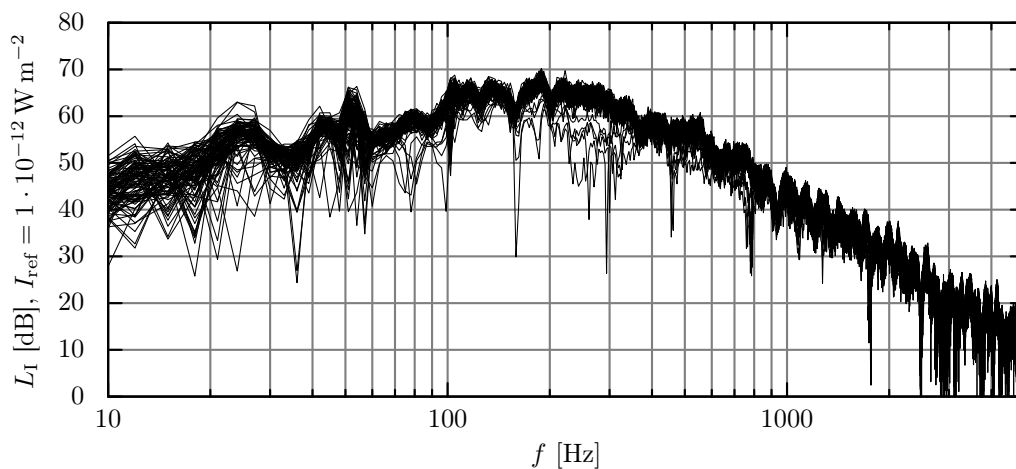


Figure 5.12: 100 single spectra of active acoustic intensity calculated from time series recorded at a constant operating point of $P_{th} = 50\text{ kW}$, $\lambda = 1.2$ and $S = 0.6$ of the non-premixed flame.

5.8 Chemiluminescence

The combustion reaction between methane and oxygen consists of a large number of sub-reactions. During reaction, radical molecules in an energetically excited state evolve, which emit light upon returning to their natural energetic state. The OH^* radical is created in an excited state during the combustion reaction of natural gas. Upon return to its normal state, it emits light centered around a wavelength of $\lambda = 307\text{ nm}$. The return to the normal state only endures a very short time period, suggesting that light emission at that wavelength only occurs at locations where chemical reaction is in progress. A line of sight integrated image of the flame can be used to gain a qualitative impression of the flame shape, but the determination of quantitative data corresponding to the local heat release, or air excess ratio is connected to difficulties [72]. However, the spatially integrated data from photomultiplier measurements can be used to detect the total power output of the flame.

In this study, an image intensified high speed camera, type Photron Fastcam Ultima APX I2, was used to capture the flame images. Its CMOS (complementary metal oxide semiconductor) sensor has a maximum resolution of 1024×1024 pixels at a rate of 2000 frames per second, and a fiber optically coupled image intensifier.

For the acquisition of global OH* intensity data, a photomultiplier is applied to convert the light emission into an electrical signal. A narrow-band interference filter restricts the incident light spectrum to the main OH* peak at $\lambda = 307$ nm. The output voltage is used to directly compare the fuel burnout percentage of premixed flames between confined and unconfined configuration.

6 Turbulent Combustion Noise from Non-Premixed and Premixed Swirl Flames

This chapter summarizes the experimental results for combustion noise obtained from the turbulent swirl flame operated in premixed and non-premixed configuration. The experimental focus is set on the non-premixed flame in order to obtain a set of experimental validation data for the extended combustion noise model comprising variation in swirl number, thermal power and air excess ratio.

The premixed flame experiments are conducted at matching operating conditions concerning thermal power, mixture composition and swirl. A burnout correction procedure ensures the direct comparability between the two flame configurations by determining the true heat release within the premixed flame.

The type-II non-premixed flame is in its essential configuration designed to achieve high degrees of fuel burnout by injecting the fuel into the inner shear layer only, leaving fuel burnout unaffected by entrainment. Virtually complete fuel burnout is reported for this type of non-premixed flame [132], which makes the resulting heat release equivalent to the theoretical value of the supplied fuel.

6.1 Non-Premixed Flame

The experimental campaign for the non-premixed flame comprises the set of operating points summarized in Tab. 6.1. From a standard operating point of $P_{\text{th}} = 50\text{kW}$, $\lambda = 1.2$ at a swirl number of $S = 0.6$, which is also suitable for premixed flame operation, variations in the operating conditions concerning thermal power output, mixture composition and swirl intensity are investigated. Operating points investigated are chosen such that they are positioned safely inside the fast chemistry regime, as indicated by the symbols in Fig. 6.1. The corresponding

Table 6.1: Operating points investigated for the non-premixed flame. The reference operating point is marked in gray.

OP	S	P_{th} [kW]	λ	\dot{m}_f [g/s]	\dot{m}_{air} [g/s]	\bar{u}_{air} [m/s]	Re	Momentum ratio
DPV1	0.6	30	1.20	0.62	12.68	7.67	25644	19.51
DPV2	0.6	40	1.20	0.82	16.91	10.23	34192	19.51
DPV3	0.6	50	1.20	1.03	21.14	12.79	42740	19.51
DPV4	0.6	60	1.20	1.23	25.37	15.34	51288	19.51
DPV5	0.6	70	1.20	1.23	29.60	17.90	59836	19.51
DLV1	0.6	50	1.00	1.03	17.62	10.72	34192	27.74
DLV2	0.6	50	1.20	1.03	21.14	12.87	41030	19.27
DLV3	0.6	50	1.40	1.03	24.67	15.01	47868	14.16
DLV4	0.6	50	1.60	1.03	28.19	17.16	54707	10.84
DLV5	0.6	50	1.80	1.03	31.71	19.30	61545	8.56
DLV6	0.6	50	2.00	1.03	35.23	21.45	68383	6.94
DSV1	0.4	50	1.20	1.03	21.14	12.87	41030	19.27
DSV2	0.6	50	1.20	1.03	21.14	12.87	41030	19.27
DSV3	0.8	50	1.20	1.03	21.14	12.87	41030	19.27
DSV4	1.0	50	1.20	1.03	21.14	12.87	41030	19.27
DSV5	1.2	50	1.20	1.03	21.14	12.87	41030	19.27
DSV6	1.4	50	1.20	1.03	21.14	12.87	41030	19.27

variation experiment can be deduced from the identifier given in the first column of Tab. 6.1, where DPV denotes the power variation study, DLV the variation in air excess ratio and DSV the variation in swirl number. The Reynolds number is given in terms of the hydraulic diameter of the annular burner exit tube and the momentum ratio relates the momentum of the fuel stream to that of the air stream.

6.1.1 Influence of Thermal Power

From the base operating point DLV2, defined in Tab. 6.1, thermal power is varied in steps of 10kW while the air excess ratio is kept constant at $\lambda = 1.2$. Figure 6.2 shows photographs of the non-premixed flame for different thermal power settings. The visible effect of increasing thermal power can be distinguished in be-

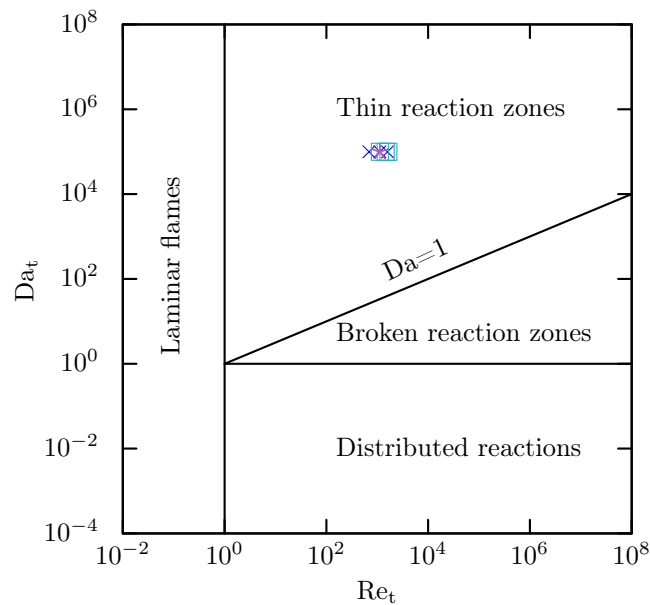


Figure 6.1: Regime diagram of non-premixed turbulent combustion. The symbols show the location of the operating points listed in Tab. 6.1.

tween the single photographs by comparing the flame length. From $P_{th} = 30\text{ kW}$ to $P_{th} = 60\text{ kW}$ the length of the light blue flame zone close to the nozzle increases slightly, which in turn leads to an increase of the total flame volume. At a fixed air excess ratio, an increase in thermal power leads to higher flow velocities and increased turbulent intensity in the reaction zone as well. Figure 6.3

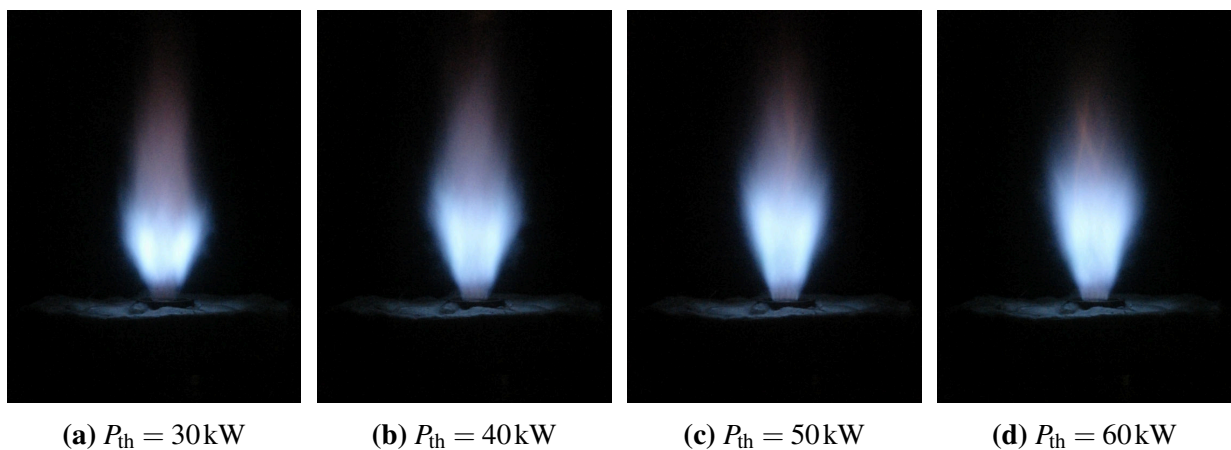


Figure 6.2: Flame shapes at different thermal power settings for a swirl number of $S = 0.6$ and an air excess ratio of $\lambda = 1.2$.

shows the influence of thermal power on the radiated sound power. Two effects can be distinguished. The spectral amplitude in the region of the peak frequency increases towards higher thermal power, from around 75 dB at $P_{\text{th}} = 30\text{kW}$ towards 85 dB at $P_{\text{th}} = 70\text{kW}$. The frequency of peak spectral amplitude moves towards higher frequencies as the firing rate is enlarged. This trend can be explained by considering Eq. (4.50). With increasing turbulent intensity within the reaction zone, the local turbulent time scales decrease, which in turn leads to increasing local peak frequencies. The effect on the overall acoustic spectrum of the flame is the observed increase in spectral amplitudes in excess of the global peak frequency. Figure 6.4 shows the measured peak frequencies and thermo-acoustic efficiencies for all operating points of the power variation study. The frequency of peak amplitude is increasing linearly in the investigated range of thermal powers. This behavior is in close agreement to the findings of Winkler et al. [151] who performed a similar study using a premixed swirl flame. Starting from a thermal power setting of $P_{\text{th}} = 30\text{kW}$, they observe a similar dependency of peak frequencies on the firing rate along with frequency values in proximity to the non-premixed data shown in Fig. 6.4. However, the slope of the frequency increase is steeper in the premixed case. The probable reason for the difference in behavior is the ratio of fuel burn-out, which is influenced by the entrained ambient air, as indicated by the global OH*-data in Sec. 6.2.1 and pointed out by Lauer [72]. As well, the burner used by Winkler et al. [151] was equipped with

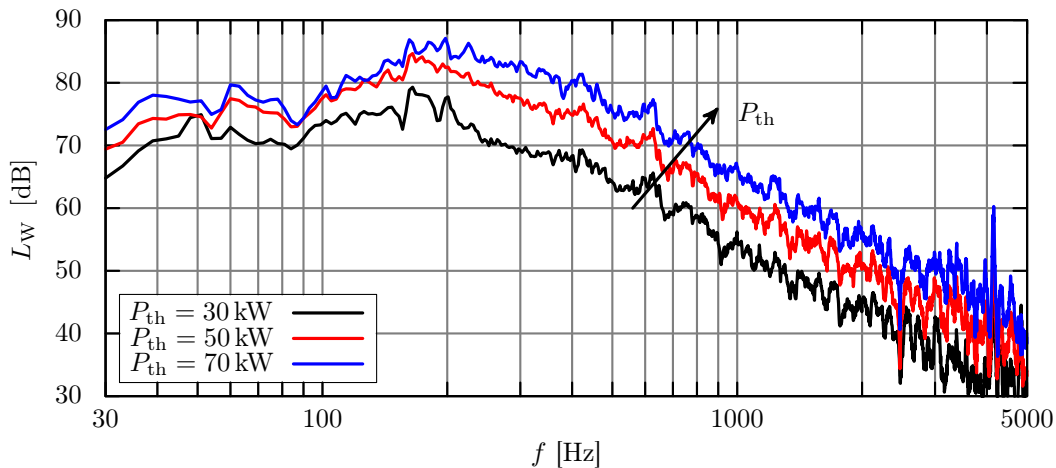


Figure 6.3: Spectral sound power emitted by the turbulent non-premixed flame at a swirl number of $S = 0.6$, an air excess ratio of $\lambda = 1.2$ and three different power settings.

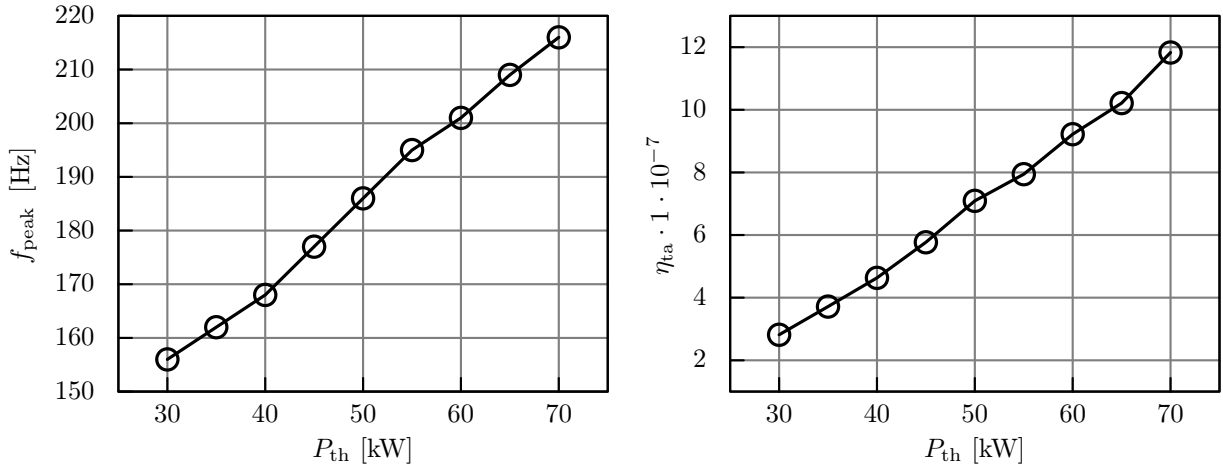


Figure 6.4: Dependency of peak frequency and thermo-acoustic efficiency on the thermal power setting of the non-premixed flame at $S = 0.6$, $\lambda = 1.2$. between $P_{th} = 30$ kW and $P_{th} = 70$ kW.

a convergent annular nozzle, creating a more intense turbulent flow field, which complicated a direct comparison of the noise spectra between those cases.

The efficiency of conversion increases linearly with thermal power following the increase in overall flame volume. A good approximation for the flame as a source of sound is that of a vibrating sphere [25]. The surface impedance of such a spherical model source depends on the radius r of the source and is given by [109]

$$Z = \frac{\hat{p}}{\hat{u}} = \frac{\rho_0 c_0}{1 + \frac{1}{(kr)^2}} \left(1 + \frac{i}{kr} \right). \quad (6.1)$$

The real part of Eq. (6.1) governs the efficiency of sound radiation and increases with the source radius (i. e. the volume). A comparison to the premixed swirl flame operated at comparable conditions concerning swirl and thermal power reveals a similar trend, as observed by Winkler et al. [151] in their study of a turbulent premixed flame.

6.1.2 Influence of Mixture Composition

By varying the global mixture composition at constant swirl and power settings for the non-premixed flame, the turbulent time and length scales in the reaction

zone are modified, while the local mixture composition remains near stoichiometric. The constant thermal power setting results in constant exit velocity of the fuel jets. Measured acoustic power spectra of the mixture composition study are presented in Fig. 6.5 for air excess ratios between $\lambda = 1.0 \dots \lambda = 2.0$. While the low frequency range remains unaffected by the switch in global mixture conditions, the high frequency decay in excess of f_{peak} is reduced with increasing air excess ratio. An increase of excess air equals an increase of the flow Reynolds number, which equals intensified turbulent fluctuations in the reaction zone. This intensification causes increased noise radiation in the high frequency range, as the local air excess ratio remains near-stoichiometric in the reaction zone in the vicinity of the fuel injection holes of the non-premixed flame. Consequently, the influence of the global air excess ratio is primarily visible in a shift of the decay slope in the high frequency range, which is a different trend when compared to the observations of Wäsle [143] with premixed flames. Here peak-frequency and spectral amplitude are shifted towards higher values at greater air excess ratio. A notable difference in the data of the mixture composition study are the essentially constant amplitude levels in the frequency range below f_{peak} . Obviously, the increasing turbulence intensity within the reaction zone barely influences this region of the combustion noise spectrum, while the effect of increasing the thermal power takes its effect on all parts of the spectrum. This can be explained by the fact, that turbulent length scales are bounded at lower wave-numbers by

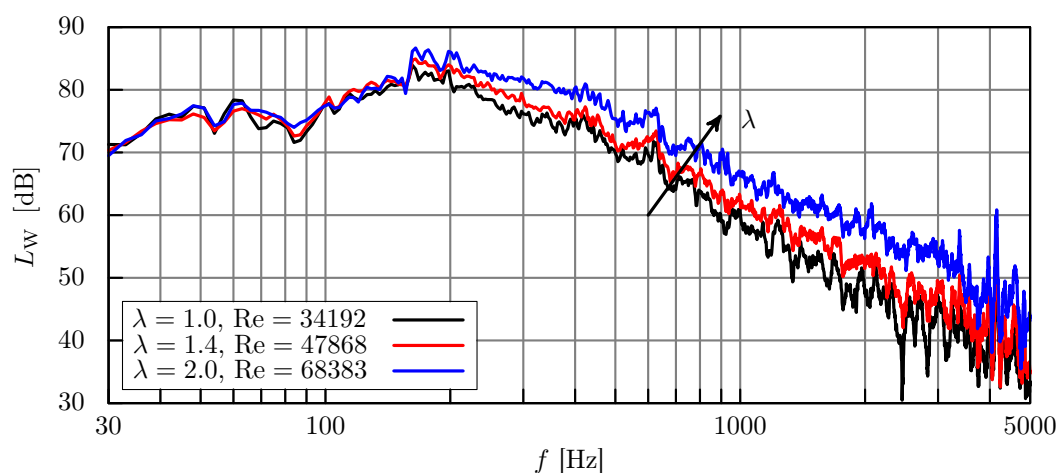


Figure 6.5: Effect of mixture composition on sound power spectra of the non-premixed flame at $S = 0.6$ and $P_{\text{th}} = 50\text{kW}$.

geometric restrictions of the burner. The turbulent integral scale can be of the order of the nozzle radius at the most, which forecloses any significant effect of altering the turbulence intensity at the low end of the spectrum.

The determined peak-frequencies and thermo-acoustic efficiencies for six operating points ranging from $\lambda = 1.0$ to $\lambda = 2.0$ as indicated in Tab. 6.1, at a fixed thermal power of $P_{th} = 50\text{kW}$ are shown in Fig. 6.6. The peak frequency departs

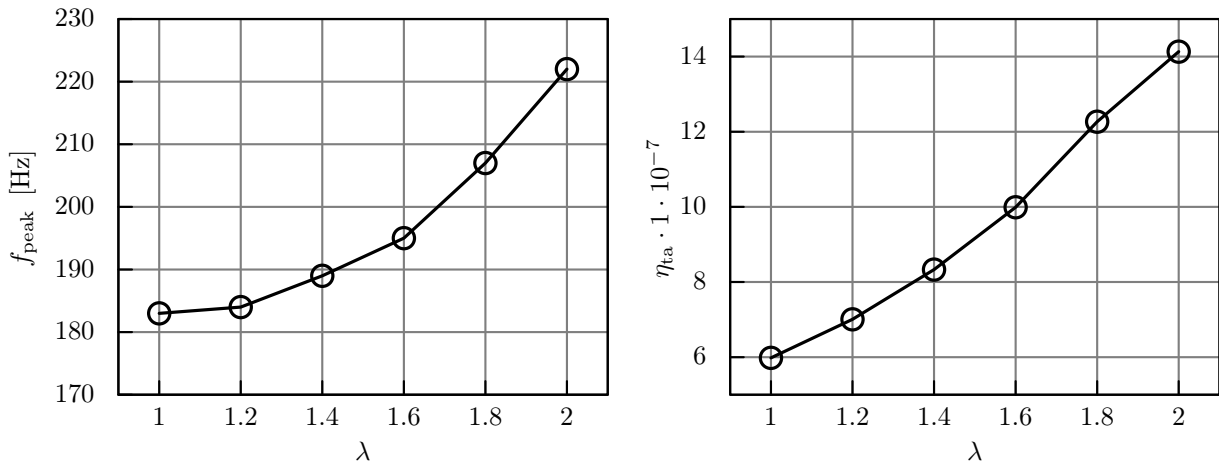


Figure 6.6: Effect of mixture composition on peak frequency and conversion efficiency of the non-premixed flame at $S = 0.6$ and $P_{th} = 50\text{kW}$.

from a linear increase around an air excess ratio of 1.3, at higher ratios the influence of mixture composition is increased. The turning point corresponds to a Reynolds number of approximately 44000, while the maximum of $\lambda = 2.0$ equals $Re = 68383$. In the case of the non-premixed flame, altering the global mixture composition can be seen as a mere alternation of the turbulence conditions in the reaction zone as the reaction mostly occurs under near-stoichiometric conditions. The shift of the peak output towards higher frequencies at greater Reynolds number is also the explanation for an enhanced efficiency in the production of acoustic energy, which is shown in Fig. 6.6 at higher air excess ratio.

6.1.3 Influence of Swirl Strength

The swirl number alters the turbulence intensity isolated from mixture composition or thermal power. In the swirl variation study, the swirl number is varied

between $S = 0.4$ and $S = 1.4$. The main effect of increasing the flow swirl number is an increase in the entrained mass flow into the flame [84]. Figure 6.7 shows the influence of swirl on the spectral amplitude and shape. An increase in turbu-

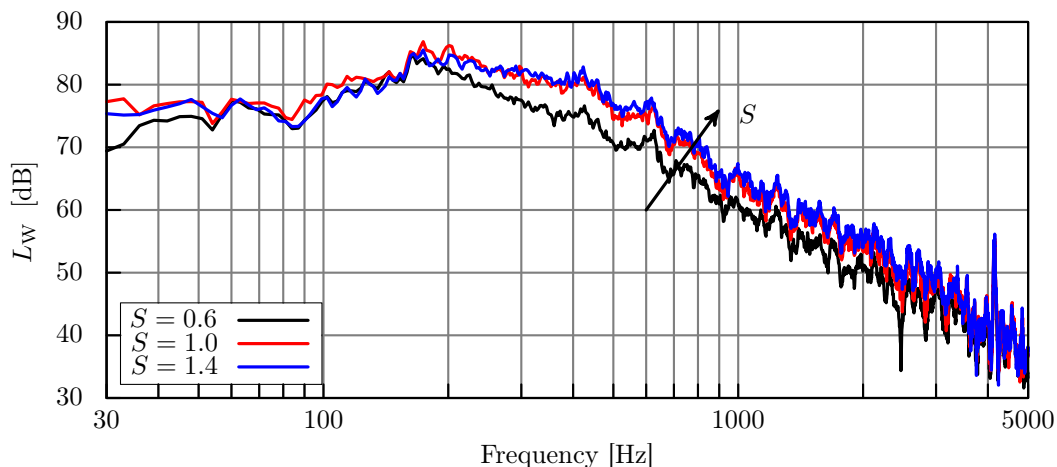


Figure 6.7: Effect of swirl number on the frequency spectrum of sound power. For swirl numbers in excess of $S = 1.0$, the flame length stagnates, leading to stagnating thermo-acoustic conversion efficiencies.

lence intensity with increasing swirl number [132] leads to an increase in spectral amplitude at larger frequencies in excess of f_{peak} . Remarkably, the slope of the spectral decay is constant for different swirl intensities. Also, the peak frequencies are shifted towards larger frequencies. The difference between the spectral amplitudes of $S = 1.0$ and $S = 1.4$ is small, which results from the stagnation in flame shortening at large swirl intensities. At $S = 1.0$, the flame reaches a minimum flame length, which remains constant if the swirl number is increased further. The stagnation of flame length is shown in the series of flame images in Fig. 6.8. Consequently, amplitude levels of the radiated noise stagnate as well, as the efficiency of noise radiation depends on the overall flame volume. This effect can easily be interpreted when considering integral data for peak frequencies and conversion efficiencies over the swirl number as shown in Fig. 6.9. At swirl numbers beyond $S = 1.0$, the thermo-acoustic conversion efficiency remains virtually constant. Consequently, the overall radiated sound power remains constant as well, as the overall firing rate is kept constant. However, the peak frequencies increase gently below $S = 1.0$ before steeply increasing until reaching a value around 273 Hz at intense swirl of $S = 1.6$.

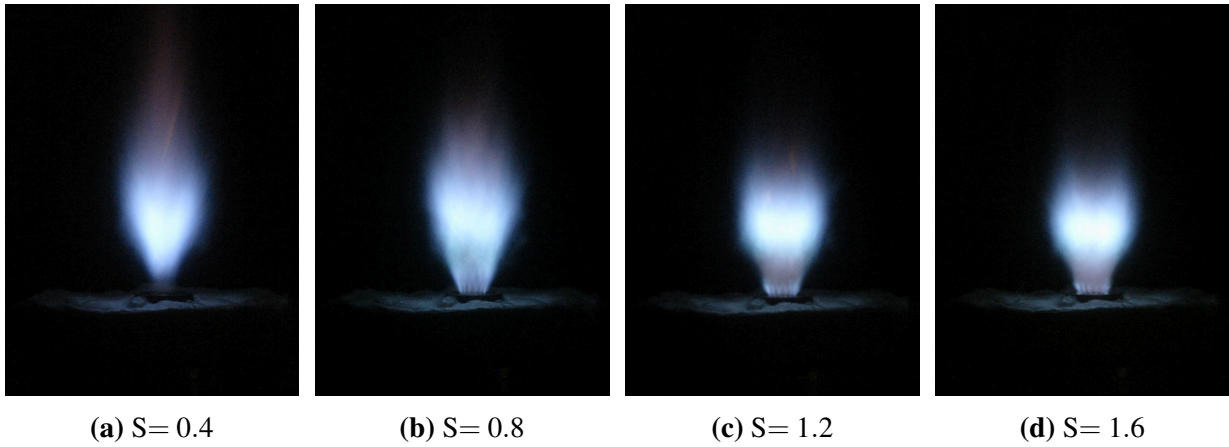


Figure 6.8: Flame images at different swirl numbers at a thermal Power of $P_{th} = 50\text{kW}$ and an air excess ratio of $\lambda = 1.2$. Beyond $S = 1.0$, the flame length remains unaltered by the swirl intensity.

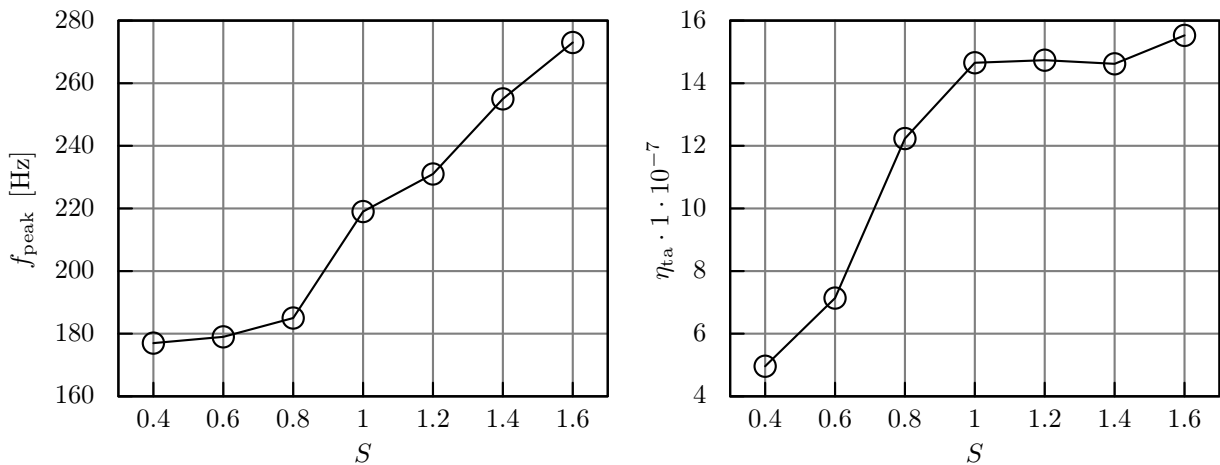


Figure 6.9: Peak frequency and thermo-acoustic conversion efficiency of the non-premixed flame for different swirl numbers. While the conversion efficiency stagnates due to stagnating flame size at swirl numbers in excess of $S = 1$, f_{peak} shows further increase due to increasing turbulence intensity.

6.1.4 Matrix Study on Mixture Composition and Thermal Power

The influence of thermal power and mixture composition on the peak frequency and the thermo-acoustic conversion efficiency can be demonstrated descriptively by evaluating these global parameters for a series of equally spaced operating points. Contours of thermo-acoustic efficiency are shown in Fig. 6.10, corresponding contours of peak frequency are shown in Fig. 6.11. The test matrix that was evaluated spans thermal power settings from $P_{th} = 30\text{kW}$ to $P_{th} = 60\text{kW}$ in

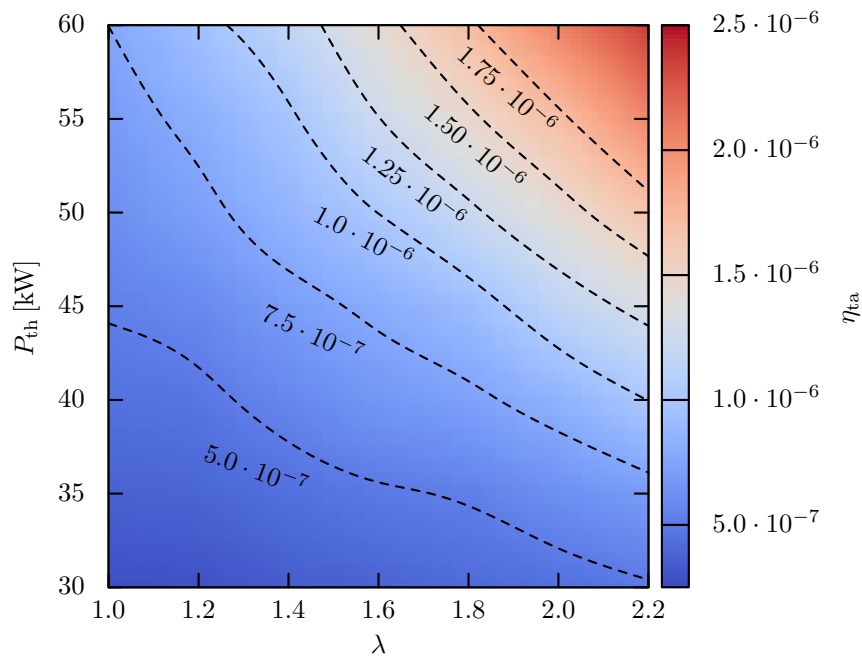


Figure 6.10: Contours of thermo-acoustic conversion efficiency over thermal power and air excess ratio for the non-premixed flame at $S = 0.6$.

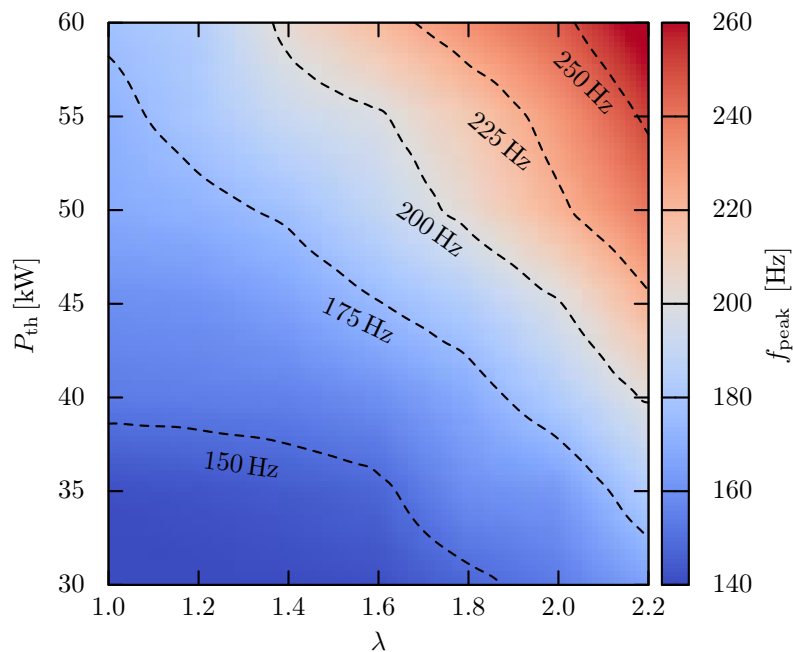


Figure 6.11: Contours of peak frequency over thermal power and air excess ratio for the non-premixed flame at $S = 0.6$.

steps of 5 kW and air excess ratios from $\lambda = 1.0$ to $\lambda = 2.2$ in steps of 0.2. The values have been interpolated using splines between the individual data points to give a continuous contour.

The results illustrate the influence of the crucial parameters governing the generation of combustion noise in turbulent flames. The global rate of heat release represented by the thermal power setting governs the thermo-acoustic conversion efficiency by influencing the total flame volume. The turbulent intensity and mixing time scale in the reaction zone is governed by the air excess ratio and additionally increases the conversion efficiency by shifting the frequency content of the emitted noise towards higher and more efficient frequencies at greater air excess ratios. This frequency shift, which also accompanies an increase in thermal power through the increased flow velocity and thus, turbulence intensity is shown in the contour plot of the peak frequencies in Fig. 6.11.

6.2 Premixed Flame

Premixed flame operation was realized by switching fuel supply from the central body to the static mixer mounted upstream of the swirler as described in Fig. 5.1. Before the results of the premixed flame noise measurement campaign are discussed, a method for the quantification of fuel burnout efficiency of open burning turbulent premixed flames, which is impaired by incomplete burnout due to entrainment of ambient air is presented. In the outer regions of the swirled flow, the lower flammability limits of the mixture can be exceeded or the reaction may be quenched due to the entrainment, leaving part of the initially supplied mixture unburnt [55, 72].

6.2.1 Fuel Burnout Efficiency of Open Premixed Flames

Lauer [72] investigated the characteristics of integral OH* radiation from open premixed flames and its correlation with the local rate of heat release. The relevant data is shown in Fig. 6.12. For flames close to stoichiometric air excess ratios, the data shows close proximity between the normalized values of the

bandpass filtered integral OH* signal and the heat release. Lauer also reports an offset between the local OH* emissions and the heat release, which can not be attributed to the entrainment of ambient air. This offset is attributed to high turbulence intensities close to the burner exit, which lead to a reduction in local OH* intensities. These findings identically apply for all equivalence ratios investigated by Lauer.

In the combustion noise experiments with the premixed configuration of the movable blocks burner, the outer shear layer of the premixed swirl flow did not self-ignite in any circumstances, nor could continuous reaction be established by initially igniting it. Thus, the main reaction zone within the inner shear layer remains unharmed by the entrainment of ambient air in terms of the prescribed air excess ratio. Consequently, the amount of fuel burnout can be determined by comparing the integral OH* intensity emitted by an open premixed flame to that of a confined flame reference case at matching operating conditions. As the offset between the OH* signal and the heat release is the same for matching air excess ratios as shown in Fig. 6.12, the global signal intensity can be used to compare the global heat release of different cases.

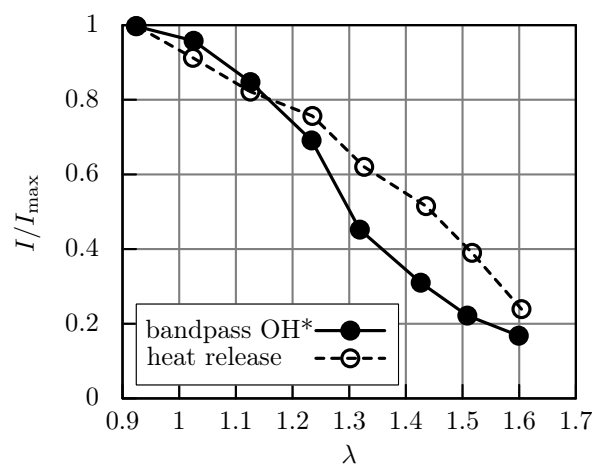


Figure 6.12: Comparison of integral chemiluminescence intensity and heat release of a premixed turbulent swirl flame of $P_{\text{th}} = 60\text{kW}$ (adapted from Lauer [72]). The curves are normalized by their corresponding maximum values and show a close match between the integral bandpass filtered OH* intensity and the integral heat release for air excess ratios up to $\lambda = 1.25$.

The reference case is generated by obstructing the entrainment of ambient air by a glass tube confinement, as previously shown in Fig. 5.5c. The quartz glass cylinder is of suitable length in order to protect the flame until complete burnout of the initially supplied premixed mixture is achieved. The effect of the glass tube confinement is shown in Fig. 6.13. The primary effect of the shielding is a radial

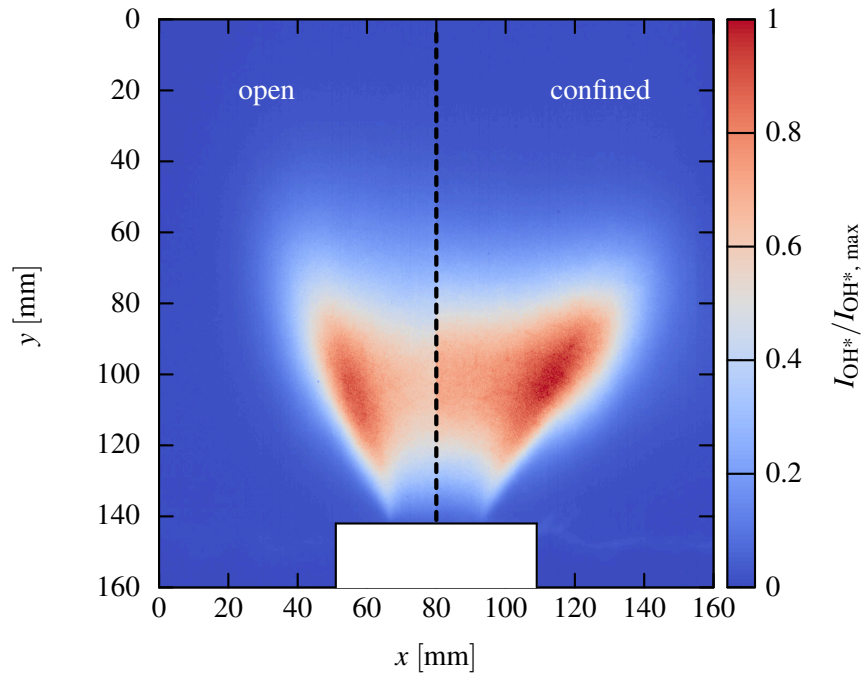


Figure 6.13: Comparison of OH* radiation of the open burning (left) and confined (right) turbulent premixed flame at $S = 0.8$, $P_{th} = 40 \text{ kW}$, $\lambda = 1.0$. The wall of the glass cylinder for the confined flame is located at $X = 160 \text{ mm}$.

extension of the reaction zone, which extends closely towards the glass surface located at $x = 160 \text{ mm}$. The now confined swirl flame can be expected to consume the complete initially supplied mixture, as the fuel burnout for confined premixed flames of similar swirl and mixture conditions is greater than 99%. [51].

With this procedure, the global OH* intensity can be recorded for the confined flame at a series of different operating conditions. This data is then compared to the OH* intensity of the unconfined flame of matching air excess ratio, so that a calibration coefficient can be generated which reveals the actual global heat re-

leased by the unconfined flame. The calibration coefficient for the determination of the supplied fuel burnout percentage is given by

$$\zeta_{\text{OH}} = \frac{I_{\text{OH, confined}}}{I_{\text{OH, unconfined}}}. \quad (6.2)$$

Then, the true thermal power output of the unconfined flame, denoted by P_{calib} can be calculated from

$$P_{\text{calib}} = \zeta_{\text{OH}} \cdot P_{\text{th}}. \quad (6.3)$$

Fuel burnout is determined for unconfined premixed flames in a range of operating conditions that show stable flame operation and an acceptable fraction of fuel burnout. This premise restricts the swirl number to a maximum of $S = 0.8$. Figure 6.14 shows the limits of stable operation for the premixed flame at $S = 0.6$ in terms of mixture composition and thermal power output. The operation field

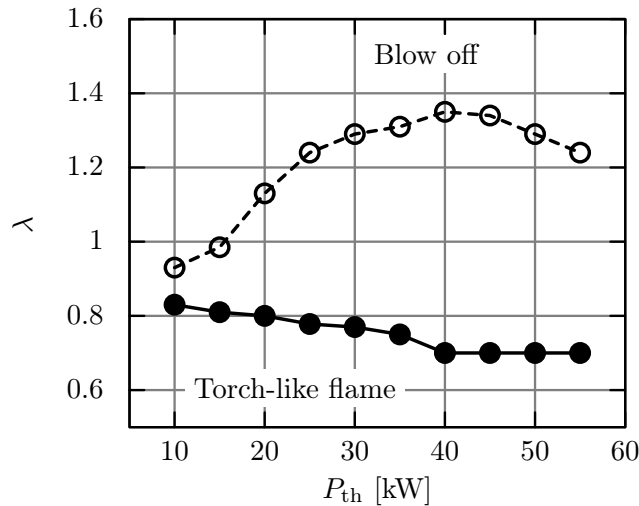


Figure 6.14: Limits of stable flame operation for the unconfined turbulent premixed flame at $S = 0.6$.

is determined by the lean (blow off of the flame) and rich limit inside which the flame can be operated under stable conditions. Stable operating conditions are especially desirable for experiments concerning combustion noise. At moderate swirl $S < 0.7$ and for rich mixtures $\lambda < 1$, the axial velocity in the annular gap does for all mixtures exceed the turbulent flamespeed, so that the rich limit of operation is not given by flashback of the flame into the swirler, but by the flame changing its shape towards a partially premixed tubular flame of extensive length. This flame type is characterized by reaction occurring solely in the outer shear

layer. The influence of entrainment for the unconfined flame is clearly visible in the data of global OH* intensity, which is shown in Fig. 6.15. For stoichio-

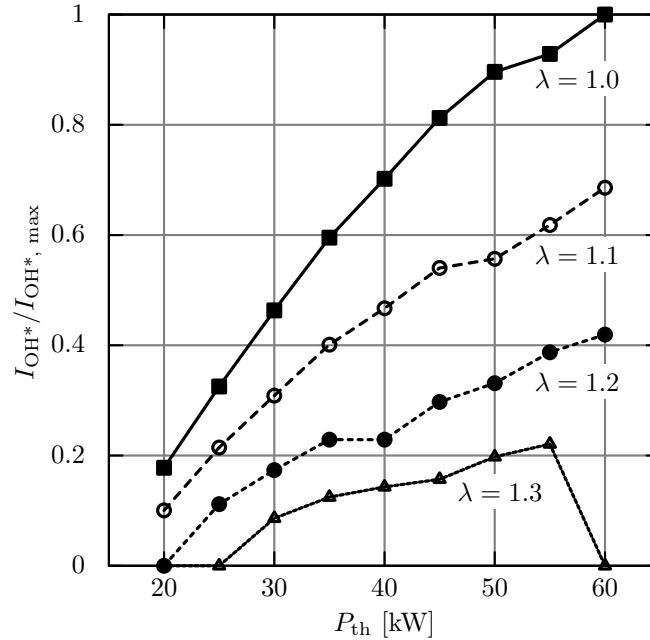


Figure 6.15: Global OH* radiation intensity for the open turbulent premixed flame at $S = 0.6$. The curves have been normalized with the maximum intensity value recorded at $\lambda = 1.0$.

metric conditions, the OH* intensity increases linearly with thermal power up to $P_{th} = 45$ kW, where the effect of increasing dilution becomes observable. Moving towards leaner mixture compositions, the slope decreases and at $\lambda = 1.3$ the flame is affected by growing dilution over the complete range of thermal power settings until flame extinction occurs at $P_{th} = 60$ kW. From the global OH* intensity data, the mean burnout efficiency ζ_{OH} is calculated using Eq. (6.2). Evaluated for the data in Fig. 6.15 the efficiencies in Fig. 6.16 are obtained. For air excess ratios in excess of $\lambda = 1.2$ the burnout is at or below 50% of the fuel initially supplied, which renders this operating range unsuitable for combustion noise experiments. Values of $\zeta_{OH} = 0$ mark extinction of the flame. At stoichiometric operation, burnout efficiency reaches its optimum at around 80% of the total supplied fuel mass flow rate. To achieve the best similarity between confined and unconfined flames in the premixed case and to ensure comparability to non-premixed flame data, the premixed flame experiments are restricted to air excess ratios of $\lambda = 1.0$ and $\lambda = 1.1$.

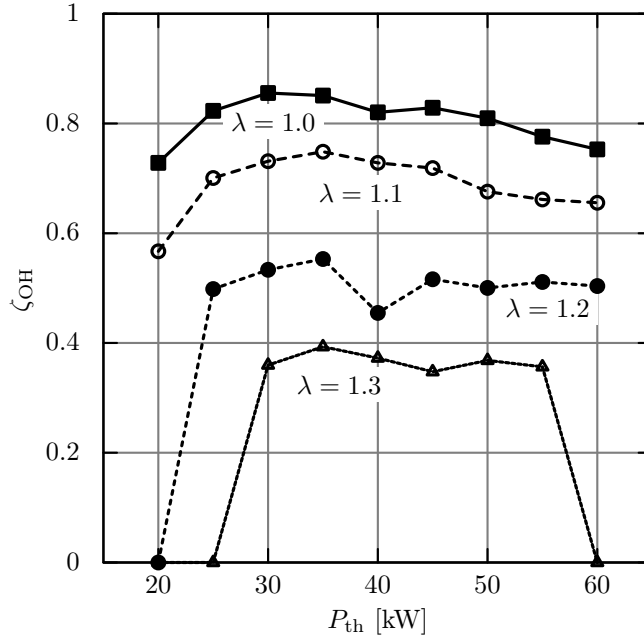


Figure 6.16: Burnout efficiency ζ_{OH} for the open premixed flame at $S = 0.6$ for varying mixture composition and thermal power output.

The investigated operating points, as summarized in Tab. 6.2, are chosen such that the calibrated thermal power matches the corresponding operating points of the non-premixed flames for comparison purposes. For the non-premixed

Table 6.2: Operating points investigated for the premixed flame configuration. P_{th} denotes the theoretical thermal power setting calculated from the supplied fuel mass flow rate, while P_{calib} is the actual thermal power released by the flame obtained with the calibration procedure.

OP	S	P_{th} [kW]	P_{calib} [kW]	λ	\dot{m}_{mix} [g/s]	\bar{u}_{mix} [m/s]	Re	ζ_{OH}
PPV1	0.6	35.07	30	1.0	13.08	7.96	25377	0.855
PPV2	0.6	41.14	35	1.0	15.34	9.34	29769	0.851
PPV3	0.6	48.76	40	1.0	18.18	11.06	35283	0.820
PPV4	0.6	54.31	45	1.0	20.25	12.32	39299	0.829

type-II flame, technically complete burnout of the supplied fuel can be assumed in moderate swirl conditions [132]. Thus, the burnout correction coefficient can be used to adjust the mass flow rate of the mixture for the premixed flame to match a desired operating point of the non-premixed flame concerning thermal power output. Then, a reliable comparison with respect to spectral amplitudes

and thermo-acoustic efficiency can be made between the premixed and the non-premixed flame.

6.2.2 Influence of Thermal Power

With swirl number and mixture composition held constant, the overall thermal power output of the premixed flame is varied, as burnout efficiency holds nearly constant at stoichiometric mixture conditions over a wide range of power settings. Figure 6.17 shows the obtained sound power spectra corresponding to the operating points given in Tab. 6.2. The given thermal powers denote the calibrated values. The influence of thermal power on the spectra closely follows the

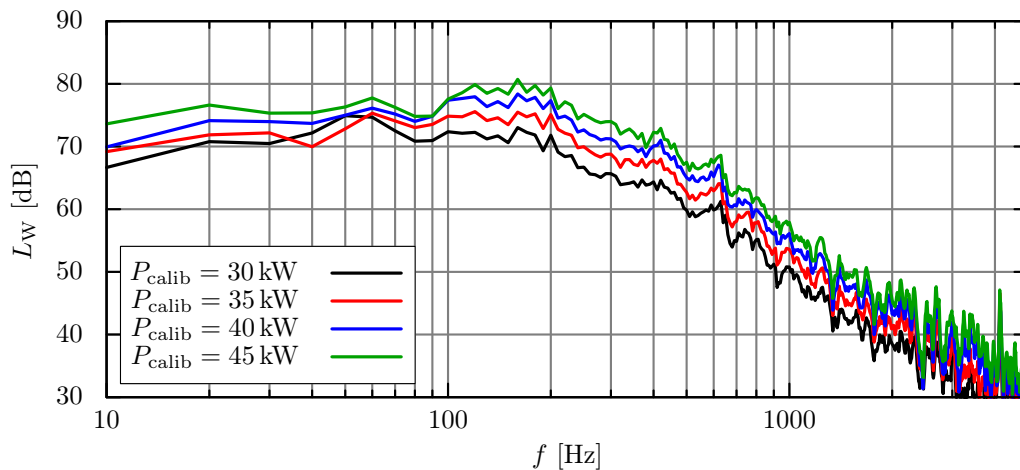


Figure 6.17: Sound power spectra for the turbulent premixed swirl flame at $S = 0.6$, $\lambda = 1.0$.

trend observed with the data of the non-premixed flame. An increase in thermal power output shifts the peak frequency towards higher frequencies and increases the peak spectral amplitude as well. The increasing axial velocity in combination with the increase of the fuel mass flow rate leads to an increase in overall flame volume, which is accompanied by an increase of the turbulence intensity in the reaction zone. Rajaram et al. [105] give a correlation for the acoustic power from premixed flames based on experimental data, which demonstrates the influence of these parameters. The acoustic power of a premixed flame follows the proportionality

$$P_{\text{aco}} \propto f_{\text{peak}}^{2.02} \bar{u}_{\text{ax}}^{-0.32} \cdot (\dot{m}_{\text{f}} H_{\text{u}})^{1.7}, \quad (6.4)$$

where \dot{m}_f denotes the fuel mass flow rate. An increase of thermal power corresponds to an increase of the fuel mass flow rate and the axial velocity, which leads to the observed increase in spectral amplitude. Figure 6.18 shows the effect of increasing power output on the peak-frequency and the efficiency of conversion. Both parameters scale with thermal power output and the smooth curves indicate, that the burnout correction procedure delivers accurate results. The steeper slope of the conversion efficiency is due to the additional effect of increasing flame volume. In general, a larger source will radiate sound more efficiently [25].

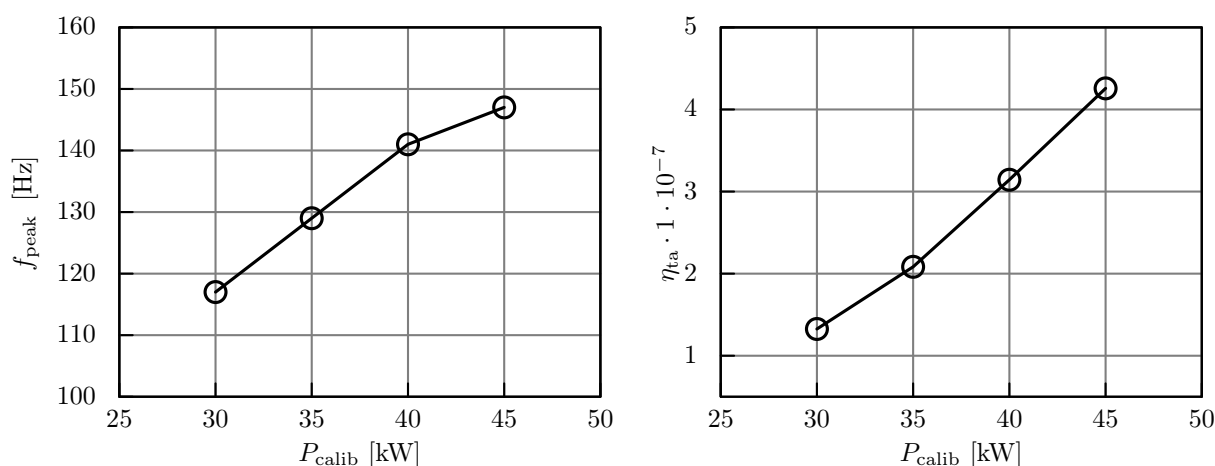


Figure 6.18: Peak frequencies and conversion efficiencies for the turbulent premixed flame at $S = 0.6$, $\lambda = 1.0$ over burnout corrected thermal power.

6.3 Comparison of Conversion Efficiencies Between Premixed and Non-Premixed Flames

For stoichiometric mixture composition, premixed and non-premixed flames show familiarities concerning flame shape and noise radiation. Both types of flames stabilize along the inner shear layer of the swirling annular flow. The main difference between the flame types are the visible jets of high fuel concentration in the vicinity of the injection holes in non-premixed mode. Average images of OH^* intensities are shown for both flame types in Fig. 6.19. The non-premixed flame extends some 30% further downstream compared to the premixed flame, which shows greater intensities in the main combustion region. This difference

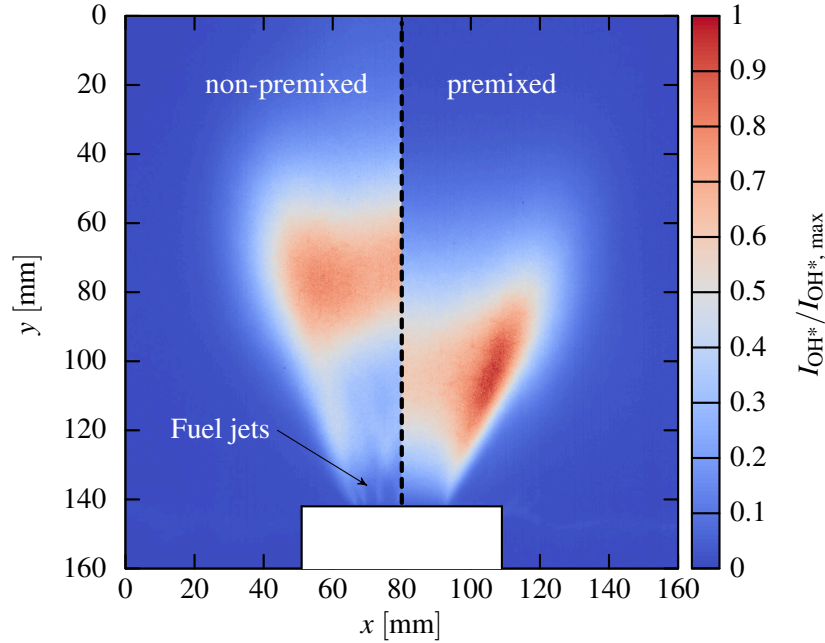


Figure 6.19: Comparison of mean OH* radiation intensity between a non-premixed (left) and premixed (right) swirl flame at $S = 0.8$, $P_{th} = 40\text{kW}$, $\lambda = 1.0$.

in length is partly caused by the difference in fuel burnout, which is nearly complete for the non-premixed flame [132], and around 82% for the premixed flame. The data in Tab. 6.3 allows direct comparison of the parameters determining the shape of the acoustic spectra. Differences in peak frequency are of the order of 20Hz and conversion efficiencies of η_{ta} around $3e^{-7}$ are characteristic for both flame types. The general trend shows slightly higher peak frequencies for the non-premixed flame. This also holds for the conversion efficiency in the

Table 6.3: Comparison of peak frequencies and acoustic conversion efficiencies of premixed and non-premixed flame for burnout corrected thermal power output at $S = 0.6$ and $\lambda = 1.0$.

P_{calib} [kW]	premixed flame		non-premixed flame	
	f_{peak}	η_{ta}	f_{peak}	η_{ta}
30	117	$1.3254e^{-7}$	134	$2.6677e^{-7}$
35	129	$2.0829e^{-7}$	151	$3.4852e^{-7}$
40	141	$3.1441e^{-7}$	165	$4.3683e^{-7}$
45	147	$4.2570e^{-7}$	174	$5.0899e^{-7}$

whole range of the investigated power settings. An explanation for these slight differences can be found by analyzing the turbulent conditions in both cases. In non-premixed configuration, fuel enters the reaction zone through the 16 fuel injection holes at an angle of 45° towards the burner axis, creating a more turbulent inner shear layer with smaller turbulent time and length scales. In particular, the turbulent length scale of the fuel jets is of the order of the hole radius, which takes effect on the turbulent spectrum shape and leads to higher frequency content of the noise emitted from the region close to the burner exit. However, the major portion of the reaction zone is located outside this zone in both cases, so that the overall impact is small.

Figure 6.20 shows a comparison of sound spectra recorded from a premixed and non-premixed flame. The thermal power output of the premixed flame has been scaled using the burnout correction coefficient. The scaling results in an increase of the fresh gas flow for a desired true thermal power output P_{calib} . In order to achieve comparability between e.g. the 45 kW premixed and non-premixed flames, the theoretical thermal power setting of the premixed flame needs to be increased to $P_{\text{th}} = 54.13 \text{ kW}$ in order to achieve a true thermal power of $P_{\text{calib}} = 45 \text{ kW}$. This adjustment results in the increase of the mean axial velocity in the burner nozzle from $\bar{u}_{\text{ax, th}} = 9.68 \text{ m/s}$ to $\bar{u}_{\text{ax, calib}} = 11.68 \text{ m/s}$, which corresponds to an increase of the nozzle Reynolds number from $\text{Re} = 32325$ to $\text{Re} = 39045$.

In order to maintain flow similarity, the non-premixed flame global air excess ratio is then adjusted to match the nozzle Reynolds number of the premixed case. This procedure leads to locally similar conditions concerning turbulent and chemical time scales within both flame types, as the local non-premixed flame is concentrated around the iso-surface of stoichiometric mixture $z = z_{\text{st}}$ [138], which is unaffected by the global mixture composition. The Reynolds scaling results in a global air excess ratio of $\lambda = 1.27$ for the non-premixed case of $P_{\text{th}} = 45 \text{ kW}$. Table 6.4 summarizes the parameters necessary for the equalization of thermal power and Reynolds number for two different power settings of premixed and non-premixed configuration. The acoustic power spectra recorded from both cases for $P_{\text{th}} = 45 \text{ kW}$ are shown in Fig. 6.20 and are in close proximity concerning spectral shape, amplitude and peak frequency. This suggests, that premixed and non-premixed flames emit sound of similar amplitude and spectral

shape if the operating conditions are selected such that turbulence and mixture properties in the main reaction zone are similar. However, this direct comparison is limited to near stoichiometric mixtures, as locally lean mixtures cannot be achieved for non-premixed flames and thus, comparability with premixed flames is not given for lean mixtures.

Table 6.4: Operating conditions selected for the direct comparison of premixed and non-premixed combustion noise spectra. The burnout correction of the premixed flame results in a higher nozzle Reynolds number, which is matched for the corresponding non-premixed flame by adjusting the global air excess ratio.

P_{calib} [kW]	premixed flame			non-premixed flame	
	P_{th}	ζ_{OH}	λ	λ	Re
35	41.14	0.851	1.0	1.12	29769
45	54.31	0.829	1.0	1.27	39299

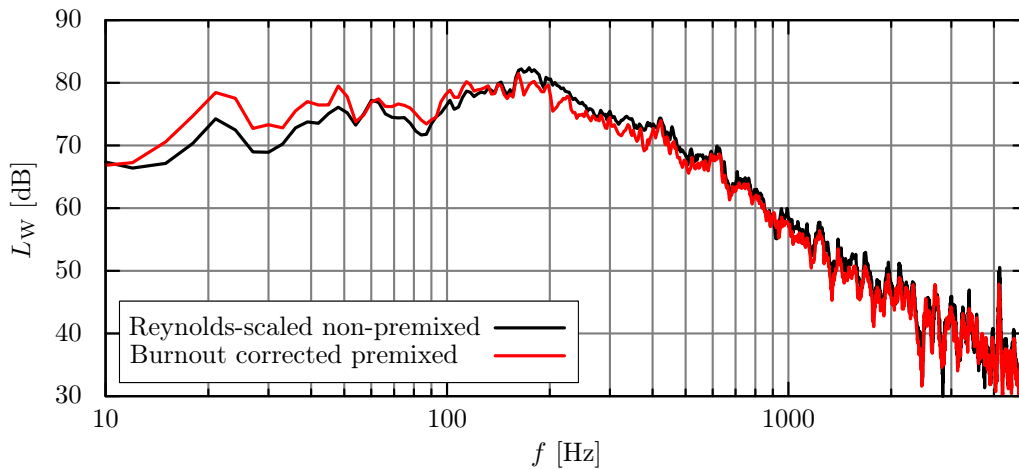


Figure 6.20: Comparison between sound power spectra of Reynolds scaled non-premixed flame and burnout corrected premixed flame for $P_{\text{calib}} = 45$ kW. The resulting spectra from both flames show close proximity.

7 Prediction of Spectral Noise Emission from Turbulent Natural Gas Swirl Flames

For validation purposes, predictions obtained with the extended combustion noise model introduced in Sec. 4.3 are compared to experimental data recorded from the open swirl flame (Chap. 6). Numerical domain models are assembled for the premixed and non-premixed flame case. With these models, input data fields are computed using CFD. The resulting variable fields are extracted from the CFD solution. Necessary data fields are organized into data vectors and are consecutively processed by the combustion noise model routines. The predicted frequency spectra of acoustic power are then compared to their experimental counterpart of matching flame operating conditions.

First, the modified amplitude scaling function is compared to the initial formulation based on the Schmid combustion model. The comparison is done for the open premixed flame, where the equivalency of both model formulations is demonstrated. Then the modified model is applied to the non-premixed flame, where the influence of thermal power, mixture composition and swirl intensity on the quality of the model predictions is analyzed.

7.1 Calculation Cycle of Combustion Noise Prediction for Premixed and Non-Premixed Cases

Premixed and non-premixed cases are evaluated using different numerical procedures as shown in Fig. 7.1. Based on the existing post-processing routines comprising the premixed flame combustion noise model of Hirsch et al. [52,53], a user define function (UDF) was developed for ANSYS Fluent. This function includes a routine for the calculation of clipped Gaussian PDF parameters, an

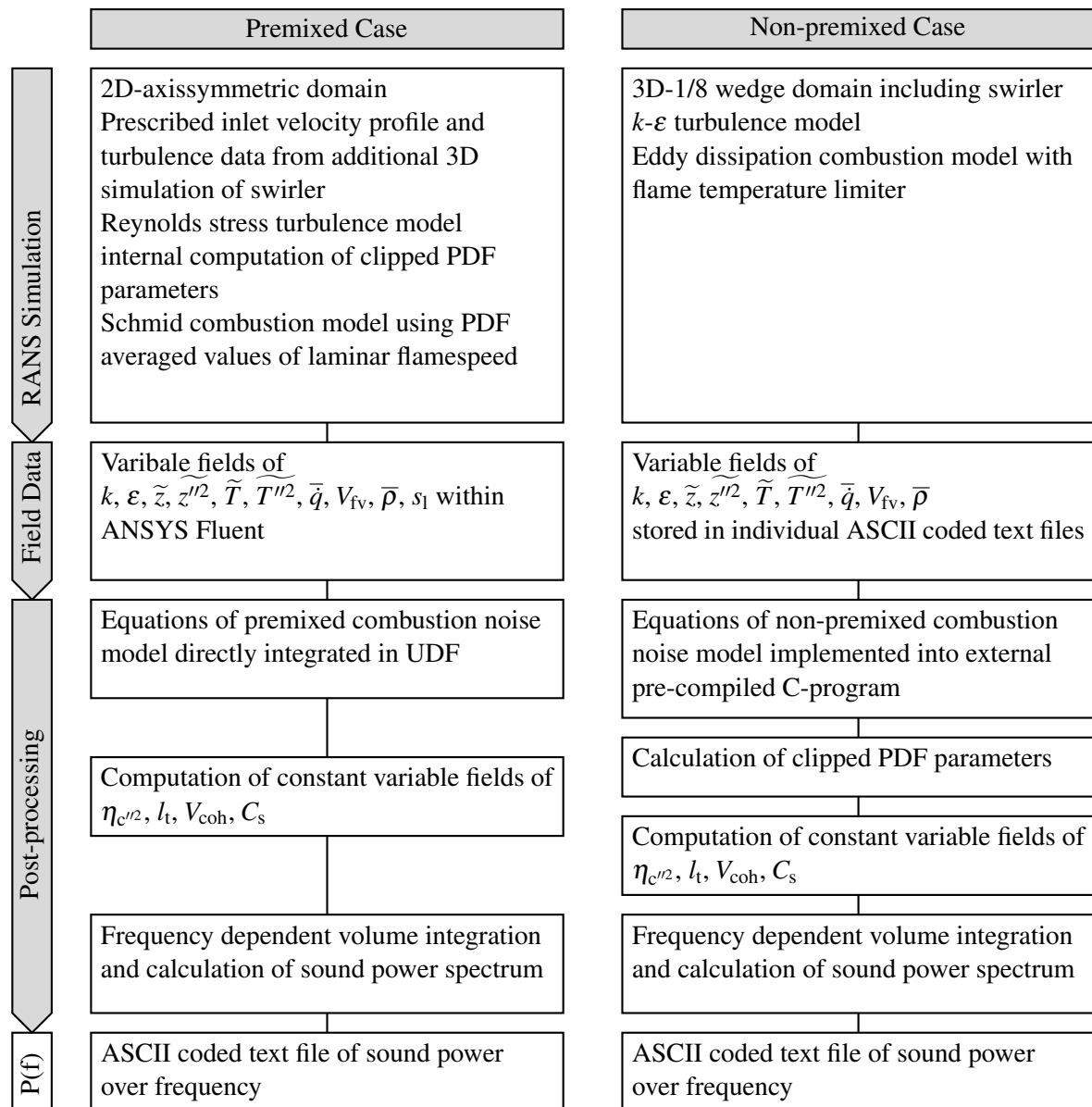


Figure 7.1: Schematic of the noise calculation for the premixed and the non-premixed case. The post-processing toolbox for the non-premixed case is explicitly developed for large amounts of input data.

implementation of the Schmid combustion model using PDF averaged values of the local laminar flamespeed, and the generalized calculation method for the amplitude scaling function. The frequency dependent routines of the combustion noise model were implemented into a separate routine which can be called at the end of each simulation run.

For the non-premixed combustion noise model, the routines for PDF-calculation as well as the generalized amplitude scaling along with the model equations for the non-premixed case (cf. Sec. 4.3) were cast into a standalone C-application. Data transfer between the CFD software and the post processor application is performed through simple ASCII data files for each variable needed for the combustion noise model. The standalone programming allows the independent and computationally efficient calculation of combustion noise spectra for large amounts of input data. For a typical 600000 element mesh, the resulting combustion noise spectrum can be calculated within three minutes on a standard quadcore desktop PC with 8 gigabytes of memory. An equivalent Matlab routine which was implemented in the course of algorithm development ran for 6 hours 20 minutes to process the same input data, which is non-practical for case studies. The initial premixed flame tool was used as a testbed for the generalized method to calculate the amplitude scaling function, which is in this form applicable to both, premixed and non-premixed combustion. The standalone implementation of the post-processor is independent from the CFD simulation. As a special requirement, the CFD solution must deliver field data for the variances of temperature and mixture fraction. This additional data can be retrieved from the solution of corresponding transport equations or algebraic expressions [45].

7.2 Premixed Flame Simulation

The premixed case is studied for the purpose of direct comparison between the premixed model amplitude scaling and the generalized scaling introduced in Sec. 4.3.3. Also, the validity of the burnout correction factor determined by the method described in Sec. 6.2.1 is analyzed numerically. The absence of the non-symmetric fuel distribution holes allows a simplified two-dimensional domain

model of the axis-symmetric premixed flame in order to reduce computation time. Turbulence is modeled using a Reynolds stress model (RSM) and premixed combustion is calculated using the extended Schmid combustion model described in Sec. 2.3.3 based on a mixture fraction and reaction progress approach of mixture description [86].

7.2.1 CFD-Results

Figure 7.2a shows a sketch of the two-dimensional fluid domain used in the premixed flame simulations and a section of the block structured computational grid in the vicinity of the burner nozzle. The farfield boundaries are set at distances of $7D$ in radial direction and $10D$ in axial direction from the burner nozzle. The domain is discretized using a structured grid of approximately 10000 rectangle elements. Profiles of axial, radial and tangential velocity along with turbulent

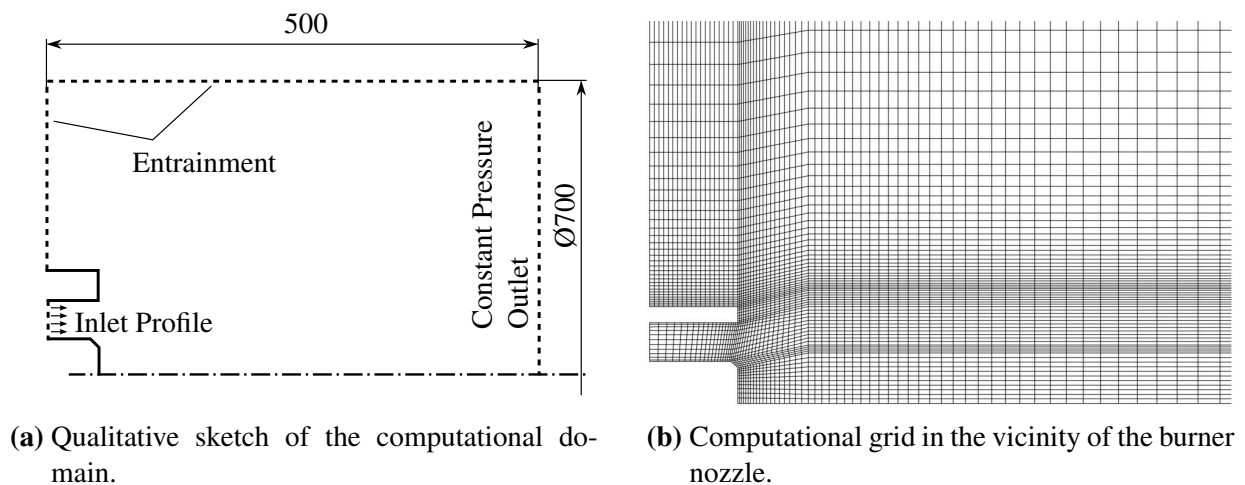


Figure 7.2: Two-dimensional domain setup and computational grid for the premixed flame simulations.

length and velocity scales are taken from simulation results of the three dimensional flow simulation through the swirl generator on an unstructured computational grid for each operating point considered. The variable profiles are imposed as inlet conditions for the 2D axis-symmetric combustion simulation.

Entrainment is modeled in the simulation model by setting an appropriate constant inlet velocity along the entrainment boundary [53]. The velocity can be

estimated considering the experimental data given by Pham et al. [99] for the entrainment coefficient of thermal plumes, and typically is of the order of centimeters per second, depending on the distance of the farfield boundary to the burner nozzle. However, Hirsch et al. [53] mention that the entrainment velocity may be varied within a large margin without affecting the predicted rate of heat release. The qualitative flame shape calculated from CFD can be compared to deconvoluted chemiluminescence images. OH^* intensity and local rate of heat release are both normalized with their peak values and shown in direct comparison in Fig. 7.3. The OH^* intensity does not give precise information about the actual density of heat release and its spatially resolved distribution as demonstrated by Lauer [72]. This limits the comparison to qualitative geometric parameters. The comparison of characteristic features, such as flame length and opening angle shows good agreement between experiment and simulation. In particular, the influence of swirl on the flame geometry is predicted well through the opening angle of the flame, indicating that the employed turbulence and reaction models are suitable for this case.

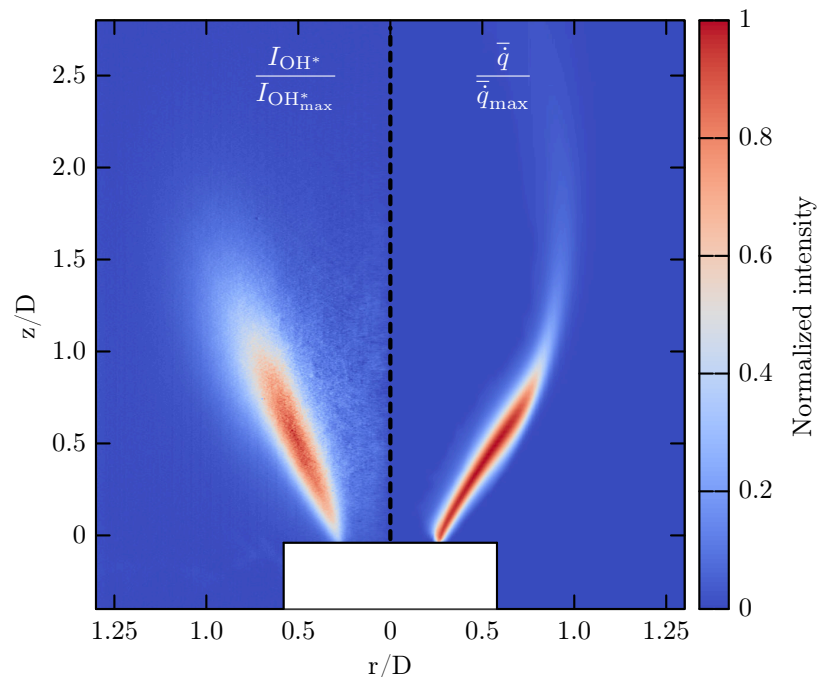


Figure 7.3: Qualitative comparison of flame shape between normalized heat release rate from CFD (right) and normalized OH^* intensity from experiment (left). The flame is operated at $P_{\text{th}} = 40\text{kW}$, $S = 0.8$ and $\lambda = 1.0$.

The burnout correction method introduced in Sec. 6.2.1 can be compared to CFD data for fuel burnout for the corresponding cases. In CFD, the local rate of heat release is known from the field data of the solution and can be used to calculate the overall heat released by the flame by a simple summation over the field resolved heat release. The corresponding burnout fraction ζ_{CFD} is then given by

$$\zeta_{\text{CFD}} = \frac{P_{\text{th, CFD}}}{P_{\text{tot, CFD}}}, \quad (7.1)$$

where

$$P_{\text{tot, CFD}} = \sum_{k=1}^n \bar{q}_{v, k}. \quad (7.2)$$

Table 7.1 shows the comparison between experimentally determined burnout correction coefficients and the corresponding values calculated from CFD for a set of four operating points of the premixed flame. Excellent agreement is

Table 7.1: Comparison between burnout efficiencies determined from experimental data (ζ_{OH}) and calculated from CFD (ζ_{CFD}) showing good agreement between experiment and simulation.

OP	P_{th} [kW]	P_{calib} [kW]	P_{CFD} [kW]	ζ_{CFD}	ζ_{OH}	Re
PPV1	35.07	30	31.11	0.887	0.855	25377
PPV2	41.14	35	35.57	0.865	0.851	29769
PPV3	48.76	40	41.16	0.844	0.820	35283
PPV4	54.31	45	45.36	0.835	0.829	39299

achieved between experiment and numerical prediction for the burnout ratio, with deviations of 3% or less. This encouraging result can be explained by the fact, that fuel burnout of open premixed swirl flames is primarily governed by entrainment and the resulting extinction of the outer shear layer. Depending on the swirl intensity of the flow, a certain fraction of the mixture supplied through the burner nozzle passes the reaction zone before the necessary mixing with hot combustion products occurs. Downstream of the nozzle, entrained ambient air continuously dilutes the initial mixture, foreclosing the reaction of the outer shear layer when mixing with hot combustion products further downstream. The process of mixing between fresh gas and hot combustion products is modeled by the gradient of reaction progress in the combustion model used for the premixed case. Fresh gas traveling along a streamline outward of a certain radius does not

meet non-zero values of the reaction progress and consequently, leaves the domain in its initial unburnt state. Thus, fuel burnout for the open premixed flame considered in this study is mainly governed by flow parameters, which explains the encouraging match between experiment and simulation.

The increasing influence of entrainment along the flow axis is demonstrated by considering the unburnt air excess ratio as calculated from CFD. Figure 7.4 shows the effect of entrainment in the range of $\lambda = 1 - 7$. The entrainment is enhanced with the flow swirl number. Consequently, at greater swirl intensities lower percentages of fuel burnout are observed in the experiments, reaching order of magnitude values of 50% for leaner mixtures. This illustrates the need to account for fuel burnout from open premixed flames when comparing experimental data to computed combustion noise spectra. The good agreement between numerical and experimental parameter values for ζ at different operating condi-

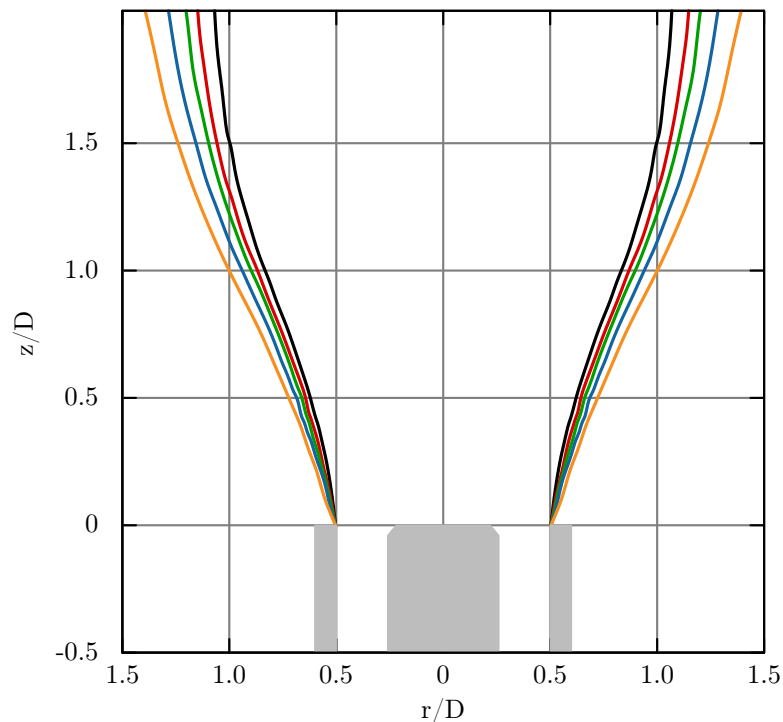


Figure 7.4: Effect of entrainment on the unburnt air excess ratio λ_{ub} for the operating point PPV4. (—): $\lambda = 1.00$, (—): $\lambda = 1.75$, (—): $\lambda = 2.50$, (—): $\lambda = 4.10$, (—): $\lambda = 7.00$

tions validates this approach to determine the fuel burnout efficiency of open premixed flames.

7.2.2 Acoustic Results

Sound power spectra are computed using the premixed combustion noise model in its form as presented in [53] in order to validate the implementation of the model equations. The comparison with corresponding experimental data is performed for an air excess ratio of $\lambda = 1.0$, swirl number of $S = 0.6$ and different thermal powers as the burnout efficiency is best for stoichiometric mixtures. At leaner mixtures or greater swirl intensities, the range of stable flame operating points becomes is narrowed down.

Influence of Thermal Power

Figure 7.5 shows the comparison between the numerical results calculated using the premixed combustion noise model and experimentally recorded spectra for the operating points PPV1, PPV3 and PPV4. The general trend visible in the experimental data is reproduced by the numerical model. Decay and high

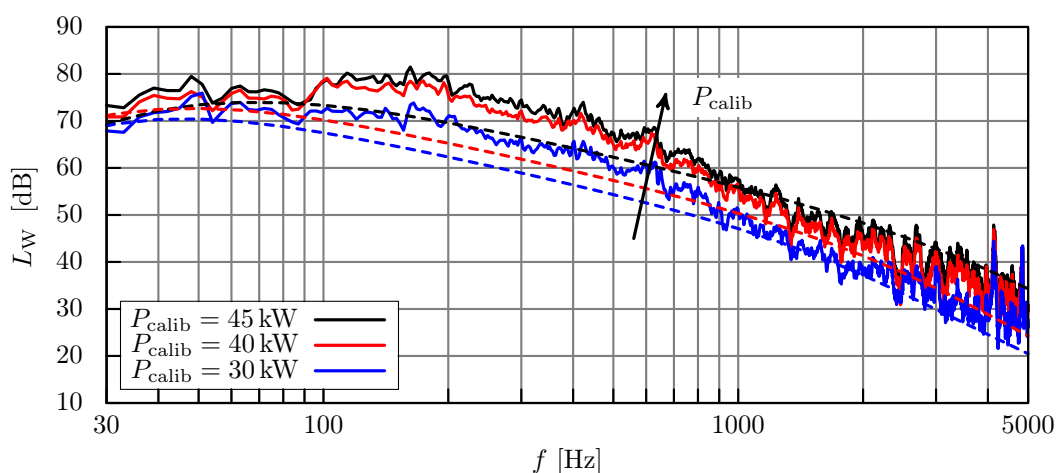


Figure 7.5: Model predictions obtained for the premixed operating points of 30kW (PPV1), 40kW (PPV3) and 45kW (PPV4) thermal power at $\lambda = 1.0$. Continuous lines mark experimental data, dashed lines show the numerical results.

frequency cutoff are captured for all three cases. Quantitatively, the frequency of peak emission, which varies between 90 Hz – 135 Hz is underestimated by around 50 Hz, which can be attributed to the computation of the turbulent length scale from CFD data. Lutz et al. describe the determination of integral length scales through CFD in the course of calculating aero-acoustic noise from wind turbine blades [81]. Similar to the combustion noise modeling, a model spectrum is used in their aero-acoustic calculation. The model spectrum depends strongly on the calculation of the integral length scale. Lutz et al. use a modeling constant to relate the ratio of turbulence kinetic energy and dissipation rate predicted by CFD to the experimentally measured data

$$l_t = c_1 \cdot \frac{k^{\frac{3}{2}}}{\varepsilon}, \quad (7.3)$$

where $c_1 = 0.387$. In most CFD simulations, as well as in the premixed combustion noise model, $c_1 = 1.0$ [52, 53, 146]. The calculated parameter value for the turbulent length scale directly enters the transformation function between wave-number and frequency in the combustion noise model, and determines the location of the maximum spectral amplitude. Turbulence kinetic energy and dissipation rate are calculated from corresponding transport equations or algebraic expressions, depending on the selection of the turbulence model in CFD. Consequently, the selection of the turbulence model used for the CFD simulation of the input data fields influences the calculated combustion noise spectra.

Equivalence of Schmid-Model Based and PDF-Based Amplitude Scaling

The generalized amplitude scaling function proposed in Sec. 4.3.3 is universal in its applicability to both, non-premixed and premixed flames. Consequently, the validity of the proposed scaling function can be proven by comparing the results calculated using the initial amplitude scaling function based on the Schmid combustion model with those computed using the generalized model formulation. Figure 7.6 compares the model solution for PPV4 calculated using both formulations of the amplitude scaling. Considering the differences in evaluating Eq. (4.11) and Eq. (4.44), the similarity between both solutions is close, outlining the theoretical equivalence of both approaches. The PDF-based scaling

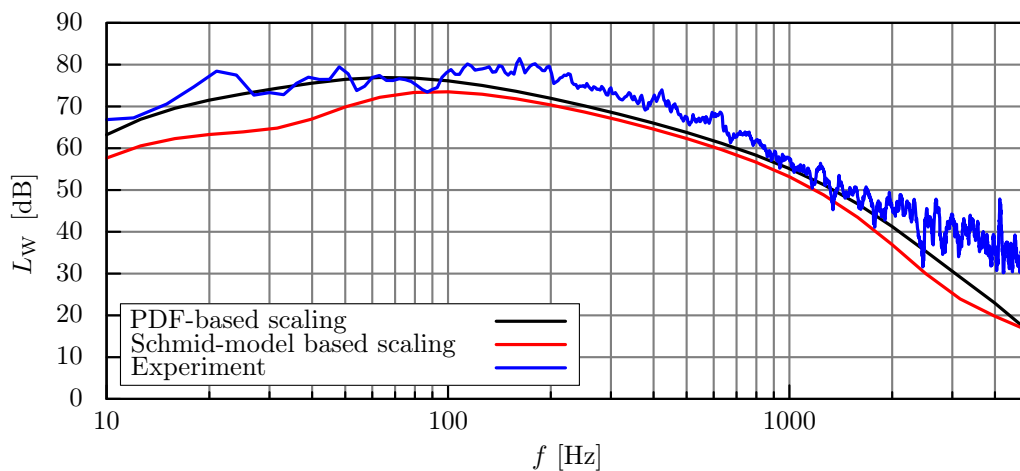


Figure 7.6: Comparison of spectra calculated from identical input data with the original amplitude scaling and the PDF-based function.

is computed from quantities which are obtained from the solution of additional transport equations for the variances of mixture fraction and temperature. Both scaling functions lead to the same qualitative shape of the calculated spectra over the complete frequency range covered. Differences in the range of 5 dB in amplitude occur in the low frequency range below 100 Hz and in the high frequency regime above 2000 Hz, where the PDF-based scaling gives slight improvements in the prediction of the spectral amplitude. In the spectral range that can be attributed to the inertial subrange of the model spectrum, both approaches show equivalent results. Consequently, Eq. (4.44) can be used as a generalized amplitude scaling function to account for the effect of finite rate chemistry on the spectrum of heat release independent of the flame type under investigation.

Influence of Turbulence Modeling on the Calculated Noise Spectra

The prediction of combustion noise spectra using the presented model approach primarily relies on the parameter values of turbulent kinetic energy and dissipation rate extracted from the initial RANS simulation. These variables are highly dependent on the selected turbulence model. Their influence on the resulting spectrum is twofold: Indirectly, the calculated noise spectrum is affected through the rate of heat release (most combustion models rely on ratios of k and ε for the modeling of the chemical reaction rate). Directly, this ratio affects the transfor-

mation function between frequency and wave-number as well as the computed integral length scale and thus, the volume of the coherent volumes. Consequently, the turbulent variables and thus, the choice of the turbulence model for the initial RANS simulation is a crucial step in the noise modeling procedure and may affect the validity of the calculated spectra.

Five turbulence models frequently used in technical application CFD were investigated regarding their influence on the predicted noise spectra. The resulting spectra for PPV4 are shown in Fig. 7.7. The results show a spread over 10dB in amplitude for the turbulence models including a transport equation for the dissipation rate. The k - ω -SST model, which is based on a transport equation for the characteristic eddy frequency ω close to wall boundaries results in a spectrum departing fundamentally from the other solutions. The differences can be attributed directly to the differences in the underlying transport equations for the turbulence variables.

This comparison outlines the impact of the turbulence variables in the RANS solution on the calculated spectrum of combustion noise. The chosen combination of turbulence and combustion model in the initial CFD simulations governs the predictions for the combustion noise spectra. As a consequence, a direct comparison between solutions obtained for cases using different turbulence models can solely be a qualitative comparison, whilst parameter studies should be performed

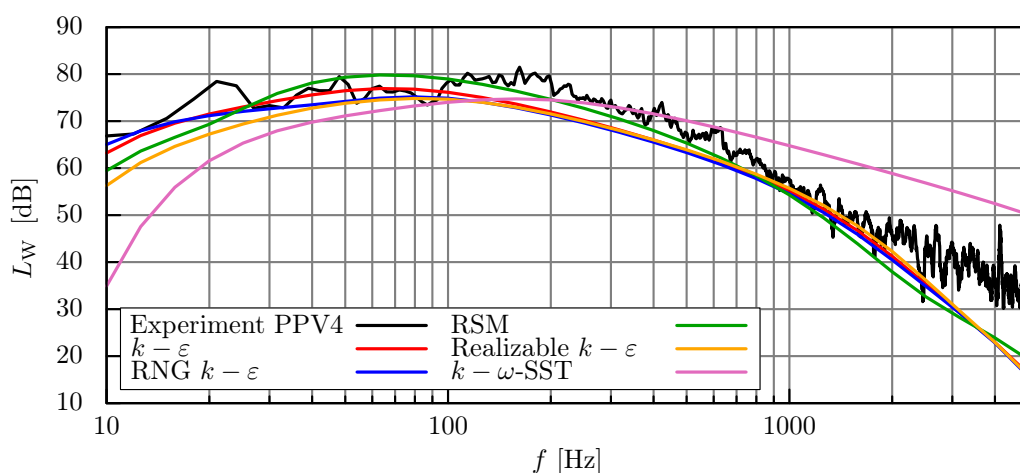


Figure 7.7: Influence of the choice of the turbulence model in CFD on the resulting acoustic power spectrum calculated for PPV4.

using matching model settings. Furthermore, the quality of results obtained using different turbulence models, depending on the flow geometry and operating conditions of the case under investigation should be monitored by comparison with experimental data, as turbulence models are variably suitable for different fundamental problems depending on their model structure [148].

A possible improvement could be introduced by using LES or PIV for the determination of the integral length scale. As shown by Ni et al. [93], good agreement is observed between experimental data and LES predictions. The parameter value of the constant in the calculation of the integral length scale Eq. (7.3) could be determined using LES by comparing the RANS prediction with the LES or experimental data for a specific flame case and combination of RANS turbulence and combustion model.

7.3 Non-Premixed Flame Simulation

The type-II non-premixed flame (cf. Sec. 5.2) is modeled on a three dimensional axis-symmetric computational grid in order to spatially resolve the non axis-symmetric region around the fuel entry holes in the center body. The swirl generator is integrated into the three dimensional domain model as well.

Operating points investigated in the experimental campaign are reproduced in the simulation to allow direct comparison between the spectral results of the proposed non-premixed model for combustion noise and experimentally determined spectra. The influences of swirl intensity, thermal power and mixture composition on the predictive performance of the model are analyzed.

7.3.1 CFD-Results

The three dimensional domain model in the non-premixed case allows the direct inclusion of the flow through the swirler into the computational model. The smallest symmetrical unit including all geometric features of nozzle and swirler is a wedge of 45° opening angle, representing $1/8$ of the full geometry. This ge-

ometry representation together with the imposed boundary conditions is shown in Fig. 7.8. The computational domain extends spherically around the burner nozzle towards a farfield boundary at a radius of $r = 0.5$ m. The farfield boundary is composed of a pressure inlet, taking up the major fraction of the boundary surface on the bottom side, and a smaller pressure outlet at the top. Both boundaries permit flow into and outside of the domain, allowing entrainment mass flow to attune itself to the current flow condition imposed by the flame. A key element of the non-premixed domain is given by the fuel injection holes of 1.3 mm in diameter. In the area around the hole openings, the mesh resolution must be chosen such that the small scale geometry is discretized appropriately. The effect of the element size around the burner nozzle was investigated in a numerical grid study by increasing the mesh resolution from a coarse grid of 100000 hexahedral elements towards a fine grid of 900000 elements in 5 steps. Computed velocities and gradients of selected variables converged towards constant profiles at a res-

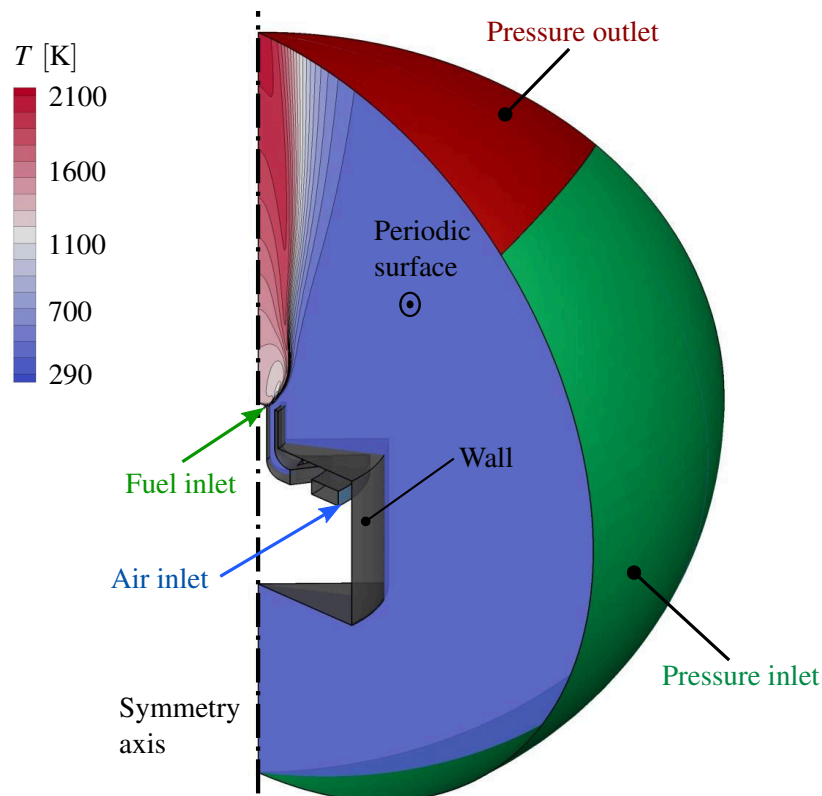


Figure 7.8: Computational 3D domain used in the flow field simulation for the non-premixed flame configuration. The contour levels show fluid temperature for the DSV6 case.

olution of 630000 mesh elements, which was then selected for the combustion noise study.

This final mesh is a block-structured grid of 158 blocks and a total of 630000 hexahedral elements. A detailed view of the computational grid near the fuel injection holes is shown in Fig. 7.9. The interior of the holes is discretized using 8 elements over the hole diameter with a cosine size distribution to refine the resolution of the shear layer at the hole exits. Elements emerging from the tapered surface of the central body are inclined against the vertical axis to improve orthogonality of the mesh near the injection holes. The chemical source

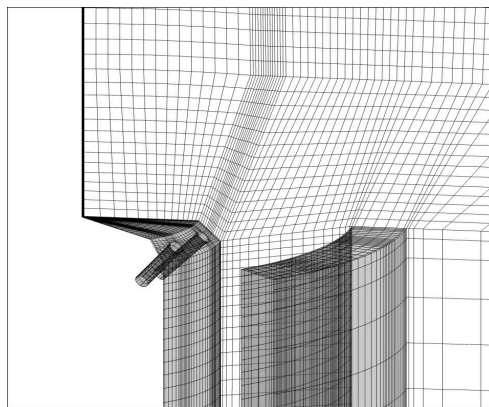


Figure 7.9: Detail view of the computational grid in the vicinity of the burner nozzle.

term is modeled using a 1-step global reaction where the turbulent reaction rate is modeled using the eddy-dissipation model introduced in Sec. 2.3.3. Turbulence is modeled using the standard $k-\varepsilon$ turbulence model to allow the computationally efficient treatment of large numbers of operating points as given in Tab. 6.1. For moderate swirl numbers as investigated in this thesis, the $k-\varepsilon$ model shows to predict the swirl number of movable block type burners with good accuracy [43, 121].

Hillemanns [50] presents a comprehensive experimental parameter study on flow parameters of an equivalent scaled-up movable block burner for swirl numbers of 0.8 and 1.5. The data is used to analyze the performance of the selected turbulence model in terms of the axial flow velocity profile in the burner exit plane. The experimental velocity data is scaled accordingly to preserve the flow Reynolds number, thus limiting the comparison to cold flow data. For the

comparison, a cold flow simulation is performed at $S = 0.8$. Matching the flow Reynolds number of $Re = 163000$ given by Hillemanns, the mean axial nozzle velocity settles at $\bar{u}_{ax} = 49.7$ m/s. A comparison between results for axial flow velocity obtained with the $k-\varepsilon$ -model on the structured grid of this study and the experimental data of Hillemanns is shown in Fig. 7.10 in the burner exit plane. Considering the complexity of the geometry in the vicinity of the nozzle and the

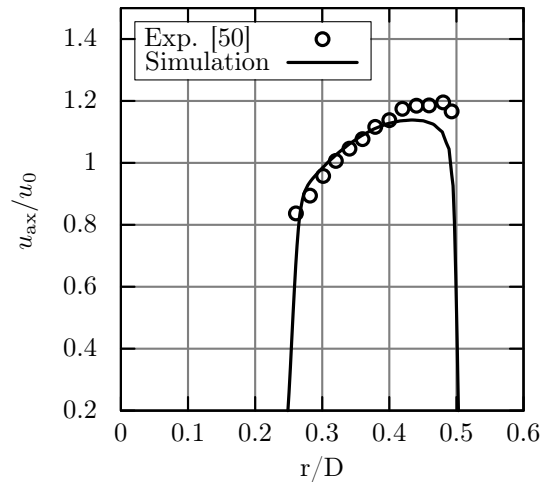


Figure 7.10: Comparison of axial velocity between experimental data given by Hillemanns [50] and numerical results using the $k-\varepsilon$ -model in the burner exit plane for cold flow conditions at $Re = 163000$.

swirling configuration the agreement in axial velocity is good, which indicates that the mesh resolution and topology in conjunction with the turbulence model are suitable for the problem.

Exemplary for the case studies performed for variations in thermal power, air excess ratio, and swirl, reactive CFD results are shown in the following for the air excess ratio variation study. Figure 7.11 shows contours of temperature in the center plane together with vectors of tangential velocity. With increasing air excess ratio, the length of the recirculation zone is increasing and the flame close to the center body is cooled down by the increasing stream of combustion air through the burner nozzle. Figure 7.12 shows the source term of consumption of CH_4 for the three different air excess ratios together with the iso-line of stoichiometric mixture. At higher air excess ratios, the surface of stoichiometric mixture

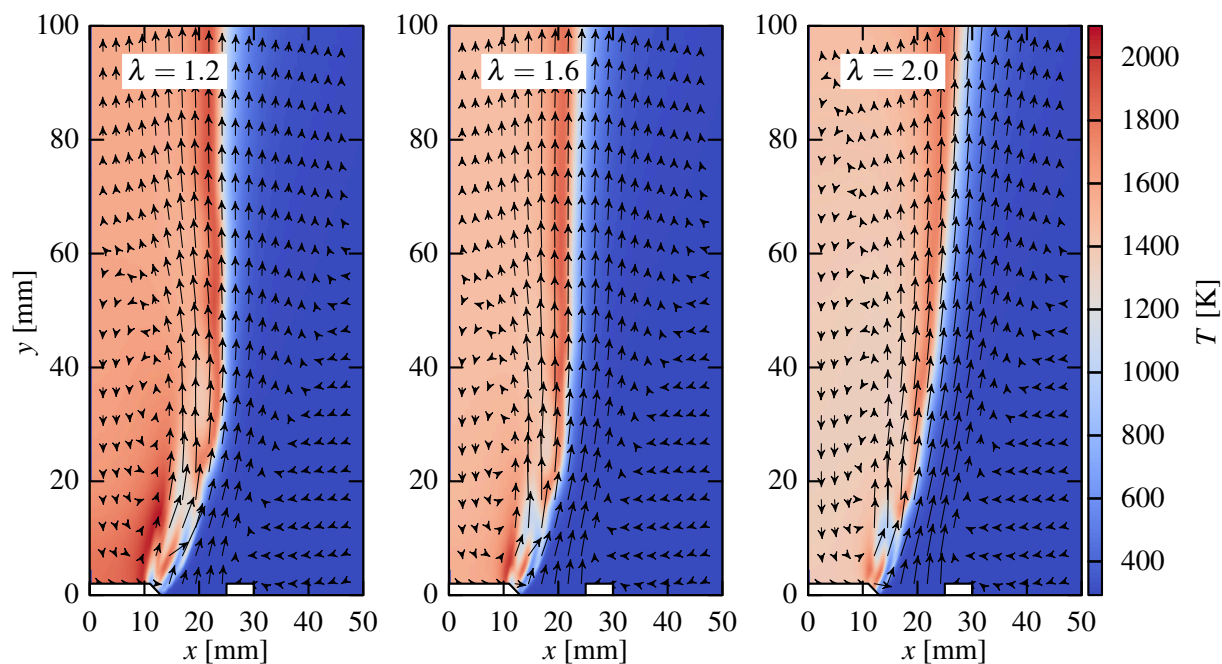


Figure 7.11: Contours of temperature for three different air excess ratios at $P_{\text{th}} = 50 \text{ kW}$, $S = 0.6$. Velocity vectors indicate the tangential velocity in the section plane.

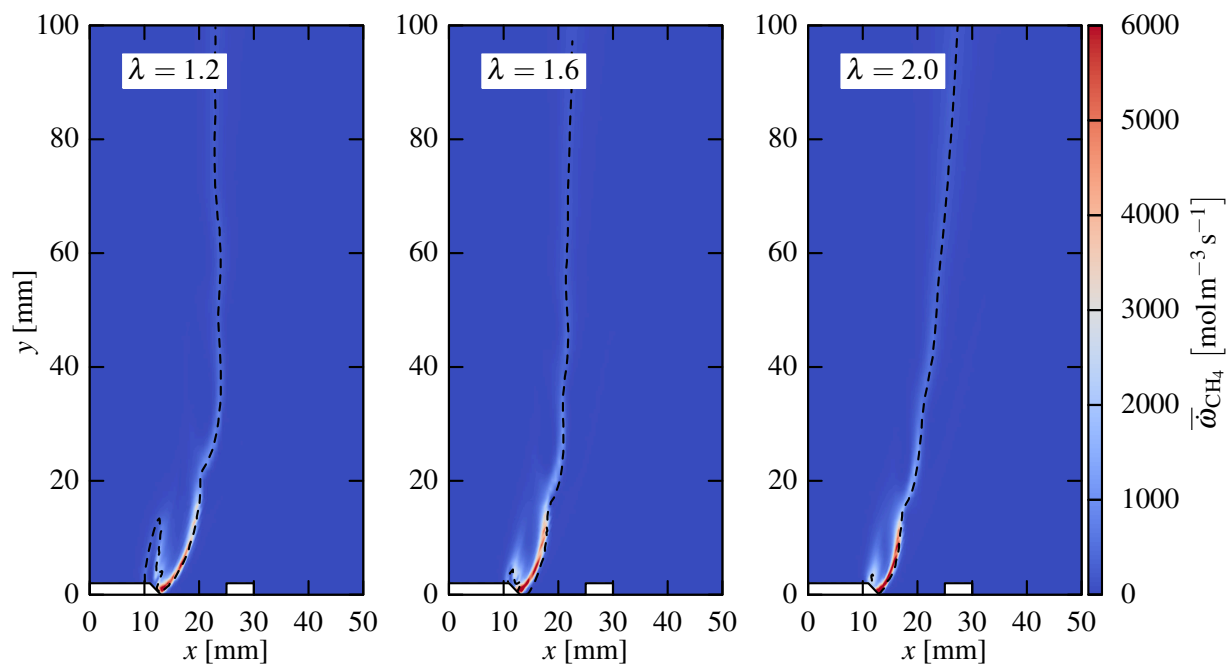


Figure 7.12: Contours of reaction source term for three different air excess ratios at $P_{\text{th}} = 50 \text{ kW}$, $S = 0.6$. The dashed line indicates the line of stoichiometric mixture, $z = z_{\text{st}}$.

fraction is shifted outward following the radial pressure gradient and increasing the overall flame volume.

7.3.2 Acoustic Results

Spectra of radiated acoustic power are computed from the mean field data of the preceding CFD simulations using the extended non-premixed combustion noise model. The exported data fields¹ are run through the post processor which calculates the PDF-parameters for the amplitude scaling function and performs the volume integration. The constants in the equations for the calculation of turbulent time and length scale (Eq. (4.30)) from the CFD solution data, which need to be defined are determined by requiring that the simplified set of model equations discussed in Sec. 4.4 predicts the correct peak frequency for the reference case of $S = 0.6$, $P_{th} = 50\text{kW}$ and $\lambda = 1.2$ based on volume averaged quantities of the input variables extracted from the corresponding CFD solution. The turbulent time and length scale entering the non-premixed combustion noise model are computed from

$$\tau_t = c_\tau \cdot \frac{k}{\varepsilon}, \quad l_t = c_l \cdot \frac{1}{|\nabla \bar{z}|}, \quad (7.4)$$

with the constants $c_\tau = 0.287$ and $c_l = 1.400$. These constants apply to all non-premixed cases investigated in the course of this study and are suitable for the specific combination of k - ε turbulence model and the eddy-dissipation combustion model. The extended model prediction obtained with the determined parameters is evaluated for variations in thermal power, mixture composition and swirl intensity.

¹ Data is exported only from cells that predict non-zero rate of reaction as only these regions contribute to the noise source.

Spatially Resolved Peak Frequency

The derived approach presented in Sec. 4.4 allows the direct calculation of the local frequency of peak emission through an algebraic expression. The expression can be evaluated locally, to directly give

$$f_{\text{peak}}(\vec{x}) = c_{\phi} \cdot \frac{\varepsilon(\vec{x})}{k(\vec{x})}, \quad (7.5)$$

or radially averaged to obtain an axial profile of the emitted peak frequencies. With the spatial data, flame regions can be distinguished regarding the frequency content which is locally contributed to the overall noise spectrum. Also the effect of measures influencing this frequency content can be analyzed directly from CFD results. Figure 7.13 shows the effect of a change in thermal power on the spatial distribution and the range of the locally emitted peak-frequencies. Qualitative analysis of the spatial frequency distribution shows high frequency signal content being emitted in the mixing zone near the fuel jets, where the turbulent

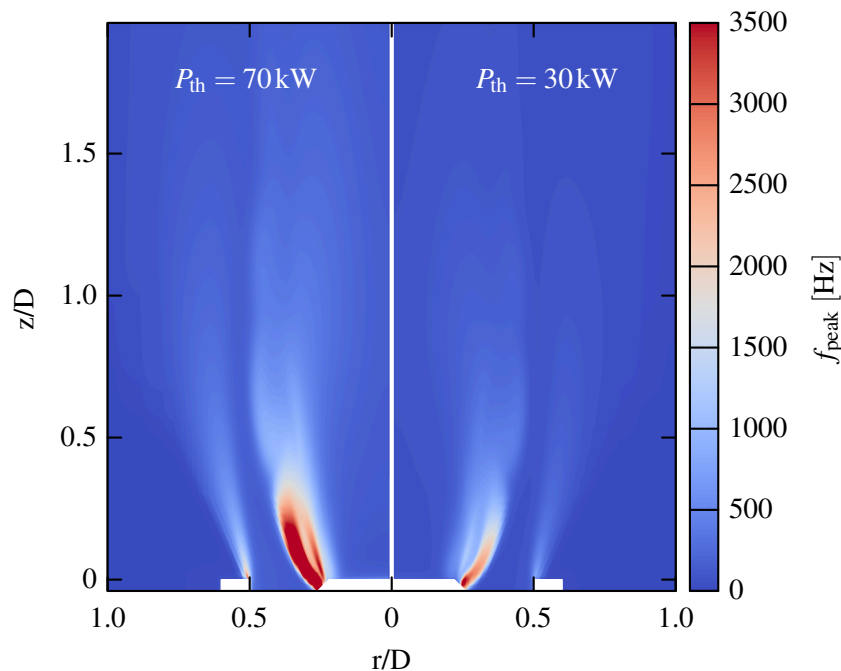


Figure 7.13: Computed local peak frequency of the emitted noise for the 30kW and 70kW non-premixed flame at $\lambda = 1.2$ and $S = 0.6$. Non-zero values of the peak frequency are given for non-zero values of the local heat release only.

length scales are small and the corresponding eddy frequencies are high. The remaining flame zone is dominated by regions of $f_{\text{peak}} < 1000\text{Hz}$, which is in agreement with the observed frequency range for turbulent hydrocarbon flames. The overall frequency content of the flame noise signal cannot be retrieved from this kind of analysis, however, the most favorable location for the major part of heat release to occur can be retrieved if a frequency shift in the overall flame noise spectrum is desired.

Influence of Thermal Power

The power variation evaluates the model capabilities concerning the replication of trends obtained in the experimental campaign at constant swirl and constant air excess ratio when altering the thermal power output of the flame. Experimentally recorded sound power spectra at three operating points are compared to the corresponding model output computed with the non-premixed noise model. The operating points comprise the complete range of thermal powers that were investigated in the experimental campaign and are summarized in their main characteristics in Tab. 7.2. Simulation results are shown in Fig. 7.14 together with the corresponding experimental spectrum data.

Table 7.2: Operating points for different thermal power settings simulated with the non-premixed combustion noise model.

OP	S	P_{th} [kW]	λ	\dot{m}_{f} [g/s]	\dot{m}_{air} [g/s]	$\bar{u}_{\text{ax, air}}$ [m/s]	Re
DPV1	0.6	30	1.20	0.62	12.68	7.67	25644
DPV3	0.6	50	1.20	1.03	21.14	12.79	42740
DPV5	0.6	70	1.20	1.23	29.60	17.90	59836

The comparison is made inside the frequency interval [10Hz;5000Hz]. The model correctly predicts the amplitude level for all power settings and captures the trend concerning the increase of peak frequency and peak amplitude with the global thermal power setting. The observed trends can be traced back to the rate of heat release and the turbulent intensity throughout the reaction zone. At frequencies in excess of 1000Hz, the theoretical shape of the model spectrum is distorted by the influence of cells in the input data, which possess high values of

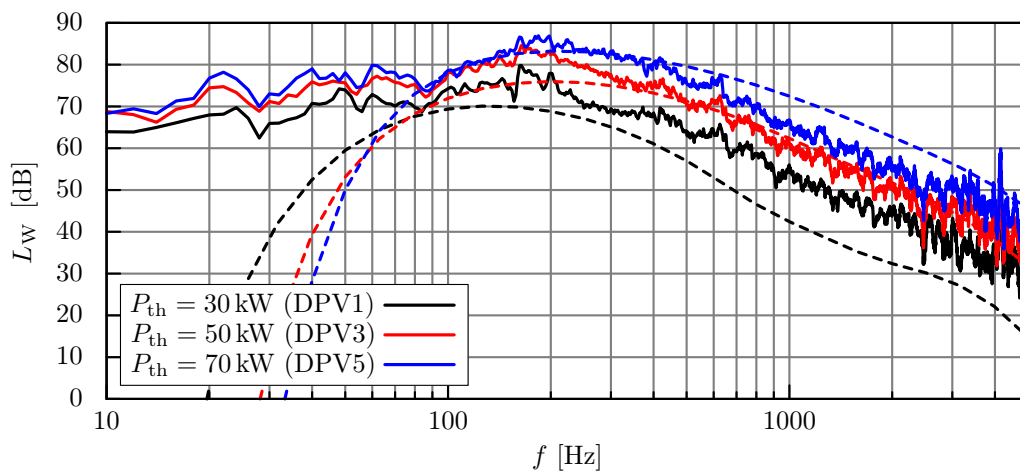


Figure 7.14: Comparison of experimentally determined and modeled sound power spectra emitted from turbulent non-premixed flames at a swirl number of $S = 0.6$, an air excess ratio of $\lambda = 1.2$ and thermal power settings of 30kW, 50kW and 70kW. (—): Experiment, (---): Model.

the turbulent mixing rate. Here, the dynamics of the combustion model in conjunction with the turbulence model influence the theoretically continuous slope through an accumulation of high peak-frequency input data values.

The global agreement between model prediction and experiment is better for higher thermal power. This behavior is most likely caused by the fast chemistry assumption of the transition modeling between the spectrum of reaction progress variance and that of the fluctuating rate of heat release. At higher Reynolds numbers, the flow is increasingly turbulence dominated and the predictive capabilities of the turbulence model in the CFD solution are better for fully turbulent flow conditions [95]. This effect is also connected to the validity of the concept of the turbulent energy cascade, as pointed out by Wäsle [143].

Influence of Mixture Composition

Figure 7.15 compares predicted spectra to the corresponding experimental data for three operating points of different air excess ratios. Increasing combustion air mass flow results in higher turbulence intensity along the inner shear layer, where the primary mixing zone of fuel and oxidizer is located. This results in a decrease of turbulent time scales in the main reaction zone, shifting the radi-

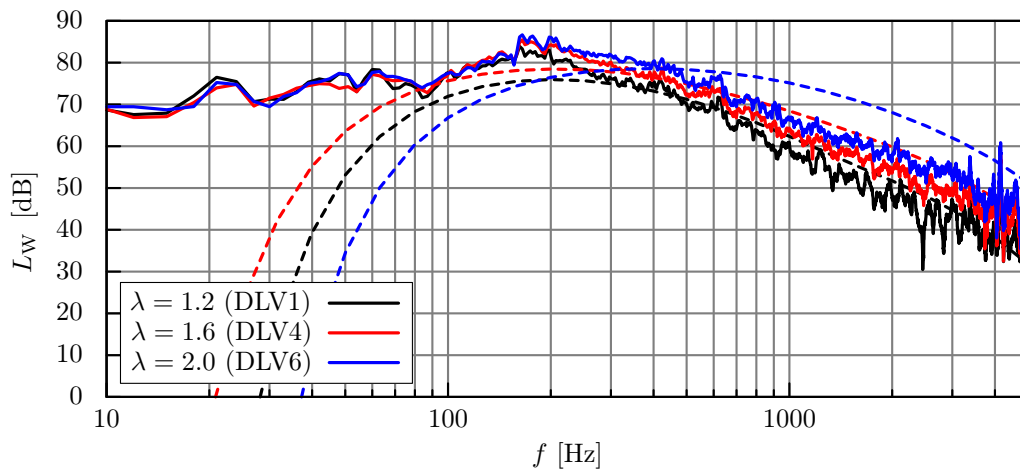


Figure 7.15: Influence of mixture composition on sound radiation from a turbulent non-premixed swirl flame at $P_{th} = 50\text{kW}$ and $S = 0.6$. (—): Experiment, (- - -): Model.

ated combustion noise towards higher frequencies. The comparison shows good agreement between the extended noise model and the experimental spectra for all three cases considered. The general trend, showing an increase of peak frequency with increasing flow velocity is captured consistently. The increase in sound power level for the case of $\lambda = 2.0$ is over-predicted in terms of peak-frequency, while the general shape features of the spectrum are depicted well. This can be attributed partly to the input data delivered by the RANS simulation data. The local peak-frequency is predominantly determined by the ratio of turbulence kinetic energy and dissipation rate, in combination with the combustion model. At high strain rates, which are present close to the fuel exit holes, partial quenching of the flame can occur, which is not captured by the eddy-dissipation model. As a consequence, the high frequency content of the computed spectrum is over-predicted as noise of these frequencies can be directly attributed to the area in the vicinity of the fuel jets, as seen in Fig. 7.13.

Influence of Swirl Intensity

A change in the swirl intensity of the flame results in a alternation of turbulence parameters within the reaction zone, as well as an increased entrainment of ambient air into the flame, without modifying the global power and mixture setting.

The flame length is reduced, as shown in Fig. 6.8 with increasing the swirl number.

Figure 7.16 shows the comparison of model predictions calculated from CFD data with the corresponding experimental spectra. The model spectra capture the experimental trend qualitatively, while the peak frequency is underestimated in all three cases. In general, experimental and modeled spectra are only slightly influenced by the considerable alternation of swirl number from moderate swirl at $S = 0.6$ to intense swirl at $S = 1.4$. The close proximity in the noise spectra is also captured by the model. Beyond $S = 1.0$, the flame length remains virtually unchanged as seen in Fig. 6.8, which explains the similarity between the data of $S = 1.0$ and $S = 1.4$. The spectral decay at frequencies in excess of f_{peak} is captured with good accuracy. In the experimental data, the flame at $S = 1.0$ exhibits the highest amplitude in sound power. This trend is also predicted by the model for the frequency range below f_{peak} , while otherwise the numerical model predicts the largest amplitude at $S = 1.4$. With increasing swirl intensity, the turbulent and chemical time scales increase simultaneously, which makes predictions of the detailed behavior difficult. This is also resembled by the close proximity of the experimentally determined spectra in terms of amplitude and peak-frequency and is also reported by Wäsle [143]. The underestimation of peak-frequencies can be related to the prediction of the integral length scale. The

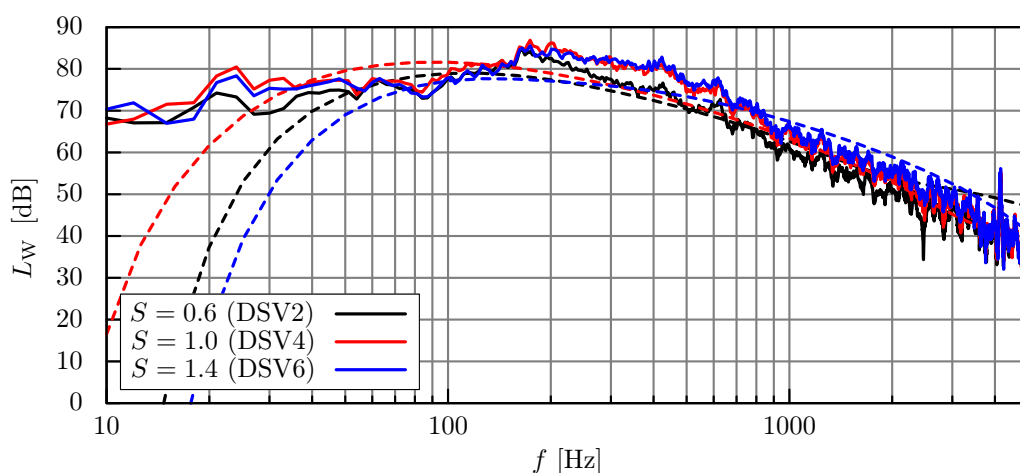


Figure 7.16: Influence of swirl intensity on sound radiation from a turbulent non-premixed flame at $P_{\text{th}} = 50\text{kW}$ and $\lambda = 1.2$. (—): Experiment, (- -): Model.

k - ε -turbulence model is based on the assumption of homogeneous isotropic turbulence [74]. In intense swirling flow, the integral length scale is non-isotropic, with differences between axial, radial and tangential length scale. These conditions especially apply to regions of strong heat release as reported by Winkler et al. [151]. In their premixed swirl flame configuration, circumferential length scales substantially differ from their radial and tangential counterparts.

Influence of Data Extraction Domain Size

The input data fields used for the calculation of the combustion noise spectra in the non-premixed case are extracted from the three-dimensional CFD field data. Technically, this includes the complete CFD domain as shown in Fig. 7.8. Computational time can be reduced significantly if only such finite volumes are included in the calculation process, that possess a non-zero rate of heat release. The selection of the lower bound of the chemical reaction rate that limits the amount of values involved in the computation process was performed based on a solution convergence method using different values of the bound and comparing the results to that of a computation run using the whole domain data. The influence of the choice of the bounding molar reaction rate on the predicted sound power spectrum is shown in Fig. 7.17 for the reference case of $S = 0.6$, $P_{th} = 50\text{kW}$ and $\lambda = 1.2$. The effect of excluding regions of lower volumetric

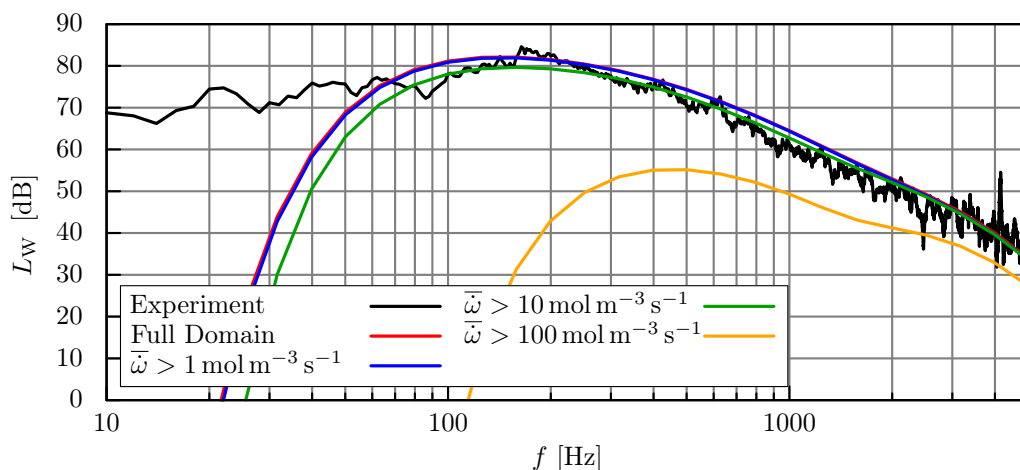


Figure 7.17: Influence of the minimum reaction rate bounding the volume of data extraction from the CFD solution.

reaction rates on the calculated model spectrum becomes evident upon considering the model spectrum calculated on data extracted only from regions of reaction rates of $\bar{\dot{\omega}} > 100 \text{ mol}/(\text{m}^3 \text{ s})$. The exclusion of a considerable portion of the overall heat release from the calculation leads to the reduced amplitude of the computed spectrum. If, however, variable values are extracted from all cells that possess a molar reaction rate greater than $1 \text{ mol}/(\text{m}^3 \text{ s})$, no deviation of the result with reference to the full domain computation can be found. Consequently, this value was chosen as the limit governing the inclusion of a computational cell into the post-processing calculations. Compared to the computation based on the full number of 630000 elements, this procedure reduced the computational time by an approximate factor of 5.

7.4 Summary of Numerical Results

The extended spectral noise model using the PDF-based amplitude scaling function was used to calculate the spectral noise emission from a gaseous turbulent swirl flame in premixed and non-premixed configuration at different operating conditions. The general finding is, that the generalized amplitude scaling function is equivalent to the original formulation based on the Schmid combustion model in the premixed case and is able to equivalently predict noise radiation in the non-premixed case. In general, combustion noise predictions based on CFD field data have to be credited with an additional margin of uncertainty due to the additional modeling involved in the calculation of the input data, when compared to the calculation based on experimental input data [143]. The primary conclusion from the numerical simulations for the open burning swirl flame is that experimental data is needed for reference at one operating point to be able to safely predict noise spectra for a range of varying operating conditions around the reference point. The great sensitivity of the model predictions with respect to the supplied field data of turbulent time and length scale is accounted for with this step. If a reference solution is known, spectral solutions can be obtained with good accuracy for a wide range of operating conditions from CFD RANS using industry standard models for turbulence and combustion.

8 Model Application to a Marine Heating Unit

The applicability of the non-premixed combustion noise model to laboratory scale open burning flames has been demonstrated in Chap. 7. The intended use of the developed combustion noise toolkit is primarily seen in early development of combustion systems, in order to detect possibilities of noise reduction at an early stage and to be aware of acoustic problems ahead. This chapter presents the application of the extended combustion noise model to an industry standard combustion system used for coolant heating in marine applications. Such coolant heaters are frequently installed on sailing boats, where silent operation is an essential requirement. This profile of operation makes the acoustic emissions of the heater a primary object of concern during development. Beneath the electrical blower which supplies combustion air to the burner, the intense turbulent flame is the major source of acoustic emissions by the heater. The heating unit investigated in this study is a Webasto Thermo 90 ST coolant heater with a peak thermal power output of 9.2kW.

8.1 Small Burner Test Rig

For the recording of noise spectra from the turbulent diesel flame of the coolant heater, the unit is stripped of all peripheral devices surrounding the combustion chamber. The combustion chamber walls are replaced by silicon glass tubes of matching diameter to allow optical access. Also, the blower supplying the combustion air is replaced by an acoustically silenced air supply system, feeding pressurized air from the laboratory air supply line into the combustion chamber. A schematic layout of the modified burner setup is shown in Fig. 8.1. The combustion chamber is constructed around a metal fleece evaporator surface which

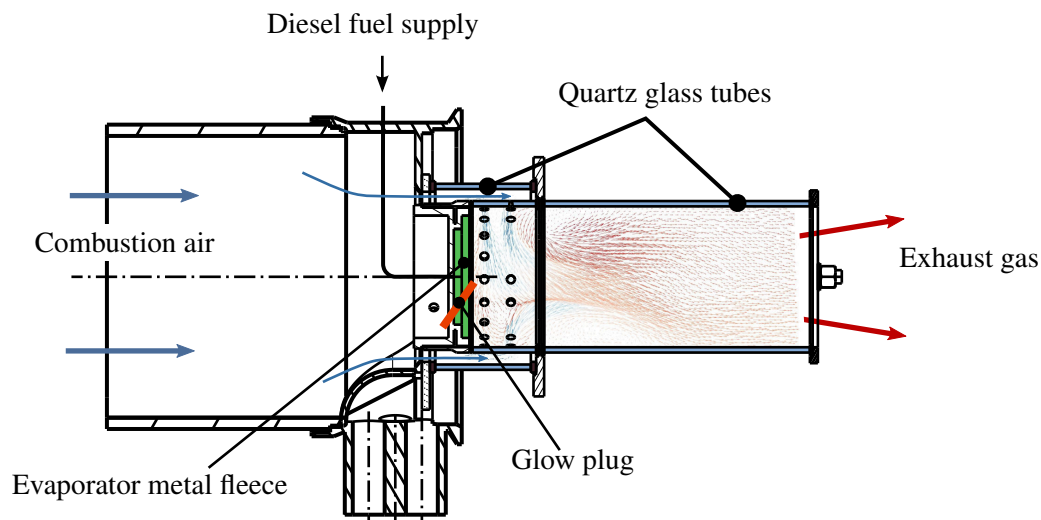


Figure 8.1: Schematic of the modified Webasto Thermo 90 ST coolant heater used in the acoustic experiments. Liquid diesel fuel is injected into a metal fleece plate on the bottom of the combustion chamber. After evaporation and mixing with the combustion air entering the combustion chamber through holes in the combustion chamber wall, combustion and burnout is performed inside the combustion chamber and the burnout tube.

supplies gaseous diesel fuel into the combustion chamber. Fuel is fed into the evaporator by a frequency clocked dosing pump. At full power, approximately seven pump strokes are performed every second. The liquid diesel fuel is heated and distributed inside the porous metal fleece evaporator and enters the combustion chamber in a vaporized state. The heat of vaporization is initially supplied by a glow plug which is also used for ignition, while in continuous operation the evaporator fleece is heated directly by the flame. The air mass flow rate is determined using a flow metering orifice disc by monitoring pressure difference across the disc [1]. The annular gap between the combustion chamber wall and the and outer wall provides cooling for the combustion chamber walls. Air enters the combustion chamber through a series of holes distributed along the circumference of the combustion chamber wall. Unlike the production version of the heating unit, the walls of combustion chamber, burnout tube and annular gap are replaced by quartz glass tubes with a wall thickness of 2 mm. The production version is equipped with sheet metal walls of 1 mm thickness. Diameters are adjusted accordingly, in order to maintain all flow cross-sectional areas.

Sound intensity spectra are recorded using the sound intensity probe described in Sec. 5.6 which is set up in a distance of 1 m from the burner exit at an angle of 15° towards the burner axis to avoid the high temperature exhaust flow. The burner is set up horizontally inside an acoustically absorptive chamber similar to that used in the measurements for the open turbulent flame (cf. Sec. 5.3) with an edge length of 1.8 m. The measurement setup is shown in Fig. 8.2.

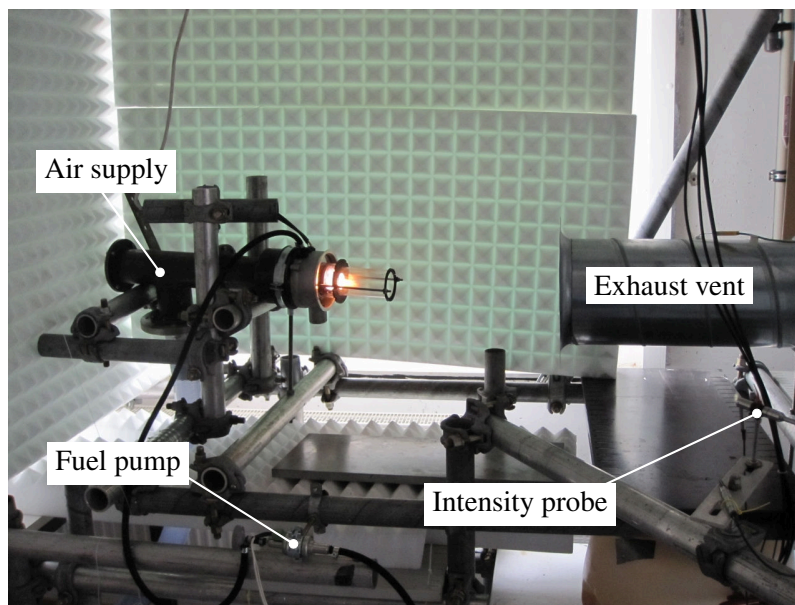


Figure 8.2: Experimental setup for the measurement of combustion noise radiated by the marine coolant heater.

8.2 Experimental Results

The acoustic properties of the turbulent non-premixed diesel flame operated in the marine coolant heater possess fundamental differences when compared to the typical characteristics of noise spectra from unconfined burning flames. Experimental results for different mixture compositions at constant thermal power output are shown in Fig. 8.3 in comparison to the noise spectrum produced by the cold air flow corresponding to $P_{\text{th}} = 8 \text{ kW}$ and $\lambda = 1.5$. All operating points show a nearly constant amplitude level up to a frequency of 1100 Hz, where the spectrum shows a characteristic narrow banded peak. Beyond that, the spec-

trum possesses further characteristic peaks and dips at discrete frequencies. Beyond 1100Hz, the spectrum decays constantly, which is consistent to the general qualitative characteristics of unconfined turbulent flames. The high-frequency content of the cold flow signal (visible around 2700Hz) is aerodynamic noise produced by the combustion air upon passing through the narrow holes in the circumference of the combustion chamber. Aeroacoustic excitation of pressure waves as a result of vortices being shed from the rim of an orifice is predominately active (depending on the geometric dimension of the orifice) in this range of frequencies [66, 135]. An interesting feature of the spectra is their similarity in the very low frequency range below 80Hz. Similar characteristics apply to the mixture composition study performed with the unconfined non-premixed natural gas flame (cf. Sec. 6.1.2). Some part of this behavior can be attributed to the frequency content of the corresponding cold flow, but the constant firing rate is the probable cause for the relatively constant noise emission in this part of the spectrum.

Generally, the measured spectra differ considerably from those observed with unconfined turbulent flames, clearly outlining the importance of the confinement for the overall acoustic emissions of a combustion system. A distinct peak is visible at 1020Hz for all three operating points. Furthermore, the lower frequency amplitude levels do not exhibit continuous growth with frequency but remain at

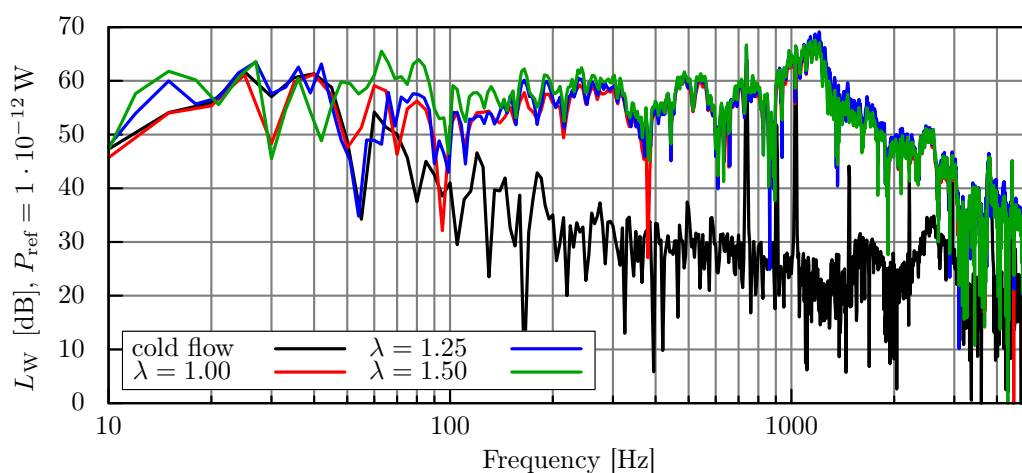


Figure 8.3: Acoustic intensity spectrum radiated by the diesel heater for different mixture compositions. The thermal power output is kept constant at 8 kW.

constant amplitude with distinct peaks and drops along the frequency axis. The distinct spectral features can be attributed to the geometric acoustic properties of the combustion system enclosing the flame. Acoustic energy is dissipated inside the system by vortex-acoustic interaction in shear layers as well as reflected, refracted and attenuated at walls and edges. The radiation of acoustic energy into the surroundings is as well dependent on the frequency of the incident sound.

8.3 Acoustic Network Model

The propagation of sound inside an enclosed combustion system can be calculated by solving the convective acoustic wave equation. The Finite-Element method can be used to solve a variety of multi-dimensional physical problems, ranging from continuum mechanics [64] to acoustic propagation problems in complex geometries [24, 146]. In acoustics, the method is used to solve the three dimensional wave-equation in frequency space to predict sound propagation and reflection. Industrial combustion systems are often assembled from duct-like structures, where the duct diameter is often considerably shorter than the acoustic wave-lengths of interest. In this case, acoustic propagation inside those systems can be treated as essentially one-dimensional along the system axis. This offers a considerable reduction in computational effort. Then, the analytical solution for sound propagation inside a duct with superimposed mean flow can be used to connect “black-box” elements describing the state variables of the acoustic field at discontinuities of flow cross-sectional area, fluid density and others to form a network of acoustic elements.

For that purpose, the geometric domain which characterizes the acoustic problem is decomposed into for themselves simple elements with an often analytical description of their individual transmission behavior. Each element connects the acoustic state variables between its upstream and downstream boundary through a specific correlation. This method takes advantage from linear theory in as much as the specific physical process which is influencing wave propagation inside the element does not need to be known. Here, only the frequency dependent parameter values of the state variables at the boundaries are of importance. Expressed

mathematically, the elements of a two-port matrix connect the vectors of the acoustic state variables through the matrix which is termed the transfer matrix (TM) of the element:

$$\begin{pmatrix} p \\ u \end{pmatrix}_j = \begin{pmatrix} T_{11} & T_{12} \\ T_{21} & T_{22} \end{pmatrix} \cdot \begin{pmatrix} p \\ u \end{pmatrix}_i \quad (8.1)$$

If the transmission characteristics of all elements describing an acoustic system are known, a system matrix describing the complete system acoustics can be assembled. The system matrix comprises a system of linear equations with the unknowns given by the acoustic state variables at the nodes connecting the single elements.

The solution of the linear equation system can be performed in a numerically efficient way. The one-dimensional network representation of the heaters combustion chamber used in this study is shown in Fig. 8.4. A summary of acoustic network elements involved in the modeling is given in Appendix C.

The burner model consists of a closed end boundary modeling the evaporator fleece, a source model including the acoustic flame source function provided by the extended combustion noise model and a model for sound reflection at the burner opening. Acoustic propagation, refraction and reflection inside the system is modeled using appropriate elements as indicated in Fig. 8.4. The acoustic reflection coefficient of the evaporator fleece was experimentally determined using a multi-microphone technique. This method uses a siren to acoustically excite the boundary of interest at discrete frequencies. The reflection coefficient can then be retrieved from a reconstruction of the one-dimensional wave-field inside a measuring duct, which is connected to the geometry of interest. Inside the measuring duct, dynamic pressure sensors record the time series of the acoustic pressure signal, which are then used to reconstruct the wave-field in frequency space. Figure 8.5 shows the experimentally measured reflection coefficient of the evaporator fleece, obtained on an experimentally setup similar to that described in [63]. Close to complete reflection of acoustic pressure waves is visible in the reflection coefficient data for frequencies up to 1700Hz, which is the range of interest for combustion noise. Consequently, the evaporator fleece can be treated as an acoustic wall boundary. However, the available phase corrected reflection

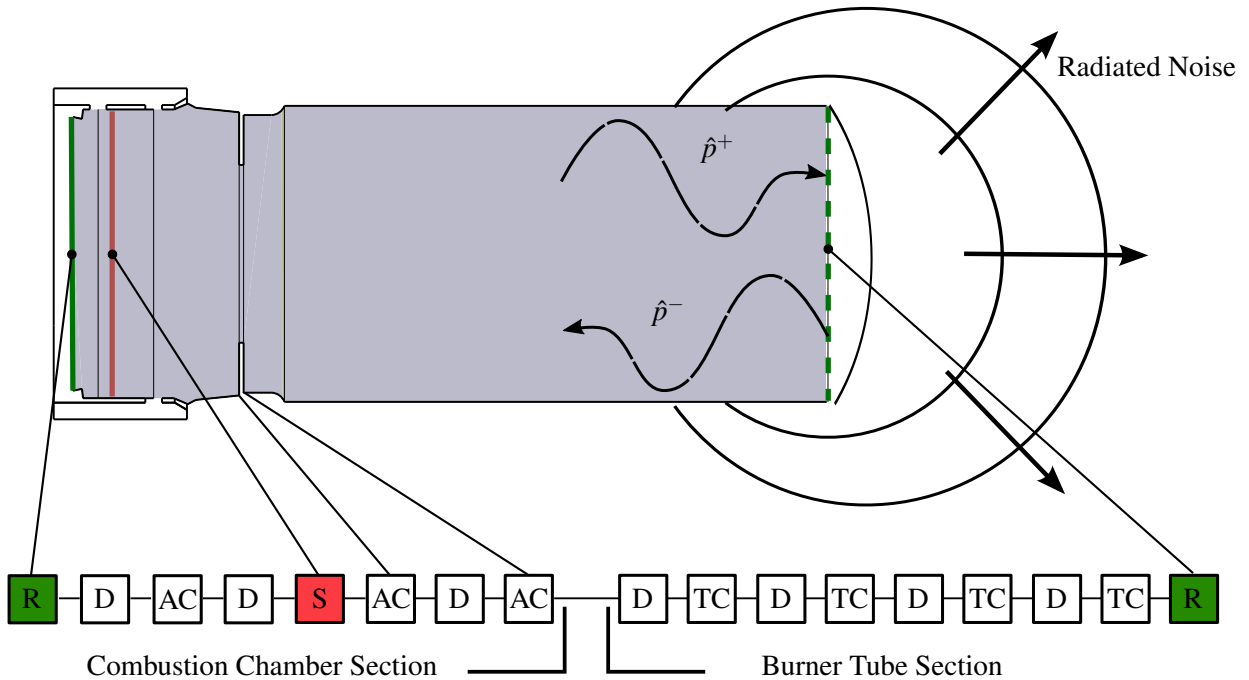


Figure 8.4: One-dimensional acoustic network representation of the diesel heater. The acoustic two-port elements denote R: reflecting boundary, D: duct, AC: discontinuity in cross sectional area, TC: discontinuity in fluid density (temperature) and S: flame element for combustion noise.

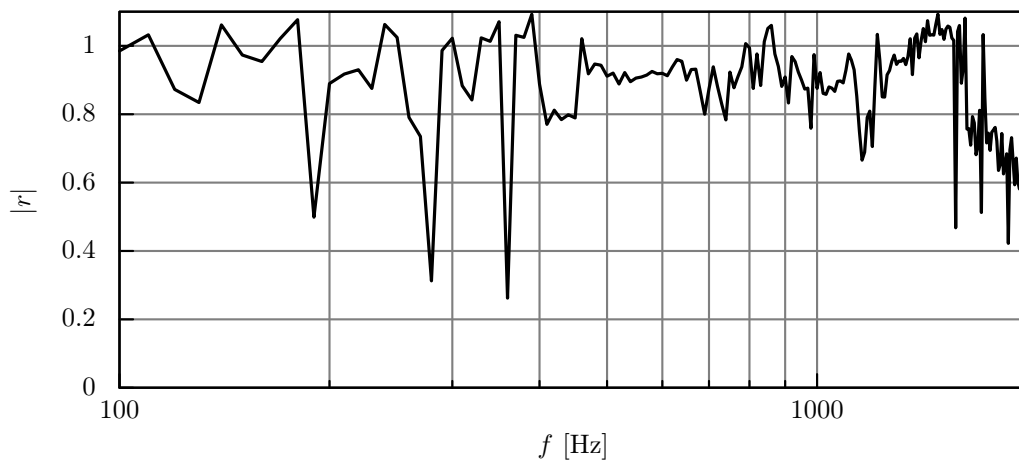


Figure 8.5: Magnitude of the pressure reflection coefficient of the evaporator fleece over frequency.

coefficient is used to represent the wall boundary given by the evaporator fleece in the network model.

The boundary condition at the burner exhaust is modeled using the numerical model by Munt discussed in Sec. 3.3.2. For the operating point studied, the exhaust reflection coefficient obtained from the solution of Munt's model equations is shown in Fig. 8.6 together with the corresponding reflection coefficient of acoustic energy calculated from Eq. (3.32). Due to the low flow velocity, the

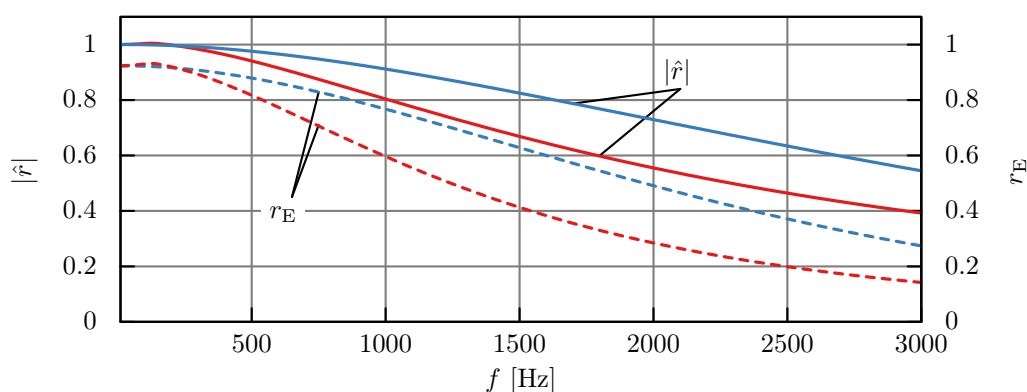


Figure 8.6: Magnitude of the pressure and energy reflection coefficient at the burner exhaust plane for a mean flow temperature of 1900K calculated using the Munt model (—) compared to the isothermal solution of Levine & Schwinger (---).

amplification of pressure waves in the shear layer downstream of the exhaust is negligible and the reflection coefficient magnitude does not exceed unity. However, the high temperature flow leads to a considerable drop of the reflection coefficient, permitting a growing fraction of acoustic energy to leave the system at higher frequencies. At 1500Hz, 60% of the incident acoustic intensity at the exhaust is radiated into the environment. The direct comparison of the solution obtained from the Munt model and that obtained from the isothermal theory of Levine & Schwinger reveals the important effect of the temperature difference between the exhaust gas and the ambient atmosphere on sound radiation into the environment. In terms of acoustic energy radiation, the difference in the particular case of the marine coolant heater reaches up to 65% in the medium frequency range, stressing the need to incorporate this effect into the system modeling.

8.4 Noise Source

Weyermann [146] proposed a method to integrate predictions of the combustion noise model into a network element which accounts for the velocity fluctuations produced by the turbulent flame. This element is based on a Rankine Hugoniot jump condition between the acoustic variables on either side of the compact flame element. The network element for the flame is [146]

$$\begin{pmatrix} p' \\ u' \end{pmatrix}_{i+1} = \begin{pmatrix} 1 & 0 \\ 0 & 1 \end{pmatrix} \begin{pmatrix} p' \\ u' \end{pmatrix}_i + \begin{pmatrix} 0 \\ \frac{\gamma-1}{\rho_i c_i^2} q'_f(f) \end{pmatrix}, \quad (8.2)$$

where the additional term on the right hand side describes the velocity fluctuation introduced by fluctuating heat release rate inside the flame volume. Apart from density and speed of sound at the location of the source element, the frequency spectrum of the heat release fluctuations is needed.

The relation between the frequency spectrum of the fluctuations of the heat release rate and the modeled wave-number spectrum included in the combustion noise model for open flames is given by [146]

$$q'_f(f) = \frac{1}{A} \sqrt{\int_{V_{\text{flame}}} (2\pi)^3 \left(\frac{\kappa E_q(\kappa)}{f} \right)^2 V_{\text{coh}} dV}, \quad (8.3)$$

where κ is given by Eq. (4.27) and the modeled spectrum of heat release $E_q(\kappa)$ by Eq. (4.7). A denotes the flow cross sectional area of the flame element.

8.5 Numerical Results

The results obtained from the solution of the acoustic network model shown in Fig. 8.4 for three different mixture compositions at a thermal power of $P_{\text{th}} = 8 \text{ kW}$. The sound intensity at the location of the intensity probe is calculated following the approach used by Weyermann [146], which assumes spher-

ical wave propagation in the ambient atmosphere from the exhaust opening. In this case, the sound intensity at radius r from the exhaust is given by

$$\hat{I}(r) = \hat{I}_e \cdot \frac{S_e}{S(r)}, \quad (8.4)$$

where S_e denotes the flow cross sectional area of the exhaust tube and $S(r)$ is the surface area of the spherical shell enclosing the exhaust at radius r . The numerical results show close agreement between the spectra of the three operating points, which matches the trend of the the experimental data. The low frequency behavior is under-predicted by the numerical model, which can be attributed to the influence of cold flow noise, which is not covered by the noise model. The general trend in terms of increasing amplitude with increasing air excess ratio is also reproduced, especially when the close match between the curves of $\lambda = 1.25$ and $\lambda = 1.5$ is considered. However, the decay of the spectrum at frequencies in excess of 1000Hz can only be reproduced qualitatively. This effect can be attributed to acoustic losses in the combustor due to interaction with shear layers in the vicinity of the circumferential air holes, which are not captured by the simple network model and grow increasingly effective at higher frequencies [63].

In conclusion it can be stated, that the overall combustion noise amplitude levels are captured well by the model. The spectrum of the radiated sound is the result

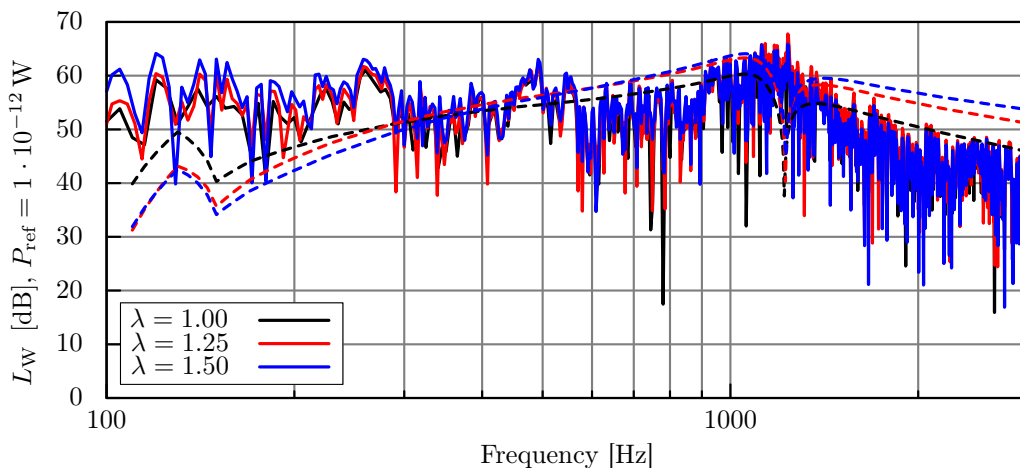


Figure 8.7: Comparison between experimental results (—) for sound power level and numerical predictions (- - -) obtained with the network model including the corresponding combustion noise source term.

of the influence by a series of different parameters, including geometry of the combustion chamber, boundary conditions, aero-acoustic noise sources and ambient conditions so that for confined flames a larger tolerance between the model predictions and the experimental data must be accepted. However, important order of magnitude estimates as well as the qualitative effects of modifications to the combustion chamber or changes in operating conditions can be performed in a numerically efficient way using the post processing toolkit developed in the course of this thesis.

9 Concluding Remarks

In the course of the development of emission optimized combustion systems, turbulent combustion noise has become an additional concern. Depending on the specific application, it can be responsible for additional pollutant emission by causing fluctuations of the combustion process, as well as perceived as disturbing noise emission, when silent operation is desired. The latter effect is of importance in domestic heating systems. The study at hand was undertaken in order to develop a noise prediction toolkit which can assist in predicting combustion noise emission from turbulent flames from industry standard numerical simulations of the reactive flow in early stages of development.

Experimental studies were conducted on an open turbulent flame test rig and an industrial coolant heater for marine applications. The open flame was used in order to study turbulent combustion noise in an isolated state, where disturbing sources of additional noise have been reduced by appropriate measures. A burnout correction procedure was developed to quantify the actual thermal power output of open turbulent premixed flames. The experiments provided a series of validation cases for the extended combustion noise model which was implemented into a numerically efficient post processing tool. The applicability of the developed approach was demonstrated by comparing model predictions to experimental data obtained from the series production marine heating unit.

The general experimental findings concerning combustion noise from turbulent premixed and non-premixed flame are the following:

- Turbulent combustion noise is inherently coupled to the global heat release rate and the turbulent time scale in the reaction zone of the flame. An increase of thermal power output results in both, an increase of the noise amplitude and the peak-frequency, independent of the flame type. These quantities determine the thermal power density of the flame.

- Fuel burnout for open turbulent premixed flames is incomplete due to dilution effects caused by the entrainment of ambient air. In order to compare experimental data to numerical predictions, fuel burnout can be quantified by comparing global OH* intensities between open turbulent premixed flames and a confined flame reference experiment at the same operating point.
- If premixed and non-premixed turbulent swirl flames are operated under similar conditions concerning local mixture composition, actual thermal power output, and Reynolds number, the resulting spectrum of combustion noise is virtually identical.

A series of numerical simulations was performed for the open premixed and non-premixed flames, validating the introduced extensions of the premixed combustion noise model in order to capture the characteristics of non-premixed flames. The following general findings can be stated regarding the numerical studies:

- The proposed model extensions address the characteristics of non-premixed turbulent flames. In particular, the generalized amplitude scaling function is equivalent to the previous formulation and can be applied to both, non-premixed and premixed flames.
- The combustion noise model is sensitive concerning the input variable fields with respect to turbulent time and length scale. Comparison should be made only between cases which have been simulated using the same combination of turbulence and combustion model.
- If experimental reference data is available, the model can be used to obtain qualitative and quantitative predictions of the radiated combustion noise for different operating parameters.
- For confined flames, which are predominately found in practical applications, other sources of noise in conjunction with acoustic damping and amplification inside the system complicate the prediction of pure combustion noise.

Appendix

A Mean and Standard Deviation of the Clipped Gaussian Distribution

The Gaussian distribution for the calculation of mean variables is used in a restricted form bounding the PDF to the range $[0; 1]$. The unbounded distribution function is given by

$$p(z) = \frac{1}{\sqrt{2\pi}\sigma} \exp\left[-\frac{(z-\mu)^2}{2\sigma^2}\right], \quad (\text{A.1})$$

where μ denotes the mean, σ denotes the standard deviation, and z is the random variable, representing the mixture fraction in the course of this thesis. The clipping procedure is described in detail by Lockwood and Naguib [80]. Essentially, the area under the PDF is conserved in its value of unity by adding the probability of the unwanted tails of the distribution as Dirac delta functions at the interval boundaries. The clipped PDF is then given as

$$p(z) = \frac{1}{\sqrt{2\pi}\sigma_c} \exp\left[-\frac{(z-\mu_c)^2}{2\sigma_c^2}\right] \cdot [\Theta(z) - \Theta(z-1)] + A\delta(0) + B\delta(1), \quad (\text{A.2})$$

where Θ is the Heaviside step function and A, B are the tails of the Gaussian distribution outside the interval of $[0; 1]$. μ_c and σ_c denote mean and standard deviation of the clipped PDF. The area of the clipped tails included in A and B is given by

$$\begin{aligned} A &= \int_{-\infty}^0 \frac{1}{\sqrt{2\pi}\sigma_c} \exp\left[-\frac{(z-\mu_c)^2}{2\sigma_c^2}\right] dz \\ B &= \int_1^{\infty} \frac{1}{\sqrt{2\pi}\sigma_c} \exp\left[-\frac{(z-\mu_c)^2}{2\sigma_c^2}\right] dz. \end{aligned} \quad (\text{A.3})$$

The unknown parameters μ_c and σ_c of the clipped PDF can be calculated numerically by solving a system of equations that is obtained by forming the first and second moment of the PDF. The first moment of Eq. (A.2) defines the mean

$$\bar{z} = A + \int_0^1 z \cdot p(z) dz + B, \quad (\text{A.4})$$

and the second moment defines the variance:

$$\overline{z'^2} = A + \int_0^1 z^2 \cdot p(z) dz + B - \bar{z}^2. \quad (\text{A.5})$$

Both, \bar{z} and $\overline{z'^2}$ are known from the solution of a corresponding transport equation so that μ_c and σ_c can be obtained by solving the resulting system of equations

$$\begin{aligned} \bar{z} = \frac{1}{2} \left\{ -(\mu_c - 1) \operatorname{erf} \left(\frac{\mu_c - 1}{\sqrt{2}\sigma_c} \right) + (\mu_c - 1) \operatorname{erf} \left(\frac{\mu_c}{\sqrt{2}\sigma_c} \right) + \sqrt{\frac{2}{\pi}} \sigma_c \right. \\ \left. \cdot \left[\exp \left(-\frac{\mu_c^2}{2\sigma_c^2} \right) - \exp \left(-\frac{(\mu_c - 1)^2}{2\sigma_c^2} \right) \right] + 2 \right\}, \end{aligned} \quad (\text{A.6})$$

$$\begin{aligned} \overline{z'^2} = \frac{1}{4} \left\{ 2 - 2 \exp \left[-\frac{(\mu_c - 1)^2}{2\sigma_c^2} \right] \sqrt{\frac{2}{\pi}} \sigma_c - 2 \exp \left[-\frac{(\mu_c - 1)^2}{2\sigma_c^2} \right] \sqrt{\frac{2}{\pi}} \mu_c \sigma_c \right. \\ + 2 \exp \left(-\frac{\mu_c^2}{2\sigma_c^2} \right) \sqrt{\frac{2}{\pi}} \mu_c \sigma_c - 2 \mu_c^2 \operatorname{erf} \left(\frac{\mu_c - 1}{\sqrt{2}\sigma_c} \right) - 2 \sigma_c^2 \operatorname{erf} \left(\frac{\mu_c - 1}{\sqrt{2}\sigma_c} \right) \\ + \frac{1}{5} \left[1 + \operatorname{erf} \left(\frac{\mu_c - 1}{\sqrt{2}\sigma_c} \right) \right] - 2 \operatorname{erf} \left(\frac{\mu_c}{\sqrt{2}\sigma_c} \right) + 2 \mu_c^2 \operatorname{erf} \left(\frac{\mu_c}{\sqrt{2}\sigma_c} \right) \\ + 2 \sigma_c^2 \operatorname{erf} \left(\frac{\mu_c}{\sqrt{2}\sigma_c} \right) - \left[2 + \left(-\exp \left(-\frac{(\mu_c - 1)^2}{2\sigma_c^2} \right) + \exp \left(-\frac{\mu_c^2}{2\sigma_c^2} \right) \right) \sqrt{\frac{2}{\pi}} \sigma_c \right. \\ \left. - (-1 + \mu_c) \operatorname{erf} \left(\frac{\mu_c - 1}{\sqrt{2}\sigma_c} \right) + (-1 + \mu_c) \operatorname{erf} \left(\frac{\mu_c}{\sqrt{2}\sigma_c} \right) \right]^2 \right\}, \end{aligned} \quad (\text{A.7})$$

numerically using a two-dimensional Newton algorithm. Based on a pair of initial values, the algorithm iteratively approaches the root of the system by following the direction of the local function gradient. The numerical implementation of the solution procedure in C and the equation system involves several subroutines, e.g. a numerical function representation of the error function. Additionally, the code representation of the equation system of Eq. (A.6) and Eq. (A.7) is a considerably complicated expression. Consequently, the correct numerical representation of the equation system together with the behavior of the solution routine need to be analyzed with respect to robustness and valid results. The validity was proofed by comparing results from the C routine to values obtained by solving the system of equations using Wolfram Mathematica, which delivered equivalent results. The behavior of the numerical solution routine can be analyzed by tracing the iterations needed for the two-dimensional Newton algorithm to converge over the corresponding pair of initial values of mixture fraction and mixture fraction variance. If the number of iterations needed for the routine to converge to a solution is recorded for each pair of initial values for \bar{z} and $\overline{z'^2}$, a contour plot is obtained, which contains the convergence behavior of the numerical algorithm. The resulting contour plot is shown in Fig. A.1 for initial values between 0 and 1 for the mixture fraction and 0 and 0.3 for the variance. From

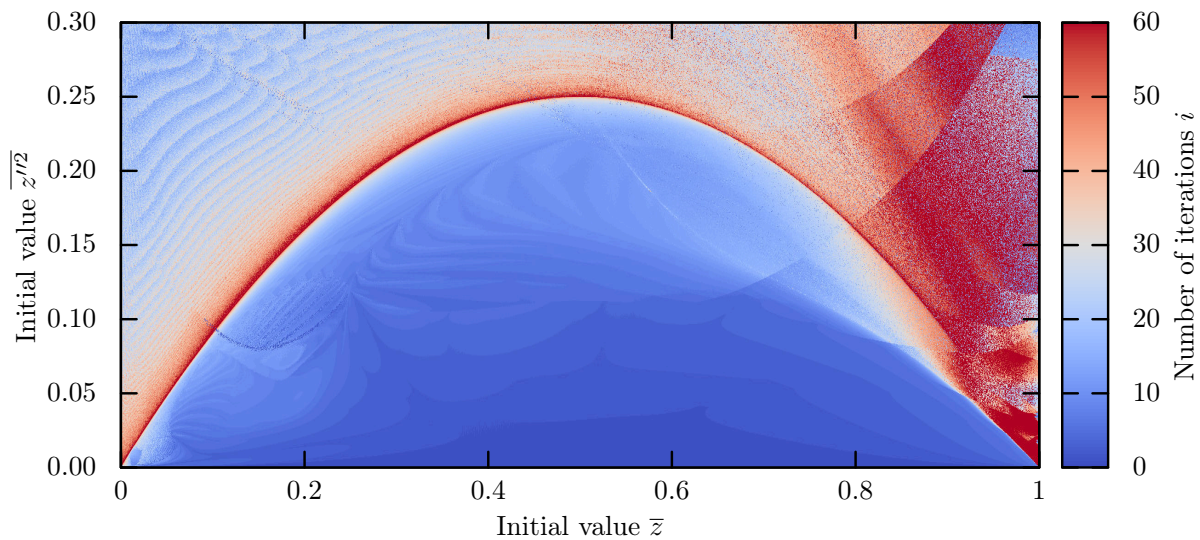


Figure A.1: Color coded contour plot showing the number of iterations needed by the stabilized Newton algorithm to converge to a solution depending on the initial value pair of mean and variance.

those values, the initial values for mean and standard deviation of the clipped PDF are calculated from $\mu_{c,0} = \bar{z}$ and $\sigma_{c,0} = \sqrt{\bar{z}''^2}$. In theory, no solutions to the equation system should exist for variances greater than the theoretical maximum of $\bar{z}''^2 = \bar{z} \cdot (1 - \bar{z})$. However, the implemented stabilized Newton algorithm is able to converge to a solution even if the initial starting value is located outside that range. The parabola following the $\bar{z} \cdot (1 - \bar{z})$ curve is clearly visible in the contour plot as a rapid increase in the number of iterations needed to find a solution, indicating the correct implementation of the determining equations as well as the iterative numerical routines. Inside the parabola, a solution is mostly found using 10 iterations or less. From this image, suitable bounds for the initial values supplied by the CFD simulation can be found which ensure the numerical stability of the routines involving the clipped PDF for all cases.

B Iterative Calculation of Adiabatic Flame Temperatures

For the determination of adiabatic flame temperatures, the local mixture is assumed to be a closed thermodynamic system undergoing chemical reaction at constant pressure, so that the first law of thermodynamics gives

$$dH = 0, \quad (\text{B.1})$$

and the fully unburnt and fully reacted states possess equal specific enthalpy.

$$h_{\text{mix, u}} = h_{\text{mix, b}} = \sum_{j=1}^n w_{j, \text{u}} h_{j, \text{u}} = \sum_{j=1}^n w_{j, \text{b}} h_{j, \text{b}} \quad (\text{B.2})$$

Under these conditions, the enthalpies of the chemical components are related through

$$h_{j, \text{b}} = h_{j, \text{u}} + \int_{T_{\text{u}}}^{T_{\text{ad}}} c_{p, j}(T) dT, \quad (\text{B.3})$$

where the indices u, b refer to the unburnt and burnt state. Equation (B.3) can be evaluated numerically by calculating the specific enthalpy h_{m} from tabulated polynomial functions for a temperature T_{m} and iterating T_{m} until h_{m} reaches a prescribed interval around the enthalpy of the fully burnt mixture state. Then, T_{m} equals the adiabatic flame temperature.

C Acoustic Network Elements

The following sections each give a short description of the network elements which were used in the network model representation of the marine coolant heater. The notation of the elements follows the convention that the Riemann invariant f travels in downstream direction (positive x).

C.1 Reflecting End

The reflecting end is used to set a specific reflection coefficient at an upstream or downstream boundary of the system. For an inlet boundary condition, the network element is formulated in the following way:

$$r = \frac{\text{reflected wave}}{\text{incident wave}} = \frac{f}{g} \quad (\text{C.1})$$

Figure C.1 illustrates the convention for upstream and downstream end graphically. For the use in network models, this boundary condition is expressed in

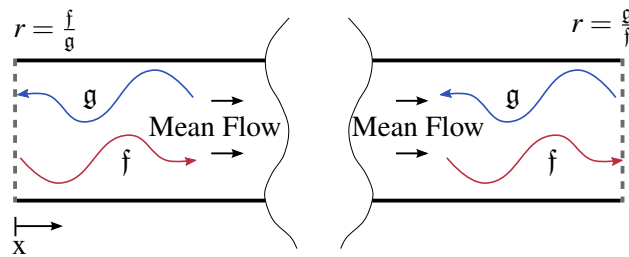


Figure C.1: Reflection coefficient boundary condition shown for upstream and downstream boundary.

matrix notation as:

$$\begin{pmatrix} 1 & -r \end{pmatrix} \cdot \begin{pmatrix} f \\ g \end{pmatrix} = 0 \quad (\text{C.2})$$

The corresponding outlet boundary end element is

$$\begin{pmatrix} r & -1 \end{pmatrix} \cdot \begin{pmatrix} \mathbf{f} \\ \mathbf{g} \end{pmatrix} = 0. \quad (\text{C.3})$$

C.2 Duct Element of Uniform Cross Section

The transfer matrix of a duct with uniform cross sectional area and of arbitrary length L can be deduced from the solution of the one-dimensional wave-equation. Figure C.2 shows the one-dimensional model of a duct in terms of the Riemann invariants. The transfer matrix in \mathbf{f} and \mathbf{g} notation is then

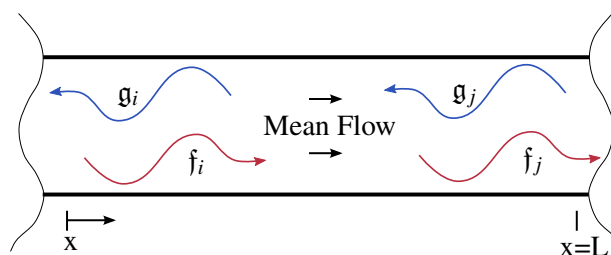


Figure C.2: One-dimensional duct model in terms of the Riemann invariants.

$$\begin{pmatrix} \mathbf{f} \\ \mathbf{g} \end{pmatrix}_u = \begin{pmatrix} e^{ik^+L} & 0 \\ 0 & e^{ik^-L} \end{pmatrix} \cdot \begin{pmatrix} \mathbf{f} \\ \mathbf{g} \end{pmatrix}_d. \quad (\text{C.4})$$

Propagation losses can be accounted for by using complex wave-numbers, as e.g. done by Delany & Bazley to model acoustic propagation in porous media [27].

C.3 Discontinuity in Cross-Sectional Area

A sudden change in cross-sectional area is a common geometric element in duct acoustics. Depending on the area ratio, a certain fraction of the incident wave is reflected at the entry plane. Losses and wave number effects on the reflection and transmission characteristics can be accounted for by setting corresponding loss parameters and effective lengths in the element transfer matrix model. The

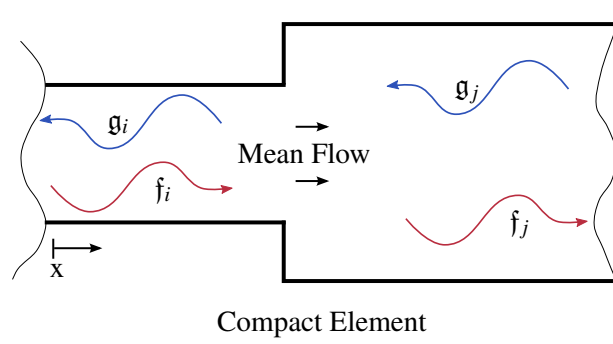


Figure C.3: Acoustic state variables at an exemplary area expansion element. The element is assumed to be acoustically compact.

conditions at an area expansion are shown exemplary in figure C.3. The transfer matrix of an area discontinuity can be derived from the conservation equations of momentum and mass at the discontinuity. The analytic model used in this work is in addition able to account for an effective length and pressure loss. The transfer matrix formulation of the area discontinuity model used in the network model is [44]

$$\begin{pmatrix} \mathbf{f} \\ \mathbf{g} \end{pmatrix}_j = \begin{pmatrix} \frac{1}{2} + \frac{A_d}{2A_u} - \frac{A_u M_u}{2A_d} + \frac{1}{2} \left(1 - \xi - \frac{A_u^2}{A_d^2}\right) M_u & \frac{1}{2} - \frac{A_d}{2A_u} - \frac{A_u M_u}{2A_d} - \frac{1}{2} \left(1 - \xi - \frac{A_u^2}{A_d^2}\right) M_u \\ \frac{1}{2} - \frac{A_d}{2A_u} + \frac{A_u M_u}{2A_d} + \frac{1}{2} \left(1 - \xi - \frac{A_u^2}{A_d^2}\right) M_u & \frac{1}{2} + \frac{A_d}{2A_u} + \frac{A_u M_u}{2A_d} - \frac{1}{2} \left(1 - \xi - \frac{A_u^2}{A_d^2}\right) M_u \end{pmatrix} \cdot \begin{pmatrix} \mathbf{f} \\ \mathbf{g} \end{pmatrix}_i, \quad (\text{C.5})$$

where A_u , A_d denote the cross sectional areas upstream and downstream of the element, M_u , M_d the corresponding Mach numbers and ξ the pressure loss coefficient. The effective and the reduced length parameter are set to zero in the network model.

List of Figures

1.1	Predicted consumption of energy for transportation within the European Union to the year 2050, colored by origin of energy (adapted from [17]).	1
1.2	The experiment conducted by Thomas and Williams [136]. a): Soap bubble filled with combustible gaseous mixture undergoing combustion. b): Resulting time series of the radiated acoustic pressure. c): Magnitude of the corresponding signal Fourier transform over frequency f	4
1.3	General shape of the spectrum of sound pressure emitted by an open burning turbulent swirl flame compared with the spectrum of a confined turbulent swirl flame inside a combustion chamber. The hatched area marks the typical frequency range for peak frequencies of turbulent hydrocarbon flames. Both spectra have been normalized with their corresponding maximum value for better comparability.	5
2.1	Schlieren image of a turbulent jet at large Reynolds number. The distribution of vortices of different sizes along the widening jet is clearly visible (from [140]).	14
2.2	The effect of a simple two-dimensional vortex on an initially straight interface line (indicated by the dashed line) separating two fluid zones plotted over the normalized vortex radius. While fluid is transported by convection, the length of the interface line representing the surface area of the fluid fluid interface is increased. . .	15
2.3	Model spectrum of turbulence kinetic energy as given by Tennekes & Lumley [134]. The size of the inertial subrange is governed by the spread between the integral length scale l_t and the Kolmogorov length scale η_{kol}	19

LIST OF FIGURES

2.4	Regime diagram of non-premixed turbulent combustion.	25
2.5	Regime diagram of premixed turbulent combustion.	27
2.6	Two dimensional mixing of unburnt and burnt gas by a simple vortex in the case of infinitely fast chemistry. The contact surface area between fresh gas and exhaust gas governs the local reaction rate. The increase in contact surface area is determined by the rate of turbulent mixing.	35
2.7	Scatter plot comparing the results of direct and PDF-averaged computation of the laminar flamespeed for an unconfined turbulent premixed flame at $P_{th} = 40\text{kW}$, $S = 0.8$ and $\lambda = 1.1$. Fluctuations of the local mixture fraction caused by the entrainment of ambient air into the flame are accounted for in the PDF-averaged value of the laminar flamespeed.	39
2.8	Sample plot demonstrating the clipping procedure that is used to fulfill the conservation of probability in the modified distribution. The unwanted tail below $x = 0$ is cut away and added to the clipped distribution as a dirac delta at the lower interval boundary.	40
3.1	Sketch of a turbulent flame assembled from n single sources $\vec{x}_{s, n}$ as in (3.9), showing the observer location \vec{x}_B in the acoustic farfield. As the distance between the flame and the observer position is large compared to the size of the flame, the radius between observer and individual sources is taken equal for all sources.	46
3.2	Plane wave reflection and sound radiation at an open pipe termination. The virtual extended pipe length δ which represents the phase-shift upon reflection is indicated at the exit plane.	52
3.3	Magnitude of the end reflection coefficient (left) and extended length scale (right) of an unflanged duct termination calculated using Eq. (3.35) and Eq. (3.36).	53
3.4	Plane-wave reflection and sound radiation at an open pipe termination in the presence of mean flow as considered by Munt [91,92].	54

3.5	Magnitude of the pressure reflection coefficient ($ \hat{r} $) and the energy reflection coefficient (r_E) at a circular pipe exit plane for an exhaust flow temperature of $T_i = 1900$ K and an ambient temperature of $T_\infty = 293$ K calculated using the Munt model [91, 92] (—) compared to the isothermal solution of Levine & Schwinger [77] (—).	54
4.1	Paradigmatic concept of coherent noise sources in a turbulent flame. The spatial coherence of the fluctuating heat release rate is accounted for by statistical coherence volumes, inside which the heat release rate is assumed to be completely coherent.	65
4.2	Contour plot of radiated acoustic power for different turbulent time scales over peak frequency as predicted by the simplified noise model analysis. The evaluation of the expression for the peak frequency (Eq. (4.49)) is shown by the dashed line.	75
5.1	Schematic of the open turbulent flame test rig. The flame can be operated in premixed or non-premixed configuration.	80
5.2	Cross sectional view of the geometric quantities of the movable-block swirler unit determining the swirl number (adapted from [76]). The swirl number can be adjusted continuously by altering the ratio between radial and tangential momentum of the flow.	82
5.3	Swirl number of the movable-block swirl generator depending on the adjustable block angle ξ . The maximum block angle of $\xi_m = 15^\circ$ leads to a maximum swirl number of $S = 1.86$	83
5.4	Schematic of the basic nozzle dimensions and general properties of the flow field of the flame produced by the movable-block burner in non-premixed configuration. Natural gas fuel enters the inner shear layer through narrowly spaced injection holes in the center body. Combustion products are recirculated along the burner axis downstream of the center body.	84
5.5	Flame types at $P_{th} = 50$ kW, $\lambda = 1.2$ and $S = 0.6$	85
5.6	Measures to improve the acoustic properties of the laboratory.	87
5.7	Magnitude of the normal incidence reflection coefficient of the sound absorbing panels enclosing the flame [143].	88

5.8	Schematic of the measurement setup showing the probe support frame and the individual measurement positions on the measurement surfaces $S_{k,i}$ enclosing the flame.	89
5.9	Sound power spectra for the 18 individual measurement positions and ratio functions computed from active intensity data. The plots show 6 spectra for each of the 3 face levels described in Fig. 5.8. Sound power level calculated with reference of $P_{\text{ref}} = 1 \cdot 10^{-12} \text{W}$. The bottom plot shows the calibration function ζ relating the sound power represented by a single measurement surface to the total sound power radiated by the flame. The calibration function is plotted based on active and reactive sound intensity used in the calculation of sound power.	91
5.10	Determination of the peak frequency using a polynomial fit function in the lower frequency range.	92
5.11	Active (I) and reactive (J) part of sound intensity radiated by a turbulent non-premixed flame. The influence of the reverberant sound field is visible below 100Hz in the reactive part of the spectrum, where the acoustic damping potential of the laboratory is low. The spectra are calculated by averaging over 10 individual spectra. . .	95
5.12	100 single spectra of active acoustic intensity calculated from time series recorded at a constant operating point of $P_{\text{th}} = 50 \text{kW}$, $\lambda = 1.2$ and $S = 0.6$ of the non-premixed flame.	96
6.1	Regime diagram of non-premixed turbulent combustion. The symbols show the location of the operating points listed in Tab. 6.1. . .	101
6.2	Flame shapes at different thermal power settings for a swirl number of $S = 0.6$ and an air excess ratio of $\lambda = 1.2$	101
6.3	Spectral sound power emitted by the turbulent non-premixed flame at a swirl number of $S = 0.6$, an air excess ratio of $\lambda = 1.2$ and three different power settings.	102
6.4	Dependency of peak frequency and thermo-acoustic efficiency on the thermal power setting of the non-premixed flame at $S = 0.6$, $\lambda = 1.2$. between $P_{\text{th}} = 30 \text{kW}$ and $P_{\text{th}} = 70 \text{kW}$	103
6.5	Effect of mixture composition on sound power spectra of the non-premixed flame at $S = 0.6$ and $P_{\text{th}} = 50 \text{kW}$	104

6.6	Effect of mixture composition on peak frequency and conversion efficiency of the non-premixed flame at $S = 0.6$ and $P_{th} = 50\text{kW}$	105
6.7	Effect of swirl number on the frequency spectrum of sound power. For swirl numbers in excess of $S = 1.0$, the flame length stagnates, leading to stagnating thermo-acoustic conversion efficiencies.	106
6.8	Flame images at different swirl numbers at a thermal Power of $P_{th} = 50\text{kW}$ and an air excess ratio of $\lambda = 1.2$. Beyond $S = 1.0$, the flame length remains unaltered by the swirl intensity.	107
6.9	Peak frequency and thermo-acoustic conversion efficiency of the non-premixed flame for different swirl numbers. While the conversion efficiency stagnates due to stagnating flame size at swirl numbers in excess of $S = 1$, f_{peak} shows further increase due to increasing turbulence intensity.	107
6.10	Contours of thermo-acoustic conversion efficiency over thermal power and air excess ratio for the non-premixed flame at $S = 0.6$	108
6.11	Contours of peak frequency over thermal power and air excess ratio for the non-premixed flame at $S = 0.6$	108
6.12	Comparison of integral chemiluminescence intensity and heat release of a premixed turbulent swirl flame of $P_{th} = 60\text{kW}$ (adapted from Lauer [72]). The curves are normalized by their corresponding maximum values and show a close match between the integral bandpass filtered OH^* intensity and the integral heat release for air excess ratios up to $\lambda = 1.25$	110
6.13	Comparison of OH^* radiation of the open burning (left) and confined (right) turbulent premixed flame at $S = 0.8$, $P_{th} = 40\text{kW}$, $\lambda = 1.0$. The wall of the glass cylinder for the confined flame is located at $X = 160\text{mm}$	111
6.14	Limits of stable flame operation for the unconfined turbulent premixed flame at $S = 0.6$	112
6.15	Global OH^* radiation intensity for the open turbulent premixed flame at $S = 0.6$. The curves have been normalized with the maximum intensity value recorded at $\lambda = 1.0$	113
6.16	Burnout efficiency ζ_{OH} for the open premixed flame at $S = 0.6$ for varying mixture composition and thermal power output.	114

6.17	Sound power spectra for the turbulent premixed swirl flame at $S = 0.6$, $\lambda = 1.0$	115
6.18	Peak frequencies and conversion efficiencies for the turbulent premixed flame at $S = 0.6$, $\lambda = 1.0$ over burnout corrected thermal power.	116
6.19	Comparison of mean OH* radiation intensity between a non-premixed (left) and premixed (right) swirl flame at $S = 0.8$, $P_{th} = 40\text{kW}$, $\lambda = 1.0$	117
6.20	Comparison between sound power spectra of Reynolds scaled non-premixed flame and burnout corrected premixed flame for $P_{calib} = 45\text{kW}$. The resulting spectra from both flames show close proximity.	119
7.1	Schematic of the noise calculation for the premixed and the non-premixed case. The post-processing toolbox for the non-premixed case is explicitly developed for large amounts of input data.	122
7.2	Two-dimensional domain setup and computational grid for the premixed flame simulations.	124
7.3	Qualitative comparison of flame shape between normalized heat release rate from CFD (right) and normalized OH* intensity from experiment (left). The flame is operated at $P_{th} = 40\text{kW}$, $S = 0.8$ and $\lambda = 1.0$	125
7.4	Effect of entrainment on the unburnt air excess ratio λ_{ub} for the operating point PPV4. (—): $\lambda = 1.00$, (—): $\lambda = 1.75$, (—): $\lambda = 2.50$, (—): $\lambda = 4.10$, (—): $\lambda = 7.00$	127
7.5	Model predictions obtained for the premixed operating points of 30kW (PPV1), 40kW (PPV3) and 45kW (PPV4) thermal power at $\lambda = 1.0$. Continuous lines mark experimental data, dashed lines show the numerical results.	128
7.6	Comparison of spectra calculated from identical input data with the original amplitude scaling and the PDF-based function.	130
7.7	Influence of the choice of the turbulence model in CFD on the resulting acoustic power spectrum calculated for PPV4.	131

7.8	Computational 3D domain used in the flow field simulation for the non-premixed flame configuration. The contour levels show fluid temperature for the DSV6 case.	133
7.9	Detail view of the computational grid in the vicinity of the burner nozzle.	134
7.10	Comparison of axial velocity between experimental data given by Hillemanns [50] and numerical results using the $k-\varepsilon$ -model in the burner exit plane for cold flow conditions at $Re = 163000$	135
7.11	Contours of temperature for three different air excess ratios at $P_{th} = 50\text{kW}$, $S = 0.6$. Velocity vectors indicate the tangential velocity in the section plane.	136
7.12	Contours of reaction source term for three different air excess ratios at $P_{th} = 50\text{kW}$, $S = 0.6$. The dashed line indicates the line of stoichiometric mixture, $z = z_{st}$	136
7.13	Computed local peak frequency of the emitted noise for the 30kW and 70kW non-premixed flame at $\lambda = 1.2$ and $S = 0.6$. Non-zero values of the peak frequency are given for non-zero values of the local heat release only.	138
7.14	Comparison of experimentally determined and modeled sound power spectra emitted from turbulent non-premixed flames at a swirl number of $S = 0.6$, an air excess ratio of $\lambda = 1.2$ and thermal power settings of 30kW, 50kW and 70kW. (—): Experiment, (- - -): Model.	140
7.15	Influence of mixture composition on sound radiation from a turbulent non-premixed swirl flame at $P_{th} = 50\text{kW}$ and $S = 0.6$. (—): Experiment, (- - -): Model.	141
7.16	Influence of swirl intensity on sound radiation from a turbulent non-premixed flame at $P_{th} = 50\text{kW}$ and $\lambda = 1.2$. (—): Experiment, (- - -): Model.	142
7.17	Influence of the minimum reaction rate bounding the volume of data extraction from the CFD solution.	143

8.1	Schematic of the modified Webasto Thermo 90 ST coolant heater used in the acoustic experiments. Liquid diesel fuel is injected into a metal fleece plate on the bottom of the combustion chamber. After evaporation and mixing with the combustion air entering the combustion chamber through holes in the combustion chamber wall, combustion and burnout is performed inside the combustion chamber and the burnout tube.	146
8.2	Experimental setup for the measurement of combustion noise radiated by the marine coolant heater.	147
8.3	Acoustic intensity spectrum radiated by the diesel heater for different mixture compositions. The thermal power output is kept constant at 8kW.	148
8.4	One-dimensional acoustic network representation of the diesel heater. The acoustic two-port elements denote R: reflecting boundary, D: duct, AC: discontinuity in cross sectional area, TC: discontinuity in fluid density (temperature) and S: flame element for combustion noise.	151
8.5	Magnitude of the pressure reflection coefficient of the evaporator fleece over frequency.	151
8.6	Magnitude of the pressure and energy reflection coefficient at the burner exhaust plane for a mean flow temperature of 1900K calculated using the Munt model (—) compared to the isothermal solution of Levine & Schwinger (—).	152
8.7	Comparison between experimental results (—) for sound power level and numerical predictions (- - -) obtained with the network model including the corresponding combustion noise source term.	154
A.1	Color coded contour plot showing the number of iterations needed by the stabilized Newton algorithm to converge to a solution depending on the initial value pair of mean and variance.	163
C.1	Reflection coefficient boundary condition shown for upstream and downstream boundary.	167
C.2	One-dimensional duct model in terms of the Riemann invariants.	168

C.3 Acoustic state variables at an exemplary area expansion element.
The element is assumed to be acoustically compact. 169

LIST OF FIGURES

List of Tables

1.1	Overview of experimental studies on combustion noise with reported ranges for peak frequency and efficiency of conversion between thermal and acoustic energy for hydrocarbon premixed (P) and non-premixed (NP) flames.	7
1.2	Overview of hybrid numerical methods used in the prediction of turbulent combustion noise.	8
3.1	Constants needed for the approximate calculation of the pipe termination reflection coefficient [117].	52
4.1	Constant parameter values used in the analysis of the simplified non-premixed combustion noise model.	74
5.1	Dimensions of the movable-block swirl generator.	83
6.1	Operating points investigated for the non-premixed flame. The reference operating point is marked in gray.	100
6.2	Operating points investigated for the premixed flame configuration. P_{th} denotes the theoretical thermal power setting calculated from the supplied fuel mass flow rate, while P_{calib} is the actual thermal power released by the flame obtained with the calibration procedure.	114
6.3	Comparison of peak frequencies and acoustic conversion efficiencies of premixed and non-premixed flame for burnout corrected thermal power output at $S = 0.6$ and $\lambda = 1.0$	117

LIST OF TABLES

6.4	Operating conditions selected for the direct comparison of pre-mixed and non-premixed combustion noise spectra. The burnout correction of the premixed flame results in a higher nozzle Reynolds number, which is matched for the corresponding non-premixed flame by adjusting the global air excess ratio.	119
7.1	Comparison between burnout efficiencies determined from experimental data (ζ_{OH}) and calculated from CFD (ζ_{CFD}) showing good agreement between experiment and simulation.	126
7.2	Operating points for different thermal power settings simulated with the non-premixed combustion noise model.	139

References

- [1] Normenausschuss Technische Grundlagen (NATG) ISO 5167-2:2003. Measurement of Fluid Flow by Means of Pressure Differential Devices Inserted in Circular Cross-Section Conduits Running Full – Part 2: Orifice Plates (ISO 5167-2:2003); German Version EN ISO 5167-2:2003, 2004.
- [2] S. Allam and M. Åbom. Investigation of Damping and Radiation Using full Plane Wave Decomposition in Ducts. *Journal of Sound and Vibration*, 292(3-5):519 – 534, 2006.
- [3] C. Bailly, P. Lafon, and S. Candel. Prediction of Supersonic Jet Noise from a Statistical Acoustic Model and a Compressible Turbulence Closure. *Journal of Sound and Vibration*, 194(2):219–242, 1996.
- [4] G. K. Batchelor. *The Theory of Homogeneous Turbulence*. Cambridge Monographs on Mechanics and Applied Mathematics, Cambridge University Press., Cambridge, 1953.
- [5] W. Béchara, C. Bailly, P. Lafon, and S. Candel. Stochastic Approach to Noise Modeling for Free Turbulent Flows. *AIAA Journal*, 32(3):455–463, 1994.
- [6] J. M. Beér and N. A. Chigier. *Combustion Aerodynamics*. Applied Science Publishers LTD London, 1972.
- [7] R. W. Bilger. Turbulent Diffusion Flames. *Annual Review of Fluid Mechanics*, 21(1):101–135, 1989.

REFERENCES

- [8] R. W. Bilger, S. B. Pope, K. N. C. Bray, and J. F. Driscoll. Paradigms in Turbulent Combustion Research . *Proceedings of the Combustion Institute*, 30(1):21 – 42, 2005.
- [9] D. Blacodon. Combustion-Noise Characterization of a Turbofan Engine with a Spectral Estimation Method. *Journal of Propulsion and Power*, 25(2):374–379, March 2009.
- [10] P. Boineau, Y. Gervais, and V. Morice. An Aerothermoacoustic Model for Computation of Sound Radiated by Turbulent Flames. Number INCE:21.3.2 in *Proceedings of Internoise 96*, page 3, Liverpool, 1996.
- [11] P. Boineau, Y. Gervais, and M. Toquard. Spatio-Frequential Optical Measurements of Acoustic Sources in a Turbulent Flame. *Proc. Internoise 97*, page 4, Budapest, Hungary, August 25-27 1997.
- [12] R. Borghi. Turbulent combustion modelling. *Prog. Energy Combust. Sci.*, 14:245–292, 1988.
- [13] S. L. Bragg. Combustion Noise. *Journal of the Institute of Fuel*, 36:12–16, 1963.
- [14] T. P. Bui and W. Schröder. Theoretical and Numerical Analysis of Broadband Combustion Noise. In *Combustion Noise*, pages 175–215. Springer Berlin Heidelberg, 2009.
- [15] T. P. Bui, W. Schröder, and M. Meinke. Acoustic Perturbation Equations for Reacting Flows to Compute Combustion Noise. *International Journal of Aeroacoustics*, 6(4):335–355, December 2007.
- [16] S. Candel, D. Durox, S. Ducruix, A. L. Birbaud, N. Noiray, and T. Schuller. Flame Dynamics and Combustion Noise: Progress and Challenges. *International Journal of Aeroacoustics*, 8(1):1 – 56, January 2009.
- [17] P. Capros, A. De Vita, N. Tasios, D. Papadopoulos, P. Siskos, E. Apostolaki, M. Zampara, L. Paroussos, K. Fragiadakis, and N. Kouvaritakis. EU Energy, Transport and GHG Emissions Trends to 2050, Reference Scenario 2013. Technical report, European Commission, Directorate-General

- for Energy, Directorate-General for Climate Action and Directorate-General for Mobility and Transport, Publications Office of the European Union, Luxembourg, 2013.
- [18] R. K. Cheng, I. G. Shepherd, and I. Gökalp. A Comparison of the Velocity and Scalar Spectra in Premixed Turbulent Flames. *Combustion and Flame*, 78(2):205 – 221, 1989.
- [19] B. T. Chu. *Mechanism of Generation of Pressure Waves at Flame Fronts*. Technical note. National Advisory Committee for Aeronautics, 1956.
- [20] J. Y. Chung. Cross-Spectral Method of Measuring Acoustic Intensity Without Error Caused by Instrument Phase Mismatch. *The Journal of the Acoustical Society of America*, 64(6):1613–1616, 1978.
- [21] P. Clavin and E. D. Siggia. Turbulent Premixed Flames and Sound Generation. *Combustion Science and Technology*, 78:147–155, 1991.
- [22] S. Corrsin. Simple Theory Of An Idealized Turbulent Mixer. *AIChE Journal*, 3(3):329–330, 1957.
- [23] S. Corrsin. The Reactant Concentration Spectrum in Turbulent Mixing with a First-order Reaction. *J. of Fluid Mech.*, 11:407–416, 1961.
- [24] A. Craggs. The Use of Simple Three-Dimensional Acoustic Finite Elements for Determining the Natural Modes and Frequencies of Complex Shaped Enclosures . *Journal of Sound and Vibration*, 23(3):331 – 339, 1972.
- [25] D. G. Crighton, A. P. Dowling, J. E. Ffowcs Williams, M. Heckl, and F. G. Leppington. *Modern Methods in Analytical Acoustics*. Springer Verlag, 1992.
- [26] N. A. Cumpsty and F. E. Marble. Core Noise from Gas Turbine Exhausts. *Journal of Sound and Vibration*, 54(2):297 – 309, 1977.
- [27] M. E. Delany and E. N. Bazley. Acoustical Properties of Fibrous Absorbent Materials. *Applied Acoustics*, 3(2):105 – 116, 1970.

REFERENCES

- [28] Acoustics - Determination of Sound Power Levels of Noise Sources Using Sound Intensity - Part 1: Measurement at Discrete Points (ISO 9614-1:1993); German Version EN ISO 9614-1:2009, 2009.
- [29] P. Duchaine, L. Zimmer, and T. Schuller. Experimental Investigation of Mechanisms of Sound Production by Partially Premixed Flames. *Proceedings of the Combustion Institute*, 32(1):1027 – 1034, 2009.
- [30] V. Easwaran and M. L. Munjal. Finite Element Analysis of Wedges Used in Anechoic Chambers. *Journal of Sound and Vibration*, 160(2):333 – 350, 1993.
- [31] B. Eckhardt, T. M. Schneider, B. Hof, and J. Westerweel. Turbulence Transition in Pipe Flow. *Annu. Rev. Fluid Mech.*, 39:447–468, 2007.
- [32] K. Ehrenfried. Skript zur Vorlesung Strömungsakustik 1. Technical report, Technische Universität Berlin, 2002.
- [33] S. Elfeky, A. Penninger, L. Karpati, and A. Bereczky. Noise Emission from Open Turbulent Premixed Flame. *Periodica Polytechnica Ser. Mech. Eng.*, 40(2):85–102, 1996.
- [34] R. Ewert, J. Dierke, A. Neifeld, C. Appel, M. Siefert, and O. Kornow. CAA Broadband Noise Prediction for Aeroacoustic Design. *Procedia Engineering*, 6(0):254 – 263, 2010. IUTAM Symposium on Computational Aero-Acoustics for Aircraft Noise Prediction.
- [35] F. J. Fahy. Measurement of Acoustic Intensity Using the Cross-Spectral Density of two Microphone Signals. *The Journal of the Acoustical Society of America*, 62(4):1057–1059, 1977.
- [36] F. J. Fahy. Measurements with an Intensity Meter of the Acoustic Power of a Small Machine in a Room. *Journal of Sound and Vibration*, 57(3):311 – 322, 1978.
- [37] F. J. Fahy. *Sound Intensity*. Elsevier Applied Science, London u.a., 1989.
- [38] F. J. Fahy. International Standards for the Determination of Sound Power Levels of Sources Using Sound Intensity Measurement: An Exposition. *Applied Acoustics*, 50(2):97 – 109, 1997.

-
- [39] D. Feikema, R.-H. Chen, and J. F. Driscoll. Enhancement of Flame Blowout Limits by the Use of Swirl. *Combustion and Flame*, 80(2):183 – 195, 1990.
- [40] A. Fischer. *Hybride, thermoakustische Charakterisierung von Drallbrennern*. PhD thesis, Technische Universität München, 2004.
- [41] S. C. Fisher and S. A. Rahman, editors. *Remembering the Giants: Apollo Rocket Propulsion Development*. Monographs in Aerospace History, No. 45, 2009. (NASA SP-2009-4545), 2009.
- [42] F. Flemming, A. Sadiki, and J. Janicka. Investigation of Combustion Noise Using a LES/CAA Hybrid Approach. *Proceedings of the Combustion Institute*, 31(2):3189 – 3196, 2007.
- [43] T. J. Fudihara, L. Goldstein Jr., and M. Mori. The Three-Dimensional Numerical Aerodynamics of a Movable Block Burner. *Brazilian Journal of Chemical Engineering*, 20:391 – 401, 10 2003.
- [44] A. Gentemann, A. Fischer, S. Evesque, and W. Polifke. Acoustic Transfer Matrix Reconstruction and Analysis for Ducts with Sudden Change of Area. In *9th AIAA/CEAS Aeroacoustics Conference and Exhibit*, number AIAA-2003-3142, page 11, Hilton Head, SC, USA, May 2003. AIAA.
- [45] P. Gerlinger. *Numerische Verbrennungssimulation: effiziente numerische Simulation turbulenter Verbrennung*. Springer, Berlin [u.a.], 2005.
- [46] R. D. Giammar and A. A. Putnam. Noise Generation by Turbulent Flames. Internal report, Battelle - Columbus, 1969.
- [47] R. D. Giammar and A. A. Putnam. Combustion Roar of Premix Burners, Singly and in Pairs. *Combust. and Flame*, 18(3):435–438, 1972.
- [48] M. M. Gibson and B. E. Launder. Ground Effects on Pressure Fluctuations in the Atmospheric Boundary Layer. *Journal of Fluid Mechanics*, 86:491–511, 6 1978.
- [49] F. Han, G. Seiffert, Y. Zhao, and B. Gibbs. Acoustic Absorption Behaviour of an Open-Celled Aluminium Foam. *Journal of Physics D: Applied Physics*, 36(3):294, 2003.

- [50] R. Hillemanns. *Das Strömungs- und Reaktionsfeld sowie Stabilisierungseigenschaften von Drallflammen unter dem Einfluss der inneren Rezirkulationszone*. PhD thesis, Engler-Bunte-Institut, TH Karlsruhe, 1988.
- [51] C. Hirsch, D. Fanaca, P. Reddy, W. Polifke, and T. Sattelmayer. Influence of the Swirler Design on the Flame Transfer Function of Premixed Flames. In *Proceedings of the ASME Turbo Expo*, number GT2005-68195, Reno-Tahoe, Nevada, USA, June 6-9 2005. ASME.
- [52] C. Hirsch, J. Wäsle, A. Winkler, and T. Sattelmayer. A Spectral Model for the Sound Pressure from Turbulent Premixed Combustion. In *31st Symposium (Int.) on Combustion*, pages 1435–1441, 2006.
- [53] C. Hirsch, A. Winkler, J. Wäsle, and T. Sattelmayer. Calculating the Turbulent Noise Source of Premixed Swirl Flames from Time Mean Reactive RANS Variables. In *13th International Congress on Sound and Vibration*, 2006.
- [54] S. Hochgreb. Measurements in Thermoacoustic Systems: Pressure, Velocity, Chemiluminescence and Imaging. Presentation, Technische Universität München, May 2014.
- [55] S. Hoffmann. *Untersuchungen des Stabilisierungsverhaltens und der Stabilitätsgrenzen von Drallflammen mit innerer Rückströmzone*. PhD thesis, TH Karlsruhe, 1994.
- [56] I. R. Hurle, R. B. Price, T. M. Sugden, and A. Thomas. Sound Emission from Open Turbulent Premixed Flames. *Proceedings of the Royal Society of London A*, 303:409–427, 1968.
- [57] M. Ihme, D. J. Bodony, and H. Pitsch. Prediction of Combustion-Generated Noise in Non-Premixed Turbulent Jet Flames Using Large-Eddy Simulation. *AIAA paper*, 2614:2006, 2006.
- [58] M. Ihme and H. Pitsch. On the Generation of Direct Combustion Noise in Turbulent Non-Premixed Flames. *International Journal of Aeroacoustics*, 11(1):25–78, 2012.

-
- [59] M. Ihme, H. Pitsch, and D. J. Bodony. Radiation of Noise in Turbulent Non-Premixed Flames. *Proceedings of the Combustion Institute*, 32(1):1545 – 1553, 2009.
- [60] ANSYS Inc. *ANSYS Fluent 14.0 Theory Guide*, 2009.
- [61] F. Jacobsen. Active and Reactive, Coherent and Incoherent Sound Fields. *Journal of Sound and Vibration*, 130(3):493 – 507, 1989.
- [62] C. Jörg, J. Gikadi, and T. Sattelmayer. Numerical Investigation of the Plane-Wave Reflection Coefficient of an Exhaust Pipe at Elevated Temperatures Using Linearized Navier-Stokes Equations. In *Proceedings of the ASME Turbo Expo*, number GT2013-94843, San Antonio, TX, USA, June 3-7 2013.
- [63] C. Jörg, M. Wagner, and T. Sattelmayer. Experimental Investigation of the Acoustic Reflection Coefficient of a Modeled Gas Turbine Impingement Cooling Section. In *Proceedings of the ASME Turbo Expo*, number GT2012-68916, Copenhagen, Denmark, June 11-15 2012.
- [64] J. Jörg. *Über den Rollvorgang in einem Walzenpaar und die Kraftübertragung auf eine durchlaufende Stoffbahn*. PhD thesis, Technische Universität München, München, 1979.
- [65] M. Katsuki, Y. Mizutani, C. Mototaka, and T. Kittaka. Sound Emission from a Turbulent Flame. *21st Symposium (International) on Combustion*, 21:1543–1550, 1986.
- [66] A. Kierkegaard, S. Allam, G. Efrainsson, and M. Åbom. Simulations of Whistling and the Whistling Potentiality of an in-Duct Orifice with Linear Aeroacoustics. *Journal of Sound and Vibration*, 331(5):1084 – 1096, 2012.
- [67] S. A. Klein. *On the Acoustics of Turbulent Non-Premixed Flames*. PhD thesis, Universität Twente, 2000.
- [68] A. N. Kolmogorov. The Local Structure of Turbulence in Incompressible Viscous Fluid for very Large Reynolds Numbers. *Proceedings of the*

REFERENCES

- Royal Society of London. Series A: Mathematical and Physical Sciences*, 434(1890):9–13, 1991.
- [69] S. Kotake and K. Hatta. On the Noise of Diffusion Flames. *Bulletin of JSME*, 8(30):211–219, 1965.
- [70] S. Kotake and K. Takamoto. Combustion Noise: Effects of the Shape and the Size of Burner Nozzle. *Journal of Sound and Vibration*, 112(2):345–354, 1987.
- [71] R. N. Kumar. Further Experimental Results on the Structure and Acoustics of Turbulent Jet Flames. *AIAA Paper*, (75-523), 1975.
- [72] M. Lauer. *Determination of the Heat Release Distribution in Turbulent Flames by Chemiluminescence Imaging*. PhD thesis, Technische Universität München, München, 2011.
- [73] B. E. Launder. Second-Moment Closure and its use in Modelling Turbulent Industrial Flows. *International Journal for Numerical Methods in Fluids*, 9(8):963–985, 1989.
- [74] B. E. Launder and D. B. Spalding. *Lectures in Mathematical Models of Turbulence*. Academic Press, London, 1972.
- [75] C. K. Law. *Combustion Physics*. Cambridge University Press, Cambridge, 2006.
- [76] W. Leuckel. *Swirl Intensities, Swirl Types and Energy Losses of Different Swirl Generating Devices*. IFRF Doc Nr. G 02/a/16, 1967.
- [77] H. Levine and J. Schwinger. On the Radiation of Sound from an Unflanged Circular Pipe. *Physical Review*, 73(4):383–406, Feb 1948.
- [78] T. Lieuwen and R. Rajaram. Acoustic Radiation from Premixed Flames Subjected to Convected Flow Disturbances. In *40th AIAA Aerospace Sciences Meeting and Exhibit*, AIAA-02-0480, 2002.
- [79] M. J. Lighthill. On Sound Generated Aerodynamically, I. General Theory. In *Proceedings of the Royal Society of London*, volume 211, pages 564–586, 1951.

-
- [80] F. C. Lockwood and A. S. Naguib. The Prediction of the Fluctuations in the Properties of Free, Round-Jet, Turbulent Diffusion Flames. *Combustion and Flame*, 24:109–124, 1975.
- [81] T. Lutz, A. Herrig, W. Würz, M. Kamruzzaman, and E. Krämer. Design and Wind-Tunnel Verification of Low-Noise Airfoils for Wind Turbines. *AIAA Journal*, 45(4):779–785, April 2007.
- [82] B. F. Magnussen. On the Structure of Turbulence and a Generalized Eddy Dissipation Concept for Chemical Reaction in Turbulent Flow. *19th Aerospace Science Meeting, St. Louis, Missouri*, page 6, January 1981.
- [83] B. F. Magnussen and B. H. Hjertager. On Mathematical Modeling Of Turbulent Combustion With Special Emphasis On Soot Formation And Combustion. *16th Symposium (International) on Combustion*, 16(1):719 – 729, 1977.
- [84] P. Maier. Untersuchung isothermer drallbehafteter Freistrahlen. *Forschung im Ingenieurwesen A*, 34(5):133–140, 1968.
- [85] J. H. Miles. Time Delay Analysis of Turbofan Engine Direct and Indirect Combustion Noise Sources. *Journal of Propulsion and Power*, 25(1), 2009.
- [86] F. Mittermayer. *CFD - Simulation der Zündung und Verbrennung in einem vorkammergezündeten Grossgasmotor*. PhD thesis, Technische Universität München, 2011.
- [87] C. J. Mueller, J. F. Driscoll, D. L. Reuss, M. C. Drake, and M. E. Rosalik. Vorticity Generation and Attenuation as Vortices Convect Through a Premixed Flame. *Combustion and Flame*, 112(3):342 – 358, 1998.
- [88] B. Mühlbauer, R. Ewert, O. Kornow, and B. Noll. Evaluation of the RPM Approach for the Simulation of Broadband Combustion Noise. *AIAA journal*, 48(7):1379–1390, 2010.
- [89] B. Mühlbauer, R. Ewert, O. Kornow, B. Noll, and M. Aigner. Numerical Simulation of Broadband Combustion Noise With the RPM-CN Ap-

REFERENCES

- proach. In *Proceedings of the ASME Turbo Expo*, number GT2009-59870, Orlando, FL, USA, June 8-12 2009.
- [90] B. Mühlbauer, R. Ewert, O. Kornow, B. Noll, J. Delfs, and M. Aigner. Simulation of Combustion Noise Using CAA with Stochastic Sound Sources from RANS. In *Aeroacoustics Conferences*. AIAA, 2008.
- [91] R. M. Munt. The Interaction of Sound with a Subsonic Jet Issuing from a semi-Infinite Cylindrical Pipe. *Journal of Fluid Mechanics*, 83(04):609–640, 1977.
- [92] R. M. Munt. Acoustic Transmission Properties of a Jet Pipe with Subsonic Jet Flow: I. The cold Jet Reflection Coefficient. *Journal of Sound and Vibration*, 142(3):413 – 436, 1990.
- [93] X. Ni, H. Jian, and A. Fitch. Evaluation of Turbulent Integral Length Scale in an Oscillatory Baffled Column Using Large Eddy Simulation and Digital Particle Image Velocimetry . *Chemical Engineering Research and Design*, 81(8):842 – 853, 2003. Particle Technology.
- [94] N. Ohiwa, K. Tanaka, and S. Yamaguchi. Noise Characteristics of Turbulent Diffusion Flames with Coherent Structure. *Combustion Science and Technology*, 90:61–78, 1993.
- [95] V. C. Patel, W. Rodi, and G. Scheurer. Turbulence Models for Near-Wall and low Reynolds Number Flows - A Review. *AIAA Journal*, 23(9):1308–1319, September 1985.
- [96] G. Pavić. Measurement of Sound Intensity. *Journal of Sound and Vibration*, 51(4):533 – 545, 1977.
- [97] M. C. A. M. Peters, A. Hirschberg, A. J. Reijnen, and A. P. J. Wijnands. Damping and Reflection Coefficient Measurements for an Open Pipe at low Mach and low Helmholtz Numbers. *Journal of Fluid Mechanics*, 256:499–534, 11 1993.
- [98] N. Peters. *Turbulent Combustion*. Cambridge University Press, 2000. ISBN 0-521-66082-3.

-
- [99] M. V. Pham, F. Plourde, and S. D. Kim. Effect of Swirl on Pure Turbulent Thermal Plume Development. *International Journal of Heat and Fluid Flow*, 27(3):502 – 513, 2006.
- [100] M. Philipp. *Experimentelle und theoretische Untersuchungen zum Stabilitätsverhalten von Drallflammen mit zentraler Rückströmzone*. PhD thesis, TH Karlsruhe, 1991.
- [101] T. Poinso and D. Veynante. *Theoretical and Numerical Combustion*. Edwards, Philadelphia, PA, 2. edition, 2005.
- [102] S. B. Pope. *Turbulent Flows*. Cambridge University Press, 2000. ISBN 978-0-521-59886-6.
- [103] A. Putnam and L. Faulkner. Overview of Combustion Noise. *Journal of Energy*, 7(6):458–469, 1983.
- [104] L. Råde and B. Westergren. *Springers mathematische Formeln : Taschenbuch für Ingenieure, Naturwissenschaftler, Informatiker, Wirtschaftswissenschaftler*. Springer, Berlin, 3. edition, 2000.
- [105] R. Rajaram, J. Gray, and T. Lieuwen. Premixed Combustion Noise Scaling: Total Power and Spectra. *AIAA paper*, 2612, 2006.
- [106] R. Rajaram and T. Lieuwen. Acoustic Radiation From Turbulent Premixed Flames. *Journal of Fluid Mechanics*, 637:357–385, 2009.
- [107] R. Rajaram, P. Preetham, and T. Lieuwen. Frequency Scaling of Turbulent Premixed Flame Noise. In *11th AIAA/CEAS Aeroacoustics Conference, AIAA-2005-2828*, 2005.
- [108] H. S. Ribner. Quadrupole Correlations Governing the Pattern of Jet Noise. *Journal of Fluid Mechanics*, 38:1–24, 8 1969.
- [109] S. W. Rienstra and A. Hirschberg. *An Introduction to Acoustics*. Eindhoven University of Technology, 2004.
- [110] T. Sattelmayer, J. Grünwald, and S. Steinbach. Wirbelmischer für SCR-Verfahren im PKW. *MTZ 1/2005*, pages 44–48, 2005.

REFERENCES

- [111] H.-P. Schmid. *Ein Verbrennungsmodell zur Beschreibung der Wärme-freisetzung von vorgemischten turbulenten Flammen*. PhD thesis, Fakultät für Chemieingenieurwesen, TH Karlsruhe, 1995.
- [112] H.-P. Schmid, P. Habisreuther, and W. Leuckel. A Model for Calculating Heat Release in Premixed Flames. *Combust. and Flame*, 113:79–91, 1998.
- [113] M. Schulze, M. Schmid, D. Morgenweck, S. Köglmeier, and T. Sattelmayer. A Conceptual Approach for the Prediction of Thermoacoustic Stability in Rocket Engines. In *Joint Propulsion Conferences*. American Institute of Aeronautics and Astronautics, 2013.
- [114] A. Schwarz and J. Janicka, editors. *Combustion Noise*. Springer Berlin Heidelberg, 2009.
- [115] B. N. Shivashankara, W. C. Strahle, and J. C. Handley. Combustion Noise Radiation by Open Turbulent Flames. In *AIAA paper 73-1025*, 1973.
- [116] C. F. Silva, M. Leyko, F. Nicoud, and S. Moreau. Assessment of Combustion Noise in a Premixed Swirled Combustor via Large-Eddy Simulation. *Computers & Fluids*, 78(0):1 – 9, 2013.
- [117] F. Silva, P. Guillemain, J. Kergomard, B. Mallaroni, and A.N. Norris. Approximation Formulae for the Acoustic Radiation Impedance of a Cylindrical Pipe. *Journal of Sound and Vibration*, 322(1–2):255 – 263, 2009.
- [118] A. V. Singh, M. Yu, A. K. Gupta, and K. M. Bryden. Investigation of Noise Radiation From a Swirl Stabilized Diffusion Flame with an Array of Microphones. *Applied Energy*, 112(0):313 – 324, 2013.
- [119] A. V. Singh, M. Yu, A. K. Gupta, and K. M. Bryden. Thermo-Acoustic Behavior of a Swirl Stabilized Diffusion Flame with Heterogeneous Sensors. *Applied Energy*, 106(0):1 – 16, 2013.
- [120] K. K. Singh, S. H. Frankel, and J. P. Gore. Study of Spectral Noise Emissions from Standard Turbulent Nonpremixed Flames. *AIAA Journal*, 42(5):931–936, 2004.

-
- [121] D. M. Small, A. D. Fitt, and M. T. Thew. The Influence of Swirl and Turbulence Anisotropy on CFD Modeling of Hydrocyclones. Presented at the Hydrocyclones 1996 International Meeting, St. Johns College, Cambridge, England, 1996.
- [122] T. J. B. Smith and J. K. Kilham. Noise Generation by Open Turbulent Flames. *Journal of the Acoustical Society of America*, 35(5):715–724, 1963.
- [123] P. R. Spalart and M. Shur. On the Sensitization of Turbulence Models to Rotation and Curvature. *Aerospace Science and Technology*, 1(5):297 – 302, 1997.
- [124] D. B. Spalding. Mixing and Chemical Reaction in Steady Confined Turbulent Flames. In *13th Symposium (International) on Combustion*, 1971.
- [125] D. B. Spalding. Development Of The Eddy-Break-Up Model Of Turbulent Combustion. *Symposium (International) on Combustion*, 16(1):1657 – 1663, 1977.
- [126] C. G. Speziale, S. Sarkar, and T. B. Gatski. Modelling the Pressure-Strain Correlation of Turbulence: an Invariant Dynamical Systems Approach. *Journal of Fluid Mechanics*, 227:245–272, 6 1991.
- [127] R. Stone, A. Clarke, and P. Beckwith. Correlations for the Laminar-Burning Velocity of Methane/Diluent/Air Mixtures Obtained in Free-Fall Experiments. *Combustion and Flame*, 114(3–4):546 – 555, 1998.
- [128] W. C. Strahle. On Combustion Generated Noise. *Journal of Fluid Mechanics*, 49(2):399–414, 1971.
- [129] W. C. Strahle. Combustion Noise. *Progress in Energy and Combustion Science*, 4:157–176, 1978.
- [130] W. C. Strahle. *Recent Advances in the Aerospace Sciences*, chapter A More Modern Theory of Combustion Noise, pages 103–114. New York, Plenum Press, 1985. ISBN A85-47304 23-31.

REFERENCES

- [131] W. C. Strahle and B. N. Shivashankara. Combustion Generated Noise in Gas Turbine Combustors. *Journal of Engineering for Power*, 98(2):242–246, 1976.
- [132] N. Syred and J. M. Beér. Combustion in Swirling Flows: A Review. *Combustion and Flame*, 23(2):143 – 201, 1974.
- [133] C. K. W. Tam, N. N. Pastouchenko, Je. Mendoza, and D. Brown. Combustion Noise of Auxiliary Power Units. *AIAA Paper*, (2005-2829), 2005.
- [134] H. Tennekes and J. L. Lumley. *A First Course in Turbulence*. The MIT Press, 11th printing edition, 1972. ISBN 0-262-200198.
- [135] P. Testud, Y. Aurégan, P. Moussou, and A. Hirschberg. The Whistling Potentiality of an Orifice in a Confined Flow Using an Energetic Criterion. *Journal of Sound and Vibration*, 325(4–5):769 – 780, 2009.
- [136] A. Thomas and G. T. Williams. Flame Noise: Sound Emission from Spark-Ignited Bubbles of Combustible Gas. In *Proceedings of the Royal Society of London*, volume 294, pages 449–466, 1966.
- [137] I. Veit. *Technische Akustik : Grundlagen der physikalischen, physiologischen und Elektroakustik*. Kamprath-Reihe. Vogel, Würzburg, 1996.
- [138] L. Vervisch and T. Poinsot. Direct Numerical Simulation of Non-premixed Turbulent Flames. *Annual Review of Fluid Mechanics*, 30(1):655–691, 1998.
- [139] V. M. Viebrock and M. J. Crocker. Miniature Anechoic Room Design. *Journal of Sound and Vibration*, 32(1):77 – IN2, 1974.
- [140] J. A. Volpe and G. S. Settles. Laser-Induced Gas Breakdown as a Light Source for Schlieren and Shadowgraph Particle Image Velocimetry. *Optical Engineering*, 45(8):080509 1–3, 2006.
- [141] Bilger R. W. A Note on Favre Averaging in Variable Density Flows. *Combustion Science and Technology*, 11(5-6):215–217, 1975.
- [142] H. Wang and W. K. George. The Integral Scale in Homogeneous Isotropic Turbulence. *Journal of Fluid Mechanics*, 459:429–443, 5 2002.

-
- [143] J. G. Wäsle. *Vorhersage der Lärmemission turbulenter Vormischflammen*. PhD thesis, Technische Universität München, 2007.
- [144] J. D. Weiler. *Numerical Simulation of Flame-Vortex Interactions in Natural and Synthetic Gas Mixtures*. PhD thesis, School of Aerospace Engineering, Georgia Institute of Technology, 2004.
- [145] P. D. Welch. The use of fast Fourier Transform for the Estimation of Power Spectra: a Method Based on Time Averaging over short, Modified Periodograms. *IEEE Transactions on Audio and Electroacoustics*, 15(2):70–73, 1967.
- [146] F. Weyermann. *Numerische Berechnung der Emission verbrennungsinduzierten Lärms automobiler Zusatzheizungen*. PhD thesis, Technische Universität München, May 2010.
- [147] F. Weyermann, C. Hirsch, and T. Sattelmayer. Numerische Simulation der Schallabstrahlung von eingeschlossenen turbulenten Flammen. In *Fortschritte der Akustik 2008*. DEGA, 2008.
- [148] D. C. Wilcox. *Turbulence Modeling for CFD*. DCW Industries, La Cañada, California, third edition, 2006.
- [149] F. A. Williams. *Combustion Theory : The Fundamental Theory of Chemically Reacting Flow Systems*. Combustion Science and Engineering Series. The Advanced Book Program. Perseus Books, Reading, Mass., second edition, 1999.
- [150] A. Winkler. *Validierung eines Modells zur Vorhersage turbulenten Verbrennungslärms*. PhD thesis, Technische Universität München, 2007.
- [151] A. Winkler, J. Wäsle, and T. Sattelmayer. Experimental Investigations on the Acoustic Efficiency of Premixed Swirl Stabilized Flames. In *11th AIAA/CEAS Aeroacoustics Conference, AIAA-2005-2908*, 2005.
- [152] A. Winkler, J. Wäsle, C. Hirsch, and T. Sattelmayer. Peak Frequency Scaling of Combustion Noise From Premixed Flames. In *13th International Congress on Sound and Vibration*, 2006.

REFERENCES

- [153] A. Winkler, J. Wäsle, C. Hirsch, and T. Sattelmayer. Validation of combustion noise modelling with optical measurement techniques. In *ICA Proceedings*, 2007.
- [154] J. Wäsle, A. Winkler, M. Lauer, and T. Sattelmayer. Combustion Noise Modeling using Chemiluminescence Data as Indicator for the Heat Release Distribution. In *ECM Proceedings*, 2007.
- [155] J. Wäsle, A. Winkler, and T. Sattelmayer. Influence of the Combustion Mode on Acoustic Spectra of Open Turbulent Swirl Flames. In *12th International Congress on Sound and Vibration*, 2005.
- [156] J. Wäsle, A. Winkler, and T. Sattelmayer. Spatial Coherence of the Heat Release Fluctuations in Turbulent Jet and Swirl Flames. *Flow, Turbulence and Combustion*, 75:29–50, 2005.
- [157] X. Zhou, Z. Sun, G. Brenner, and F. Durst. Combustion Modeling of Turbulent Jet Diffusion H₂/Air Flame with Detailed Chemistry. *International Journal of Heat and Mass Transfer*, 43(12):2075 – 2088, 2000.